

ASSESSMENT OF THE FRICTION BEHAVIOUR OF SELECTED  
BASE OILS UNDER OSCILLATORY SLIDING CONDITIONS

Sipho Masilela

# ASSESSMENT OF THE FRICTION BEHAVIOUR OF SELECTED BASE OILS UNDER OSCILLATORY SLIDING CONDITIONS

By

Sipho Masilela

A dissertation submitted in partial fulfilment of the requirements of the  
degree

Master of Engineering (Chemical Engineering)

In the  
Department of Chemical Engineering  
University of Pretoria  
Pretoria

08 April 2018

# ASSESSMENT OF THE FRICTION BEHAVIOUR OF SELECTED BASE OILS UNDER OSCILLATORY SLIDING CONDITIONS

## Synopsis

This work reports on a comparative study of the tribological characteristics of seven base oils, which include mineral and synthetic oils with different physical properties. The friction behaviour of the base oils was studied through friction tests which were performed under varying operating temperatures and sliding loads using a steel-on-steel point contact under pure sliding conditions. Friction coefficients of the seven oils were measured with an SRV4<sup>®</sup> tribometer using a ball-on-disc contact configuration, and were summarized in the form of Stribeck curves. These curves, which make use of a modified Stribeck parameter, were examined in order to analyze the influence of the operating temperature, sliding load and the physical properties of the base oils on the coefficient of friction in the elastohydrodynamic and mixed friction lubrication regimes. Particular attention was given to the coefficient of friction in the mixed film lubrication regime. The surfaces were AISI 52100 steel ball and disc. The average loads (range: 50 – 250 N), temperatures (range: 40 – 120 °C), and a sliding speed of 0.2 m.s<sup>-1</sup> were selected as the test conditions. The seven base oils were selected from four API base oil groups (I, III, III+ and IV).

The following findings were made from this study:

- The friction coefficient showed a strong dependency on the operating temperature, normal applied load and base oil type.
- The coefficients of friction decreased gradually as the load was increased from 50 to 250 N at all test temperatures.
- The presence of dissolved water strongly affects friction behaviour of the base oils studied.
- The PAO (4cSt) base oil was the most affected by dissolved water.

- High base oil polarity alone is not enough to conclude strong adsorption, film formation and friction reduction.
- The type of adsorption mechanism followed by the base oil molecules influences the strength of the bonding on the steel surfaces.
- The highly saturated (PAO and GIII+) base oils proved to adsorb via the H atom of the C-H molecules which creates a weak van der Waals bond with the steel surface.
- The less saturated base oils (GI and GIII) demonstrated chemisorption, via the C-C atoms where a double bond is broken, forming covalent bond with the steel surfaces.
- The highly saturated (PAO and GIII+) base oils demonstrated better thermal stability compared to the less saturated base oils (GI and GIII).
- The less saturated base oils (GI and GIII) experienced bond dissociations which result in film breakdown, largely between 80 and 120 °C.
- The mixed film regime was the dominating operating regime at all the experimental conditions with all seven base oils.
- External friction mechanisms dominated the friction behaviour observed with all the base oils, even in the EHD regime where internal friction is significant with the increasing normal load.
- Viscosity showed a predominant influence on the film forming characteristics of the seven base oils at 40 and 60 °C.
- The pressure-viscosity coefficient decreases with increasing temperature.
- The pressure-viscosity coefficient can be used to predict the film forming behaviour of base oils. The response of the pressure-viscosity coefficient to temperature gave a direct indication of the oils ability to form a lubricating film at a particular temperature and under a gradual application of pressure.
- The base oils from supplier 1 (GIII S1 (4cSt) and GIII S1 (6cSt)) showed similar friction behaviour with the gradual load increase at similar temperatures.

KEYWORDS: base oil, coefficient of friction, viscosity, Stribeck parameter, saturation.

## **Acknowledgements**

I would like to thank the Sasol Research team, Dr Stefan de Goede and Ms Belinda Fraser, for the continuous support and guidance, and for the supply of lubricating oils for my research.

I would also like to thank my family, my mother Mrs Elizabeth Masilela and my siblings Nicholas, Rodney and Charlotte, for all the support they have provided throughout my studies.

Finally, I would like to thank my study leader, Prof. Philip de Vaal, for giving me the opportunity to complete a master's degree in tribology and for the mentorship, guidance and patience throughout my research.

## Contents

Synopsis.....	i
Nomenclature.....	viii
1. Introduction.....	1
2. Theory .....	5
2.1 Tribology and the tribosystem .....	5
2.2 Solid surfaces.....	7
2.2.1 Conformal and nonconformal surfaces.....	9
2.2.2 Contacts between solid surfaces.....	10
2.2.3 Surface stresses.....	15
2.2.4 Nominal Point Contacts .....	16
2.2.5 Surface sliding contacts.....	18
2.3 Friction in sliding contacts .....	20
2.3.1 Coefficient of friction .....	20
2.3.3 Friction in lubricated contacts .....	21
2.3.2 Internal friction .....	22
2.3.3 Effect friction force on friction characteristics.....	37
2.3.4 Initial sliding in metal contacts (Running-in).....	38
2.3.4 Thermal Effects of Friction.....	40
2.3.5 Seizure .....	40
2.3.6 Physicochemistry on sliding surfaces .....	42
2.4 Wear in sliding contacts .....	50
2.4.1 Adhesive wear in a sliding contact.....	50
2.4.2 Fatigue wear in a sliding contact .....	52
2.4.3 Abrasive wear in a sliding contact .....	53

2.4	Lubricating regimes.....	56
2.4.1	Hydrodynamic Lubrication .....	57
2.4.2	Elastohydrodynamic Lubrication.....	60
2.4.3	Mixed Lubrication .....	63
2.4.4	Hydrodynamic films .....	66
2.4.5	Boundary Lubrication.....	69
2.4.6	Stribeck Diagram .....	71
2.5	Properties of base oils.....	74
2.5.1	Mineral oil base stocks .....	74
2.5.2	Synthetic Oil Base Stocks.....	78
2.5.3	Base oil properties.....	80
2.5.4	Group III+ Base oils .....	80
2.5.5	Viscosity and VI .....	81
2.5.6	Viscosity temperature relationship.....	84
2.5.7	Viscosity pressure relationship .....	85
2.5.7	Viscosity Index.....	89
2.6	Water: role in lubrication .....	90
2.6.1	Solubility of water in hydrocarbons .....	91
2.6.2	Relative Humidity.....	93
2.6.3	Diffusion.....	94
2.6.4	Forms of water in oil .....	96
3.	Experimental.....	98
3.1	Test apparatus .....	98
3.1.1	SRV tribometer .....	98
3.1.2	Viscometer.....	99

3.1.3	Ultrasonic Cleaner .....	99
3.1.3	Relative humidity control.....	100
3.2	Experimental conditions and procedure .....	101
3.3	Lubricants.....	103
3.4	Film thickness calculation .....	103
4.	Results and discussion .....	105
4.1	Physical properties.....	105
4.1.1	Viscosity Index (VI):.....	105
4.1.2	Viscosity: Effects of temperature .....	105
4.1.3	Viscosity: Effects of pressure.....	108
4.2	Friction tests.....	116
4.2.1	Effects of water on friction .....	116
4.2.2	Effects of load and temperature on the coefficient of friction .....	118
4.2.2	Stribeck curves .....	138
4.2.3	Pressure-viscosity coefficient: Effects of temperature .....	143
4.2.4	Modified Stribeck curves.....	146
4.2.5	Modified Stribeck curves: Comparison of the base oils .....	155
4.3	Film thickness .....	166
5.	Conclusions .....	172
5.1	Physical Properties .....	173
5.1.1	Effects of temperature on viscosity .....	173
5.1.2	Viscosity Index.....	173
5.1.2	Effects of pressure on viscosity .....	173
4.1.3	Pressure viscosity coefficient.....	174
5.2	Effects of load on COF .....	174



5.3	Effects of temperature on COF .....	174
5.4	Stribeck curves.....	175
5.5	Film thickness .....	176
6.	Recommendations.....	178
7.	References .....	179
	Appendices .....	184
	Appendix A.....	184
	Viscosity determination at 120 °C.....	184
	Appendix B.....	185
	Hertzian Pressure calculation .....	185
	Appendix C .....	186
	Piezoviscous effect results .....	186
	Appendix D .....	186
	Standard deviation from COF raw data .....	186
	Appendix E.....	190
	Central film thickness calculation.....	190
	Appendix F.....	192
	Humidity control.....	192

## Nomenclature

A	cross sectional area	[m <sup>2</sup> ]
A <sub>r</sub>	real area of contact with tangential force present	[m <sup>2</sup> ]
A <sub>ro</sub>	real area of contact with tangential force absent	[m <sup>2</sup> ]
a	radius of the contact circle	[m]
a <sub>k</sub>	semi-axis of the contact ellipse in the transverse direction	[m]
b	semi-axis in the direction of motion	[m]
C <sub>m</sub>	Chu and Cameron viscosity-pressure parameter	[Pa <sup>-1</sup> ]
C	arbitrary constant assumed to have a value close to 10	[-]
C <sub>p</sub>	Roelands constant	[N/m <sup>2</sup> ]
c	is the total concentration	[mol/m <sup>3</sup> ]
D <sub>AB</sub>	is the diffusivity of A in B	[m <sup>2</sup> /s]
d	displacement	[μm]
E	Young's modulus	[GPa]
E <sub>b</sub>	ball young's modulus	[GPa]
E <sub>d</sub>	disc young's modulus	[GPa]
E*	Effective Young's modulus	[GPa]
F <sub>N</sub>	normal contact load	[N]
F <sub>R</sub>	ploughing friction load or force	[N]
F <sub>R</sub>	reciprocating friction load or force	[N]
F	is the friction force	[N]

G	material influence parameter, $\alpha E^*$	[-]
h	height	[m]
$H_m$	Hardness of material	[HV}
H	parameter for VI determination at 100 °C of the oil	[-]
$h_{min}$	minimum film thickness	[m]
$h_c$	centre film thickness	[m]
$H_c$	is the Henry's law solubility constant	[kPa/mol. fr.]
$K_{eq}$	equilibrium constant	[-]
$\kappa$	eliptic parameter	[-]
L	parameter for VI determination at 100 °C of the oil	[-]
$M_w$	adsorbate molecules	[-]
$M_{AW}$	adsorbed complex	[-]
$N_\infty$	Roelands constant	[N.s/m <sup>2</sup> ]
N	neutral point in gear meshing (non-slip, pure rolling)	[-]
n	Chu and Cameron pressure-viscosity constant	[-]
P	pressure	[Pa]
$P_m$	mean pressure	[Pa]
$P_s$	Saturation pressure of water	[Pa]
$P_w$	is the partial pressure of water vapor in air	[Pa]
$P_o$	maximum Hertzian pressure	[GPa]
$P_y$	plastic flow stress (yield pressure) of the material	[Pa]
$p_x$	plastic flow stress in the absence of frictional force	[Pa]

R	reduced surface roughness	[ $\mu\text{m}$ ]
$R_b$	ball surface roughness	[ $\mu\text{m}$ ]
$R_d$	disc surface roughness	[ $\mu\text{m}$ ]
$R_a$	arithmetic mean surface roughness	[ $\mu\text{m}$ ]
$R_q$	root mean square	[ $\mu\text{m}$ ]
$R_z$	ten point mean surface roughness	[ $\mu\text{m}$ ]
$R_x$	is the reduced radius of curvature	[m]
$r_b$	ball radius	[m]
$r_d$	disc radius	[m]
$r_x$	ball radius in the x-direction	[m]
$r_y$	ball radius in the y-direction	[m]
S	Solubility of water	[ppm]
s	constant for pressure-viscosity calculation	[-]
$S_E$	the empty site on adsorbent surface	[-]
$S_o$	Roelands thermoviscosity parameter	[-]
$S_p$	Stribeck parameter	[ $\text{m}^{-1}$ ]
$S_p$	modified Stribeck parameter	[-]
t	constant for pressure-viscosity calculation	[-]
T	temperature	[ $^{\circ}\text{C}$ ]
$T_o$	reference temperature or oil bath temperature	[ $^{\circ}\text{C}$ ]
U	speed influence parameter, $u\eta/E^*R_x$	[-]

$u_a$	disc surface speed	$[\text{m}\cdot\text{s}^{-1}]$
$u_b$	ball surface speed	$[\text{m}\cdot\text{s}^{-1}]$
$u_d$	disc surface speed	$[\text{m}\cdot\text{s}^{-1}]$
$U_v$	kinematic viscosity of oil at 40 °C for VI determination	$[\text{cSt}]$
$u_{\text{avg}}$	average tangential speed	$[\text{m}\cdot\text{s}^{-1}]$
$V_M$	is the volume of the monolayer	$[\text{m}^3]$
$V$	volume of adsorbate adsorbed onto a solid adsorbent	$[\text{m}^3]$
VI	Viscosity index	$[-]$
$v_1$	initial speed of the sheet metal	$[\text{m}\cdot\text{s}^{-1}]$
$v_2$	final speed of the sheet metal	$[\text{m}\cdot\text{s}^{-1}]$
$v_3$	speed of the roller	$[\text{m}\cdot\text{s}^{-1}]$
$v_r$	speed difference in the roll gap (sliding part)	$[\text{m}\cdot\text{s}^{-1}]$
$W$	load influence parameter, $F_N/E^*R_x^2$	$[-]$
$w_a$	squeeze velocity	$[\text{m}\cdot\text{s}^{-1}]$
$w_z$	bearing load	$[\text{N}]$
$W_A$	molar flux of component A	$[\text{mol}/\text{m}^2\text{s}]$
$W_B$	molar flux of component B	$[\text{mol}/\text{m}^2\text{s}]$
$y_A$	is the molar fraction of component A	$[-]$
$y_B$	is the molar fraction of component B	$[-]$
$\omega_1$	angular velocity of body 1	$[\text{rad}\cdot\text{s}^{-1}]$
$\omega_2$	angular velocity of body 2	$[\text{rad}\cdot\text{s}^{-1}]$

$Z_1$	Roelands Viscosity-pressure index	[-]
A,B,C	regression coefficients	[-]
$\mu$	Coefficient of friction	[-]
$\Lambda$	specific film thickness	[-]
$\tau$	shear stress	[Pa]
$\tau_{\max}$	maximum shear stress	[Pa]
$\alpha$	pressure-viscosity coefficient	[N.m <sup>-2</sup> ]
$\nu$	Poisson's ratio	[-]
$\eta$	dynamic viscosity	[Pa.s]
$\eta_o$	dynamic viscosity at $P_o$ ( $P_{\text{atm}}$ ) and constant temperature	[Pa.s]
$\eta_k$	Kinematic viscosity	[cSt]
$\eta_{40}$	kinematic viscosity at 40 °C	[cSt]
$\eta_{100}$	kinematic viscosity at 100 °C	[cSt]
$\rho$	density	[Kg.m <sup>-3</sup> ]
$\sigma$	combined root mean square roughness	[m]
$\sigma_n$	surface normal stresses	[Pa]
$\sigma_{rr}$	surface stresses in the r direction	[Pa]
$\sigma_{\theta\theta}$	surface stresses in the $\theta$ direction	[Pa]
$\sigma_{zz}$	surface stresses in the z direction	[Pa]
$\theta_A$	is the fractional occupancy of the adsorption sites	[-]

## 1. Introduction

Friction consumes large amounts of energy, which along with wear-related energy and material losses, costs about 5%–7% of the gross national product in most industrialized nations. The reduction of friction is therefore a priority, since it will benefit the economic well-being of all nations (Meirong et al, 2017). One of the most common ways to reduce friction is through lubrication. Lubrication aims to reduce the friction on a surface with a bearing capacity and tangential shear strength, and it has become one of the core techniques for the purpose of reducing carbon emissions and saving energy. The use of lubricants to control friction has been practiced since ancient times, however, the scientific focus on lubricants and lubrication technology is fairly recent (Dresel & Mang, 2017: 11 and Ichiro, 2017).

The worldwide drive for better performing and more environmentally-friendly lubricating oils is a continuous process supported by on-going research (Dresel & Mang, 2017: 5). The world's biggest consumers of lubricating oils are automobile and truck engines, going through 20 million tons per year, which is about half of the world's total lubricant use. The automobile and truck engine makers are pushing continuously to meet the stiffening efficiency and pollution standards and as a result, the need for better quality engine oils becomes inevitable. Oil companies are therefore forced to develop better formulation technologies to meet these demands (Brown, 2015 and Dresel & Mang, 2017: 2). Providing affordable, energy efficient and lasting lubrication for automobile and truck engines (whose operation produces large amounts of sliding, high temperatures and high contact pressures) is important in order to reduce friction losses and improve fuel economy (Vengudusamy *et al*, 2014 and Cai *et al*, 2015).

The ability of a lubricant to reduce friction in mechanical surfaces which are in relative sliding motion depends on the base oil behavior during operation. This behaviour is determined by properties such as the molecular structure (carbon chain length, degree of unsaturation and branching of the molecular chains), the presence of contaminants and the physical properties such as viscosity, viscosity index and contamination (Brown, 2015 & Maru *et al*, 2013). The contributing mechanical factors which influence the

overall tribological performance of lubricated systems generally include the mechanical design of the systems, material compositions, mechanical properties and operation conditions (Cai et al, 2015). Lubricating oils with a strong film-forming ability can effectively separate interacting metal surfaces, leading to reduced friction between the surfaces under specified operating conditions (Ichiro, 2017). This reduction in friction directly results in a reduction of unpleasant noises, vibrations and wear, and ultimately, a prolonged operational life. Therefore, measurements of friction and wear are essential to understand the effectiveness of a lubricant during operation (HSU et al, 2014 and Zhao et al, 2016).

The friction variation with operating conditions at the lubricated interfaces may be compared in terms of the coefficient of friction by means of Stribeck curves. These curves are for the coefficient of friction as a function of the Hersey number. The Hersey number is a parameter which shows the dependency of the coefficient of friction on the three parameters [i.e., speed ( $u$ ), oil viscosity ( $\eta$ ) and normal load ( $F_N$ )] is given by the dimensionless ratio  $(u \eta) / F_N$ , whereby  $F_N$  is the load applied per unit length. The Stribeck curve concept has been accepted as an overall observation of friction variation in the entire range of lubrication conditions including the hydrodynamic, mixed and boundary lubrication regimes (Zhao et al, 2016). Many researchers have used this concept as the basis to analyze the influences of lubricant viscosity, which is related to both base oil and operating conditions (i.e., temperature), on tribological properties of lubricants and contact interfaces (Brandao et al, 2012 & Zhao et al, 2016). Also, most of the research work done highlights the dependency of the coefficient of friction on the operating speed under various operating conditions, more work still has been done to illustrate the relationship between coefficient of friction and applied normal load.

Base oils are classified into groups, ranging from Group I to Group V, according to the source of crude and their formulation process which fixes their physical properties and performance (Dresel and Mang, 2017: 72). The molecular structure (carbon chain length, degree of unsaturation and branching of the molecular chains), the presence of contaminants and the physical properties such as viscosity, viscosity index and purity



properties which have a significant impact on base oil behaviour have a critical influence on base oil behaviour during service (Brown, 2015 & Maru et al, 2013). The classification system for base oils, as done by the American Petroleum Institute (API), is a useful way of keeping track of the development of base oils (Dresel and Mang, 2017: 72).

Group I base oils are solvent-refined mineral oils and the least expensive base stock which provides satisfactory volatility and oxidation stability, low temperature performance, good solvency for additives. Group II base oils are mostly solvent refined oils with improved oxidation stability and volatility compared to Group I base oils. Group III base oils are hydro-processed paraffinic mineral oils and can also be produced by wax isomerization. These are known for ultra-high viscosity, better oxidation stability and volatility than the Group I and Group II mineral base oils (Dresel and Mang, 2017: 55 - 72). Group IV and Group V base oils are fully synthetic oils and are polyalphaolephin (PAO) and Polyisobutylene (PIB) based, respectively. The synthetic base oils have, by far, proved to be the most efficient, environmentally friendly and commercially available base oils. They have good oxidative stability, volatility and low pour points. However, they are more expensive compared to the base oils in the lower API Groups. This makes the need for more economical base oils prevalent (Donaghy et al, 2013).

The development of the hydrocracked base oils has shown great potential to achieve the balance between cost and performance. The physical characteristics of the hydrocracked base oils vary between Group III base oils and polyalphaolefins (Group IV). These oils are classified as Group III+ (plus) base oils, which forms a subgroup of the API Group III (Dresel and Mang, 2017: 73). The latter category is not official, but it is recognized by industry for marketing purposes (Baker et al, 2007 and Wheeler, 2016). The overall tribological performance of commercial Group III+ base oils is expected to vary between that of Group III base oils and PAO's, or to be similar to that of PAO's. Therefore, the characteristic tribological performance of the Group III+ base oils has to be determined and measured against other commercial base oils, with

the focus on the Group III and Group IV (PAO) base oils. This formed a basis for this investigation.

The aim of this investigation was to study and compare the characteristic tribological performance of base oils from different API groups (including a Group III+ base oil) using Stribeck curves. The work was done by performing friction tests on a steel-on-steel point contact under pure sliding conditions using the SRV tribometer. The friction coefficients for the seven base oils were measured with the SRV tribometer, and were summarized in the form of Stribeck curves. These curves, which make use of a modified Stribeck parameter, were constructed under a gradually increasing load condition at different temperatures. They were then examined in order to analyze the influence of the operating temperature, increasing load and the chemical composition of the base oils on the coefficient of friction in the hydrodynamic, elastohydrodynamic, mixed and boundary friction lubrication regimes. Particular attention was given to the coefficient of friction in the mixed and boundary lubrication regimes. The contacting surfaces were AISI 52100 steel ball and disc. The average contact load range (50 – 250 N), temperatures (40, 60, 80, 100 and 120 °C), and average sliding speed of 0.2 m.s<sup>-1</sup> were selected as the test conditions. A total of seven base oils were selected from four API base oil groups (I, III, III+ and IV).

## **2. Theory**

In this section, the principles, terminology and theories which play an important role in this investigation are discussed. The first part focuses on tribology as a topic and tribosystems in general. This is followed by a discussion of the tribological characteristics of the mechanical components which form a tribosystem, and the underlying principles involved in the operation of tribosystems. The last part of this section discusses the physical and chemical properties of the lubricants which are the focus of this investigation.

### **2.1 Tribology and the tribosystem**

Tribology is the study of the interaction between surfaces in contact (Bhushan, 2013: 1). This study mainly focuses on friction, wear and lubrication of interacting surfaces. Tribology spans many disciplines, from physics and chemistry to mechanical engineering and material science, and is of extreme technological importance (Dresel & Mang, 2017: 11).

Tribology is widely applicable in components of moving mechanical machinery which include i.e., bearing applications and piston rings and the cylinder wall or camshaft lobes, which are the main components of internal combustion engines. A tribosystem (shown in Figure 2.1) consists of four components:

1. the one contacting body;
2. the opposing contacting body (material pair);
3. the interface between the two contacting bodies and the medium in the interface;
4. the environment.

In lubricated bearing applications, the lubricant is located in the gap (3 in Figure 2.1) between the contacting bodies. The material pair in plain bearings is the shaft and the bearing shells, and in internal combustion engines they are the piston rings and the cylinder wall or the camshaft lobes (Dresel & Mang, 2017: 12).

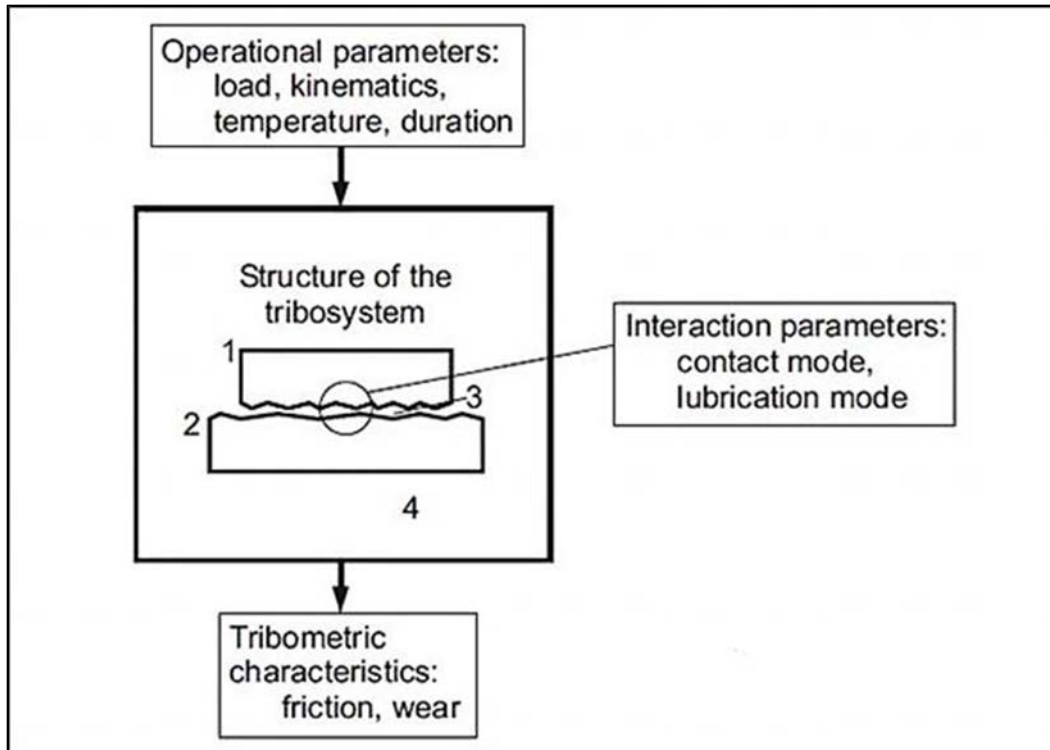


Figure 2.1: Structure of a tribosystem (Dresel & Mang, 2017: 12).

In a tribosystem, there are several variables (sometimes referred to as tribometric variables) which can be manipulated to ensure operation of the system. Also, there are tribometric parameters which can be measured in to gain understanding about the operation of the system. The tribometric variables are the type of movement, the forces involved, temperature, speed, and duration of the stress. The tribometric parameters include data of friction, wear, and temperature measurements which can be gathered from the stress area (Dresel & Mang, 2017: 12).

The tribological stress is the result of the different types of surface geometries; surface loading; type of surface contact and lubricant thickness (commonly referred to as viscosity). There are several types of tribological processes which can occur in the contact area between two surfaces in relative motion. Some of these processes can be physical, physicochemical (i.e., adsorption, desorption), and/or chemical in nature (i.e., tribochemistry) (Dresel & Mang, 2017: 12).

## 2.2 Solid surfaces

On the microscopic scale, no real solid surface is truly smooth. Solid surfaces contain irregularities from their prescribed geometrical form, which give them a level of roughness on the surface, irrespective of the method of formation (Bhushan, 2013: 9). Even the smoothest solid surfaces such as those obtained by cleavage of crystals contain irregularities with heights exceeding the interatomic distances (Bhushan, 2013: 9). These irregularities are of differing orders which range from shape deviations to the orders of interatomic distances. However, the random components of the surface profiles look very much the same whatever their source, irrespective of the absolute scale of size involved. Solid surfaces are composed of atoms arranged in a two-dimensional configuration. This configuration closely approximates to a plane in most cases but there are nearly always significant deviations from a true plane (Stachowiak & Batchelor, 2014: 477).

For technological applications, the surface texture of solid surfaces is important, especially when surface interactions are concerned. This is because surface texture affects the real area of contact of the contacting bodies, the friction and wear, and lubrication (Bhushan, 2013: 9). Figure 2.2 shows similarities between a roller bearing and ball bearing surfaces profiles at different scales.

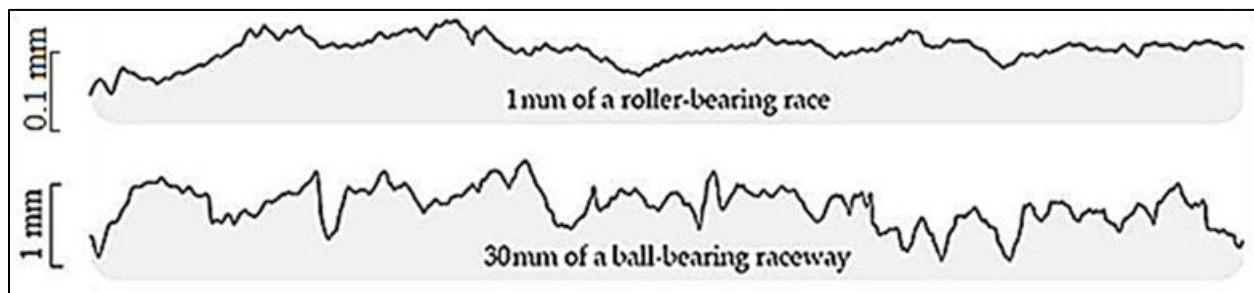


Figure 2.2: Similarities between surface profiles of bearings (Stachowiak & Batchelor, 2014: 477).

Studies have shown that without the irregularities, the surfaces would probably be inert to chemical reactants. The properties of the solid surfaces promote chemical reactions between the surface and the lubricant. The reactions between lubricant and surface normally produce a surface layer (film) which reduces friction and wear (Stachowiak & Batchelor, 2014: 477). Surface textures are also important for thermal performance of solid surfaces, especially where heat transfer is of critical importance (Bhushan, 2013: 9). The atoms present on solid surfaces normally have a lower bonding strength than interior atoms because they have a lower number of adjacent atoms. Therefore, most solid surfaces contain areas which have physicochemical properties that are different to those of the overall material (Stachowiak & Batchelor, 2014: 477).

Due to the forming process followed in some metals and alloys, there is a section of deformed material on top of which is a region of microcrystalline or amorphous layer which is termed the Beilby layer. The Beilby layers are of critical importance because their surface properties can be entirely different from the bulk material itself. The differences in surface properties of the Beilby layer to the bulk material influence the material mechanical behaviour, depending on the amount and depth of deformation of the surface layers (Bhushan, 2013: 10).

The development of the Beilby layer also changes the texture of the surface (Bhushan, 2013: 10). Surface texture is defined as surface roughness in surface engineering terms, and it generally refers to the differences in the peaks (height) on the solid surface relative to a reference plane, and is measured along a set of parallel line profiles or along a single line profile (Stachowiak & Batchelor, 2014: 480). All metal, alloys and many nonmetals form surface oxide layers in the presence of oxygen (air). There are other environments which also promote formation of other layers such as nitrides, sulfides, and chlorides. The presence of solid surface films affects tribometric parameters such as friction and wear. A schematic of the typical solid surface layers is shown in Figure 2.3. Apart from the surface oxide layers, there are also adsorbed films that are produced by chemical processes such as physisorption or chemisorption of

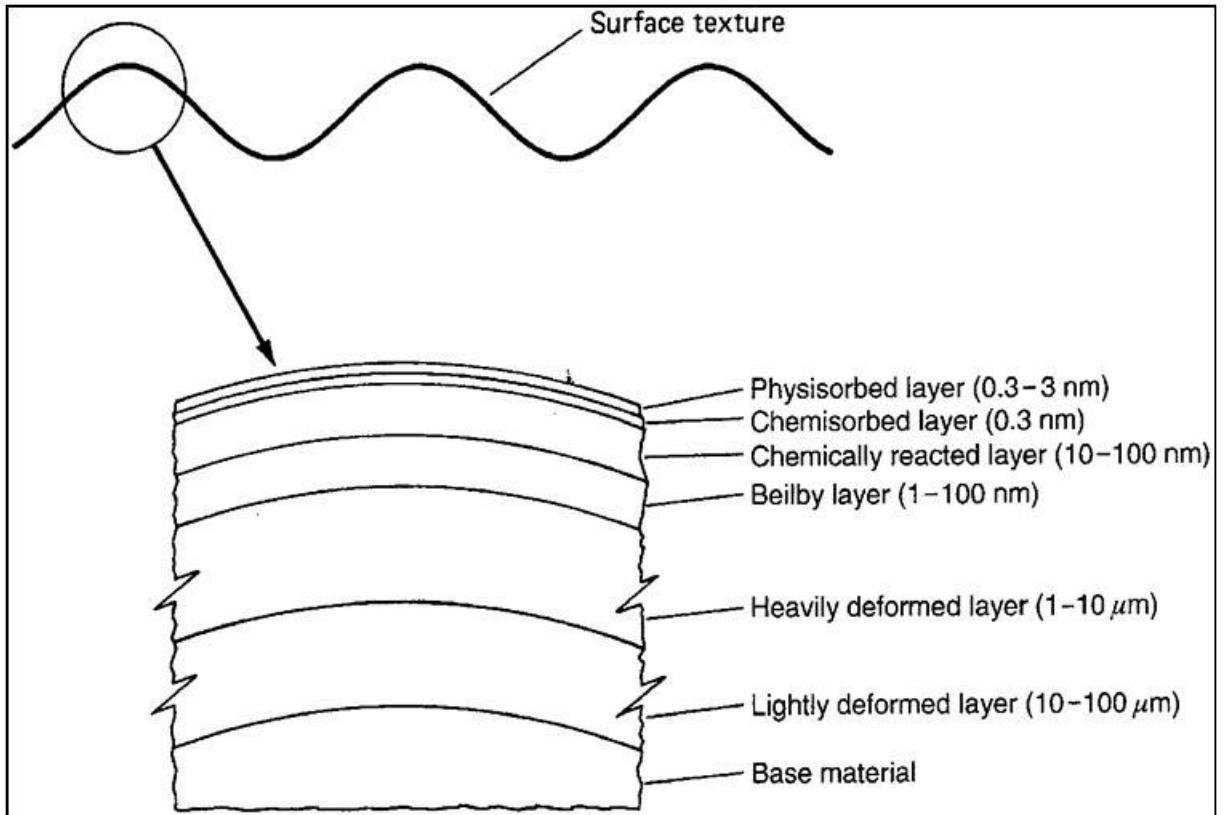


Figure 2.3: Solid surface layers and texture (magnified) (Bhushan, 2013: 10).

oxygen, water vapor and hydrocarbons, from the surrounding environment (Bhushan, 2013: 10). The effects of the adsorbed films are significant on the surface interactions of solid surfaces. In most instances, the surface films wear out during the initial “running-in period” and ultimately end up having no effect on the surface interactions (Bhushan, 2013: 10).

### 2.2.1 Conformal and nonconformal surfaces

Interacting surfaces in most practical tribosystems are of different geometries (Hamrock *et al*, 2004: 2). The geometry of the interacting surfaces determines the level of conformity during contact. Conformal surfaces fit closely into each other with a high degree of geometrical conformity. In most cases conformal surfaces have the same radii of curvature. The high degree of conformity in conformal surfaces results in a large area of contact between the interacting surfaces and as a result, the applied load is

carried over a large area. This load-carrying surface area remains the same while the load is increased (Hamrock *et al*, 2004: 2). Most interacting mechanical components that are lubricated have surfaces that are nonconformal. In these applications, the full burden of the applied load must then be carried by a small lubrication area. The lubrication area of a nonconformal contact is typically three orders of magnitude less than that of a conformal contact. The lubrication area between nonconformal surfaces increases significantly with increasing applied load, however, it is still smaller than the lubrication area between conformal surfaces (Hamrock *et al*, 2004: 2).

### 2.2.2 Contacts between solid surfaces

Since no real surface is perfectly smooth on the microscopic scale, when the two solid bodies are forced to make contact they will touch first at the peaks (asperities) and some deformation of the material occurs on a very small scale at these asperities. Figure 2.4 gives a schematic representation.

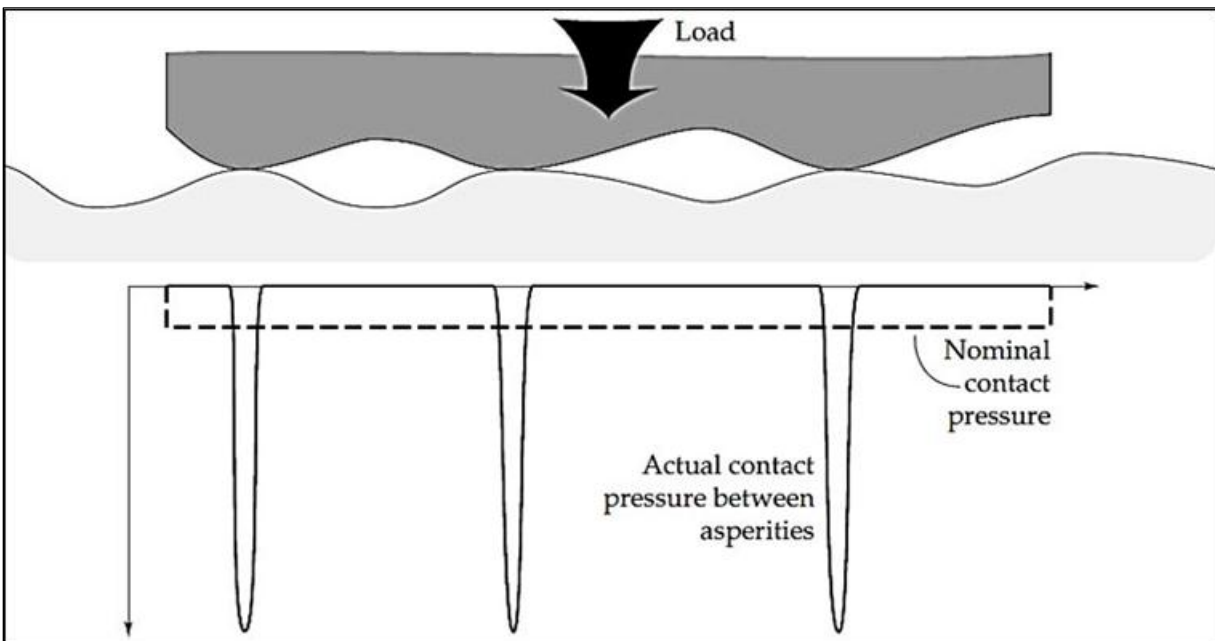


Figure 2.4: Contact stresses between asperities (Stachowiak & Batchelor, 2014: 494).



As shown in Figure 2.4, surface roughness limits the contact between solid bodies to a very small portion of the apparent contact area. In these areas of contact, stresses are generated, whose total effect are to balance the applied load. The assumption is made in mechanics that the deforming materials are isotropic and homogeneous and in principle, this means that the results from the contact at the asperities can be applied both to global contacts and to those between interacting asperities (Bhushan, 2013: 91). When two solid surfaces are loaded together there will always be some level of deformation of each of them (Bhushan, 2013: 91).

The deformations that occur can be elastic or may have some level of plasticity which may result in permanent changes in shape. These changes in the surface profiles of the components can be looked at from two different scales, the macroscopic scale and the microscopic scale. If one considers the type of contact between a heavily loaded roller and the inner and outer races in a rolling element bearing, the level of flattening of the rollers can be expressed as a proportion of their radii at a relatively macroscopic scale (Bhushan, 2013: 91 and Stachowiak & Batchelor, 2014: 494).

### **Contacts of spheres and flat planes**

When two bodies with different radii of curvature are pressed into contact, they will touch at a point initially. If the force applied between the bodies is increased, elastic deformation enlarges these points into contact areas across which the loads are distributed as pressures (Bhushan, 2013: 92). These types of contacts are referred to as Hertzian contacts since the contact between the two solids is at a point and involves large stresses (Bhushan, 2013: 92). An illustrated is given in Figure 2.5, and Figure 2.6 for various other contacts found in:

1. Roller bearing;
2. Gear wheels;
3. Chain wheels;
4. Roller on flat path;
5. Cam lifter.

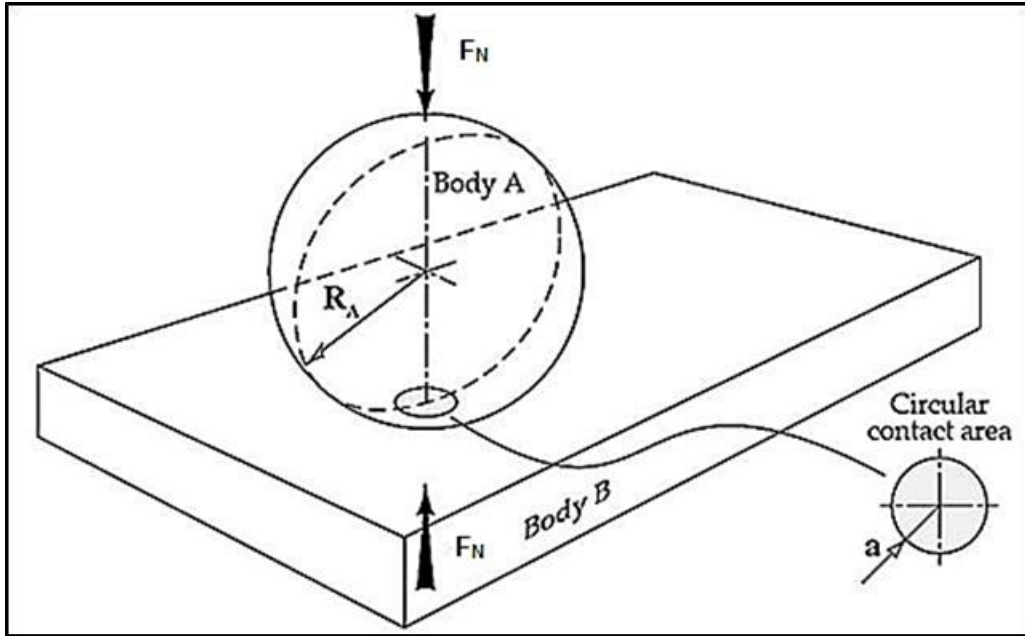


Figure 2.5: Contact of sphere and a flat plane (Stachowiak & Batchelor, 2014: 305).

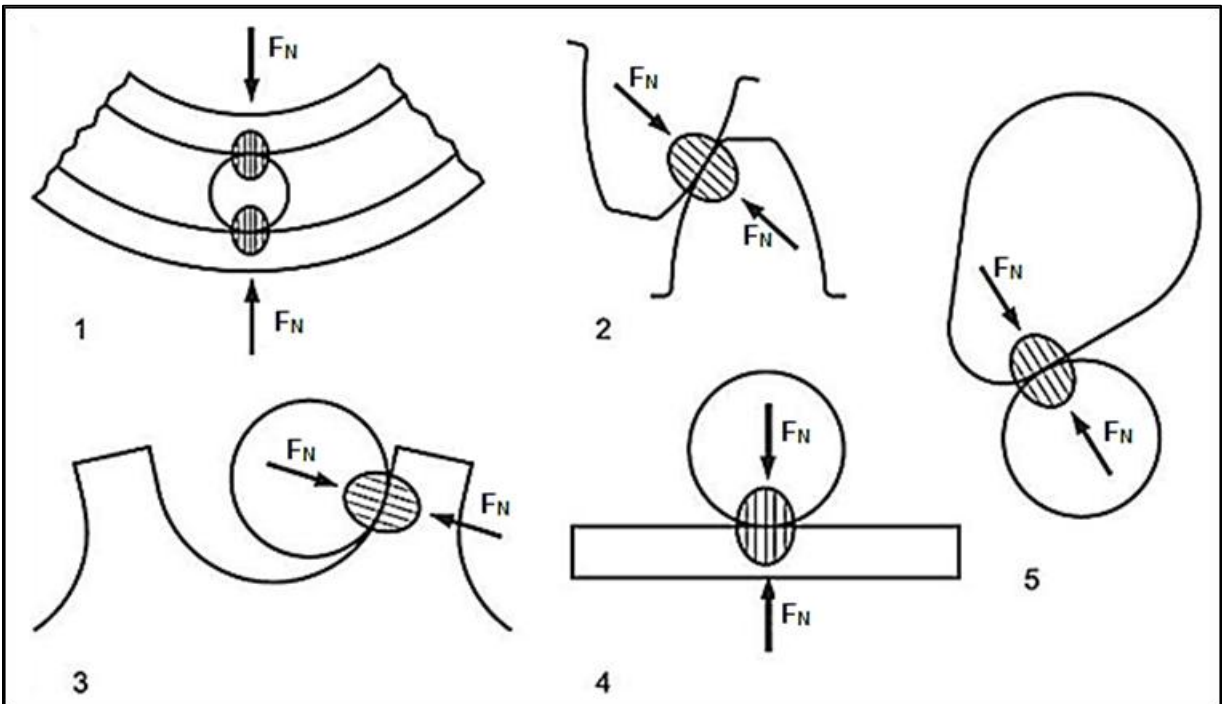


Figure 2.6: Hertzian contacts for different pairs with nonconformal lubricant clearance.

(Dresel & Mang, 2017: 21).

The analysis of this scenario was first presented by Heinrich Hertz in 1881 and is based on the following assumptions:

1. The surfaces are continuous, smooth, nonconforming and frictionless;
2. The size of the contact area is small compared to the size of the bodies (i.e., the strains associated with the deformations are small);
3. Each solid can be considered to behave as an elastic half-space in the vicinity of the contact zone; and
4. The gap (h) between the undeformed surfaces can be approximated by an expression of the form:

$$h = Ax^2 + By^2 \quad (2.1)$$

x and y are orthogonal coordinates lying in the common tangent plane to the two surfaces. Although the fourth assumption requires parabolic surface profiles, by implication, the Hertzian analysis is relevant to the contact between spheres, cylinders, and ellipsoids (Bhushan, 2013: 93). The contact parameters for these configurations can be calculated according to the formulae summarized in this section (Stachowiak & Batchelor, 2014: 495). An elastic sphere of radius r indents an elastic plane to depth d, and thus creates a resultant circular contact area of radius (a) such that:

$$a = \left[ \frac{3F_N R_x}{4E^*} \right]^{\frac{1}{3}} \quad (2.2)$$

Where  $E^*$  is the contact modulus defined by:

$$\frac{1}{E^*} = \frac{1-\nu_b^2}{E_b} + \frac{1-\nu_d^2}{E_d} \quad (2.3)$$

Where  $\nu_b$  and  $\nu_d$  are the Poisson ratios of the ball and disk specimen respectively and  $R_x$  is the reduced radius of curvature related to those of the ball and disk specimen by the relation:

$$\frac{1}{R_x} = \frac{1}{R_b} + \frac{1}{R_d} \quad (2.4)$$

Convex surfaces are taken to have positive radii of curvature; those of concave surfaces are negative. The resulting pressure distribution  $P(r)$  is semielliptical of the form:

$$P(r) = P_0 \left[ 1 - \frac{r^2}{a^2} \right]^{\frac{1}{2}} \quad (2.5)$$

Where:

$$a^2 = x^2 + y^2 \quad (2.6)$$

Such a distribution is shown in Figure 2.7 and is characteristic of Hertzian contacts.

The relationship between the maximum pressure  $P_0$  which occurs on the axis of symmetry and the mean pressure  $P_m$  as shown on Figure 2.5 are given by:

$$P_0 = \frac{3}{2} P_m = \frac{3F_N}{2\pi a^2} \quad (2.7)$$

$P_0$  is sometimes known as the Hertzian stress. Under this loading, the centers of the two contacting surfaces move together by the small displacement  $d$  where:

$$d = \frac{a^2}{R} = \frac{a\pi P_0}{2E^*} = \left[ \frac{9F_N^2}{16R_x E^{*2}} \right]^{\frac{1}{3}} \quad (2.8)$$

This situation is illustrated in Figure 2.7 the effective radius of the loaded plane surface then becomes infinite so that the reduced radius of the contact is numerically equal to that of the opposing sphere where (a) illustrates the indentation and (b) illustrates pressure distribution (Bhushan, 2013: 94 and Stachowiak & Batchelor, 2014: 495).

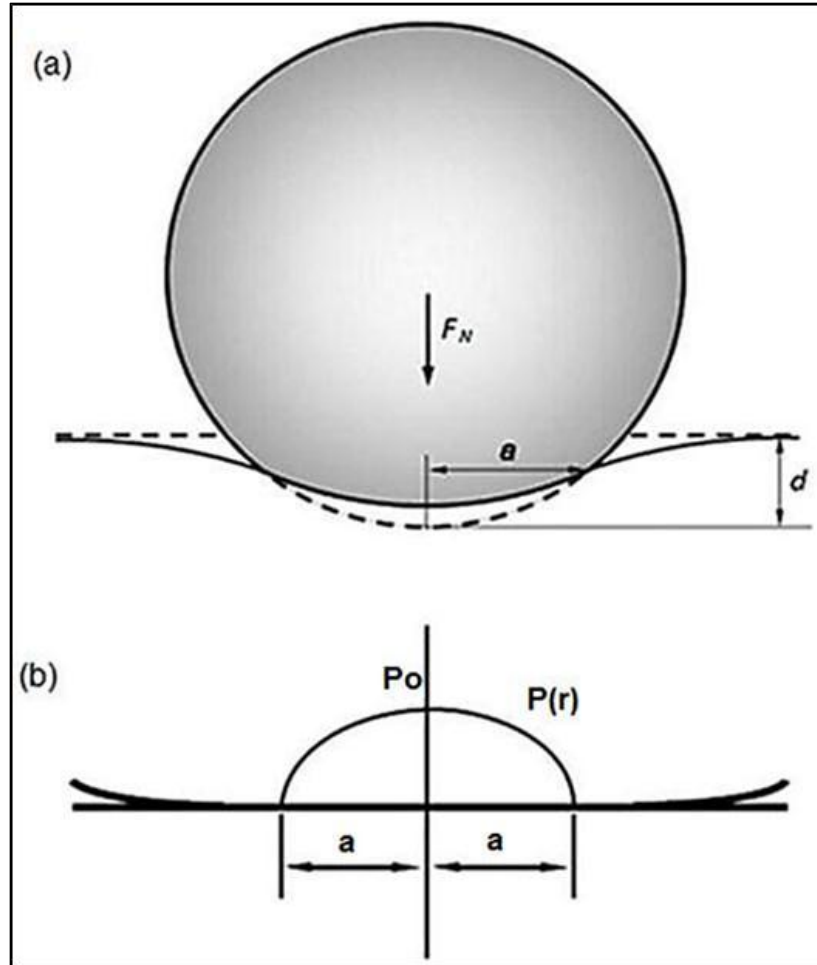


Figure 2.7: Illustration of elastic contact of a sphere with a flat plane (Bhushan, 2013: 94).

### 2.2.3 Surface stresses

The most severe stresses develop in non-conformal contact conditions which apply in most mechanical systems. The Hertzian contacts are of particular interest because the most heavily loaded elements of material lie not at the surface but a small distance beneath it. This is, thus, the site of initial plastic yielding. However, this is in contrast to the situation when the curvature of the surfaces is not continuous, such as those where one of the bodies has the profile of a wedge or cone, when the site of maximum stress lies adjacent to its apex. The analytical solutions for subsurface stresses are known for a limited number of cases (Bhushan, 2013: 95).

## 2.2.4 Nominal Point Contacts

In a situation where of a sphere pressed into contact with a flat plane the pressure within the contact patch (when  $r \leq a$ ) is given by Equation 2.5, and the surface stresses (at  $z = 0$ ) are given in polar coordinates by the following equations (Bhushan, 2013: 95):

$$\frac{\sigma_{rr}}{P_0} = \frac{1-2\nu}{3} \left( \frac{a^2}{r^2} \right) \left[ 1 - \left( 1 - \frac{r^2}{a^2} \right)^{\frac{3}{2}} \right] - \left( 1 - \frac{r^2}{a^2} \right)^{\frac{1}{2}} \quad (2.9)$$

$$\frac{\sigma_{\theta\theta}}{P_0} = -\frac{1-2\nu}{3} \left( \frac{a^2}{r^2} \right) \left[ 1 - \left( 1 - \frac{r^2}{a^2} \right)^{\frac{3}{2}} \right] - 2\nu \left( 1 - \frac{r^2}{a^2} \right)^{\frac{1}{2}} \quad (2.10)$$

$$\frac{\sigma_{zz}}{P_0} = -\frac{p(r)}{P_0} = -\left( 1 - \frac{r^2}{a^2} \right)^{\frac{1}{2}} \quad (2.11)$$

Outside contact patch ( $r \geq a$ )

$$\frac{\sigma_n}{P_0} = -\frac{\sigma_{\theta\theta}}{P_0} = (1 - 2\nu) \frac{a^2}{3r^2} \quad (2.12)$$

Where  $\sigma_{rr}$ ,  $\sigma_{\theta\theta}$  and  $\sigma_{zz}$  are the surface stresses in the radial, angular and vertical direction and  $\nu$  is the Poisson ratio. The form of these surface stress distributions is shown in Figure 2.8 for the case where the Poisson ratio  $\nu = 0.3$  (Steel surfaces). Here, (a) illustrates the stress distributions at the surface and contours of principal shear stress in the subsurface and (b), the stresses along the  $z$  axis of symmetry caused by Hertz pressure acting on a circular area of radius  $a$ . The radial stress is tensile outside the loaded circle and has its maximum value at the edge of the loaded zone when  $a = r$ . This is the site of the largest tensile stress occurring anywhere in the material and is held responsible for the ring cracks often observed when brittle materials make contact (Bhushan, 2013: 97). The radial stress which develops at the center of the contact is compressive. The magnitude of this stress is expressed by  $(1 - 2\nu)P_0/2$ . Therefore, for an incompressible material, with  $\nu = 0.5$ , the stress at the origin is hydrostatic (Bhushan, 2013: 97). Since this is the largest shear stress in the material, the position at which it occurs is most likely the site of the initiation of plasticity (Bhushan, 2013: 94).

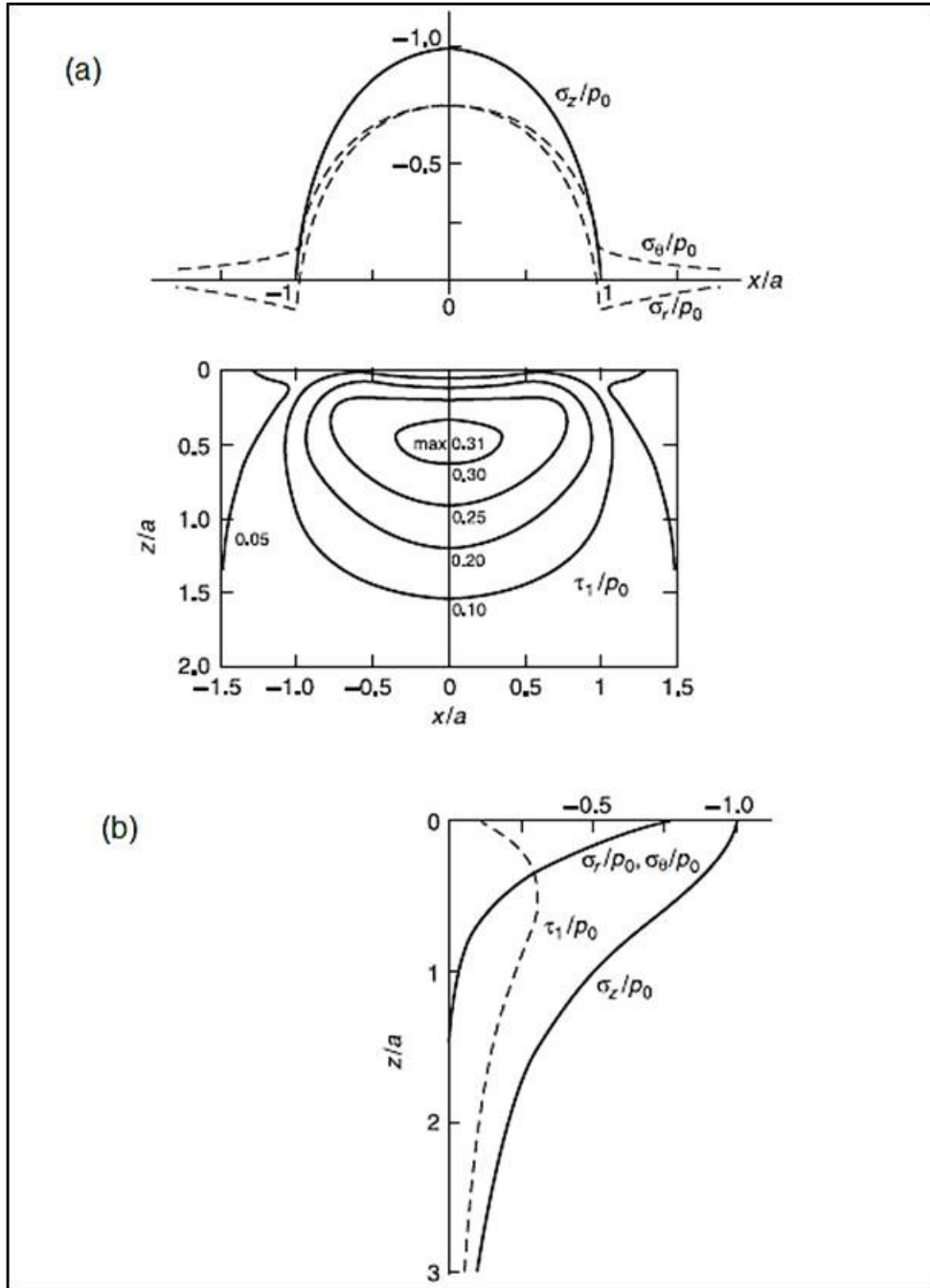


Figure 2.8: Stress distributions at the surface of a point contact; Poisson's ratio  $\nu = 0.3$  (Bhushan, 2013: 97).

The value of the ratio  $T_{\max}/P_0$  and its location ( $z/a$ ) is influenced by the value of Poisson's ratio as shown in Table 2.1.

Table 2.1: Normalized maximum shear stress ( $\tau_{\max}/P_0$ ) and location for Materials (Bhushan, 2013: 99).

Material	Poisson's Ratio	$\tau_{\max}/P_0$	Position (z/a)
Glass	0.20	0.34	0.45
Steel	0.30	0.31	0.48
Aluminium	0.33	0.30	0.50
Rubber	0.50	0.27	0.55

### 2.2.5 Surface sliding contacts

When solid bodies make contact, they are said to roll together if there is a difference in the components of their angular velocities measured along an axis parallel to their common tangent plane (Bhushan, 2013: 482). Consider two cylinders 1 and 2 touching along a common generator, as shown in Figure 2.9a. If the angular velocity  $\omega_1$  is not equal to  $\omega_2$ , both in magnitude and direction (clockwise or counterclockwise), the two cylinders are said to be in rolling contact. Therefore, the angular velocity of roll has a magnitude which is equal to the difference between  $\omega_1$  and  $\omega_2$ . In Figure 2.9, the O-x-y plane is the common tangent plane; if there is any difference in the components of the linear velocities of the two points in contact at O within this plane, then, as well as rolling on one another, the surfaces also have a relative sliding velocity. In Figure 2.9a this sliding velocity is equal in magnitude to  $(u_1 - u_2)$  and therefore equal to  $|R_1\omega_1 - R_2\omega_2|$  (Bhushan, 2013: 482).

The term rolling velocity  $u$  has to be defined carefully, especially if the point of contact between the solid surfaces is not at rest, in other words if one or both of the centers of the cylinders has a linear motion. In Figure 2.9a, if bodies 1 and 2 are rotating about fixed centers then the rolling velocity  $u = (u_1 + u_2)$ . In the case of a more general three-dimensional contact, e.g., that of two spheres in contact as in Figure 2.9b, or of a sphere on a plane, there can also be a difference in the components of the angular



velocities of the two bodies in the direction of the common normal, i.e., at right angles to the common tangent plane. This represents a spinning motion of magnitude  $|\omega_{1z} - \omega_{2z}|$  (Bhushan, 2013: 482). For a two-dimensional case of Figure 2.9a, when the cylinders are pressed together by a normal load (force), the contact will spread over a finite area which can be determined for this non-conformal contact by Hertz theory (Equations 2.1 to 2.8).

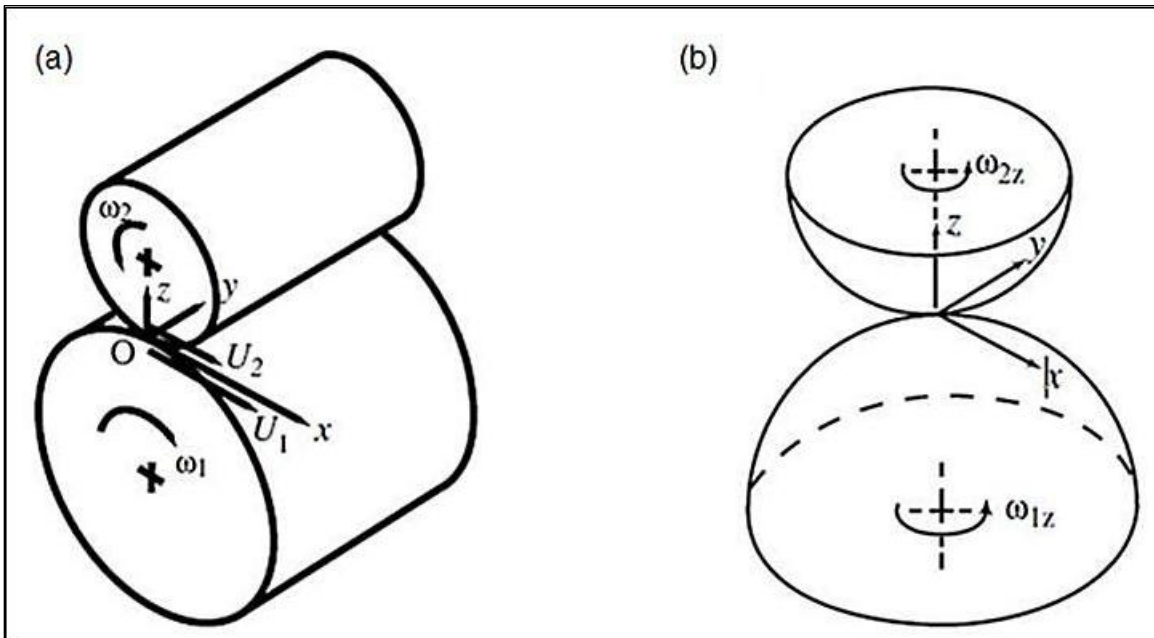


Figure 2.9: Contacts of solids in motion (Bhushan, 2013: 483).

In Figure 2.9, (a) Cylinder 1 and 2 are in contact along the parallel axes: there can be rolling and sliding at the point of contact; (b) in the three-dimensional case, body 1 can spin relative to body 2. Once it has been considered that the contact spreads into a strip which has a finite width, rather than occurring along a line, the specification of sliding is not straightforward. This is because some pairs of points in contact at the interface may slip relative to one another while others stick, in the presence of friction between the surfaces. A difference between the tangential surface strains in the two bodies in the region of stick can lead to a small degree of overall relative movement, which is known as creep (Bhushan, 2013: 483).

## **2.3 Friction in sliding contacts**

There are several definitions of friction, each based on the existing sliding conditions. Friction is generally defined as the resisting force tangential to the interface between two bodies when, under the action of an external force, one body moves relative to the other (Blau, 2009: 17). Frictional force is the force necessary to overcome the resistance to motion (HSU *et al*, 2014). Static frictional force is the force necessary to overcome the resistance to motion from rest and kinetic frictional force is the force necessary to maintain motion of the sliding mass (HSU *et al*, 2014). Under dry contacts, friction can be viewed as the force necessary to break the cold weld junctions which form between the tips of the contacting asperities of the contacting surfaces during sliding (Stachowiak & Batchelor, 2014: 502).

Friction always results in a dissipation of energy between the sliding bodies (Stachowiak & Batchelor, 2014: 502). Therefore, friction is nothing but the dissipation of energy. The description of friction as the cause of wear and energy losses in sliding contacts has always posed significant problems because of the complexity of these systems, and there is also no internationally-recognized nomenclature (Dresel & Mang, 2007: 8).

Friction can also result in the generation of noise and vibrations associated with the noise emission. The vibrations can also be harmful tribosystems. Friction is usually controlled by lubrication to provide smooth and silent sliding as well as to suppress wear (Stachowiak & Batchelor, 2014: 503 and Dresel & Mang, 2007: 8). In this investigation friction is viewed as the dissipation of energy, and will be discussed according to specific sliding conditions.

### **2.3.1 Coefficient of friction**

The coefficient of friction (COF) is a parameter which is used to measure the friction force. This parameter is defined as the ratio of the force resisting tangential motion between two bodies to the normal force pressing those bodies together (Blau, 2009: 17,

HSU *et al*, 2014 and Stachowiak & Batchelor, 2014: 503). With reference to Figure 2.10, the friction coefficient ( $\mu$ ) is given as:

$$\mu = \frac{F}{F_N} \quad (2.13)$$

Where  $F$  is the friction force (N),  $F_N$  is the normal load (N) and  $\mu$  is the coefficient of friction. The normal range of friction coefficients in sliding contacts can range from about 0.5 to 1.2. Lower friction is desirable between sliding parts in combustion engines and in many other mechanical devices (Bhushan, 2013: 201).

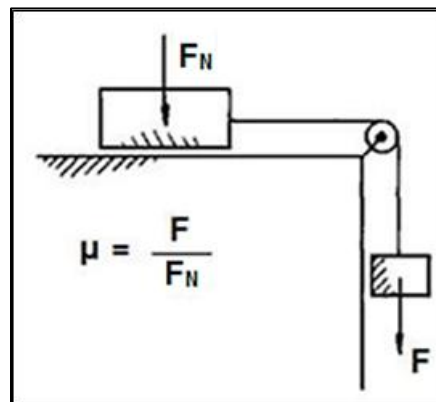


Figure 2.10: Coefficient of friction (Dresel & Mang, 2017: 14 and Szeri, 2005: 10).

This approach taken to define  $\mu$  shows some proportionality between the COF on the normal load. However, it should be noted that this basic approach is very simplistic since the COF depends also on parameters such as temperature and sliding speed and, in other cases, there is no exact proportionality between friction force and normal load (Batchelor & Stachowiak, 2006: 483). A more general approach is defined in the following sections.

### 2.3.3 Friction in lubricated contacts

There are two types of friction i.e., external friction and internal friction (Dresel & Mang, 2017: 13). Friction often remains constant, regular and well behaved, but this is

observed mostly in mechanical systems that operate under relatively constant sliding conditions averaged over time. Actually, every sliding condition produces a different level of friction. This is mainly because of the continuous change surface materials with time (Bhushan, 2013: 206).

Even in a vacuum, the surfaces of materials A and B are likely not really A and B, but rather have a higher composition of an alloying element that has migrated to the free surface from an alloyed substrate. Over time, the surfaces exposed to oxygen (air) are likely to oxidize. These formed films change the frictional behaviour of the system and this form of friction is referred to as external friction. The causes of external friction are mostly the contacting asperity tips of the sliding surfaces which may cause adhesion, material deformation and ploughing (Bhushan, 2013: 206).

### **2.3.2 Internal friction**

Internal friction results from the friction between lubricant molecules. Internal friction is caused mainly by the rheological properties of the lubricant (i.e., viscosity) which causes frictional resistance within the molecules (Dresel & Mang, 2017: 9 & 13). Internal friction occurs mostly in hydrodynamic lubrication where the surfaces in motion do not touch but are separated by a lubricant film in which shear occurs (Tu and Fort, 2004).

The film separating the surfaces is commonly formed hydrodynamically, or hydrostatically in less common instances (Batchelor & Stachowiak, 2014: 357 - 361). The internal friction can be estimated by defining the coefficient of friction, assuming that the friction is entirely from the shearing lubricant molecules, as illustrated below (Batchelor & Stachowiak, 2014:357 – 361 and Szeri, 2005: 120):

Frictional force:

$$F = \int_0^L \int_0^B \tau dx dy \quad (2.14)$$

Where:

$$(\tau = \eta \frac{du}{dz}) \quad (2.15)$$

Therefore, the coefficient of friction is calculated from the load and friction forces:

$$\mu = \frac{F}{F_N} = \quad (2.16)$$

Where the Load force is given as:

$$F_N = \int_0^L \int_0^B P dx dy \quad (2.17)$$

And:

P Pressure ( $P = f(x,y)$ ) (Pa)

L Contact length from  $x = 0$  to  $x = L$  (m).

B Contact width from  $y = 0$  to  $y = B$  (m)

$\tau$  Shear stress on the film (Pa)

$\eta$  Lubricant viscosity (N/m.s).

Z Distance separating the two surfaces (m)

u Speed of the surfaces (m/s)

### 2.3.3.1 External friction

#### Sliding friction from direct contacts

This type of friction occurs in lubricated and un-lubricated (dry) systems where direct asperity contact between the sliding surfaces is inevitable, and occurs frequently (Dresel & Mang, 2017: 13). In lubricated systems, this condition is experienced in operations involving high loads, high speeds and temperatures, where viscosity loss of the lubricant is severe, and minimal separation (protection) of the interacting surfaces

results. Such operating conditions are classified as mixed or boundary film lubrication and result in high energy dissipation (Brandao et al, 2012 & Hamrock *et al*, 2004: 57).

The mechanisms resulting in this form of friction are very difficult to explain, as much of the contact stresses are carried by both the surface asperities and the lubricant molecules (Bhushan, 2013: 207). It is therefore, very critical for one to understand surface topography of the sliding surfaces. Since much of the contact between the sliding surfaces only occurs at the asperity tips, the localized pressures at the tips is are very high. As a result, adhesion may occur at the tips of the contacting asperities (Bhushan, 2001: 207). Figure 2.11 below shows a summarized schematic representation of the mechanism resulting in this situation, where the top solid (body 2) slides relative to a stationary solid (Body 1).

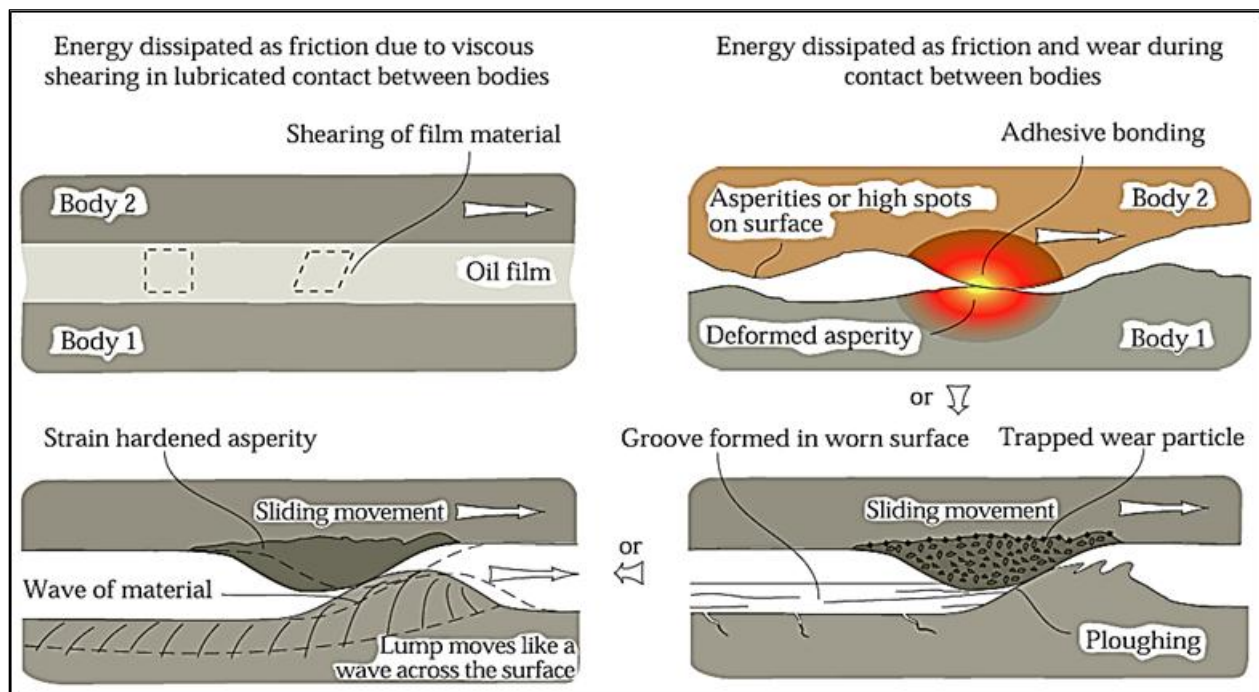


Figure 2.11: Mechanisms of frictional energy dissipation (Stachowiak & Batchelor, 2014: 503).

The mechanism of sliding friction is dependent on the surface properties and, in lubricated systems, the chemical form of the lubricant between the surfaces

(Stachowiak & Batchelor, 2014: 502). There are four underlying empirical laws of sliding friction which were developed by Da Vinci and Amonton. These laws are as follows (Stachowiak & Batchelor, 2014: 502, HSU *et al*, 2014 and Szeri, 2005: 9):

- There is proportionality between the maximum tangential force prior to sliding and the normal force when a static body is subjected to an increasing tangential load;
- The frictional force is directly proportional to the applied load (i.e., the total force acting normal to the sliding surfaces);
- For a constant load, the frictional force is independent of the apparent contact area;
- The kinetic frictional force is independent of the sliding speed (i.e., at very low speeds: the frictional force increases with speed; at medium speeds: the frictional force is nearly independent of speed; at high speeds: the frictional force decreases with speed).

Early research conducted on sliding real surfaces depicts that the surface asperities must deform plastically, since it was assumed that the contact stresses between asperities are very high. This assumption was consistent with Amontons' law of friction which states that the friction force is proportional to the applied load, providing that this force is also proportional to the real contact area. Recent studies have shown that the contacting asperities, after an initial plastic deformation, attain a certain shape where the deformation is elastic (Stachowiak & Batchelor, 2014: 503 & Bhushan, 2013: 236). Therefore, much of the characteristics of friction are a result of the properties of rough surfaces in contact (Stachowiak & Batchelor, 2014: 503). Studies have also shown that there are three main contributing sources, which bring about the mechanism of friction due to asperity contacts.

The main contributors to the mechanism are (Bhushan, 2013: 236, Dresel & Mang, 2017: 13 and Szeri, 2005: 20):

1. The force required to shear adhesive junctions.
2. The force required to deform asperities.
3. The force required to plough through asperities and wear debris.

This therefore means that the friction coefficient equals the weighted sum of the three friction elements. The dominating element of friction determines the mechanism and the resulting magnitude of the coefficient of friction. This is dependent on the contact type and operating conditions. In most cases where sliding between identical solids occurs, the largest contributors towards friction are the adhesion and deformation between interacting asperities (Dresel & Mang, 2017: 14, HSU *et al*, 2014 and Szeri, 2005: 20).

Equation 2.18 below shows the equation for the coefficient of friction:

$$\mu = f_a\mu_a + f_p\mu_p + f_d\mu_d \quad (2.18a)$$

Where

$$\sum_i f_i = 1 \quad (2.18b)$$

In equation 2.18a,  $\mu$  is the coefficient of friction,  $f_a\mu_a$  is the adhesion component (normally ranges from 0 to 0.4),  $f_p\mu_p$  is the ploughing component (usually smaller 0.1 in contacts of identical solids) and  $f_d\mu_d$  is the asperity deformation contribution (usually ranges from 0.4 to 0.75) (Dresel & Mang, 2017: 14, Suh, 1993 and Szeri, 2005: 20).

### 2.3.3.1.1 Friction due to adhesion

Under certain conditions, most solids will adhere on contact with another solid to some extent. The earth's atmosphere and terrestrial organic matter provide layers of surface contaminant on objects which reduce any adhesion between solids very effectively. Therefore, adhesion between two bodies casually placed together is not observed because intervening contaminant layers are present (Stachowiak & Batchelor, 2014:



577). Increased surface roughness or hardness of the contacting bodies also reduces adhesion of solid surfaces (Bhushan, 2013: 207).

### **Metal-Metal Adhesion**

Due to the free electrons which are present in metals, when metals make contact, the electrons may be exchanged between the two solids to establish bonding. These electrons are not bound by a strong and stable structure. Under the condition that the distance between two interacting solids is sufficiently small ( $< 1\mu\text{m}$ ), they can move from one solid to the other, and as a result the electrons can bond the two solids despite their differing atomic structures. The electron transfer between metals allows a strong adhesive bond to be formed between two identical or different metallic elements. This model used to describe adhesion in solids is referred to as the Jellium model (Stachowiak & Batchelor, 2014: 577 and Bhushan, 2013: 209).

A limiting factor in adhesion is the minimum load which causes plastic flow and therefore the establishment of a true contact between surfaces (Bhushan, 2013: 209). Apart from the noble metals, almost all metals are always covered by an oxide film which is normally present in its unreacted form under an oxidizing atmosphere. This film, which is nanometres thick, prevents direct contact between interacting metals and prevents severe wear unless when removed. It has been found in experiments conducted in vacuum that as the degree of surface contamination (surface films) is reduced, adhesion between metallic surfaces becomes very large (Bhushan, 2013: 209).

The strength of adhesion is determined by measuring the force needed to pull two surfaces apart. Adhesion force data for various metals against iron measured at 0.2 mN of a contact load and  $10^{-10}$  Torr of chamber pressure are shown in Table 2.2.

Table 2.2: Adhesion force of various metals with iron under vacuum (Stachowiak & Batchelor, 2014: 579).

Metal	Solubility in iron [atomic %]	Adhesion force to iron [mN]
Iron		>4.0
Cobalt	0.35	1.2
Nickel	9.5	1.6
Copper	<0.25	1.3
Silver	0.13	0.6
Gold	<1.5	0.5
Platinum	0.2	1
Aluminium	0.22	2.5
Lead	Insoluble	1.4
Tantalum	0.2	2.3

From Table 2.2, it can be seen that in all cases, the adhesion force is greater than the contact force of 0.2 mN. The tendency to adhere does not discriminate between metals on the basis of their similar solubility or atomic sizes. In most cases, the greatest adhesion occurs in a combination of like materials. The bonding (adhesion) process is almost instantaneous and can occur at moderate or low temperatures (Stachowiak & Batchelor, 2014: 577). A number of tests were conducted on a variety of metal combinations and have shown that when there is strong adhesion, transfer of the weaker metal to the stronger occurs as illustrated schematically in Figure 2.12 (Stachowiak & Batchelor, 2014: 578).

Metals exist in four principal types of crystal structures i.e., face-centred cubic, body-centred cubic, hexagonal close packed and tetragonal. Previous studies have shown that metals with hexagonal close packed structure experience much less adhesion than other crystal structures (Stachowiak & Batchelor, 2014: 578).

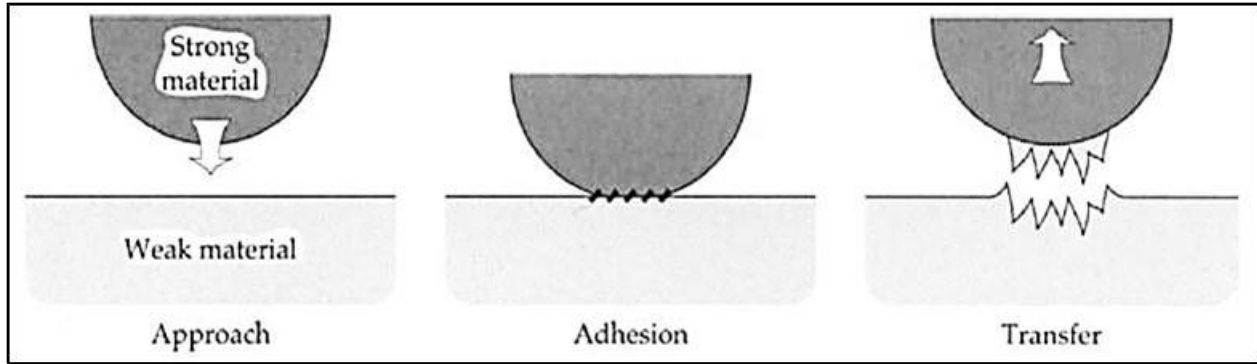


Figure 2.12: Mechanism of metal transfer due to adhesion (Stachowiak & Batchelor, 2014: 577).

Other physical properties such a high hardness, large elastic moduli and surface energy of metals also suppress adhesion (Bhushan, 2013: 211). The difference in adhesion forces between metals of similar hardness is believed to be a result of the necessity for some degree of plastic deformation between asperities before a true contact can be established. The applied load greatly affects this, through the establishment of a true contact between surfaces at high loads (Bhushan, 2013: 211).

### Calculation of Friction Due to Adhesion

The theory of adhesion as developed by Bowden and Tabor defines the coefficient of friction as (Stachowiak & Batchelor, 2014: 582 and Bhushan, 2013: 208):

$$\mu = \tau/p_y \quad (2.19)$$

where:

$\tau$  is the effective shear stress of the material [Pa];

$p_y$  is the plastic flow stress (yield pressure) of the material [Pa].

If the materials of contacting bodies are different, the yield stress of the softer material and the shear stress of the weaker material or the interface shear stress, whichever is the least, are used in Equation 2.19. Previous studies have shown that most of the

frictional resistance in lubricated sliding conditions is due to the deformation of asperities rather than the fracture of adhesive bonds. Frictional forces due to adhesion are dominant when there is a total absence of lubrication and such circumstances correspond to the original experiments performed in vacuum (Stachowiak & Batchelor, 2014: 582). The friction theory presented so far implies that the limiting values of friction are less than unity. But, in practice contradicting results are found which indicate much higher values of the coefficient of friction (Stachowiak & Batchelor, 2014: 582).

#### **2.3.3.1.2 Friction due to junction growth between the asperities**

When a contaminant or lubrication is introduced to clean surfaces, friction levels decline to the moderate values (Stachowiak & Batchelor, 2014: 583). This was illustrated through an experiment done with sliding iron surfaces under vacuum, where the coefficient of friction was measured continuously. The results showed that, in high vacuum total seizure between the contacting iron surfaces occurred. Also, it was observed that as when oxygen (contaminant) was supplied to the iron surfaces, a film of iron oxide formed, resulting in a reduced coefficient of friction (Stachowiak & Batchelor, 2014: 582). The coefficient of friction for clean iron surfaces was very high, up to  $\mu = 3$ . The theory of adhesion, described in the previous section, fails to predict such high values of friction coefficient, and in order to explain this phenomenon the process of asperity junction growth is considered (Stachowiak & Batchelor, 2014: 584).

In plastically deforming adhesion junction both normal and tangential stresses are involved (Stachowiak & Batchelor, 2014: 584). To explain the asperity junction growth process, it is first assumed that initially there is a normal load acting on the asperity which is high enough for the asperity to plastically yield. Since the contact is in the plastic state (meaning the material flows), the contact area will easily be increased by the tangential stress introduced. The increase in the contact area will result in a reduction in the normal pressure (the same load is now carried by an increased area). This is shown in Figure 2.13.

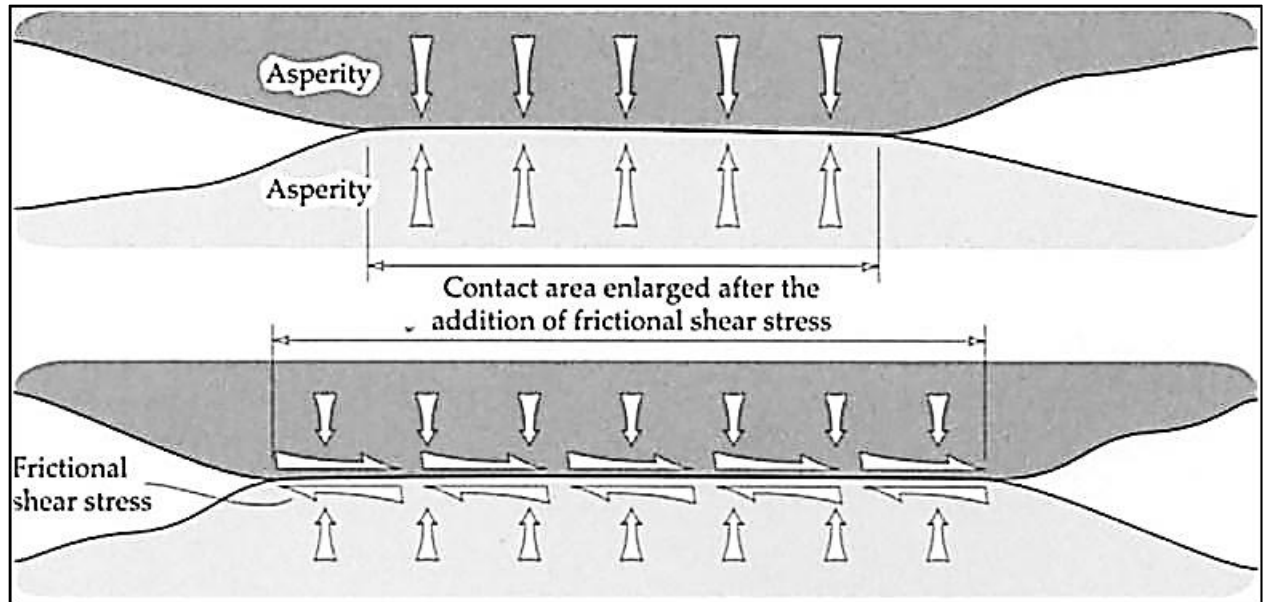


Figure 2.13: Asperity junction growth under frictional force (Stachowiak & Batchelor, 2014: 584).

The increased contact area also enables a larger tangential force to be sustained (Stachowiak & Batchelor, 2014: 584 and Szeri, 2005: 18). The tangential force and the contact area will grow until the maximum (yield) shear stress of the material is reached. As a result the coefficient of friction will also increase. Since the loop with a positive feedback is created, the system may become unstable. The onset of instability is followed by a rapid increase in the coefficient of friction which eventually leads to seizure of the operating parts (Stachowiak & Batchelor, 2014: 584 and Szeri, 2005: 18). This mechanism assumes that under sliding conditions, each asperity contact is loaded to a maximum stress before to it ruptures.

The mechanism of junction growth can be described by considering the von Mises yield criterion. According to this criterion a material will plastically deform when:

$$p^2 + 3\tau^2 = p_y^2 \quad (2.20)$$

Where:

$P$  is the normal contact stress (pressure) [Pa];

$\tau$  is the effective shear stress in the contact [Pa];

$P_Y$  is the plastic flow stress of the material [Pa].

Since the plastic yielding of a junction is controlled by the combined effect of the normal stress ( $p$ ) and tangential stress ( $\tau$ ) a similar relation to describe its behaviour was proposed (Stachowiak & Batchelor, 2014: 585 and Szeri, 2005: 18),

$$p^2 + C\tau^2 = P_X^2 \quad (2.21)$$

Where:

$C$  is an arbitrary constant assumed to have a value close to 10;

$P_x$  is the plastic flow stress of the material in the absence of tangential (frictional) force [Pa].

It can be seen from equation (2.21) that when a normal load only is acting on the asperity (when  $\tau = 0$ ) then:

$$p = p_x \quad (2.22)$$

The stresses ( $p$ ,  $\tau$  and  $P_x$ ) can be expressed as follows:

$$P = F_N / A_r \quad (2.23)$$

$$\tau = F / A_r \quad (2.24)$$

$$P_x = F_N / A_{r0} \quad (2.25)$$

Where:

$F$  is the friction force [N];

$F_N$  is the normal load [N];

$A_r$  is the real area of contact with tangential force present [ $m^2$ ];

$A_{ro}$  is the real area of contact in the absence of tangential force [ $m^2$ ].

Substituting for these expressions into (2.21) gives:

$$(F_N / A)^2 + C(F/A_r)^2 = (F_N / A_{ro})^2 \quad (2.26)$$

Rearranging gives:

$$\frac{A_r}{A_{ro}} = \left[ 1 + C \frac{F^2}{F_N^2} \right]^{0.5} \quad (2.27)$$

It can be seen from equation (2.27) that increasing the tangential force causes the adhesion to increase since the real area of contact grows. For example, if  $C = 10$  and the ratio of tangential force to normal force is 0.3 then the contact area is enlarged by a factor of 1.4. The enlargement of the real contact area is particularly marked at the high values of  $F$  observed for clean surfaces (Stachowiak & Batchelor, 2014: 585 and Szeri, 2005: 19).

### **2.3.3.1.3 Friction due to asperity deformation and ploughing**

The combined action of adhesion between asperities and sliding motion causes severe plastic deformation of the asperities (Bhushan, 2013: 214). Figure 2.14 illustrates the mechanism of shearing and cracking to form a transfer particle in the adhesive contact between asperities (Stachowiak & Batchelor, 2014: 586). The mechanism in Figure 2.14 shows that the material in the softer or sharper asperity deforms in a series of shear bands to accommodate the relative movement. In this case there is no sliding along the asperity contact line. When each shear band reaches a certain limit, a crack is initiated or an existing crack progresses till a new shear band is formed. The crack extends across the asperity and eventually a particle detaches from the deformed asperity (Stachowiak & Batchelor, 2014: 587 and Bhushan, 2013: 215).

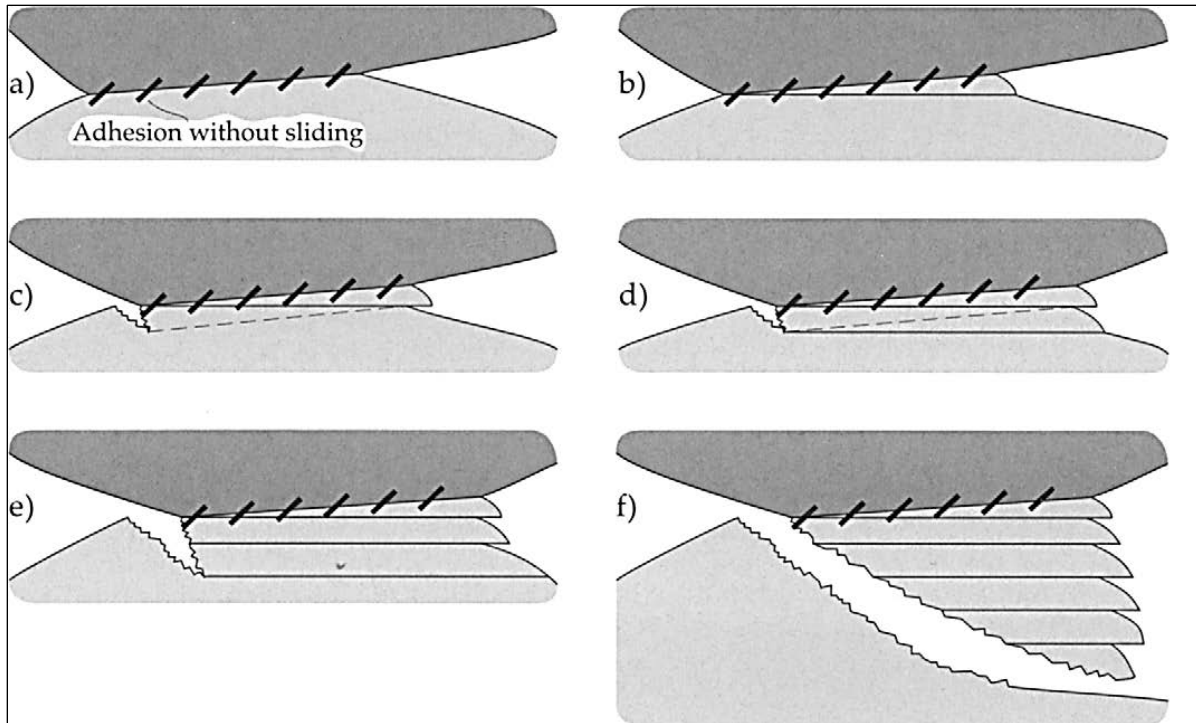


Figure 2.14: Formation of an adhesive transfer particle (Stachowiak & Batchelor, 2014: 587).

Previous studies have shown that sharper asperities tend to lose material to the blunt asperities. The properties of the contacting materials have a strong influence on asperity deformation and the severity of adhesive wear. It has also been shown that the asperities of brittle materials tend to break away cleanly with little deformation and produce fewer wear particles compared to those of ductile materials (Bhushan, 2013: 215). In the contacts between asperities which do not produce wear particles, there may still be extensive plastic deformation as illustrated in Figure 2.15 (Stachowiak & Batchelor, 2014: 588).



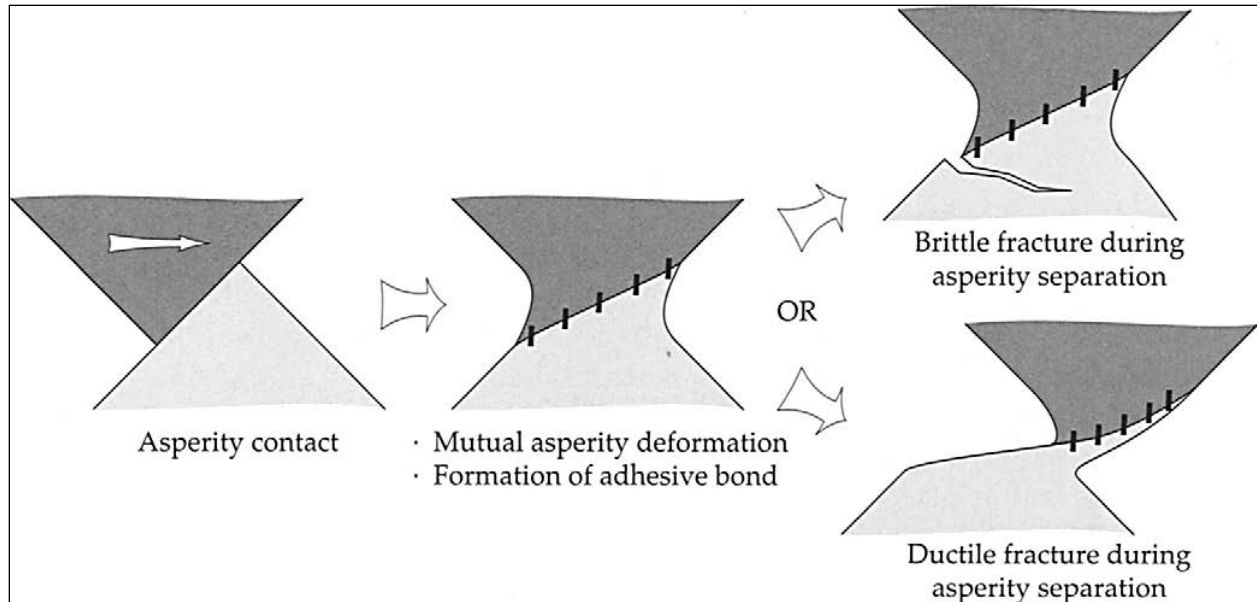


Figure 2.15: An alternative model for deformation in adhesive asperity contacts (Stachowiak & Batchelor, 2014: 588).

The particle of the metal as detached from one of the asperities shown in Figure 2.15 remains attached to the other surface. Depending on conditions it may eventually be removed by further asperity contact to form a true wear particle or it will remain on the surface to form a transfer film (Stachowiak & Batchelor, 2014: 588). As sliding and wear continues, the trapped particles modify the nature of contact between the sliding surfaces. Figure 2.16 illustrates this effect. This particle entrapment causes the progressive growth of a lump that becomes sufficiently large to displace the asperities as the site of true contact. The average diameter and depth of these lumps also increase with increasing frictional power (Stachowiak & Batchelor, 2014: 501).

### Transfer films

The formation of transfer films is a characteristic feature of adhesive friction and wear. Here the material is transferred from one surface to another before being released as a wear particle (Stachowiak & Batchelor, 2014: 588).

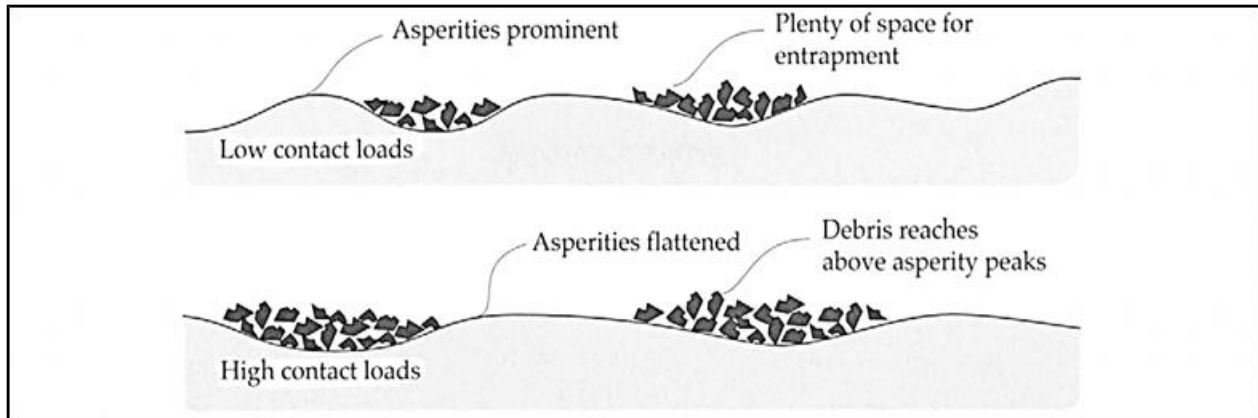


Figure 2.16: Illustration of the effect of trapped particles under low and high contact loads (Stachowiak & Batchelor, 2014: 501).

### Ploughing

For a hard conical shaped asperity sliding on a softer metal, the magnitude of the ploughing term can be illustrated by considering a conical asperity of semi-angle  $\theta$ , shown in Figure 2.17 (Bhushan, 2013: 216 and Szeri, 2005: 20).

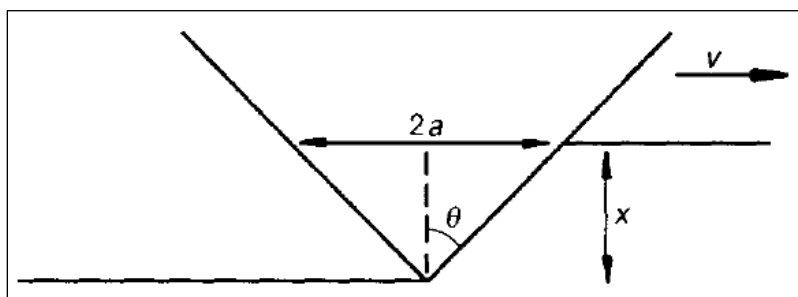


Figure 2.17: A conical asperity of semi-angle  $\theta$  sliding on a softer metal: a model for ploughing (Bhushan, 2013: 216 and Szeri, 2005: 20).

In this, scenario, the pressure needed to make the softer material flow ahead of the advancing hard asperity can be taken to be the hardness,  $H_m$ , of the softer material. The normal and tangential forces supported by the asperity may then be calculated as (Bhushan, 2013: 217 and Szeri, 2005: 20):

$$F_N = \left(\frac{\pi r^2}{2}\right) H_m = \frac{1}{2} H_m \pi h^2 \tan^2 \theta, \quad (2.28)$$

$$F = r h H_m = H_m h^2 \tan \theta \quad (2.29)$$

Therefore, the coefficient of friction due to ploughing is given as:

$$f_p = \frac{F}{F_N} = \frac{2 \cot \theta}{\pi} \quad (2.30)$$

Under normal circumstances, the slope of the asperities rarely exceeds 5-10°. By fixing the range of  $\theta$  at 85-80°; this yields the ploughing component of the coefficient of friction lying between 0.07 and 0.14. As the ploughing component is small, it may be considered additive to the adhesion component (Bhushan, 2013: 217 and Szeri, 2005: 20).

### 2.3.3 Effect friction force on friction characteristics

Previous studies have shown that the rate at which friction force (sliding force) is applied has a significant effect on frictional characteristics (Stachowiak & Batchelor, 2014: 588). This effect is illustrated in Figure 2.18, where the applied friction force versus displacement is shown for:

- (a) low rate frictional force of 20 N/s and;
- (b) High rate frictional force of 20,000 N/s.

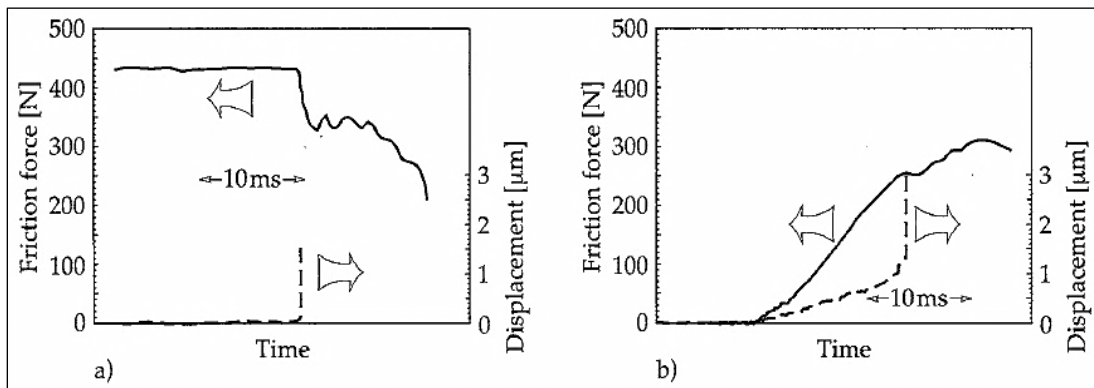


Figure 2.18: Rate of friction force application on friction characteristics (Stachowiak & Batchelor, 2014: 506).

It can be seen from Figure 2.18 that the low rates of friction force application correspond with the model of friction which illustrates that sliding is initiated at the critical friction load, and the friction force declines discontinuously from that point. On the other hand, at the high rate of friction force application, there is no discontinuity in friction force and sliding movement. This means, as soon as sliding is started the friction force continues to increase up to a maximum (Stachowiak & Batchelor, 2014: 506).

According to Stachowiak & Batchelor (2014: 507), the applied friction force depends on the stiffness of the support system and the displacement of the system. “The rate at which the support system is displaced corresponds to the rate of load application. At moderate rates of friction change, the speed of the support system displacement follows the rate at which the friction rises or falls. If there is a very rapid change in friction force, then the support structure adjacent to the sliding contact moves at a linear speed determined by its resonant frequency. When the support structure is able to resonate, then a severe 'stick-slip' motion may occur. If the stiffness of the system is too low, then the rate of load application is also low and a discontinuity in friction occurs. For a stiffer system, however, this discontinuity can be suppressed and smooth motion is possible. Although this view of 'stick-slip' motion is only hypothetical, it serves to illustrate the complex nature of the phenomenon in the absence of more detailed research” (Stachowiak & Batchelor, 2014: 507).

This is important to note, especially for cases where the sliding motion is oscillatory (continuous start-stop motion). The rate of application of the friction force has a severe effect on the type of friction mechanism between sliding solids at the initial stage of sliding. This initial stage of sliding is referred to as running-in (van Drogen, 2009: 1).

#### **2.3.4 Initial sliding in metal contacts (Running-in)**

Many researchers have reported the initial sliding (running-in) as having the most severe effect on the surface roughness of the contacting solids. In most cases, this stage determines the type of friction mechanism which will dominate during the sliding

process, as most of the surface changes occur during this stage (van Drogen, 2009: 1). This stage is severely affected by the mode of application of the friction force, the type of sliding and the normal force applied (Stachowiak & Batchelor, 2014: 509). van Drogen, 2009: 1 shows that the running-in process can be divided into 3 stages i.e., A, B and C. Basically, the change in surface roughness (coefficient of friction) after the initiation of sliding can be divided into three stages and during each stage there are specific changes which occur on the topography of the sliding surfaces (in line with Amontons' law). Figure 2.19 shows an illustration of the stages of running-in.

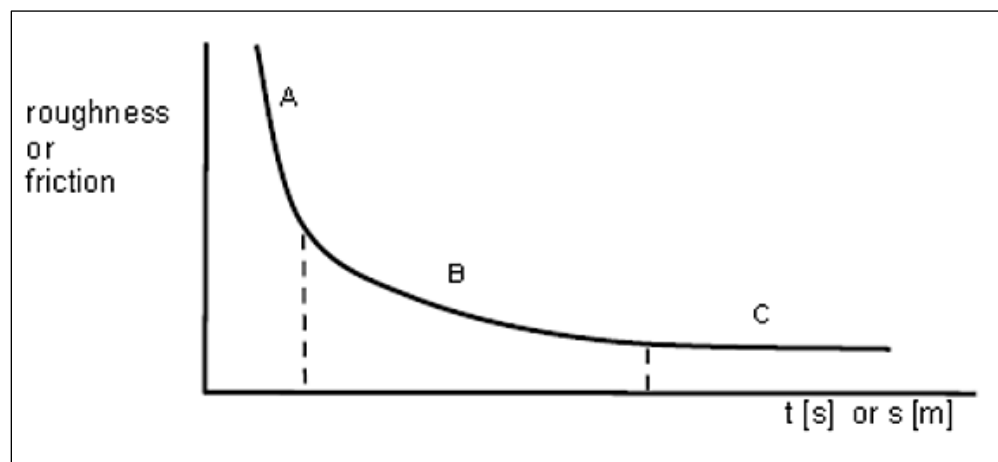


Figure 2.19: Stages of running-in in sliding contacts (van Drogen, 2009: 1).

From Figure 2.19, during stage A, the maximum load is applied and the largest decrease in roughness (friction) can be observed. During this stage, a large fraction of surface asperities get flattened during the initiation of sliding, mainly, due to plastic deformation depending on the magnitude of the applied load and the method of application of friction force, and the presence of contamination on/between the sliding surfaces. From this point, as sliding continues, the system enters Stage B where a significant decrease in roughness (friction) is also observed. According to van Drogen, 2009: 1, wear due to chemical reactions occurs during this stage which causes more change in the surface roughness. Further flattening of the asperities occurs to a point where much of the surface roughness in the area of contact is even. In stage C, a constant roughness (friction) is reached and no further surface changes occur.

### **2.3.4 Thermal Effects of Friction**

About all frictional energy is dissipated in the form of heat (Stachowiak & Batchelor, 2014: 513 and Szeri, 2005: 22). The continuous rubbing of surfaces can build up significantly high temperatures and large temperature gradients in the contacting bodies. Frictional heat is generated instantaneously at the random asperity contacts of the sliding surfaces and these instantaneous and random asperity temperatures are significantly higher than the nominal temperature given by our steady-state energy conservation equations (Stachowiak & Batchelor, 2014: 514 and Szeri, 2005: 22).

### **2.3.5 Seizure**

The high values of the coefficients of friction are found with clean surfaces under a vacuum. As explained in the previous discussions, this can also occur in practical lubricated mechanical contacts when there is a lubricant film breakdown or absence of lubrication. This situation is referred to as seizure. Under these conditions normal operation of the tribosystem is impossible and significant damage from overheating as well as adhesion will result (Stachowiak & Batchelor, 2014: 586).

#### **2.3.5.1 Lubricant film breakdown**

Most reported film breakdowns occur due to molecular modifications taking place at the tribo-surfaces. The possible causes are (Ichiro, 2017):

- Exo-electrons could be emitted from rubbing surfaces. Those electrons have low energy to promote chemical reactions but can produce radical intermediates for chemical reactions.
- Elevated pressure up to Giga-Pascal could be generated at tribo-contacts. Since chemical reactions are initiated by a collision of molecules, compression of reactant raises the probability of the collision.
- Orientation of molecules may occur if they are moved through a narrow area. This means that the reacting functional groups are close to each other and this

increases the probability of reaction. This, together with elevated pressure, contributes to the entropy factor of the reaction.

- Shearing can dissociate chemical bonds in a molecule directly. It is a well-known phenomenon that molecular mass of polymers can decrease under shearing conditions.

Since the breakdown of molecules result in lower film strengths, due to the lowered molar mass or formation of weaker bonds, the sliding motion can rip apart the molecular bonds and thereby exposing the sliding surfaces to one another causing seizure.

### **2.3.5.2 Lubricant film removal**

Another important phenomenon which causes seizure is the removal of a lubricant film from the contact surface. This is largely influenced by the wettability of the lubricant. Wettability is the ability of a liquid to spread and adhere on a flat surface due to its surface tension (Meirong *et al*, 2017). Surface tension refers to the resistance of a liquid to deform or break as a result of its intermolecular forces of attraction (Van der Waals). Surface tension indicates the strength of the cohesive forces of a liquid and it's affinity to freely spread on a metal surface (Stachowiak & Batchelor, 2014: 41). In a sample of liquid, there are two groups of molecules i.e.; those that are outside and those that are inside (on the surface). The interior molecules are attracted to all the molecules around them, while the molecules on the outside are attracted to the other surface molecules and to those below the surface. This makes the energy state of the surface molecules higher than that of the inside molecules. Due to this, the molecules try to allow more molecules to have a lower energy stage by covering a minimum surface area (Stachowiak & Batchelor, 2014: 41). This phenomenon creates surface tension.

A liquid with a high surface tension (large cohesive forces) will wet a smaller area on a flat surface than will a liquid with a lower surface tension of the same volume. Water is one example. This is because of the large attraction of the liquid molecules by the bulk

liquid, which tends to minimize the surface area. Surface (free) energy is the excess energy at the surface of a material compared to the bulk. Metals like steel have large surface energies and therefore allow low surface tension liquids to wet very easily. An oil with a poor wettability (high surface tension) can result in stick slip conditions due to the poor adhesion properties. Such a liquid can easily be pushed out of the contact zone by the sliding motion at high loads and high speeds. This is a common occurrence on polished surfaces (Stachowiak & Batchelor, 2014: 578). Figure 2.20 shows how an application of load on a wetting oil and non-wetting oil affects its behaviour on a flat surface.

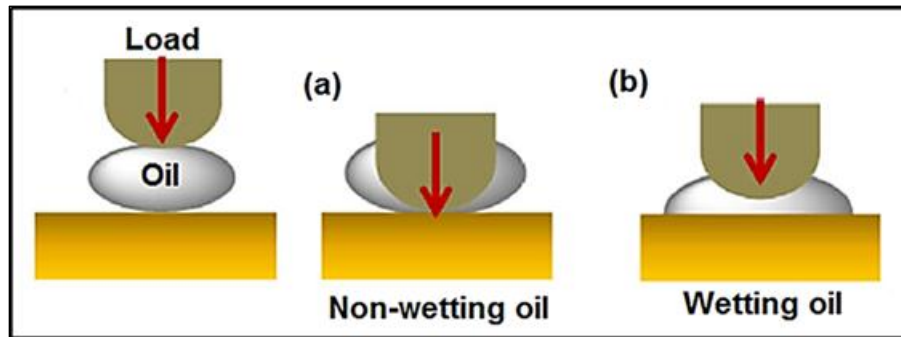


Figure 2.20: Stability of oils upon increasing load (Meirong *et al*, 2017).

Non wetting oils (a) are prone to be squeezed out of the contact area (repels the surface) of sliding, leading to dry friction (seizure). Good wetting oils (b) required to form a stable lubricating film. Wettability is also a function of molecular polarity which will be discussed in the following sections (Meirong *et al*, 2017).

## 2.3.6 Physicochemistry on sliding surfaces

### 2.3.6.1 Polarity

Polarity is defined as result of unequal sharing of the bonding electron pair between atoms in a molecule, due to the differences in electron negativity of the atoms that form the covalent bond (Meirong *et al*, 2017 and Ichiro, 2017). Hydrocarbons formed by the combination of a carbon–carbon bond and carbon–hydrogen bonds whereby the electron negativity of hydrogen, carbon, sulfur and oxygen are 2.2, 2.5, 2.6 and 3.5,



respectively. Since the differences in the electron negativity of the atoms of these bonds are low (0 for C–C bond, 0.1 for C–S bond and 0.3 for C–H bond), hydrocarbons normally displays “non-polar” properties. On the other hand, esters and polyethers have carbon–oxygen bonds (the difference in the electron negativity is 1.0), together with C–C and C–H bonds. Some compounds are made of hydrogen–oxygen bonds in which the difference in the electron negativity is 1.3. These oxygen involving bonds make the molecule polar. However, the overall chemical structure should be considered for the polarity of the molecule (Ichiro, 2017).

Polar liquids are good solvents and hence esters and polyethers can dissolve common additives for Groups I oils up to high concentrations (Ichiro, 2017). Polar molecules have an affinity to steel surfaces. This induces adsorption of polar liquids on tribo-surfaces (Meirong *et al*, 2017). Most industrial mineral oils have lubricating performance and load carrying capacities which are not satisfactory at severe conditions, such as high loads or low sliding velocities. Besides the improvement of dynamic viscosities of base oils by molecular design, the lubricating and antiwear properties are normally improved by enhancing the surface affinity of lubricants. Increasing the polarity of mineral oils and polyolefins to polyether and polyol ester lubricants has led to increased load carrying capacity, because the latter oils have stronger interaction with the frictional surfaces as shown in Figure 2.21 (Meirong *et al*, 2017 and Ichiro, 2017).

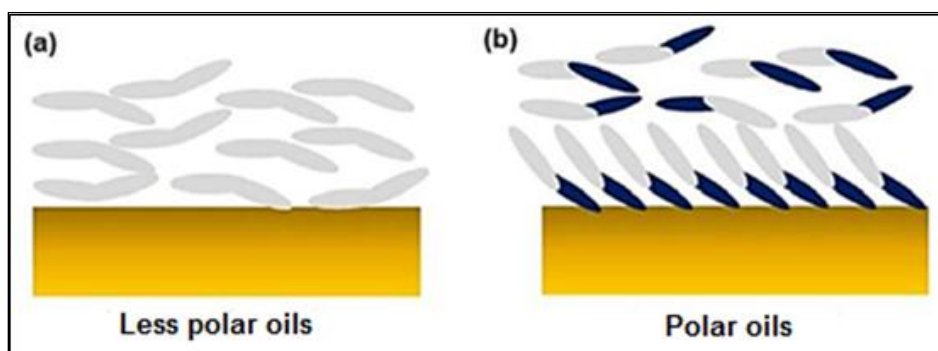


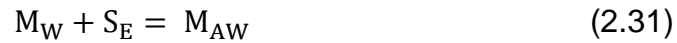
Figure 2.21: Oil interaction with frictional surface (Meirong *et al*, 2017).

Figure 2.21(a) shows that the less polar (nonpolar) oils have a poor ability to form ordered molecular layers on the metal surfaces. This leads to less stable (compact) films which give limited protection to the sliding surfaces. This also leads to poor alignment of the lubricant molecules in the direction of the sliding motion, which promotes more molecular collisions and increased shear stresses. On the contrary, the high polarity oils, Figure 2.21(b), form ordered layers on the metal surfaces due to their high surface affinity and thereby protecting the metal surfaces. This also allows the molecules on the inner portions to align to the sliding motion and thereby giving lower molecular shear stresses. Van der Waals forces can be generated between the properly aligned molecules, which strengthen the molecular film and allow proper support for high normal loads. The disadvantage of a high polarity structure is the easy attack by external contaminants such as water (Ichiro, 2017).

### **2.3.6.2 Adsorption**

Adsorption is a process that occurs when molecules of a liquid (adsorbate) accumulate and adhere on a solid surface (adsorbent), forming a molecular or atomic film. Desorption is mainly the process of detaching of the adsorbed molecules from the adsorbate surface (Nilsson *et al*, 2008: 148). Adsorption and desorption are a consequence of surface energy of the metal and the polarity of the liquid. In the bulk liquid, all the bonding requirements (be they ionic or covalent) of the constituent atoms are filled. But atoms on the surface experience a bond deficiency, because they are not surrounded wholly by other atoms. Thus, it becomes energetically favorable for them to bond with any surface available. The bonding generally involves sharing of atomic charges (electrons) between atoms of the adsorbent and adsorbate, which move from high energy levels (orbitals) to lower energy levels (Nilsson *et al*, 2008: 103). The exact type of the bonding depends on the atomic nature of the species involved (Meirong *et al*, 2017 and Ichiro, 2017). There are two forms of adsorption i.e., associative and dissociative. Associative adsorption involves adsorption of molecules on a surface without molecular fragmentation. Dissociative adsorption involves molecular fragmentation of the adsorbate (Nilsson *et al*, 2008: 222).

There are several adsorption models used to explain the adsorption processes, and to estimate the level of adsorption. The Langmuir model is the most common (Crittenden & Thomas, 1998:38). According to the Langmuir adsorption model, the volume ( $V$ ) of the adsorbate adsorbed onto a solid adsorbent is related to its partial pressure ( $P_w$ ) near the surface. In this case, the adsorbate is assumed to have ideal gas behaviour and the adsorbent assumed to be an ideal solid surface consisting of sites which are able to bind with the adsorbate. The binding of the adsorbate is treated as a chemical reaction between the adsorbate molecules ( $M_w$ ) and the empty site ( $S_E$ ) which produces an adsorbed complex ( $M_{AW}$ ), with an equilibrium constant ( $K_{eq}$ ) (Crittenden & Thomas, 1998:38):



From the above assumptions, the Langmuir isotherm can be derived and states that:

$$\theta_A = \frac{V}{V_M} = \frac{K_{eq}P_w}{1+K_{eq}P_w} \quad (2.32)$$

Where  $\theta_A$  is the fractional occupancy of the adsorption sites and  $V_M$  is the volume of the monolayer. A conceptual basis of this model is the continuous monolayer of the adsorbate molecules surrounding a homogeneous solid surface. Langmuir further supposed that the rate of desorption from the surface is directly proportional to the fractional surface coverage  $\theta_A$  and that the rates of adsorption and desorption are equal at equilibrium (Crittenden & Thomas, 1998:38).

There are two forms of adsorption by the adsorbate, namely: chemisorption and physisorption. Chemisorption is as a result of surface reactions, which form a chemical bond between the adsorbent and the adsorbate (Meirong *et al*, 2017 and Ichiro, 2017). Engineering surfaces are usually covered with oxide layers which can be removed by sliding which provides the energy to the molecules to react with the exposed surface forming organic salts (salt of carboxylic acid) and results in chemisorption (adsorption with chemical bond between molecule and metal surface). Physisorption is the attraction through van der Waals forces between the adsorbate molecules and the

adsorbent surface, with no chemical bond formation. According to Pawlak (2003), if the lubrication process involves less than 50 kJ/mol of energy, it is most probably physisorption, and if it involves more than 50 kJ/mol it is chemisorption. Chemisorption possesses a strong interaction with the surface compared to that of physisorption and hence it is beneficial for protecting the film against rubbing. Direct contact upon rubbing can be mitigated by the adsorbed oil molecules (Meirong *et al*, 2017 and Ichiro, 2017).

#### **2.3.6.2.1 Adsorption mechanisms**

When a molecule collides with a surface, it transfers some of its translational energy to the lattice through momentum transfer (Nilsson *et al*, 2008: 159). High incident energies can allow adsorption directly into the molecularly chemisorbed states, which then act as a predecessor to molecular dissociation. At lower incident energies, a molecule first adsorbs in the physisorption well, and then proceeds through sequential predecessors to dissociation depending on the availability of the energy (Nilsson *et al*, 2008: 220). To illustrate these processes, Figure 2.22 below shows a schematic for an oxygen molecule approaching a platinum (111) surface at two different energies.

$E_A$ ,  $E_P$ ,  $E_S$  and  $E_D$  are the measured potential energies required to form atomic adsorption (with dissociation), peroxy-chemisorption, superoxy-chemisorption and physisorption of the  $O_2$  molecule respectively. As can be seen, a large energy is required for formation of atomic adsorption coupled with molecular dissociation of  $O_2$ . The incident energy is the measure of energy (usually heat energy) striking a surface (Nilsson *et al*, 2008: 220). Under lubricated sliding conditions, the incident energy of a lubricant molecule may be enough for physisorption, but the energy (heat) which is provided by friction and the normal applied stress during sliding may facilitate the advancement of the adsorption to atomic adsorption.

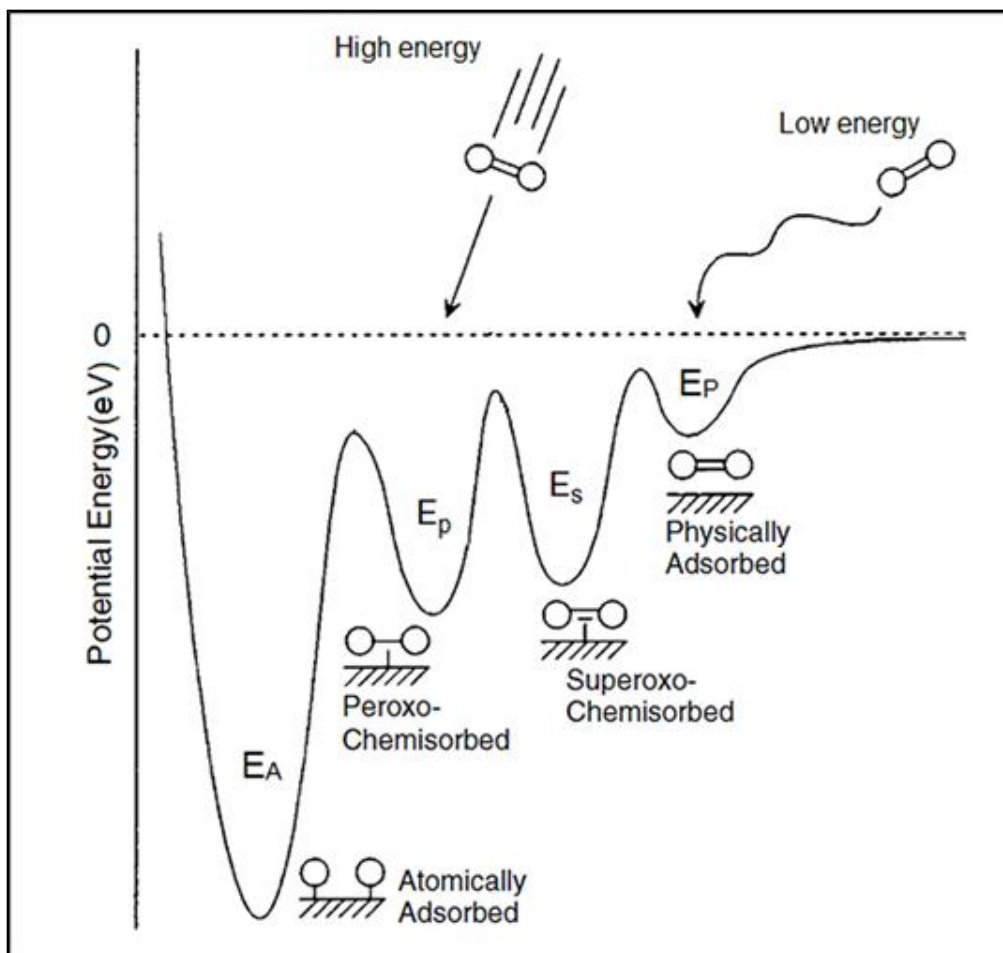


Figure 2.22: Potential energy changes for  $O_2$  dissociation on Platinum (111) (Nilsson *et al*, 2008: 220).

### 2.3.6.2.2 Electronic interactions during adsorption

When an atom or molecule is adsorbed on a surface, new electronic states are formed due to the bonding to the surface. The nature of the surface chemical bond will determine the properties and reactivity of the adsorbed molecule. In the case of physisorption, the bond is rather weak. In this case, the overlap of the wave functions of the molecule and the substrate is small and no major change in the electronic structure is usually observed. On the other hand, when the interaction energy is higher, there are rearrangements of the valence levels of the molecule. This process is denoted chemisorption. The discrete molecular orbitals interact with the substrate to

produce a new set of electronic levels, which are usually broadened and shifted. In some cases completely new electronic levels emerge which have no resemblance to the original orbitals of the free molecule (Nilsson *et al*, 2008: 220). The adsorption of saturated hydrocarbons on metallic substrates is typically considered as an example of a weak physical interaction, which is dominated by van der Waals forces. A physisorbed state is considered to be one in which the heat of adsorption is comparable to the heat of vaporization or sublimation (Nilsson *et al*, 2008: 119).

A small adsorption energy cannot by itself be used to conclude a weak interaction. Previous studies have demonstrated that for n-octane physisorbed on a copper surface [Cu(110)] there are still large and important chemical bonding interactions with the surface that are beyond a physical adsorption picture. There are relatively large internal geometry distortions in the molecule and a relatively short H-Cu bond distance due to this interaction. The C-C bond is shortened and the C-H bonds pointing towards the surface elongated due to the Cu-H interaction. This means that the molecule has taken a small step towards dehydrogenation. There is thus an important interaction of the molecular orbitals involving the CH groups that point to the surface with the sp and d-bands in the metal. It leads to a weak electron-pairing between the CH and Cu atoms. Similar effects were observed even for very weakly physisorbed methane, CH<sub>4</sub>, on Pt(111) (Nilsson *et al*, 2008: 119).

#### **2.3.6.2.3 Bonding mechanisms during adsorption**

Most adsorbates of unsaturated hydrocarbons interact with the metal substrate via covalent bonding i.e., electron-pair sharing. In the formation of electron-pair sharing, a radical state has to be created in the interacting molecule to form the bond to the substrate. For a molecular adsorbate the bond-prepared radical state can be obtained upon partial bond-breaking where the molecular fragments will have unpaired electrons that can interact with unpaired electrons in the metal surface (Figure 2.23a). Molecules that lack radical bonding either through broken bonds or virtual via the n-electron system usually have much lower adsorption strength (Nilsson *et al*, 2008: 134).

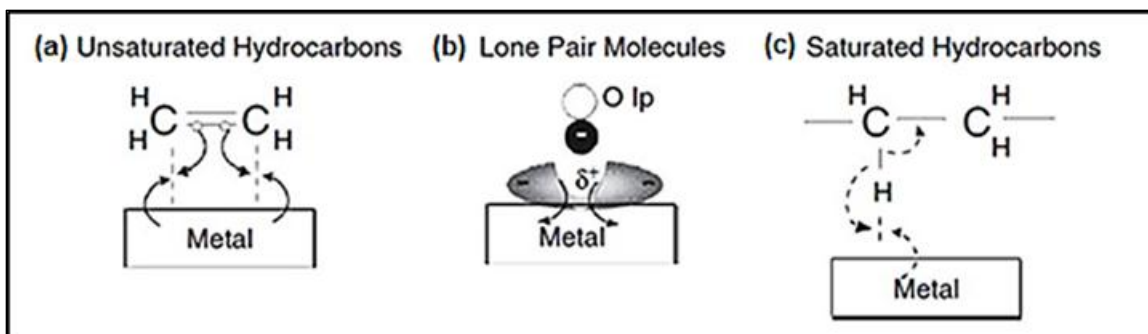


Figure 2.23: Chemical bond formation on metal surfaces (Nilsson *et al*, 2008: 135).

The interaction of molecules, such as water, that bond through their lone-pairs is stronger than physisorption. The lone-pair interaction is similar to the  $\pi$ -system interaction (electron exchange) but occurs at much longer bond distances where it becomes attractive. The bond is mainly of electrostatic character, both through the permanent dipole of the adsorbate and through a contribution induced by the strong polarization of the  $sp$ -electrons away from the bonded metal atom to increase the local positive charge on the interacting metal atom (Figure 2.23b). Water mainly bonds with the adsorbent via the O-atom (Nilsson *et al*, 2008: 137).

The bonding of R-H groups to metal surfaces constitutes the weakest bonding. Consider the type of R-H interaction where n-octane is adsorbed on a copper surface [Cu(110)]. With n-octane on Cu, there is a weak electron-pairing between the hydrogen atom in the C-H group and the metal surface. This arises through interaction of both C-H bonding and anti-bonding orbitals with the  $d$ - and  $sp$ -bands. In order to create the bond the internal C-H bond is weakened to reduce the bond-order and simultaneously the C-C bond is strengthened as shown in Figure 2.23c. This type of interaction occurs with saturated hydrocarbons absorbing on metal surfaces (Nilsson *et al*, 2008: 137).

## **2.4 Wear in sliding contacts**

Wear is the progressive loss of substance of a body, due to relative motion at its surface. Many different types of wear have been identified (Stachowiak & Batchelor, 2014: 503 and Szeri, 2005: 22). Sliding friction and sliding wear are caused by the same type of surface interactions (Stachowiak & Batchelor, 2014: 5103 and Szeri, 2005: 22).

Research into wear is divided into two, wear modeling and surface analyses. Wear modeling is done with the objective of predicting the wear rates. The study of the damaged surfaces owes its existence to the recent progress made with experimental methods and microscopy equipment. The wear mechanisms which are of practical significance to the system under investigation will be considered in the following section.

### **2.4.1 Adhesive wear in a sliding contact**

Adhesive wear is a severe type of wear characterized by high wear rates and a large unstable friction coefficient. Sliding contacts can get destroyed by adhesive wear rapidly and, in extreme cases, sliding motion may be prevented by very large coefficients of friction or seizure (Stachowiak & Batchelor, 2014: 577).

Most lubricant failures in sliding metal contacts result in adhesive wear since this relates to a breakdown in the lubricant's basic purpose of providing some degree of separation between the sliding surfaces. If sliding surfaces are not separated then adhesion and wear are almost unavoidable (Stachowiak & Batchelor, 2014: 587). The mechanism of adhesive wear is illustrated in Figure 2.24.



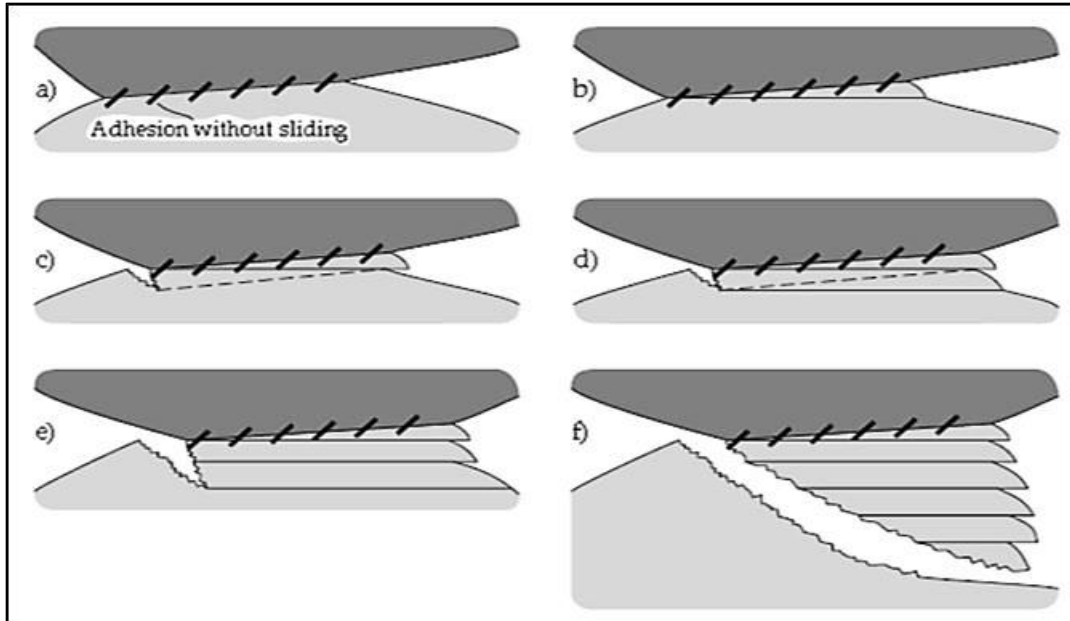


Figure 2.24: The mechanism of adhesive wear on sliding solids (Stachowiak & Batchelor, 2014: 587).

From Figure 2.24, the asperity of the softer surface deforms in a series of shear bands (b) to accommodate the relative motion between the surfaces. The shear band reaches a certain limit during sliding upon which a crack is initiated (c). The crack propagates until a new shear band is formed (d). The crack continues along the length of the asperity (e) and eventually, the particle detaches from the damaged asperity (f).

Following this is an explanation of the cyclic process which shows the cycle that the transfer film undergoes during sliding. This is illustrated in Figure 2.25. On Figure 2.25, it can be seen that the transfer film is basically a “wear particle” which is transferred from one surface to another before being released as a wear particle. The wear particle undergoes severe work hardening during this process and can cause severe surface damage categorized by the formation of grooves.

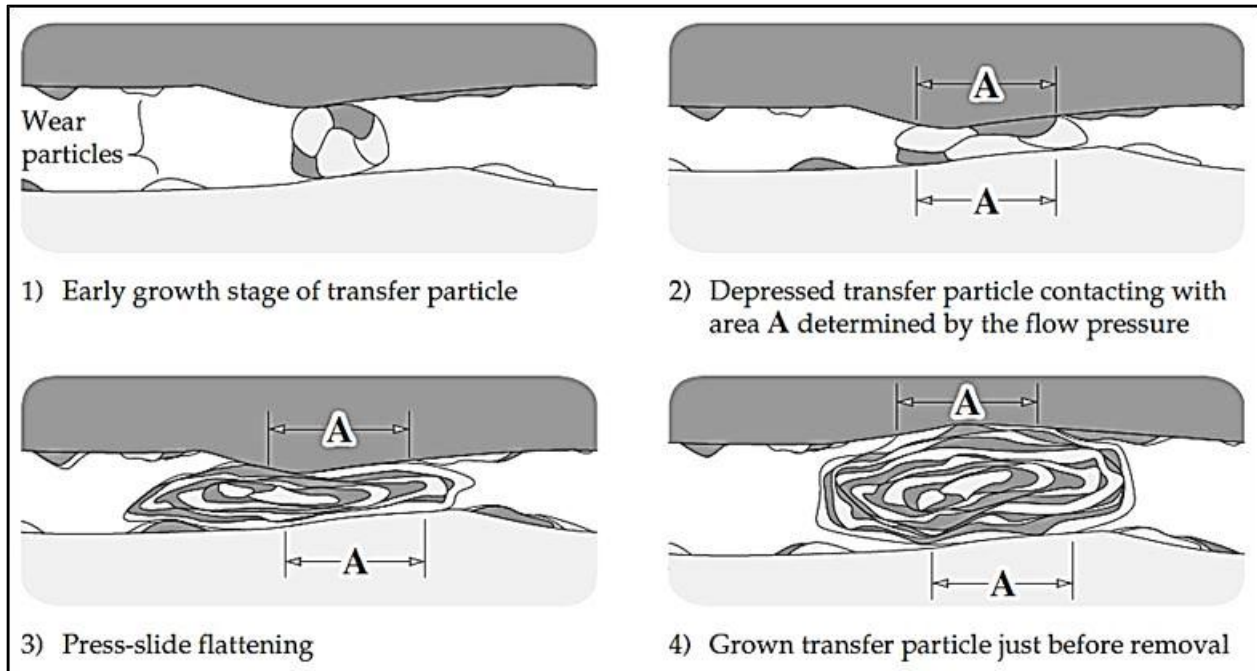


Figure 2.25: Steps of transfer film formation and transfer (Stachowiak & Batchelor, 2014: 590).

### 2.4.2 Fatigue wear in a sliding contact

The deformation of the asperities during continued sliding may cause the formation of cracks on the surfaces. The propagation of the cracks can result in fracture and eventually lead to the formation of transfer films which turn into wear particles. This type of sliding wear mechanism is commonly known as fatigue wear (Stachowiak & Batchelor, 2014: 592). Figure 2.26 shows a schematic of this wear process.

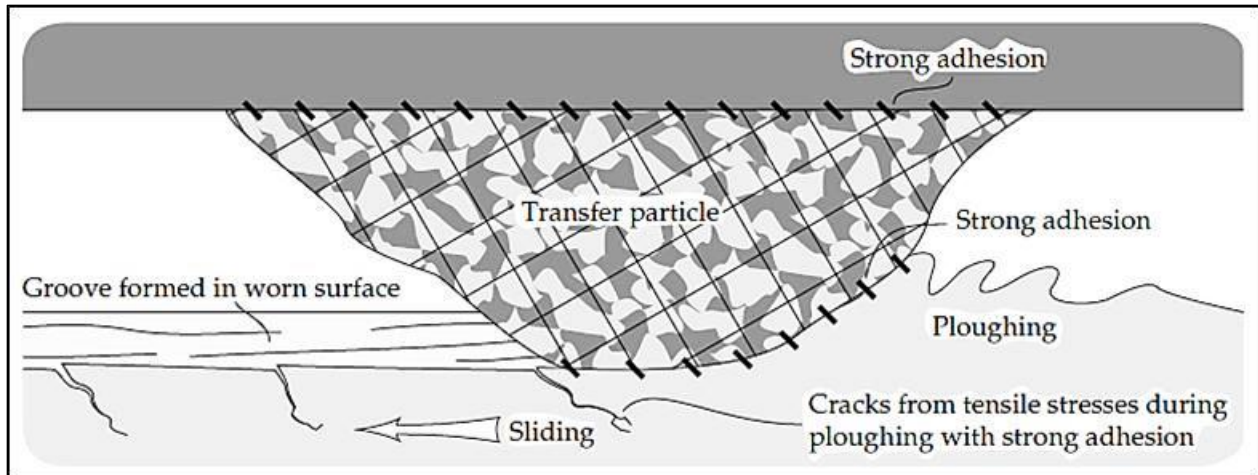


Figure 2.26: The mechanism of fatigue wear (Stachowiak & Batchelor, 2014: 592).

### Mechanism of fatigue crack formation

During sliding, the grain boundaries of the metal are drawn out and oriented parallel to the surface. This leads to the formation of dislocation cells. The dislocation cells are free of dislocations and are separated from adjacent dislocation cells by regions of highly entangled dislocations. Crack nucleation and void formation then most likely occurs at the cell boundaries. Crack propagation then proceeds along the dislocated grain boundaries or slip planes to produce a wear particle in the deformed surface layer.

### 2.4.3 Abrasive wear in a sliding contact

Two-body abrasion wear occurs between two sliding bodies, normally with differing hardness, in which the asperities of the harder surface abrade the softer surface. Three-body abrasion occurs when hard particles trapped between two surfaces abrade one or possibly both surfaces. The mechanics of two-body abrasion is similar to that of ploughing, except, in ploughing part of the material is only pushed aside whereas in abrasive wear some cutting is also involved (Stachowiak & Batchelor, 2014: 525 and Szeri, 2005: 22).

## Mechanism of abrasive wear

Surface damage during abrasive wear can occur via (a) cutting, (b) fracture, (c) fatigue and (d) grain pull-out (Stachowiak & Batchelor, 2014: 526). Figure 2.27 illustrates the mechanism of abrasive wear, followed by a discussion of the each stage.

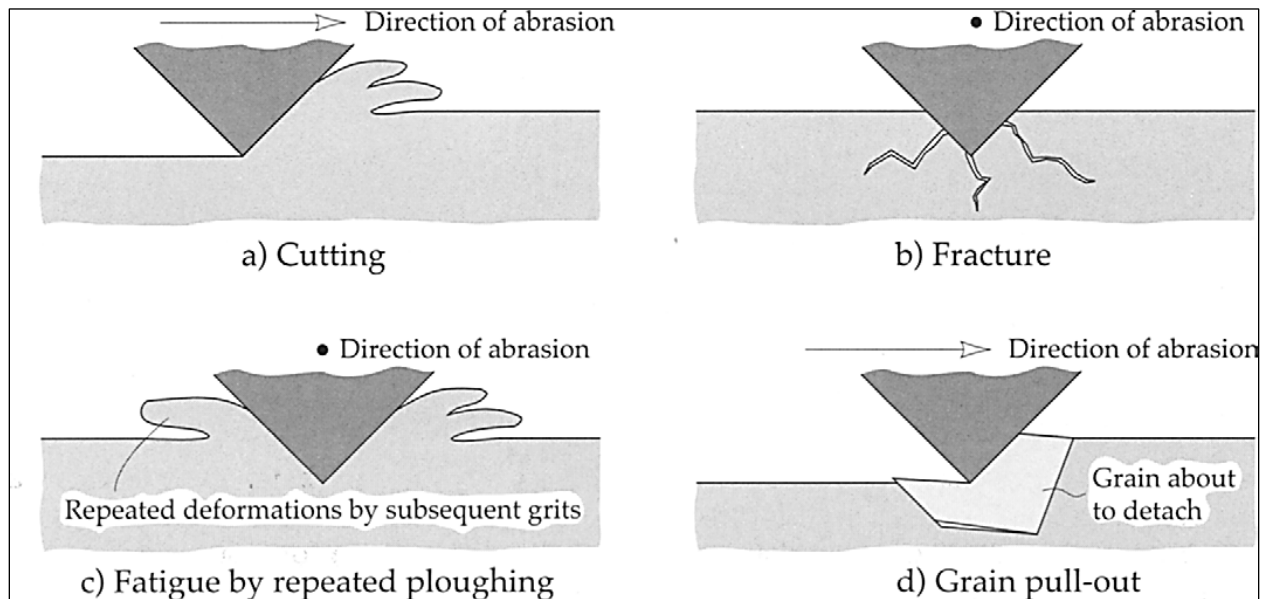


Figure 2.27: The mechanism of abrasive wear; (Stachowiak & Batchelor, 2014: 526).

### Cutting

There are ways with which cutting occurs, namely micro-cutting or ploughing. Ploughing occurs via a wedge build-up mechanism and is less severe than micro-cutting. Micro-cutting is however strongly affected by the shape of the grit particle.

### Fracture

Brittle fractures may result in the surface cracks which cause abrasion on the contacting surface.

## Fatigue

Metal fatigue may be caused by the continued strain from grits which deform the contact surface.

## Grain Pull-Out

Grain pull-out is common is with ceramic surfaces.

## Types of abrasive wear

The mode of abrasive wear is determined by how the grit interacts with the surface and with other grit particles. Two modes of abrasive wear have been defined and are referred to as two-body and three-body abrasive wear.

### Two-body abrasive wear

During the two-body abrasive wear mechanism, the grit particles are rigidly held on the surface. The grits therefore pass over the surface like a cutting tool. This process is illustrated in Figure 2.28.

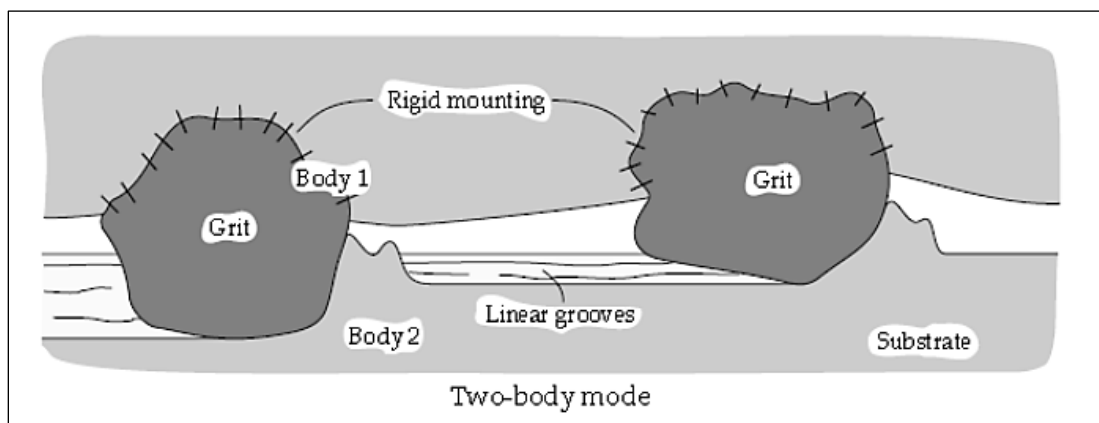


Figure 2.28: Two-body abrasive wear (Stachowiak & Batchelor, 2014: 529)

### Three-body abrasive wear

When grits are free to roll and slide in the contact of the sliding surfaces, three-body abrasion occurs. This mode of wear is illustrated in Figure 2.29. The wear due to two-body abrasive wear has been reported to be approximately 10 times higher than that with three-body abrasive wear (Stachowiak & Batchelor, 2014: 529).

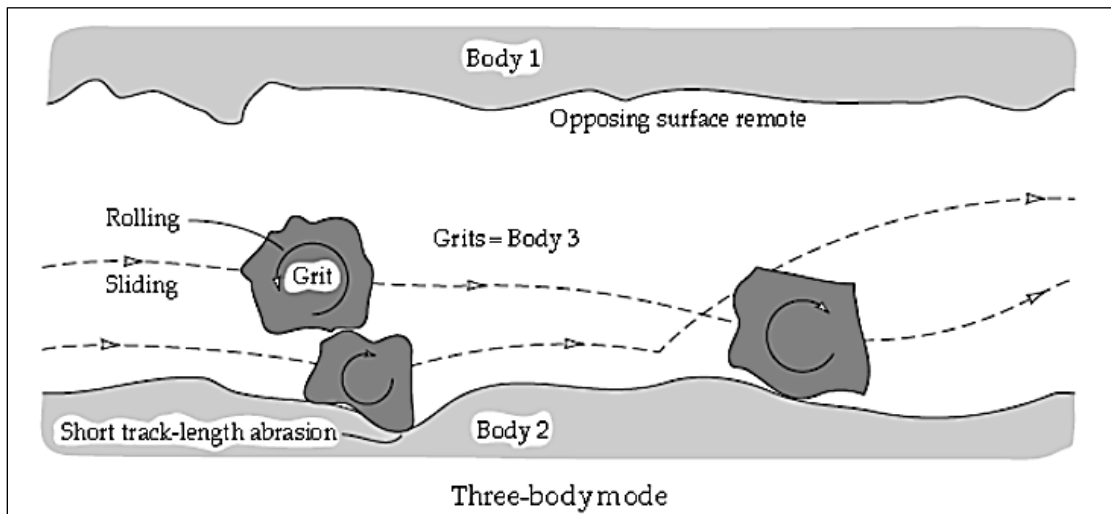


Figure 2.29: Three-body abrasive wear (Stachowiak & Batchelor, 2014: 529).

### 2.4 Lubricating regimes

The ability of a lubricant to protect mechanical components such as bearings, piston rings and other rotating and reciprocating components which require continuous lubrication depends mainly in the base oil behaviour (Brown, 2015). On the other hand, the ability of a lubricant to reduce friction depends on the lubrication regime (Vengudusamy *et al*, 2014). In order to discuss the regimes of lubrication, it is useful to introduce the concept of specific film thickness ( $\Lambda$ ) which is defined by:

$$\Lambda = \frac{h_{\min}}{\sigma} \quad (2.33)$$

Where  $h_{\min}$  is the lubricant minimum film thickness and  $\sigma$  is the combined root mean square (RMS) roughness of the interacting surfaces. The evolution from full-film lubrication to boundary film lubrication is described as  $\Lambda$  is gradually lowered, and it is classified as (Brandao et al, 2012 & Hamrock *et al*, 2004: 57):

- **Hydrodynamic (thick film) lubrication** ( $\Lambda > 5$ ) - The lubricant film thickness is much greater than the roughness; no direct contact occurs between the surfaces; oil entrainment and thus film thickness and pressure distribution are undisturbed by the roughness of the surfaces.
- **Elastohydrodynamic (thin film) lubrication** ( $\Lambda > 3$ ) - The lubricant film thickness is still much greater than the roughness; although regular direct contact may occur, its contribution to load bearing is negligible; the variation in the inlet geometry due to roughness is sufficient to affect lubricant entrainment and therefore film thickness and pressure distribution.
- **Mixed film lubrication** ( $\Lambda > 0.5$ ) - The lubricant film is not thick enough to prevent the regular collisions between surface asperities: the load is carried through direct contact and film pressure; the coefficient of friction is caused by both elastohydrodynamic and boundary friction.
- **Boundary film lubrication** ( $\Lambda < 0.5$ ) - The film does no longer form; the load is supported by asperity contact and the coefficient of friction is caused by boundary friction.

#### 2.4.1 Hydrodynamic Lubrication

The hydrodynamic lubrication (HL) is generally characterized by conformal surfaces and normally applies in bearing applications. A positive pressure develops in a journal bearing that is lubricated hydrodynamically because the bearing surfaces converge, and the relative motion and the viscosity of the liquid separate the surfaces (Hamrock *et al*, 2004: 4). The presence of this positive pressure implies that the applied load can be supported, and for a normal load to be supported by a bearing, positive-pressure profiles must be developed over the bearing length. This condition is often referred to

as the ideal form of lubrication, since it provides low friction and high resistance to wear on the interacting surfaces. Figure 2.30 shows a schematic of the characteristics of HL (Hamrock *et al*, 2004: 5).

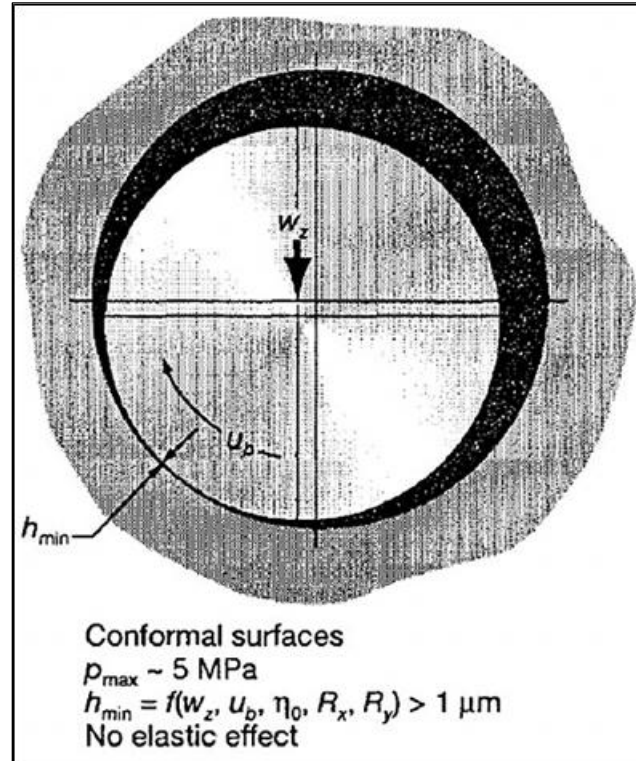


Figure 2.30: Characteristics of hydrodynamic lubrication (Hamrock *et al*, 2004: 5).

The minimum film thickness in a hydrodynamically lubricated bearing is a function of normal applied load  $F_N$ , velocity ( $u$ ) of the lower surface, lubricant viscosity ( $\Gamma_0$ ), and geometry ( $R_x$  and  $R_y$ ). The magnitude of the pressure developed is not generally large enough to cause significant elastic deformation of the surfaces. Minimum film thickness  $h_{min}$  as a function of  $F_N$  and  $u$  for sliding motion is given as (Hamrock *et al*, 2004: 4):

$$(h_{min})_{HL} \propto \left(\frac{u}{F_N}\right)^{\frac{1}{2}} \quad (2.34)$$

As is shown in Figure 2.24, the minimum film thickness normally exceeds  $1 \mu\text{m}$ . In hydrodynamic lubrication the films are thick so that opposing solid surfaces are prevented from making direct contact. The lubrication of the solid surfaces is controlled



by the bulk physical properties of the lubricant, mainly the viscosity. The frictional characteristics come purely from the shearing of the viscous lubricant (Hamrock *et al*, 2004: 4). Figure 2.31 shows the three ways of developing positive pressure in a hydrodynamically lubricated bearing i.e., (a) Slider bearing; (b) squeeze bearing; (c) externally pressurized bearing.

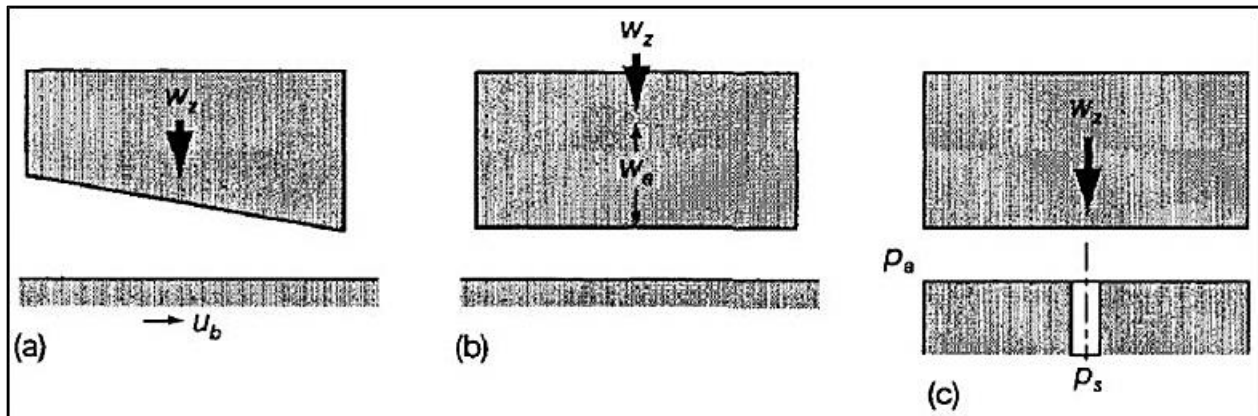


Figure 2.31: Three mechanisms of pressure development in hydrodynamic lubrication (Hamrock *et al*, 2004: 5).

In Figure 2.31a, it is shown that for a positive pressure to be developed in a slider bearing the lubricant film thickness must be decreasing in the sliding direction. In Figure 2.31b, it is shown that for a squeeze film bearing the squeeze action with squeeze velocity  $w_a$ , has the bearing surfaces approach each other. The squeeze mechanism of pressure generation provides a significant “cushioning effect” when the bearing surfaces approach each other. It was observed that positive pressures will be generated only when the film thickness is diminishing. In Figure 2.31c, it is shown that for an externally pressurized bearing (hydrostatic bearing), the pressure drop across the bearing supports the load. The load-carrying capacity is independent of bearing motion and lubricant viscosity. In this case, there is no surface contact wear at starting and stopping as there is with the slider bearing (Hamrock *et al*, 2004: 5).

## 2.4.2 Elastohydrodynamic Lubrication

The elastohydrodynamic lubrication (EHL) is defined as a form of hydrodynamic lubrication where elastic deformation of the lubricated surfaces becomes significant. Elastohydrodynamic lubrication is normally associated with nonconformal surfaces. The features which are important in a hydrodynamically lubricated slider bearing (i.e. converging film thickness, sliding motion, and a viscous liquid between the surfaces) are also important in EHL (Hamrock *et al*, 2004: 5). Also, the hydrodynamic calculation on lubricant films was extended to include the elastic deformation of contact faces (i.e. Hertzian contacts and Hertz's equations of elastic deformation and the influence of pressure on viscosity) which has enabled application of these elasto-hydrodynamic calculations to other contact geometries different from plain bearings, like those of roller bearings and gear teeth (Dresel & Mang, 2017: 20). There are two distinct forms of EHL (Hamrock *et al*, 2004: 6).

### 2.4.2.1 Hard EHL

Hard EHL is related to materials of high elastic modulus such as metals. In this type of lubrication the elastic deformation and the pressure-viscosity effects are equally important (Hamrock *et al*, 2004: 6). The characteristics of hard elastohydrodynamically lubricated conjunctions are shown in Figure 2.32. These conditions of hard EHL are different from those found in a hydrodynamically lubricated conjunction. The maximum pressure is typically between 0.5 and 3 GPa; and the minimum film thickness  $> 0.1 \mu\text{m}$ . At loads normally experienced in nonconformal mechanical components, the elastic deformations are several orders of magnitude larger than the minimum film thickness. Also, in hard EHL the lubricant viscosity can change by as much as 10 orders of magnitude within the lubricating conjunction (Hamrock *et al*, 2004: 7).

The minimum film thickness is a function of the same parameters as for hydrodynamic lubrication, however, with the additions of the effective elastic modulus ( $E^*$ ) and the pressure-viscosity coefficient ( $\alpha$ ) of the lubricant.

$$E^* = \frac{2}{\frac{1-\nu_b^2}{E_b} + \frac{1-\nu_d^2}{E_d}} \quad (2.35)$$

Where  $\nu_b$  and  $\nu_d$  are the poisson parameters of body A and body B, and  $E_b$  and  $E_d$  the elastic modulus of body A and body B respectively.

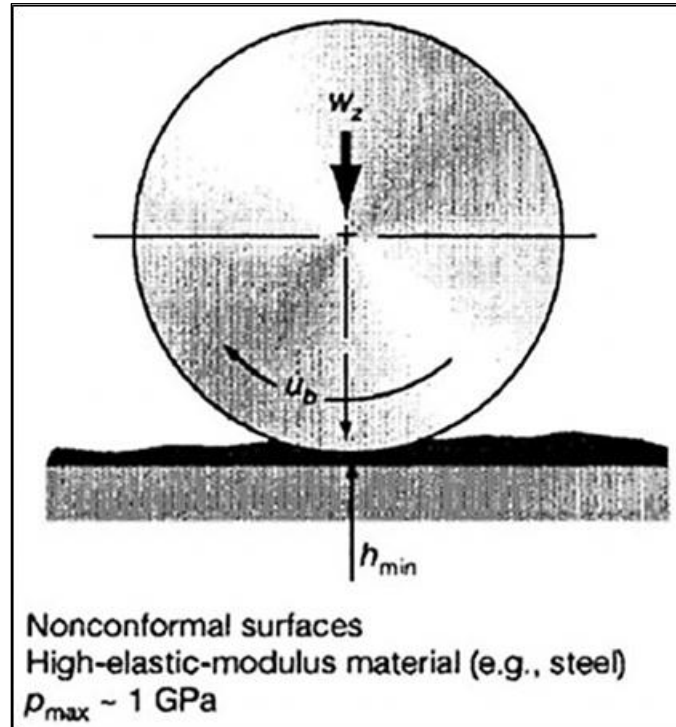


Figure 2.32: The characteristics of hard elastohydrodynamic lubrication;  $W_z = F_N$ ;  
(Hamrock *et al*, 2004: 6).

In Figure 2.13, the minimum film thickness ( $h_{min}$ ) is a function of the normal load ( $F_N$ ), the velocity ( $u_b$ ), lubricant viscosity ( $\Gamma_o$ ), surface geometry ( $R_x$  and  $R_y$ ), effective elastic modulus ( $E^*$ ), and the pressure-viscosity coefficient ( $\alpha$ ). Also, in hard EHL  $h_{min}$  is normally  $> 0.1 \mu\text{m}$  and the elastic and viscous effects are both important. The relationships between the minimum film thickness and the normal applied load and speed for hard EHL, as obtained from Hamrock *et al*, (2004: 7) are:

$$(h_{min})_{\text{EHL}} \propto F_N^{-0.073} \quad (2.36)$$

$$(h_{min})_{\text{EHL}} \propto u_b^{0.68} \quad (2.37)$$

When comparing the results for hard EHL [Equation (2.36) and (2.37)] with those for hydrodynamic lubrication [Equation (2.34)] the following two conclusions are obtained (Hamrock *et al*, 2004: 7):

- The exponent on the normal applied load is nearly seven times larger for hydrodynamic lubrication than for hard EHL. This is an indication that the film thickness is only slightly affected by load for hard EHL but significantly affected for hydrodynamic lubrication.
- The exponent on mean velocity is slightly higher for hard EHL than for hydrodynamic lubrication.

#### **2.4.2.2 Soft EHL**

Soft EHL relates to materials of low elastic modulus such as rubber whose characteristics shown in Figure 2.33. Elastic deformations are large in soft EHL, even with light loads. The maximum pressure is typically 1 MPa, in contrast to 1 GPa for hard EHL. This low pressure has a minor effect on the changes in viscosity throughout the conjunction (Hamrock *et al*, 2004: 7). In Soft EHL, the minimum film thickness ( $h_{\min}$ ) is a function of  $(F_N, u_b, \eta_o, R_x, R_y, E^*)$  and has average values of approximately 0.1  $\mu\text{m}$ , and also, elastic effects are predominant. Engineering applications in which soft EHL is important for low elastic-modulus materials include seals, human joints, tires, and a number of lubricated machine elements that use rubber as a material (Hamrock *et al*, 2004: 6).

According to Hamrock *et al* (2004: 7), common features of hard and soft EHL are that the local elastic deformation of the solids results in liquid films which are consistent and the asperity interaction is prevented significantly. Therefore, the frictional resistance to motion is due to lubricant shearing (Hamrock *et al*, 2004: 7).

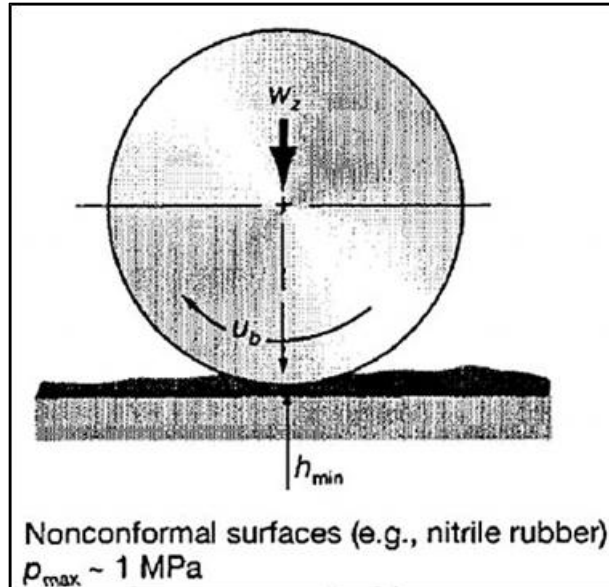


Figure 2.33: Characteristics of soft elastohydrodynamic lubrication;  $W_z = F_N$  (Hamrock *et al*, 2004: 6).

### 2.4.3 Mixed Lubrication

Most practical sliding contacts which operate under extreme conditions e.g high speed gearing, are not lubricated by either purely hydrodynamic or elastohydrodynamic lubrication. In most cases, two lubrication mechanisms work simultaneously, and both are essential for lowering friction in the contact. Also, most of the applied load is supported by hydrodynamic or EHL lubrication (Stachowiak & Batchelor, 2014: 335). A model of mixed lubrication is shown in Figure 2.34. Normally, an additional lubrication mechanism is always required to reduce friction contacts between large asperities from opposing surfaces. Even if the fraction of load supported by non-hydrodynamic means is small, seizure can occur if this additional component of lubrication is not available. This particular lubrication regime where several mechanisms act simultaneously is termed 'mixed lubrication' (Stachowiak & Batchelor, 2014: 335). This condition happens in many cases of EHL, where the direct contact between the deformed asperities will still occur despite the presence of micro-EHL. In mixed lubrication, the contact load is shared between the contacting asperities and the film.

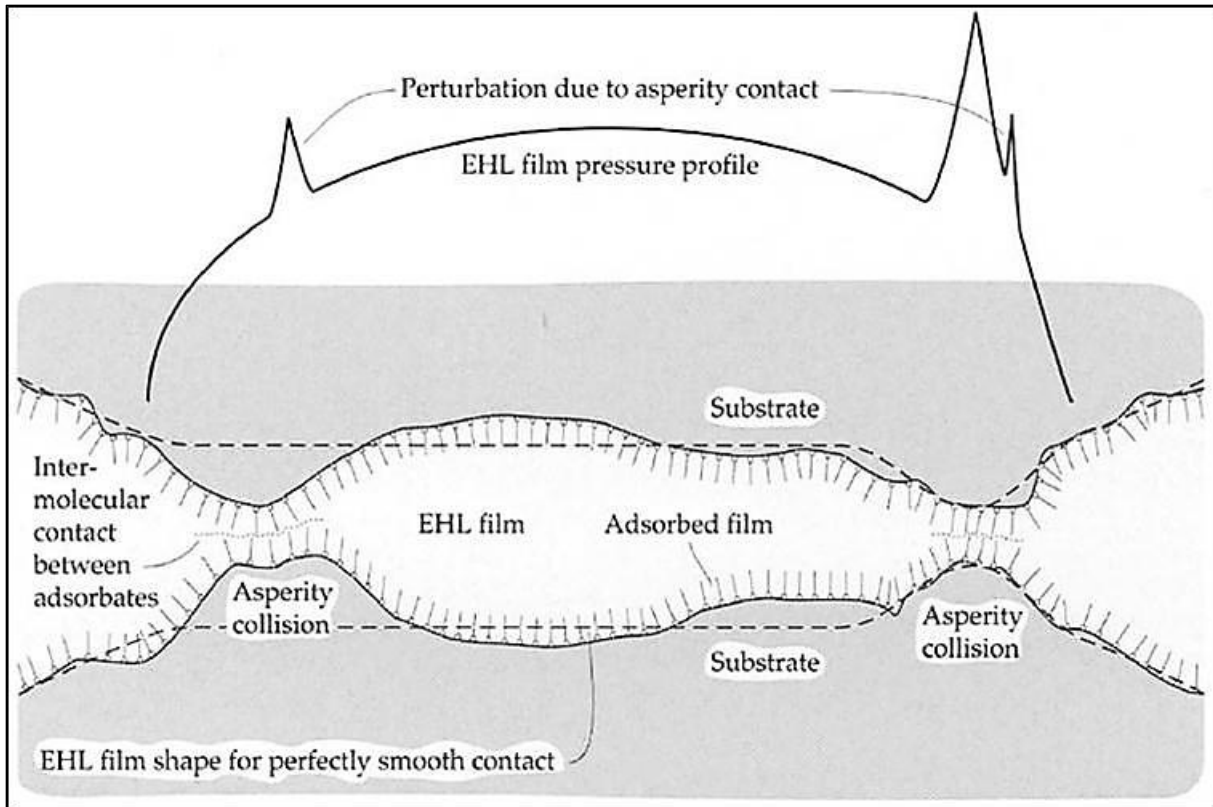


Figure 2.34: Model of mixed lubrication (Stachowiak & Batchelor, 2014: 338).

The mechanism of mixed elastohydrodynamic lubrication shows that during mixed lubrication, the average surface separation between two rough surfaces is about the same as predicted for smooth surfaces (Stachowiak & Batchelor, 2014: 338). In this theory, it was also found that the average asperity pressure depends on the composite surface roughness (RMS) which is given by ' $\sigma$ '. Since in mixed lubrication, the mean separation of rough surfaces approximately equals the minimum film thickness ( $h_0$ ), the number of contacting asperities is also a function of ' $\Lambda$ ', which is given by the equation  $\Lambda = h_0/\sigma$ . Another finding was that the asperity pressure is nearly uniform in the central part of the EHL film. From the examination of the EHL film thickness equations it is clear that the film thickness is almost independent of load. Therefore, the asperity pressure must also be load independent. With the increasing load, the contact area increases and the number of asperity contacts also increases (Stachowiak & Batchelor, 2014: 338).

In mixed or partial lubrication, the shape of the asperities compared to the EHL film thickness is believed to be important. The size of the asperities compared to the EHL film thickness is also important. The shape of asperity peaks can be prismatic with a rounded tip whereas others can have a hemispherical shape of the peaks. It has been found that the sharp peaks sustained a higher proportion of the contact load than blunt/flat peaks (Stachowiak & Batchelor, 2014: 338). This is illustrated in Figure 2.16. It was also found that an improved surface finish allows for a lowered fraction of contact load to be carried by the asperities, and also, the likelihood of a perfect elastohydrodynamic film is promoted as shown for blunt asperities in Figure 2.16. If the surfaces are polished to an extreme smoothness, the load-carrying capacity can be lowered.

It has often been observed that if the surface is too smooth, with a surface roughness of about  $0.001 \mu\text{m}$  [ $R_a$ ], then there is a risk of sudden seizure. In this situation, small asperities play a useful role as a reservoir for the lubricant by entrapment between asperities. In a situation where there are extreme contact pressures, the trapped lubricant can be expelled by asperity deformation to provide a final reserve of lubricating oil. The effect of surface roughness in partial EHL is illustrated in Figure 2.35 (Stachowiak & Batchelor, 2014: 338).

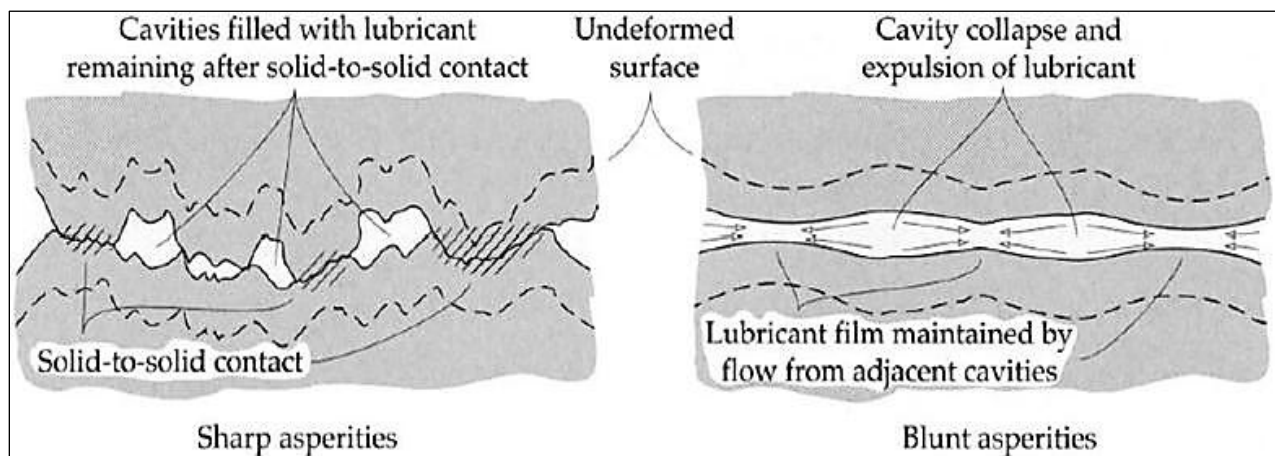


Figure 2.35: Effect of roughness and asperity shape on EHL films (Stachowiak & Batchelor, 2014: 337).

#### **2.4.4 Hydrodynamic films**

The term elastohydrodynamic lubricating film refers to the lubricating oil which separates the opposing surfaces of a concentrated contact. The properties of this minute amount of oil, typically 1  $\mu\text{m}$  thick and 400  $\mu\text{m}$  across for a point contact, and which is subjected to extremes of pressure and shear, determine the efficiency of the lubrication mechanism under rolling contact (Stachowiak & Batchelor, 2014: 317).

#### **Effects Contributing to the Generation of Elastohydrodynamic Films**

The three following effects play a major role in the formation of lubrication films in elastohydrodynamic lubrication:

- the hydrodynamic film formation,
- the modification of the film geometry by elastic deformation,
- the transformation of the lubricant's viscosity and rheology under pressure.

All three effects act simultaneously and cause the generation of elastohydrodynamic films.

#### **Hydrodynamic Film Formation**

The geometry of interacting surfaces in Hertzian contacts contains converging and diverging wedges so that some form of hydrodynamic lubrication occurs. The basic principles of hydrodynamic lubrication outlined in Chapter 4 apply, but with some major differences.

Unlike classical hydrodynamics, both contact geometry and lubricant viscosity are a function of hydrodynamic pressure. It is therefore impossible to specify precisely a film geometry and viscosity before proceeding to solve the Reynolds equation. Early attempts were made to estimate the film thickness in elastohydrodynamic contacts



using a pre-determined film geometry, and erroneously thin film thicknesses were predicted (Stachowiak & Batchelor, 2014: 318).

### Modification of Film Geometry by Elastic Deformation

For all materials whatever their modulus of elasticity, the surfaces in a Hertzian contact deform elastically. The principal effect of elastic deformation on the lubricant film profile is to interpose a central region of quasi-parallel surfaces between inlet and outlet wedges (Stachowiak & Batchelor, 2014: 318). This geometric effect is shown in Figure 2.36 where two bodies, i.e., a flat surface and a ball, in elastic contact are illustrated. The contact is shown in one plane and the contact radii are ' $\infty$ ' and ' $R$ ' for the flat surface and ball, respectively (Stachowiak & Batchelor, 2014: 319).

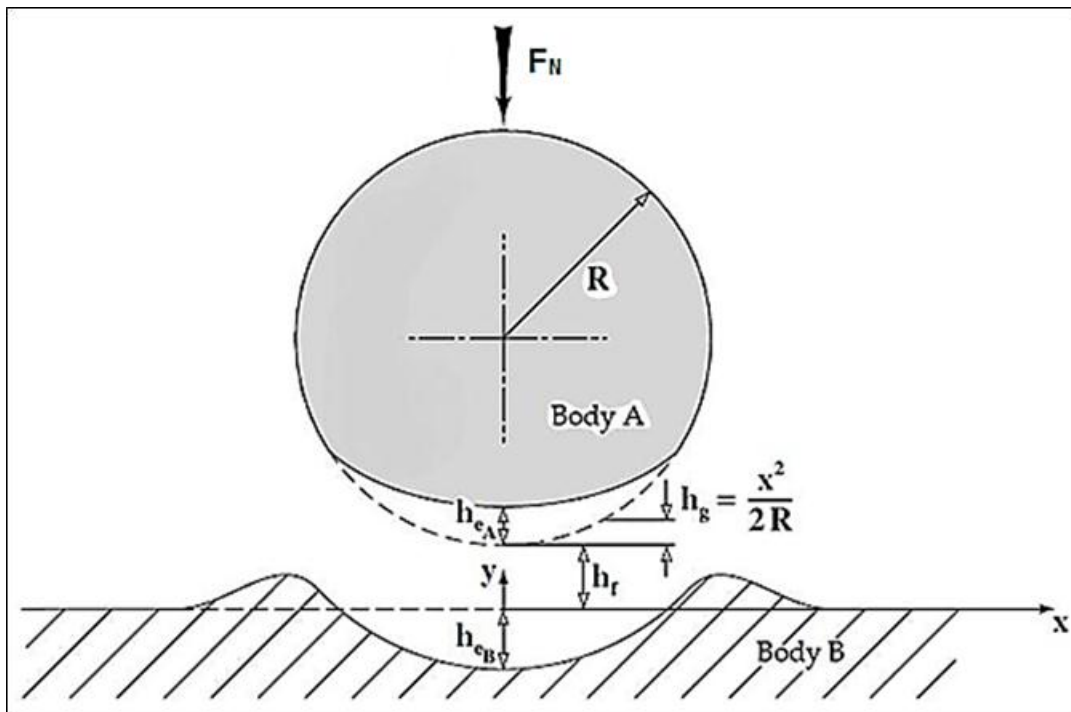


Figure 2.36: Effects of local elastic deformation on the lubricant film profile (Stachowiak & Batchelor, 2014: 318).

The film profile in the 'x' direction is given by:

$$h = h_f + h_e + h_g \quad (2.38)$$

where:

$h_f$  is constant (m);

$h_e$  is the combined elastic deformation of the solids [m], i.e.,

$$h_e = h_{eA} + h_{eB}; \quad (2.39)$$

$h_g$  is the separation due to the geometry of the undeformed solids (m), i.e., for the ball on a flat plate shown in Figure 2.28

$$h_g = x^2/2R; \quad (2.40)$$

R is the radius of the ball (m).

### Film thickness

The exact analysis of elastohydrodynamic lubrication by Hamrock and Dowson provided the most important information about EHL. The results of this analysis are the formulae for the calculation of the minimum film thickness in elastohydrodynamic contacts. The formulae derived by Hamrock and Dowson apply to any contact, such as point, linear or elliptical, and are now routinely used in EHL film thickness calculations. The formulae can be used for many material combinations including steel on steel even up to maximum pressures of 3-4 GPa (Hamrock *et al*, 2004: 7 and Stachowiak & Batchelor, 2014: 324). The minimum film thickness is given as:

$$h_{\min} = R_x 3.63 U^{0.68} G^{0.49} W^{-0.073} (1 - e^{-0.68k}) \quad (2.41)$$

With:

$$W = \frac{F_N}{E^* R_x^2} \quad (2.42)$$

$$U = \frac{u_{\text{avg}} \eta_0}{E^* R_x} \quad (2.43)$$

$$G = \alpha E^* \quad (2.44)$$

$$u_{avg} = \frac{(u_a + u_b)}{2} \quad (2.45)$$

Where:

$h_o$  is the minimum film thickness [m];

$u_{avg}$  is the entraining surface velocity [m/s]; given by Equation 2.45.

Where ' $u_a$ ' and ' $u_b$ ' refer to the velocities of bodies A and B, respectively;

$\eta_o$  is the viscosity at atmospheric pressure of the lubricant [Pa.s]

$E^*$  is the reduced Young's modulus [Pa];

$R_x$  is the reduced radius of curvature [m];

$F_N$  is the contact load [N];

$\alpha$  is the pressure-viscosity coefficient [ $N/m^2$ ],

$k$  is defined as:  $k = a_k/b$ , where  $a$  is the semi-axis of the contact ellipse in the transverse direction [m] and ' $b$ ' is the semi-axis in the direction of motion [m].

The value of  $k$  varies from 1 (a ball-on-plane configuration) to 8 (a configuration approaching a rectangular conjunction).  $U$  is the dimensionless speed parameter,  $W$  is the dimensionless load parameter and  $G$  is the dimensionless materials parameter (Hamrock *et al*, 2004: 7).

### 2.4.5 Boundary Lubrication

In boundary lubrication (BL), the interacting solid surfaces are not separated by the lubricant. Direct asperity contact is considerable and the liquid film effects are negligible. The physical and chemical properties of the thin surface films of molecular

proportions govern the lubrication contact mechanisms. The properties of the bulk lubricant are of minor importance, and the friction coefficient is not dependent on the lubricant viscosity. In boundary lubrication, the frictional characteristics are determined by the properties of the solids and the lubricant film at the contact interfaces (Hamrock *et al*, 2004: 7). Figure 2.37 illustrates the film conditions which occur in liquid film, mixed and boundary lubrication.

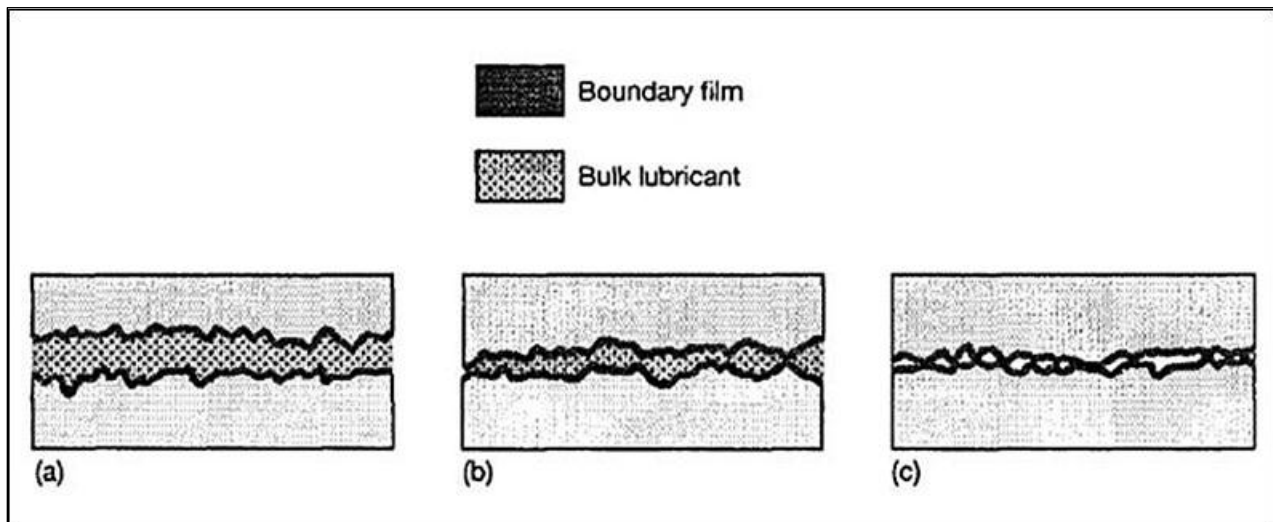


Figure 2.37: Liquid film conditions for; (Hamrock *et al*, 2004: 8).

- (a) Liquid film lubrication - surfaces separated by a bulk lubricant film;
- (b) Mixed lubrication - both bulk lubricant and boundary film play a role;
- (c) Boundary lubrication - friction depends entirely on surface boundary film.

The surface slopes in this Figure are greatly distorted for purposes of illustration. To scale, real surfaces would appear as gently rolling hills rather than sharp peaks. The surface asperities are not in contact for liquid film lubrication but are in contact for boundary lubrication. In practical applications, boundary lubrication occurs when the film thickness is very small, typically less than the composite surface roughness. However, it should be noted that this corresponds to the mean separation of the surface. The minimum film thickness in the boundary regime is on the order of molecular dimensions. (Hamrock *et al*, 2004: 9). In BL, depending on the molecular

size of the lubricant, the film thicknesses normally vary from 1 to 10 nm (Hamrock *et al*, 2004: 8).

### 2.4.6 Stribeck Diagram

The friction variation with operating conditions at interfaces lubricated with different lubricants may be compared in terms of friction by means of the Stribeck curves, which are for friction as a function of the Hersey number (Zhao *et al*, 2016). This concept has proven to be very useful and convenient concept to assess the frictional behaviour (Maru *et al*, 2013). This curve, which was originally developed for journal bearings of known length, is shown in Figure 2.38.

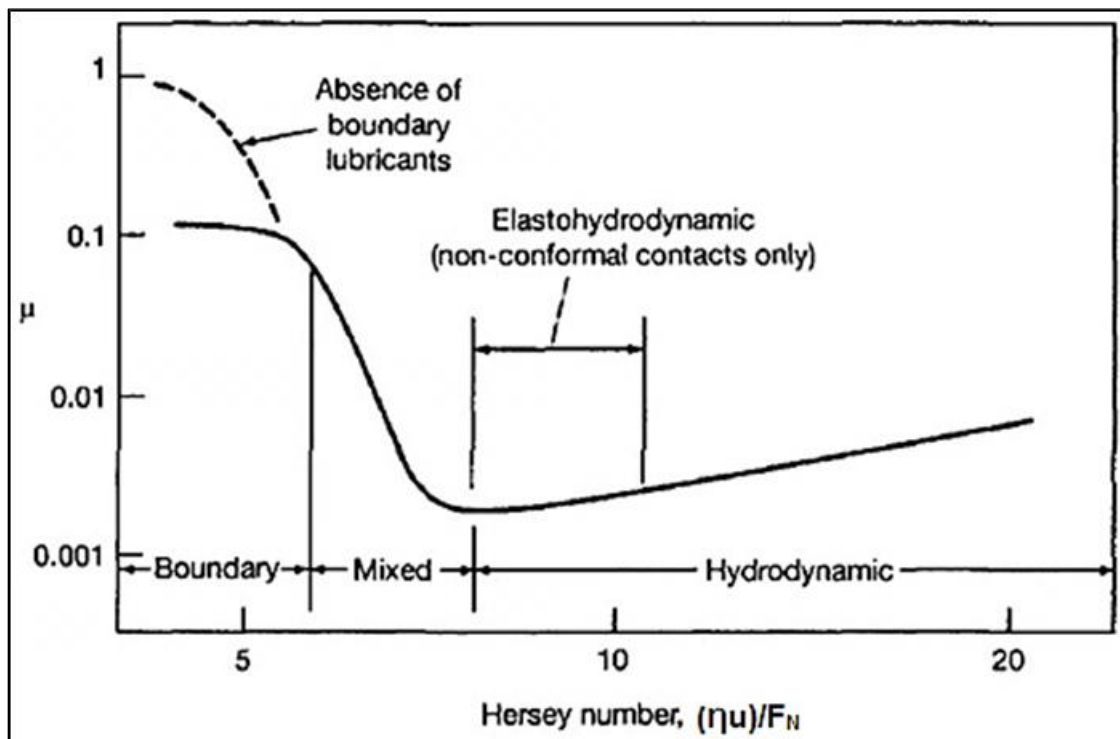


Figure 2.38: The Stribeck curve (Hamrock *et al*, 2004: 18 and Zhao *et al*, 2016).

The Stribeck curve shows the effect of the different lubrication regimes on the coefficient of friction (Hamrock *et al*, 2004: 17). The curve relates the coefficient of friction ( $\mu$ ) with three important variables which affect the friction of lubricated bearing

systems i.e product of lubricant viscosity ( $\eta$ ), sliding speed ( $u$ ) and the normal contact load per unit length ( $F_N$ ) between the interacting surfaces. The product which shows the dependency of the coefficient of friction on the three parameters is given by the ratio  $(u \eta) / F_N$ . This dimensionless ratio is named Hersey number (or Stribeck parameter), and influences the liquid film formation between the two interacting surfaces (Maru *et al*, 2013; Tu and Fort, 2004). Many researchers have used this concept as the basis to analyze the influences of lubricant viscosity related to both the base oil and operating conditions on tribological properties of lubricants and contact interfaces (Zhao *et al*, 2016).

On a Stribeck curve, a high Hersey number usually means a relatively thick lubricant film, whereas a small number results in a very thin film. A very low Hersey number would mean no real lubricant film can develop and there is significant asperity contact, resulting in high friction (Hamrock *et al*, 2004: 17). The Stribeck curve encompasses four lubrication regimes (i.e Hydrodynamic, mixed and boundary lubrication). In the boundary regime the slope of the curve is zero, in the mixed lubrication regime the slope is negative and in the hydrodynamic lubrication regime the slope is positive (Tu and Fort, 2004). The different slopes result from different sliding mechanisms and different kinds of friction forces. In hydrodynamic lubrication, the surfaces do not touch but are separated by a lubricant film in which shear occurs. In mixed lubrication both boundary and hydrodynamic factors contribute to slip resistance.

In boundary lubrication, the sliding surfaces actually touch and true cold weld junctions are formed between the tips of asperities in these surfaces (Zhao *et al*, 2016 and Tu and Fort, 2004). On Figure 2.38 the Stribeck curve starts at relatively high COF values in the boundary regime. The high COF values remain with the increasing Hersey number until a first threshold value is reached. This represents the dominance of boundary lubrication in determining load transfer and friction between surfaces. As the Hersey number increases further, a noticeable rapid decrease in COF values is observed. This is mainly due to the increasing lubricant film thickness and the load being supported between the surface asperities and the pressurized liquid lubricant

present in the conjunction (Dresel & Mang, 2017: 19). This represents the dominance of mixed/partial lubrication. In this regime, widely varying friction values can be measured and are strongly dependent on operating conditions (Hamrock *et al*, 2004: 18).

As the Hersey number continues to increase, the COF reaches a lower plateau value, corresponding to the onset of hydrodynamic lubrication. The curve passed a minimum coefficient of friction value and then increased after that. At this point, the surfaces are effectively separated by the liquid lubricant, and asperity contact has negligible effect on load support and friction (Dresel & Mang, 2017: 19). It should be noted the plateau value of friction in the boundary regime may not be present if the lubricant does not have the proper chemistry, and the friction may continue increasing with decreasing film thickness. Figure 2.38 shows a slightly increasing friction coefficient with the increasing Hersey number in the hydrodynamic regime. Increased friction can be attributed to the increases in shear strength of the lubricant, but these relatively minor effects (Hamrock *et al*, 2004: 18).

An ideal Stribeck curve is shown in Figure 2.39 (Brandao *et al*, 2012). This curve shows the clear boundaries (which were obtained experimentally) separating the lubricating regimes on the abscissa (Hersey number). On this figure, the elastohydrodynamic regime is fixed in the range  $4 \times 10^{-5} < Sp < 1 \times 10^{-3}$ , the mixed lubrication regime is in the range  $2 \times 10^{-6} < Sp < 4 \times 10^{-5}$  and the boundary lubrication regime range is  $1 \times 10^{-7} < Sp < 2 \times 10^{-6}$ , where  $Sp$  is the Hersey number or more conveniently, the Stribeck parameter (Brandao *et al*, 2012).

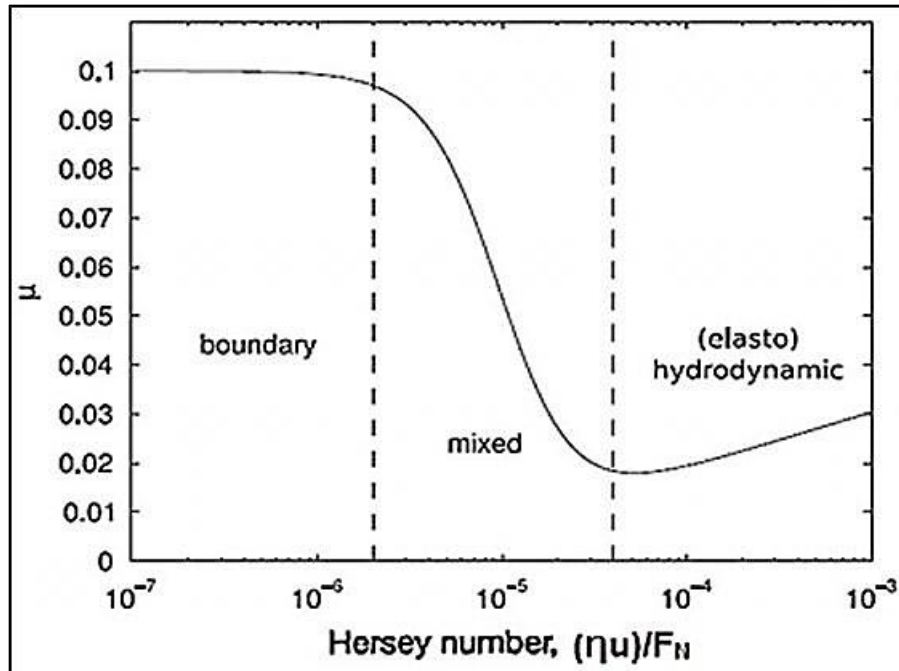


Figure 2.39: The ideal Stribeck curve: non-conformal contacts (Brandao *et al*, 2012).

## 2.5 Properties of base oils

In this section, the properties of the lubricants which are of focus in this investigation are discussed. The lubricants fall mainly into two groups of base oils i.e., mineral and synthetic oils.

### 2.5.1 Mineral oil base stocks

Mineral oils originate from crudes which are from different sources, and which correspond to an exact chemical type (Stachowiak & Batchelor, 2014: 52). These oils are complex mixtures of hydrocarbons which can roughly be divided according to the chemical family to which their predominating constituents belong, such as paraffins, aromatics or naphthenes which are sometimes referred to as cycloparaffins (Hamrock *et al*, 2004: 70). Paraffinic implies a straight chain hydrocarbon, as shown in Figure 2.40, and naphthenic means cyclic hydrocarbon with no unsaturated bonds and aromatic oils contain benzene type compounds.



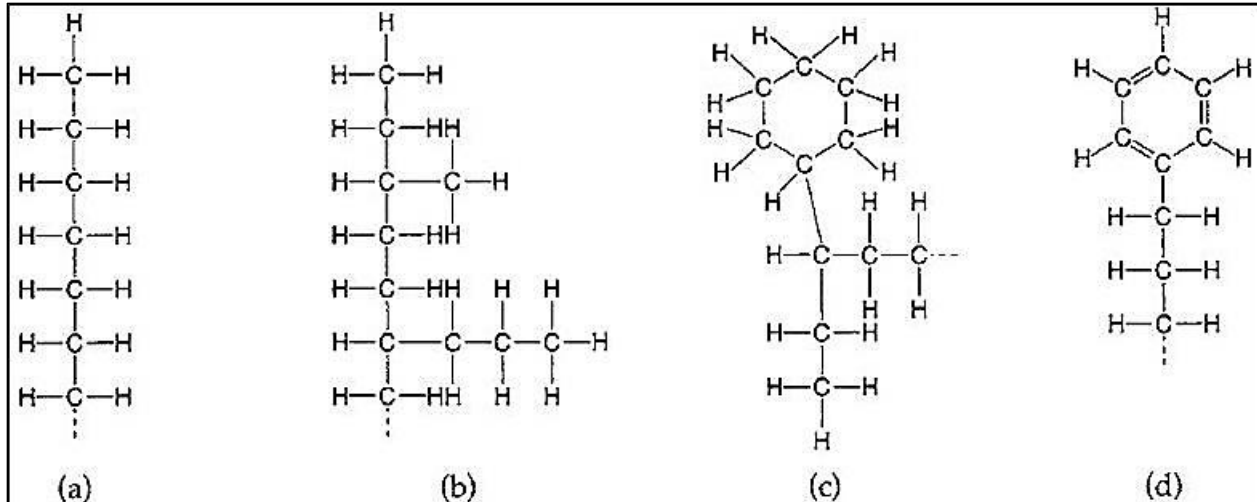


Figure 2.40: Forms of mineral oils (Stachowiak & Batchelor, 2014: 57).

Mineral base oils are distinguished based on the relative proportions of paraffinic, naphthenic and aromatic components present (Stachowiak & Batchelor, 2014: 53). In figure 2.40, the molecular structures shown by (a) is for straight paraffins, (b) are branched paraffins, (c) are naphthenes, and (d) are aromatics. Lubricants are named based on the chemical type makes up its major proportion, i.e. a paraffinic oil means that the majority of the hydrogen and carbon atoms are present as paraffinic chains. A naphthenic oil has much smaller paraffinic chains in each hydrocarbon molecule and most carbon is incorporated in cyclic molecules. These paraffinic chains are then linked by carbon atoms which are bonded in a cyclic manner to form a more complex molecule. There is also only about 20% of simple paraffins (alkanes) present in the oil. The aromatic oil is present only as a minor component of naphthenic or paraffinic oils. The presence of one type or the other of these molecules determines some of the physical properties of the lubricants, namely: pour point, viscosity index, pressure-viscosity characteristics (Stachowiak & Batchelor, 2014: 53).

There are large differences in viscosity-temperature characteristics and viscosity-pressure characteristics between paraffinic and naphthenic oils and care must be taken in distinguishing between them (Stachowiak & Batchelor, 2014: 56). A detailed analysis of crude oil revealed 125 different compounds of which only 45 have been analysed in

detail (Stachowiak & Batchelor, 2014: 53). A result of this is that it is not possible to give an exact analysis of a mineral oil. The major part of mineral oils consists of hydrocarbons with approximately 30 carbon atoms in each molecule. The structure of each molecule is composed of several straight chains and cyclic carbon chains bonded together (Stachowiak & Batchelor, 2014: 57). Almost any composition of cyclic and straight chains may occur and a large number of the possible forms of the complex molecule are present in any single oil sample.

Mineral oils are also impure. The impure nature of mineral oils results in a range of useful and harmful properties. This implies the presence of trace compounds which can provide anti-oxidants and boundary lubrication properties. However, these compounds can also cause deposits which can hinder lubrication (Stachowiak & Batchelor, 2014: 53). Mineral oils differ from each other depending on the source of crude oil and refining process (Stachowiak & Batchelor, 2014: 56). The differences between the mineral oils are based on:

- Chemical forms (paraffinic, naphthenic or aromatic);
- Sulphur content;
- Viscosity

### **2.5.1.1 Chemical forms**

The differences in chemical forms of paraffinic mineral oils results in different physical properties between the oils. Due to this, paraffinic mineral oils can further be characterized by their physical properties, including pour points, which normally range from -17.8 to -6.7 °C, and also, viscosity index (VI) which is mainly the moderate change in viscosity with an increase in temperature. In general, the viscosity index of paraffinic oils will range from 85 to 100 (Hamrock *et al*, 2004: 70). Furthermore, paraffinic oils are high in paraffin hydrocarbons and contain some wax, whereas naphthenic oils are high in naphthenic hydrocarbons and contain little wax (Hamrock *et al*, 2004: 70).

Waxes which are virtually useless and can easily be oxidized to form harmful organic acids. Special additives are needed to neutralize these waxes and related compounds (Stachowiak & Batchelor, 2014: 56). The naphthenic oils have a higher density than paraffinic oils. Naphthenic oils, like paraffinic oils, are characterized by their pour points which normally range from -50 to -12 °C and have a larger change in viscosity with an increase in temperature. Their viscosity index will range from 0 to 60. Therefore, a naphthenic oil would be less suitable than a paraffinic oil in applications that operate over a wide range of temperatures (Hamrock *et al*, 2004: 70).

### **2.5.1.2 Sulphur Content**

The content of sulphur in mineral oils varies. This is largely dependent on the source of the crude oil and the type of refining process. Research has shown that between 0.1% and 1% of natural sulphur content ensures reduced wear, and on the other hand, too much sulphur may accelerate the corrosion of seals in mechanical machinery. Small quantities of sulphur are required for good lubricity. Excess sulphur can be removed from oil by refining, but this process can be expensive. Depending on the source of crude oil and the severity of refining, the sulphur content in mineral oils can vary between between 0% and 8% (Stachowiak & Batchelor, 2014: 57).

### **2.5.1.3 Viscosity**

Mineral oils can also be classified by their kinematic viscosity, which depends on the degree of refining. For commonly used mineral oils, kinematic viscosity can vary between about 4 cSt to 700 cSt at 100 °C. For example, the kinematic viscosity of a spindle oil is about 20 cSt, engine oil between 30 and 300 cSt, and that of bright stock is about 600 cSt at 100 °C (Stachowiak & Batchelor, 2014: 57).

## 2.5.2 Synthetic Oil Base Stocks

Synthetic hydrocarbons are compounds which are synthesized by chemical reactions starting with low-molecular-weight materials, and contain only carbon and hydrogen (Hamrock *et al*, 2004:71). The synthetic hydrocarbons mainly possess narrower boiling point ranges for a given viscosity than petroleum oils. However, they are similar to mineral oils in terms of compatibility with metals (Hamrock *et al*, 2004:71). Synthetic hydrocarbons were originally developed early in the 21<sup>st</sup> century by countries which were lacking a reliable supply of the mineral oils. The use of synthetic oils increased gradually, especially in more specialized applications for which mineral oils were inadequate (Stachowiak & Batchelor, 2014: 57).

The primary reasons for preparing synthetic hydrocarbons for use as lubricants are that chemical synthesis provides specific structures and characteristics and that molecular weight can be controlled within narrow ranges. Properties that are functions of molecular weight, such as viscosity and low-temperature characteristics, can be controlled within narrow ranges (Hamrock *et al*, 2004: 71). However, certain properties which are fixed by the chemical structures must be accepted in many cases. Synthetic oils generally have good thermal and oxidation stability, but their common weakness is limited lubricity (the ability of the lubricant to reduce friction other than by its purely viscous properties) (Hamrock *et al*, 2004: 71).

The limited lubricity is associated with oxidation and viscosity loss at high temperatures (Stachowiak & Batchelor, 2014: 57). Synthetic oils cost considerably more per unit volume than the petroleum oils they replace, though the real value of the lubricant is calculated on a price-for-performance basis (Hamrock *et al*, 2004: 71). Synthetic oils comprise of hundreds of organic and semi-organic compounds which cannot be easily classified, and therefore, will be grouped in terms chemical structure and in terms of physical properties, as was discussed with mineral oils (Hamrock *et al*, 2004: 71).

The most important commercial synthetic hydrocarbon lubricants are based on polyalphaolefin (PAO). The PAOs have high viscosity indexes, allowing for a wider operating temperature range, especially given its generally better oxidation stability and lower volatility than hydrocarbon liquids. Also, PAOs can have varied performance depending on the structure of the particular molecule (Hamrock *et al*, 2004:71). Three different molecular structures of PAO molecules synthesized from hexane molecules to form CIS alkanes, and of these structures, the CIS alkane in the "star" orientation displays superior lubrication properties. The three different PAO structures are illustrated in Figure 2.41 where; (a) star structure; (b) highly-branched structure and; (c) linear structure. Another common synthetic hydrocarbon lubricant is Polyisobutylene (PIB), which is mostly used as a metalworking liquid. However, the applications of PIB are limited because of its poor thermal stability (Hamrock *et al*, 2004: 73).

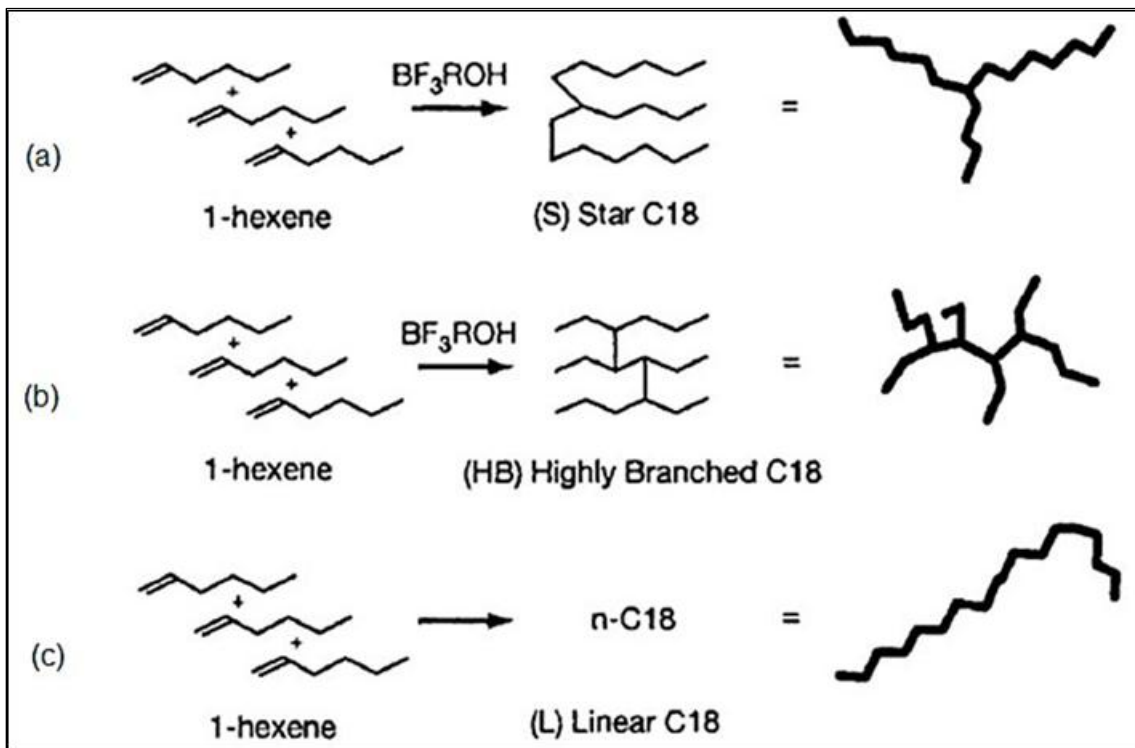


Figure 2.41: PAO structures (Hamrock *et al*, 2004: 73).

### **2.5.3 Base oil properties**

As discussed in the previous section, base oils are categorized using four physical properties. These important physical properties, which dictate how base oils will perform in service, are listed and described below (Brown, 2015 & Dresel & Mang, 2017: 71):

1. Pour point - The lowest temperature at which a sample of oil can be poured determines the pour point.
2. Viscosity - The oil's resistance to flow at a given temperature defines the viscosity. For example, honey is more viscous than water.
3. Viscosity index (VI) - As an oil's temperature changes, so does its viscosity, defining its VI. A high-VI oil changes viscosity less with temperature than a low-VI oil. The multi-grade engine oils specified by vehicle makers require high-VI base oils as a starting place in the formulation process. High-VI base oils have lower volatility and are designed to operate at low as well as high temperatures.
4. Purity - Constituents of many lubricants such as sulfur and polycyclic aromatic compounds must be limited.

The formulation method followed in the manufacture of base oils determines these properties. Purity is an important chemical property as it indicates the level of saturation of a base oil, which increases from Group I to Group V (Dresel & Mang, 2017: 72). The synthetic base oils have the highest level of saturation, whereas the solvent refined mineral base oils have the lowest level of saturation.

### **2.5.4 Group III+ Base oils**

Over the years, there have been continuous developments of more advanced base oils which have shown great potential to achieve the balance between cost and performance. The base oils of interest are those which are classified as Group III+ (group three plus) base oils according to their physical characteristics. The physical characteristics of Group III+ base oils vary between ultra-high viscosity base oils

(Group III) and polyalphaolefins (Group VI). These oils are categorized as Group III+ base oils (Dresel & Mang, 2017: 73). This category is not official, but it is recognized by industry for marketing purposes. Thus, the API classes can be updated as shown in Table 2.3.

As can be seen on Table 2.3, the Group III+ base oils have long and complex molecular structures with 20 to 30+ carbon atoms and are more than 90 % saturated with minor cyclic paraffins. Also, these oils have very low pour points ( $\approx -30$  °C depending on viscosity grade), narrow boiling ranges and high viscosity index (VI) ( $\geq 140$  for some grades) (Dresel & Mang, 2017: 72).

Table 2.3: Classes of base oils: Including GIII+ base oils (Baker et al, 2007; Dresel & Mang, 2017: 72 and Wheeler, 2016).

API Group	Sulfur (% w/w)		Saturates (% w/w)	Viscosity Index (VI)
I	> 0,03	and/or	< 90	80 - 120
II	$\leq 0,03$	and	$\geq 90$	80 - 120
III	$\leq 0,03$	and	$\geq 90$	> 120
III+	$\leq 0,03$	and	$\geq 90$	$\geq 140$
IV	All polyalphaolefins (PAO)		$\geq 90$	> 135
V	All base oils not included in Groups I-IV			

### 2.5.5 Viscosity and VI

This property is a measure of a liquids gradual deformation due to resistance to shear stress (Stachowiak & Batchelor, 2014: 11). An increase in temperature or a decrease in pressure weakens the intermolecular forces in a liquid. This invariably leads to a reduction in viscosity. Hence, the viscosity of a liquid should always be quoted at a specific temperature and pressure. If the pressure is omitted, it is generally understood

to be atmospheric pressure. For all liquids, as the temperature increases, the viscosity decreases. Oil viscosity also changes with shear rate. Different oils exhibit different resistances to shear stress, hence the differences in viscosities (Stachowiak & Batchelor, 2014: 11).

The thickness of the generated oil film is usually proportional to the viscosity. In practical situations, it normally appears that the more viscous oils would give better performance, since the generated films would be thicker and a better separation of the two surfaces in contact would be achieved. However, this is not always true since the more viscous oils require more power to be sheared, and as a result, the power losses are higher and more heat is generated. This results in an increase in the temperature of the contacting surfaces, and may lead to the failure of the component or tribo-chemical reactions (Stachowiak & Batchelor, 2014: 11).

For practical applications the oil viscosity is chosen to give optimum performance at the required temperature. Therefore, the knowledge of the temperature at which the oil is expected to operate is critical as oil viscosity is heavily temperature dependent. Apart from temperature, the viscosity of different oils can also be affected by the velocities of the operating surfaces (shear rates). Therefore, the knowledge of the viscosity characteristics of a lubricant is very important in the design and the prediction of the behaviour of a lubricated mechanical system (Stachowiak & Batchelor, 2014: 12). Viscosity is presented in two forms which are discussed in the following sections.

#### **2.5.4.1 Dynamic Viscosity**

Consider two flat surfaces separated by a film of liquid of thickness or height ( $h$ ) as shown in Figure 2.42. The force required to move the upper surface is proportional to the wetted area ( $A$ ) and the velocity gradient ( $u/h$ ), as the individual liquid layer in a thicker film will be subjected to lesser shear than in a thin film. This relationship is maintained for most liquids. Different liquids will exhibit a different proportionality constant ( $\eta$ ) which is called the dynamic viscosity.



The relationship can be written as:

$$F = \eta \times A \times \frac{U}{h} \quad (2.46)$$

Rearranging gives:

$$\eta = \frac{\left(\frac{F}{A}\right)}{\left(\frac{U}{h}\right)} = \frac{\tau}{\left(\frac{u}{h}\right)} \quad (2.47)$$

Where:

$\eta$  is the dynamic viscosity [Pa.s];

$\tau$  is the shear stress acting on the liquid [Pa];

$u/h$  is the shear rate, i.e., velocity gradient normal to the shear stress [ $s^{-1}$ ].

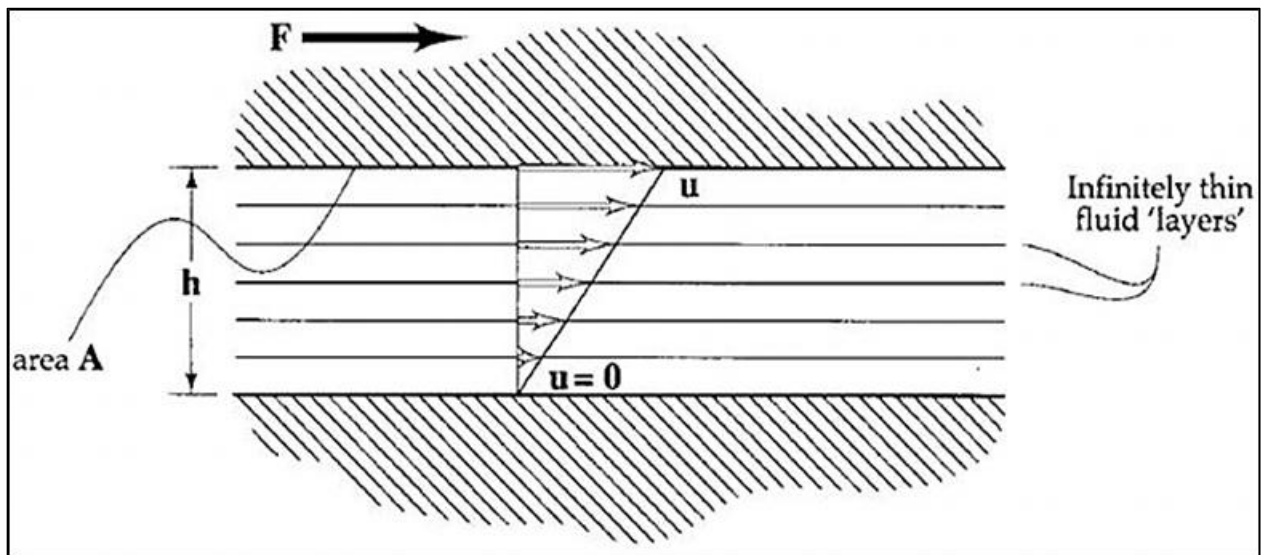


Figure 2.42: Schematic representation of the liquid separating two surfaces (Stachowiak & Batchelor, 2014: 12).

Prior the introduction of the SI system, the dynamic viscosity unit was the Poise [P]. For practical applications the Poise was too large, thus a smaller unit, the centipoise [cP],

was more commonly used. The SI unit for dynamic viscosity is Pascal-second [Pa.s] (Stachowiak & Batchelor, 2014: 12). The relationship between Pascal-second and Poise is as follows:

$$1 \text{ P} = 100 \text{ cP} \approx 0.1 \text{ Pa.s}$$

### 2.5.4.2 Kinematic Viscosity

The kinematic viscosity is defined as the ratio of dynamic viscosity to liquid density:

$$\eta_k = \frac{\eta}{\rho} \quad (2.48)$$

where:

$\eta_k$  is the kinematic viscosity [ $\text{m}^2/\text{s}$ ];

$\eta$  is the dynamic viscosity [Pa.s];

$\rho$  is the liquid density [ $\text{kg}/\text{m}^3$ ].

Prior the introduction of the SI system, the kinematic viscosity unit was the Stoke [St]. This unit was too large for most practical applications, thus a smaller unit, the centistoke [cSt], was introduced (Stachowiak & Batchelor, 2014: 13). The SI unit for kinematic viscosity is [ $\text{m}^2/\text{s}$ ], and the relationship between the two units is:

$$1 \text{ St} = 100 \text{ cSt} = 0.0001 \text{ m}^2/\text{s}$$

### 2.5.6 Viscosity temperature relationship

The viscosity of lubricating oils is extremely sensitive to the operating temperature (Stachowiak & Batchelor, 2014: 13). With increasing temperature, the viscosity of oils falls quite rapidly. The trend normally shows a power relationship between the two. In some cases the viscosity of oil can fall by about 80% with a temperature increase of

25 °C. It is important to know the viscosity at the operating temperature since it influences the lubricant film thickness separating two surfaces. Viscosity at a specific temperature can be either calculated from the viscosity-temperature equation or measured as per ASTM methods or obtained from the viscosity-temperature ASTM chart (Stachowiak & Batchelor, 2014: 14).

### 2.5.7 Viscosity pressure relationship

Most organic liquids exhibit a reversible increase in viscosity with the application of high pressure. This is due to molecular mobility restrictions imposed by the pressure (force) being exerted (Mia *et al*, 2010). This phenomenon is called the piezoviscous effect. The piezoviscous effect is especially important for base oils because, in most mechanical applications, films of liquid are compressed between sliding surfaces under very high loads (Mia *et al*, 2010). The degree to which a liquid thickens under pressure can be approximated by equations such as the Barus and Roelands equation (Hamrock *et al*, 2004: 88). As long ago as 1893, Barus proposed the following formula for the isothermal viscosity-pressure dependence of liquids (Hamrock *et al*, 2004: 88 and Stachowiak & Batchelor, 2014: 17):

$$\ln\left(\frac{\eta}{\eta_0}\right) = \alpha P \quad (2.49)$$

Where:

$\ln$  is the natural logarithm,  $\log_e$

$\eta$  is the dynamic viscosity [Pa.s];

$\eta_0$  is the dynamic viscosity at  $p = 0$  and at a constant temperature [Pa.s];

$\alpha$  is the pressure-viscosity coefficient dependent on temperature [ $\text{m}^2/\text{N}$ ];

$P$  is the gauge pressure [ $\text{N}/\text{m}^2$ ].

Although Equation 2.49 is extensively used, it is not generally applicable and is valid as a reasonable approximation only at moderate pressures. Because of this limitation, several isothermal viscosity-pressure models have been proposed that usually fit experimental data better than that suggested by Barus (1893). One of these models was developed by Roelands in 1966, who undertook a wide-ranging study of the effect of pressure on lubricant viscosity. For isothermal conditions the Roelands formula can be written as (Hamrock et al, 2004: 89 and Stachowiak & Batchelor, 2014: 17):

$$\log \eta + 1.200 = (\log \eta_0 + 1.200) \left(1 + \frac{P}{2000}\right)^{Z_1} \quad (2.50)$$

Where:

Log = common logarithm,  $\log_{10}$

$\eta$  is the dynamic viscosity [Pa.s];

$\eta_0$  is the absolute (dynamic) viscosity at  $P = 0$  and a constant temperature [Pa.s];

$P$  is the gauge pressure [ $\text{kg}_{\text{force}}/\text{cm}^2$ ];

$Z_1$  is the viscosity-pressure index, a dimensionless liquid specific constant.

Taking the antilog from both sides of the above equation and rearranging gives:

$$\frac{\eta}{\eta_0} = 10^{-(1.200 + \log \eta_0) \left[1 - \left(1 + \frac{P}{2000}\right)^{Z_1}\right]} \quad (2.51)$$

Rearranging this equation gives

$$\eta = \eta_0 \left(\frac{\eta_\infty}{\eta_0}\right)^{1 - \left(1 + \frac{P}{C_p}\right)^{Z_1}} \quad (2.52)$$

Where:

$\eta_\infty$   $6.31 \times 10^{-5}$  N.s/m<sup>2</sup>;

$C_p$   $1.96 \times 10^8$  N.s/m<sup>2</sup>;

Table 2.4 gives values of the viscosity-pressure index  $Z_1$  (Hamrock *et al*, 2004: 91). Roelands (1966) found that for most liquids  $Z_1$  is usually constant over a wide temperature range. This is confirmed in Table 2.4, the only exceptions being the synthetic hydrocarbon (traction liquid) and the C-ether (Hamrock *et al*, 2004: 91).

Table 2.4: Dimensionless viscosity-pressure index for liquids at three temperatures (adopted from Hamrock *et al*, 2004: 93).

Liquid	Temperature		
	38	99	149
	Viscosity-pressure index ( $Z_1$ )		
Advanced ester	0.42	0.45	0.48
Formulated advanced ester	0.44	0.45	0.49
Polyalkyl aromatic	0.52	0.59	0.59
Synthetic paraffinic oil (lot 3)	0.4	0.47	0.42
Synthetic paraffinic oil (lot 4)	0.45	0.47	0.5
Synthetic paraffinic oil (lot 2) plus antiwear additive	0.41	0.43	0.44
Synthetic paraffinic oil (lot 4) plus antiwear additive	0.44	0.48	0.48
C-ether	0.57	0.45	0.44
Superrefined naphthenic mineral oil	0.71	0.64	0.66
Synthetic hydrocarbon (traction liquid)	0.97	0.83	0.57
Fluorinated polyether	1.03	1.1	1.27

There are several other empirical formulae which are recommended in literature for the determination of viscosity with changing pressure. Most of these formulae are modifications of the Barus equation and have limited applications. There are two main forms which the equations can take namely (Marusik-Paloka and Pazanin, 2013 & Guo *et al*, 2018):

1. The linear law. This takes the form:

$$\eta(P) = \eta_o(1 + \alpha P) \quad (2.53)$$

2. The exponential law. This takes the form:

$$\eta(P) = \eta_o e^{\alpha P} \quad (2.54)$$

The Roelands equation takes the exponential form. For extreme pressure conditions, a model by Chu and Cameron is recommended. This model is given below (Stachowiak and Bachelor, 2014: 17):

$$\eta(P) = \eta_o(1 + C_m P)^n \quad (2.55)$$

where  $C_m$ ,  $n$  are constants. The value of  $n$  is approximately 16 for most cases and  $C_m$  can be obtained graphically from the diagram shown in Figure 2.43.

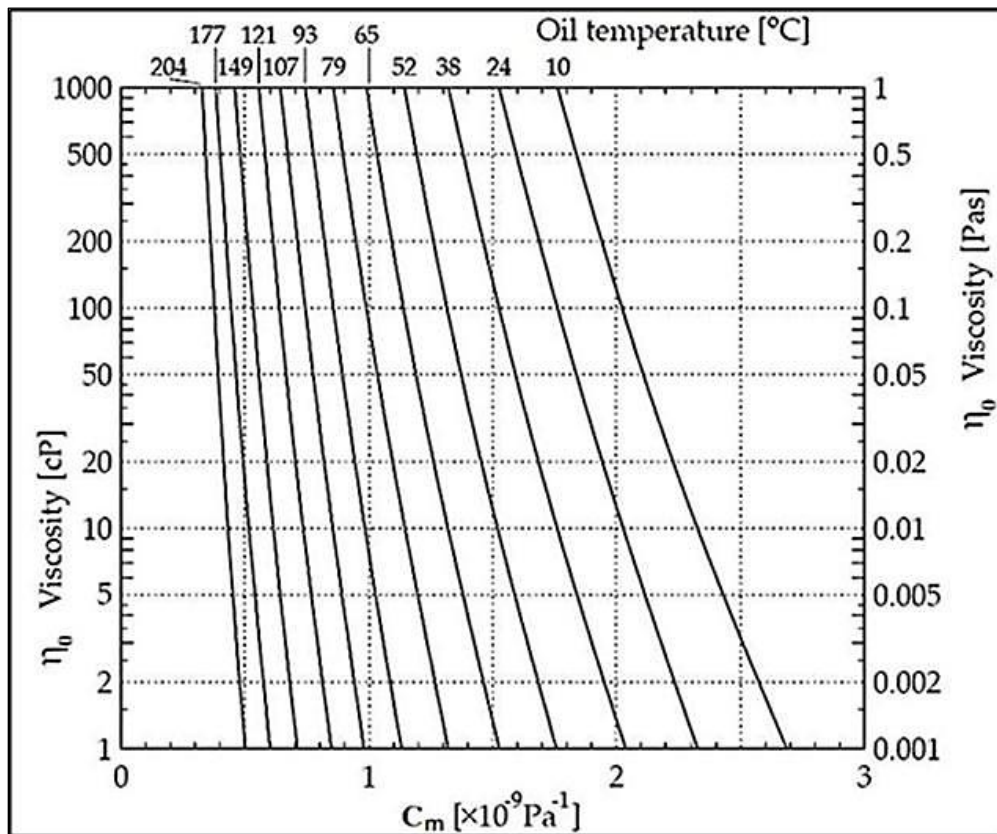


Figure 2.43: Graph for determination of the constant “ $C_m$ ” (Stachowiak and Bachelor, 2014: 19).

### 2.5.7 Viscosity Index

The viscosity index (VI) is an empirical parameter that compares the kinematic viscosity of the oil of interest to the viscosities of two reference oils that have a considerable difference in sensitivity of viscosity to temperature (Stachowiak & Batchelor, 2014: 15). In a practical sense, there is always a need to accurately describe the viscosity-temperature characteristics of oils. Some oils are less sensitive to changes in viscosity with temperature (whether mineral or synthetic), these liquids are said to have a high viscosity index. Likewise, some liquids are more sensitive to changes in viscosity with temperature and are said to have a low viscosity index (Stachowiak & Batchelor, 2014: 15).

In 1920, it was known that Pennsylvania crude oils were better than the Gulf Coast crude oils. Pennsylvania crude had the best viscosity temperature characteristics while the Gulf Coast crude had the worst since its viscosity varied much more with temperature. In 1929 a Viscosity Index was developed by Dean and Davis (Stachowiak & Batchelor, 2014: 15). The reference oils have been selected in such a way that one has a viscosity index equal to zero (VI=0) and the other has a viscosity index equal to one hundred (VI=100) at 37.8 °C but they both have the same viscosity as the oil of interest at 98.89 °C. Since Pennsylvania and Gulf Coast oils have the same viscosity at 98.9 °C they were initially selected as reference oils. Oils made from Pennsylvania crude were assigned the viscosity index of 100, whereas oils made from the Gulf Coast crude the viscosity index of 0 (Stachowiak & Batchelor, 2014: 15).

The viscosity index can be calculated from the following formula (ASTM D2270):

$$VI = \frac{(L - U_v)}{(L - H)} \quad (2.56)$$

Firstly, the kinematic viscosity ( $U_v$ ) of the oil of interest is measured at 40 °C and at 100 °C. Then the values of L and H that correspond to the viscosity at 100 °C of the oil of interest are read as illustrated in Figure 2.44 following the procedure as per

ASTM D2270. Substituting the obtained values of U, L and H into Equation 2.52 yields the viscosity index. The viscosity index is an inverse measure of the decline in oil viscosity with temperature. High values indicate that the oil shows less relative decline in viscosity with temperature (Stachowiak & Batchelor, 2014: 16):

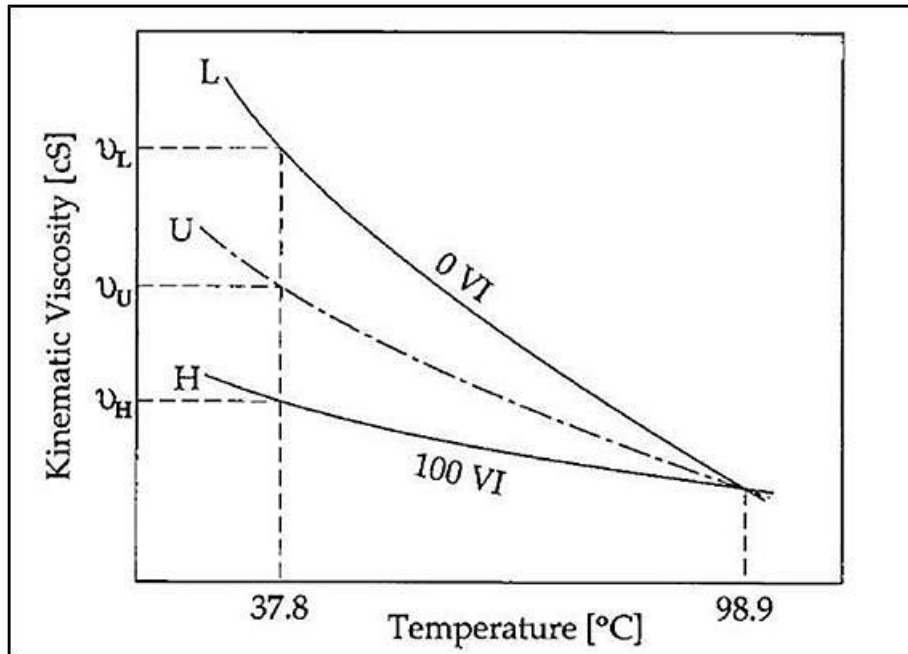


Figure 2.44: Evaluation of viscosity index (Stachowiak & Batchelor, 2014: 16).

## 2.6 Water: role in lubrication

Studies have shown that the presence of water in the atmosphere can affect oil lubricity (Zheng-bing *et al*, 2015). Water is a ubiquitous contaminant in all lubrication systems. Due to its solubility in hydrocarbons (oils), water causes many problems in lubrication systems including viscosity drop and corrosion of metallic materials (Ichiro, 2017). Water molecules from the atmosphere can dissolve in oil during manufacture. This is an unavoidable situation in many cases. Also, water vapor in the air can also condense at dew point and enter the oil in the form of water droplets during operation/storage (Johnson, 2009). These water molecules can diffuse through the oil and end up at the surfaces of the interacting bodies, causing severe changes in the surface chemistry.



This can improve or harm the interacting surfaces, depending on the nature of oil and operating conditions (Zheng-bing *et al*, 2015). In the following sections, the interactions between oil and water under lubricated conditions are discussed.

### 2.6.1 Solubility of water in hydrocarbons

The solubility of water in oils is affected by the chemical structure of the oil and the pressure and temperature of the water/oil system (Yaws & Yadav, 2012). For the purpose of this discussion, water will be taken as available in the atmosphere in the vapour phase. The solubility limits of water can be correlated to the temperature of the water/hydrocarbon system at a constant pressure by the empirical equation by Yaws & Yadav (2012) given as:

$$\log_{10}S = A + \frac{B}{T} + C \times \log_{10}T \quad (2.57)$$

Where:

S is the solubility of water, [ppm (wt)]

T temperature of the system, [°C]

A, B and C are regression coefficients for the hydrocarbon (oil), available in solubility data sources. Figure 2.45 shows variation in solubility for mineral oils (i.e.; aromatic, hydraulic and transformer oil) at various temperatures (Johnson, 2009).

It can be seen from Figure 2.45 that for mineral oils, the solubility increases non-linearly with temperature. It is well known that the boiling temperature increases with increasing molecular chain length. Solubility for most straight chain hydrocarbons has been found to decrease with increasing chain length at one temperature (i.e., 25 °C), and water solubility increases more with temperature for molecules with shorter chain lengths than for those with longer chain lengths (Yaws & Yadav, 2012).

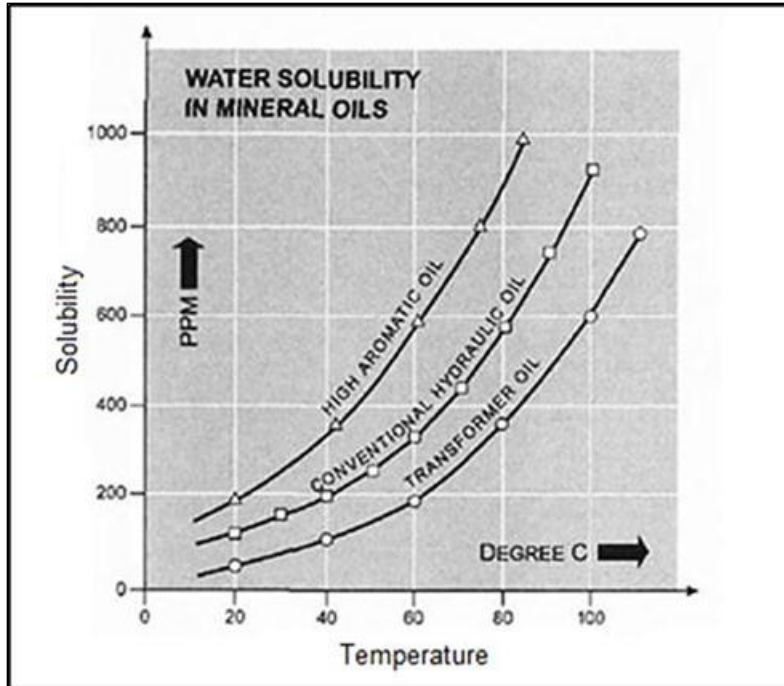


Figure 2.45: Water solubility with changing temperature (Johnson, 2009).

The solubility of water vapor in oils can be correlated to the partial pressure of water in the atmosphere by the Henry's law (Yaws, 2010). Henry's law developed by William Henry in 1803 states that at a constant temperature, the amount of gas that dissolves in a given volume of liquid is directly proportional to the partial pressure of the gas in equilibrium with the liquid provided the partial pressure is not very large. The Henry's law is described as:

$$S = H_c P_w \quad (2.58)$$

Where:

S is the solubility of water in a liquid, [ppm (wt)]

$H_c$  is the Henry's law solubility constant, [kPa/mol. fr.]

$P_w$  is the partial pressure of water vapor, [kPa].

It is clear from the above equation that the system has to be in equilibrium for the equation to hold. The Henry's law constants ( $H_c$ ) for various hydrocarbons can be

found from the sources of data at different temperatures. Yaws (2010) found the values of  $H_c$  and  $S$  to be decreasing with the hydrocarbon chain length under constant pressure and 25 °C. An increase in the partial pressure of the water vapor at the interface of the liquid increases the solubility (Yaws, 2010). Both temperature and pressure have an effect on the solubility of water in hydrocarbons. Therefore, both have to be considered where solubility is of concern. The partial pressure of water vapor is a function of amount of moisture present in an atmosphere which is presented as relative humidity.

### 2.6.2 Relative Humidity

Relative humidity (RH) indicates the amount of moisture (water) in the air as a percentage of the maximum amount the air can hold (below 100 °C). Unfortunately, the amount of moisture the air can hold depends on the temperature of the air. The maximum percentage of moisture that the air can hold increases with temperature. Above 100 °C, it is possible for air to be totally water vapour (steam) and the % moisture can reach 100% by volume (The Rotronic Humidity Handbook, 2005). Relative humidity is expressed as a ratio of two pressures. This parameter is normally given as a percentage (%) from 0 to 100, and calculated as:

$$\%RH = 100 \times \frac{P_w}{P_s} \quad (2-59)$$

Where:

$P_w$  is the partial pressure of water vapor in air [kPa]

$P_s$  is the saturation (vapour) pressure of water at the ambient temperature [kPa]

The saturation pressure of water vapor is the partial pressure of water vapor at 100% humidity (The Rotronic Humidity Handbook, 2005). 100% humidity is the point where liquid water and water vapor are in equilibrium, which means the water is evaporating into vapor and the vapor is condensing into liquid. Since water boils at 100 °C at atmospheric pressure, the pressure  $P_s$  must go above atmospheric pressure when the

temperature goes above 100 °C. The partial pressure of a gas is the part of the total pressure that is exerted by that gas alone (The Rotronic Humidity Handbook, 2005). For an air and water vapor mixture this can be expressed as:

$$P_T = P_w + P_{air} \quad (2-60)$$

Where:

$P_T$  is the total pressure of the atmosphere [kPa];

$P_{air}$  is the partial pressure of air in the atmosphere [kPa].

Above 100 °C  $P_w$  is equal to the atmospheric pressure ( $P_{atm}$ ) when the moisture level is 100%, but  $P_s$ , the saturation pressure, increases rapidly with temperature. This suggests that under normal conditions, the atmospheric temperature is the only factor that affects relative humidity.

### 2.6.3 Diffusion

For a water soluble molecule to reach the lubricated contact area, it has to diffuse through the bulk oil. Diffusion is the spontaneous mixing of atoms or molecules by random thermal motion. Diffusion gives rise to motion of the species relative to motion of the mixture (Fogler, 2006: 758). In the presence of a concentration gradient, molecules of a given species within a single phase will always diffuse from regions of higher concentrations to regions of lower concentrations. Temperature, electric potential and gravitational potential are gradients which also promote diffusion. A gradient results in a molar flux ( $W$ ) of the one species (i.e., water) in the direction of the concentration gradient (Fogler, 2006: 758). For a two component system, Ficks law describes the molar diffusive flux of a component A in the vertical ( $z$ ) direction related to its concentration gradient as (Fogler, 2006: 761):

$$W_A = -cD_{AB} \frac{\partial y_A}{\partial z} + y_A(W_A + W_B) \quad (2.61a)$$

Where:

$W_A$  is the molar flux of component A, [mol/m<sup>2</sup>s];

$W_B$  is the molar flux of component B, [mol/m<sup>2</sup>s];

$y_A$  is the molar fraction of component A, [-];

$y_B$  is the molar fraction of component B, [-];

$c$  is the total concentration [mol/m<sup>3</sup>];

$D_{AB}$  is the diffusivity of A in B, [m<sup>2</sup>/s].

In the case where component B is stationary,  $W_B$  assumes a value of 0, and Equation 2.61a simplifies to Equation 2.61b as shown below:

$$W_A = -cD_{AB} \frac{\partial y_A}{\partial z} + y_A W_A = -D_{AB} \nabla C_A + y_A W_A \quad (2.61b)$$

Where:

$C_A$  is the molar concentration of component A, [mol/m<sup>3</sup>].

The diffusivity ( $D_{AB}$ ) is a strong function of temperature and pressure. Studies have shown that for liquid solvents it increases with increasing temperature of the system, and for gases it decreases with increasing pressure. Therefore, at a specific time,  $D_{AB}$  can be kept constant by fixing the temperature and pressure of the system (Fogler, 2006: 770). For liquid solvent, the diffusivity-temperature dependency has been found to be given by:

$$D_{AB, T_2} = D_{AB, T_1} \frac{\eta_1 \left( \frac{T_2}{T_1} \right)}{\eta_2} \quad (2.62)$$

Where,  $\eta_1$  and  $\eta_2$ , and  $D_{AB, T_1}$  and  $D_{AB, T_2}$  are the liquids viscosities and diffusivities at temperatures  $T_1$  and  $T_2$ , respectively. The above shows the strong dependency of diffusivity on the viscosity of the liquid (Fogler, 2006: 770).

#### 2.6.4 Forms of water in oil

Water can be available in three forms in oil, namely:

1. Dissolved water
2. Emulsified water
3. Free water

Dissolved water is basically small individual water molecules dispersed throughout the oil. This state occurs naturally, which means that the oil can accumulate most of the moisture during manufacturing with concentrations is too small for the molecules to agglomerate. Because the water concentration is very low, it is not visible through the naked eye. Every oil has a water holding capacity limit which is dependent of the hydrocarbon structure, chain length and the temperature of the system (Zheng-bing *et al*, 2015). The dissolved water can be evaporated out of the lubricating interfaces at elevated temperatures, typically 70 – 100 °C (Johnson, 2009). For water to evaporate properly from lubrication interfaces the following may be required:

1. Large air to oil surface area;
2. Low relative pressure (below the saturation pressure of water at the operating temperature);
3. High degree of oil movement (turbulence);
4. Good lubricant chemical health (high interfacial tension).

Should it happen that the oil accumulate too much water beyond its saturation limit, the dissolved water molecules agglomerate and form droplets which separate from the oil and are visible to the naked eye. This happens when the amount of moisture in the air/atmosphere surrounding the oil exceeds the oils saturation limit. This water can turn into emulsified water or free water. Emulsified water is a state where a mixture of separated phases of oil and water droplets occurs without forming two distinct layers, while free water is a state where water and oil have formed two distinct separate layers which appear as haze or fog, in most cases the oil layer will be suspended at the top of the mixture (Zheng-bing *et al*, 2015).

Lubricating properties of a water–oil emulsion have been reported with poorer than those of water-free oils. Particularly, emulsion or free water in oil would cause more damage than does dissolved water because the former causes higher compressibility of the oil film at the contact area, increased risk of cavitation and lubricant film collapse. On the other hand, the dissolved water in the lubricant, almost inevitable in most industrial applications, is known to increase metal surface oxidation (Zheng-bing et al, 2015).

### 3. Experimental

#### 3.1 Test apparatus

In this section, the equipment that was used in this investigation is listed and discussed.

##### 3.1.1 SRV tribometer

The friction experiments were carried out using the SRV tribometer with a ball-on-disc configuration. SRV is an abbreviation for Schwingung, Reibung, Verschleiss, which is the German translation for oscillation, friction and wear. The model of the SRV tribometer used in this investigation is the SRV4<sup>®</sup> from Optimol instruments, shown in Figure 3.1. In this tribometer, the normal load is applied from the top, on the steel ball, which is then rubbed against a stationary steel disc through a sideways oscillatory motion.

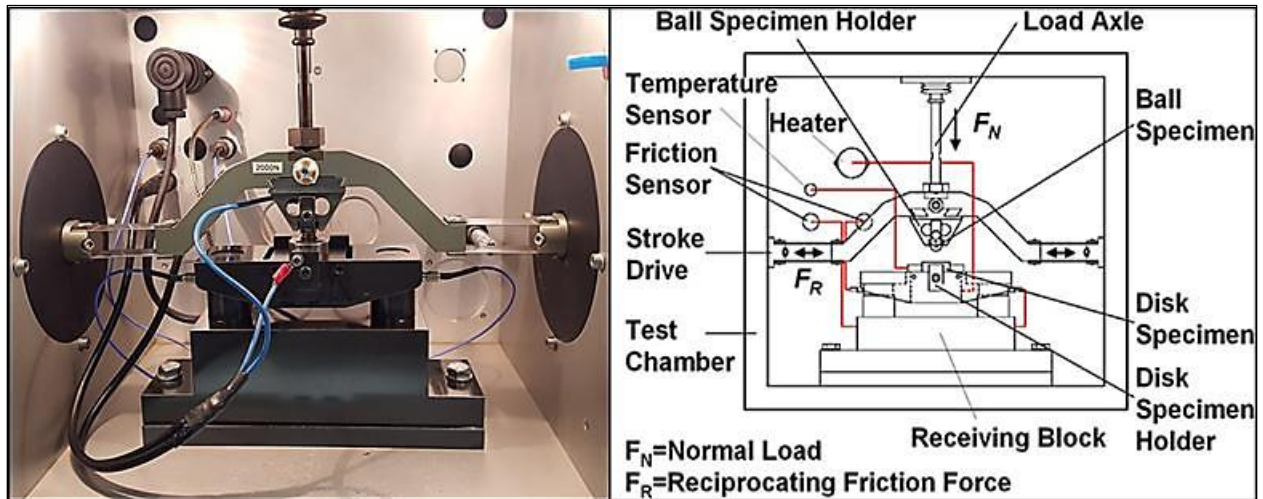


Figure 3.1: Image and schematic view of the test chamber of the SRV<sup>®</sup> 4 reciprocating ball-on-disc tribometer with installed oscillation block (SRV4<sup>®</sup>, Optimol Instruments, Germany).

Table 3.1 presents the temperature, load and frequency ranges for the experimental work done on the SRV tribometer.



Table 3.1: Operating limits for the SRV4<sup>®</sup> tribometer (SRV4<sup>®</sup>, Optimol Instruments, Germany).

<b>Variable</b>	<b>Range</b>
Temperature	-35 to 350 °C
Load	Up to 2000 N
Frequency	1 to 511 Hz
Stroke length	1 to 5 mm

### 3.1.2 Viscometer

The Viscosities of the base oils investigated in this study were measured using Stabinger Viscometer SVM 3000/G2 at atmospheric pressure (Anton Paar, 2011: 14). This instrument conducts the measurements as per ASTM D7042. This viscometer contains a tube in which the oil sample passes through. This tube rotates at a constant speed. Inside this rotating tube is a low density rotor, with a built-in magnet, which floats in the sample and is centered by centrifugal forces due to its low density. The viscometer measures the rotational speed of the floating rotor which is used to estimate the samples viscosity with a Hall Effect sensor. The Stabinger viscometer has an operating temperature range of -56 °C to 105 °C (Anton Paar, 2011: 14 - 33). The viscosities at 120 °C were estimated by the function fitting method as described in appendix A, with an average correlation value  $R^2 > 0.98$ .

### 3.1.3 Ultrasonic Cleaner

The PS-40 ultrasonic cleaner was used to clean the test specimen prior and after each experiment, at atmospheric temperature and pressure i.e., 25 °C and 101 kPa. This machine agitates a liquid by using cavitation bubbles which are induced by a high frequency sound. The agitation produces high forces on the contaminants on the test specimen, forcing them to dissolve in solvent at a user set temperature. The operating limits for the PS-40 ultrasonic cleaner are given in Table 3.2.

Table 3.2: Operating limits for the PS-40 ultrasonic cleaner (Ultrasonic cleaners made in China, 2017).

<b>Variable</b>	<b>Range</b>
Operating Frequency	40 kHz
Ultrasonic Power	240 W
Heating Power	400 W
Tank Capacity	10 L
Timer	1-30 min

### 3.1.3 Relative humidity control

In a study done by Cai *et al* (2015), it was found that atmospheric water content severely affected the friction behaviour of an SAE 0W30 and a PAO (4cSt) base oils, with containing no additive package. This was observed in the temperature range 75 – 100 °C. In a study done by Benadé (2014), it was found atmospheric water content affected the repeatability of friction tests which were done on a metal working liquid at 100 °C. Therefore, to ensure good repeatability from the experiments and minor effects of moisture on friction in this study, the atmospheric water content of the test chamber was kept constant using an in house built humidity control system.

The relative humidity (RH) of the SRV test atmosphere/chamber was manually maintained at 20 % throughout the investigation. A schematic diagram and working principle of this setup are presented in Appendix E. Due to the change in the partial pressure with temperature, the solubility of water increases with increasing temperature, up to about 100 °C (Zheng-bing *et al*, 2015). This low % RH value was chosen to ensure minute absorption of water molecules by the base oils under study at the five experimental temperatures. The oils were stored in the same ambient environment, so their dissolved water contents were thought to have been at or near saturation. Though the test atmosphere consisted of air and water vapor, only water vapor was of particular interest in this investigation.

### 3.2 Experimental conditions and procedure

Pure sliding friction experiments were carried out using the SRV4<sup>®</sup> tribometer where a 10 mm reciprocating steel ball was loaded and rubbed against a 24 mm diameter stationary steel disc, under a fixed reciprocating frequency of 50 Hz and a stroke length of 2 mm, resulting in a mid-stroke velocity of 0.2 m.s<sup>-1</sup>. Each experiment was conducted under a fixed temperature condition using unused ball and disc specimens. The lubricating oils were loaded on the disc which was held on a block, prior to the start of each test, to ensure a lubricated contact with the reciprocating ball throughout the test duration. For each test, 5–6 mL of lubricating oil was used on a batch basis. Table 3.3 summarizes the experimental conditions and the properties of the materials used.

Prior to the start of each experiment the test specimen were cleaned by soaking in toluene under ultrasonic vibration for 10 minutes. After that they were oven dried at 50 °C for 5 minutes and then placed in a desiccator with inert moisture absorbing silica (SiO<sub>2</sub>) granules for 10 minutes. This was followed by soaking in acetone under ultrasonic vibration for 10 minutes at room temperature, oven drying at 50 °C for 5 minutes and desiccation for 10 minutes. This was then followed by the assembling of the test specimen on the holders and the loading of the lubricant. A clean syringe was to load the base oils on the disc specimen.

After assembling the specimen on the SRV test block, the SRV test chamber was conditioned for 10 minutes, at 20 % RH prior the start of each test. The block which held the disc had a heater underneath with a temperature control system allowing for experiments to be conducted at the desired temperatures. In this study, temperature means the temperature of the electrical resistance heater placed under the disc specimen. Because each disc specimen was heated for approximately 10 min, before starting the oscillatory motion between the ball and disc, the test temperature was regarded as the initial temperature of the lubricating oil and disc specimen.

Table 3.3: Experimental conditions and properties of test specimen

<b>Test conditions</b>		
Load applied	50 – 250 N (@ 40 N/min)	
Stroke length	2 mm	
Frequency	50 Hz	
Temperature	40, 60, 80, 100 & 120 °C	
Relative Humidity (RH)	20 %	
<b>Properties</b>	<b>Ball</b>	<b>Disc</b>
Material	AISI E52100 steel	AISI E52100 steel
Surface finish ( $R_a$ )	0.025 +/- 0.005 $\mu\text{m}$	0.45 to 0.65 $\mu\text{m}$ $R_z$ lapped
Diameter	10 mm	24 mm (Height: 7.9 mm)
<b>Material properties for ball and disc</b>		
Bulk modulus	140 GPa	
Modulus of elasticity	210 GPa	
Hardness (Rockwell)	600 HV	
Shear modulus	80 GPa	
Thermal conductivity	46.6 W/mK	
Heat capacity	0.475 kJ/kgK	


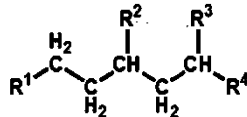
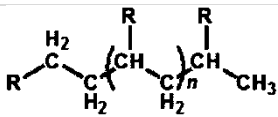
During each test, the reciprocating frequency, relative humidity (RH) and temperature were kept almost constant (accuracy within  $\pm 1$  Hz of reciprocating frequency,  $\pm 5$  % of RH and  $\pm 1$  °C of temperature) by feedback control. The friction experiments were conducted from low to high contact loads with the range: 50 N to 250 N. Each test was repeated three times, and the COF values obtained for each test were averaged for every 5 seconds, and the average values of the three repeat tests was calculated and reported. These experiments were conducted following the ASTM D7421-11 as a guide, by allowing a 1 minute run-in. First, the load was held at 30 N for 30 seconds, and then followed by a 30 seconds gradual load increase (40 N/min) to 50 N. After this run-in period the gradual load increase was continued from 50 N at a gradient of 40 N/min until a final load of 250 N or until seizure. This portion of the load increase

following the run-in was used to generate Stribeck curves. In this investigation, seizure was viewed as a sharp rise in the coefficient of friction, which can go beyond a value of 0.2.

### 3.3 Lubricants

A total of seven lubricants that were selected for this study were commercial base oils from various suppliers were as listed in Table 3.4.

Table 3.4: Oil sample matrix (Ichiro, 2017).

Base Oil	Preparation process	Chemical structure (Examples)	Viscosity Grade(s)
<b>Group I</b>	Solvent refined	 Organic Sulphides	4 cSt
<b>Group III</b> (Supplier 1)	Hydroprocessed	 Paraffinic	4 cSt & 6 cSt
<b>Group III</b> (Supplier 2)	Hydroprocessed		4 cSt & 6 cSt
<b>Group III+</b>	Hydrocracked from wax		4 cSt
<b>Group IV</b>	Oligomerized (Synthetic)	 PAO	4 cSt

### 3.4 Film thickness calculation

The minimum film thickness empirical equation that was used for film thickness calculations is Equation 2.42 given below, as derived by Hamrock and Dowson for point contacts.

$$h_{\min} = R_x 3.63 U^{0.68} G^{0.49} W^{-0.073} (1 - e^{-0.68k}) \quad (2.41)$$

With:

$$W = \frac{F_N}{E^*R_x^2} \quad (2.42)$$

$$U = \frac{u_{avg}\eta_0}{E^*R_x} \quad (2.43)$$

$$G = \alpha E^* \quad (2.44)$$

$$u_{avg} = u_b = 0.2 \text{ m.s}^{-1}$$

Where  $h_{min}$  is the minimum film thickness in nm,  $U$  is the speed parameter,  $G$  is the materials parameter,  $W$  is the load parameter and  $k$  is the ellipticity parameter with a value of 1 for a ball-on-disc configuration (Hamrock *et al*, 2004: 7 and Stachowiak & Batchelor, 2014: 324).

This formula is routinely used for materials of high elastic modulus including steel on steel, even up to maximum hertzian pressures of 3 - 4 GPa (Stachowiak & Batchelor, 2014: 324).

## 4. Results and discussion

In this section, the results as obtained from the experimental work done with the seven base oils under study are presented and discussed.

### 4.1 Physical properties

#### 4.1.1 Viscosity Index (VI):

The VI's of the seven base oils were calculated using an online calculator from <http://oil-additives.evonik.com/product/oil-additives/resources/viscosity-index-en.html> according to ASTM D2270 as summarized in section 2.5.7. Table 4.1 presents the results. From the seven base oils under investigation, the GIII+ (4cSt) base oil was found to have the highest VI with a value of 131. This indicates that this base oil's viscosity is the least affected by the changes in temperature. The base oil with the lowest VI (103) was found to be the GI (4cSt) base oil, indication of a viscosity that is the most affected by the changes in temperature. The GIII S2 (4cSt) base oils had a higher VI compared to the GIII S1 (4cSt) base oil, whereas the GIII S1 (6cSt) base oil showed a higher VI than the GIII S2 (6cSt) base oil. The VI behaviour arranged in decreasing order and represented by the base oils is: GIII+ (4cSt) > GIII S2 (4cSt) > PAO (4cSt) and GIII S1 (4cSt) > GIII S1 (6cSt) > GIII S2 (6cSt) > GI (4cSt).

#### 4.1.2 Viscosity: Effects of temperature

Figure 4.1 shows the dynamic viscosities ( $\eta_0$ ) of the seven base oils under investigation at the five experimental temperatures. On this Figure, the dynamic viscosity is given in the y-axis in units of mPa.s, and the temperature in °C is given on the x-axis. From Figure 4.1, the trends show a power relationship between dynamic viscosities of the base oils, which follows a decrease in dynamic viscosity with increasing temperature. At 40 °C, the GIII S1 (6cSt), GI (4cSt) and GIII S2 (6cSt) base oils had the largest dynamic viscosities of 28.6, 28.3 and 27.7 mPa.s respectively. The remaining four base oils had viscosities decreasing in the order: GIII S1 (4cSt), GIII S2 (4cSt), GIII+ (4cSt) and PAO (4cSt) with the values 16, 15, 14.3 and 14.2 mPa.s respectively.

Table 4.1: Base oil properties at atmospheric pressure.

Base Oil	$\eta_k$ (cSt)		Density ( $\rho$ ) at 15 °C, (g/cm <sup>3</sup> )	Sulfur (% w/w)	Saturates (% w/w)	$\alpha$ at 100 °C (GPa <sup>-1</sup> )	VI
	40 °C	100 °C					
<b>GI (4cSt)</b>	28.38	5.03	0.86	> 0.03	< 90	12.1	103
<b>GIII S1 (4cSt)</b>	20.06	4.33	0.84	≤ 0.03	≥ 90	12.1	125
<b>GIII S1 (6cSt)</b>	34.00	6.03	0.84	≤ 0.03	≥ 90	12.8	124
<b>GIII S2 (4cSt)</b>	19.09	4.23	0.84	≤ 0.03	≥ 90	8.9	129
<b>GIII S2 (6cSt)</b>	33.43	5.92	0.85	≤ 0.03	≥ 90	9.4	122
<b>PAO (4cSt)</b>	17.74	4.00	0.82	-	≥ 90	8.9	125
<b>GIII+ (4cSt)</b>	18.00	4.10	0.82	≤ 0.03	≥ 90	12.1	131

**S1** – supplier 1  
**S2** – supplier 2

$\eta_k$  - Kinematic Viscosity  
**VI** - Viscosity Index

$\alpha$  - pressure-viscosity coefficient

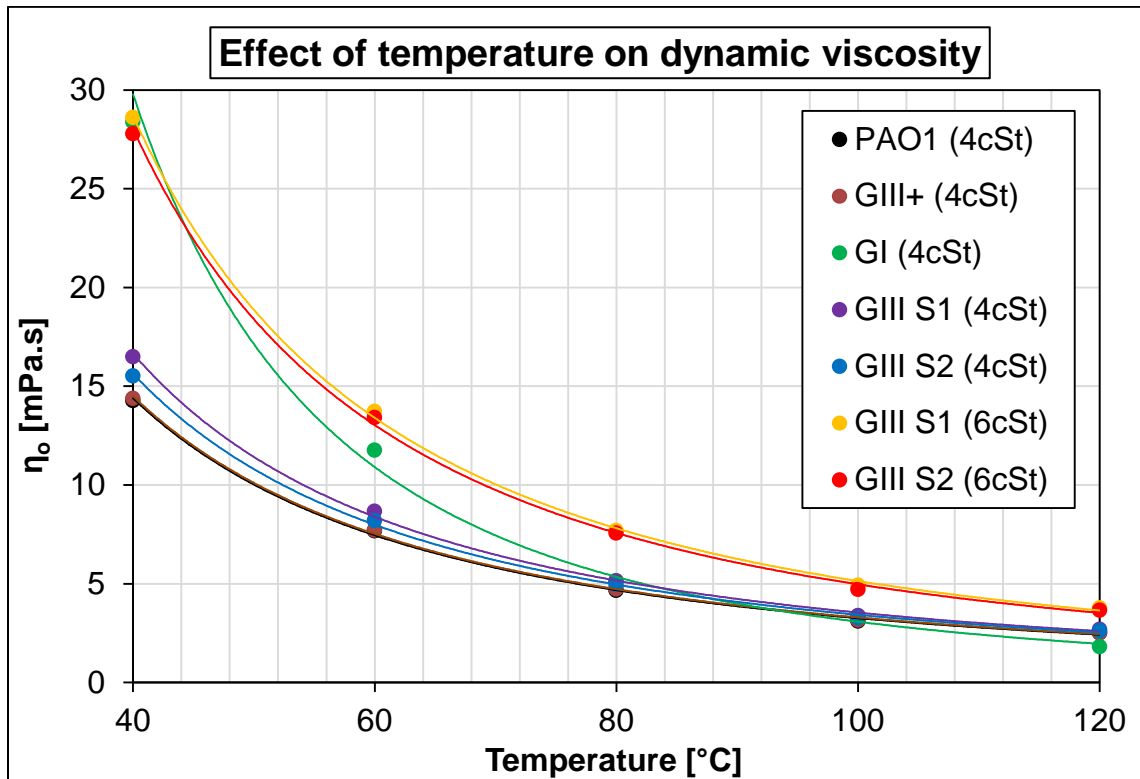


Figure 4.1: Correlation of dynamic viscosity and temperature at atmospheric pressure.



pressure. As the temperature was increased to 60 °C, the dynamic viscosities of all seven base oils decreased. The base oil which showed the largest decrement is the GI (4cSt) whose viscosity decreased from 28.7 to 11.7 mPa.s. This is followed by GIII S1 (6cSt) and GIII S2 (6cSt) having viscosities of 13.7 and 13.4 mPa.s at 60 °C respectively. The remaining four base oils are GIII S1 (4cSt), GIII S2 (4cSt), GIII+ (4cSt) and PAO (4cSt), and had viscosities of 8.6, 8.2, 7.7 and 7.6 mPa.s for respectively. As the temperature was further increased to 80 °C, the dynamic viscosities further decreased to 7.6 and 7.5 mPa.s for GIII S1 (6cSt) and GIII S2 (6cSt) respectively and varied between 5.1 and 5.6 mPa.s for the remaining 4 cSt base oils. At 100 °C, the viscosities of the two 6 cSt base oils GIII S1 (6cSt) and GIII S2 (6cSt) were 4.8 and 4.7 mPa.s, and those for the 4cSt base oils varied from 3.3 to 3.1 mPa.s, with the PAO (4cSt) having the lowest viscosity of 3.1 mPa.s. At 120 °C, the estimated viscosities for the 6 cSt base oils GIII S1 (6cSt) and GIII S2 (6cSt) were 3.7 and 3.6 mPa.s, and those for the 4cSt base oils varied from 2.6 to 1.8 mPa.s, with the GI (4cSt) having the lowest viscosity of 1.8 mPa.s.

The differences in dynamic viscosity between the base oils are due to the different base oil formulation processes (Couseau *et al*, 2012). The GI (4cSt) base oils had the second highest viscosity (28.3 mPa.s) at 40 °C, and the lowest (1.8 mPa.s) at 120 °C. Of the seven base oils under investigation, the viscosity of the GI (4cSt) base oils is the most affected by the increase temperature, as observed from the 26.5 mPa.s drop in viscosity as the temperature was increased from 40 to 120 °C. This is a direct result of the low viscosity index of this base oil (Stachowiak & Batchelor, 2014: 15). The intermolecular forces of the GI (4cSt) base oil weaken the most, giving more molecular movements, as the temperature was increased. This causes the drastic drop in viscosity (Couseau *et al*, 2012 and Stachowiak & Batchelor, 2014: 12). The dynamic viscosities that were affected the least by the increasing temperature were those of the GIII+ (4cSt) and PAO (4cSt) base oils with a 11.88 and 11.8 mPa.s drop respectively. The PAO (4cSt) viscosity was 14.3 mPa.s at 40 °C, and decreased to 2.5 mPa.s at 120 °C. The GIII+ (4cSt) viscosity was 14.38 mPa.s at 40 °C, and decreased to

2.5 mPa.s at 120 °C. These results show a good correlation between VI and the changes in dynamic viscosities with temperature.

#### 4.1.3 Viscosity: Effects of pressure

At this point, it became important to investigate the significance of the piezoviscous effect in this investigation, since the experiments were conducted under an increasing load (pressure). The piezoviscous effect is defined as the reversible increase in dynamic viscosity (thickening) of lubricating liquids due to molecular restrictions caused by the application of pressure (Fernandez *et al*, 2014). The friction tests were done under a gradually increasing normal load ( $F_N$ ) from 50 N to 250 N which resulted in maximum hertzian pressures ( $P_0$ ) ranging from 2.7 GPa to 4.7 GPa respectively.

The hertzian pressures were estimated using the empirical **Equation 2.7** below following the method discussed in Appendix C:

$$P_0 = \frac{3F_N}{2\pi a^2} \quad (2.7)$$

It is clear that the pressures applied in this investigation are in the extreme range. The changes in dynamic viscosities of the base oils in this study due to the application of pressure were approximated by the model by Chu and Cameron as recommended for extreme pressure conditions. This empirical formula gives the dynamic viscosity ( $\eta$ ) of an oil at any pressure applied on it as given below (Stachowiak and Bachelor, 2014: 17)

$$\eta(P) = \eta_0(1 + C_m P_0)^n \quad (2.55)$$

$\eta_0$  are the oil viscosities at any atmospheric pressure,  $P_0$  the maximum hertzian pressure.  $C_m$  and  $n$  are constants and 'n' assumes a value of 16 while 'C<sub>m</sub>' has a specific value for each base oil obtained graphically from the diagram in Figure 2.34 of the Theory section at each test temperature. In Figure 2.34, the x-axis shows the values of the constant  $C_m$ , the y-axis shows the oil's predicted viscosity and the curves lines which run across the y-axis represent the oil's temperature (Isotherms). The legend shows the colors of the curves representing each of the base oils under study.

To obtain the values of the constant  $C_m$ , the viscosity of the oil at each test temperature and atmospheric pressure was determined. On figure 2.43, the value of the viscosity was spotted on the y-axes and a horizontal line was drawn at the viscosity value to the point where the line crosses the isotherm representing the test temperature (in this case, from the left to the right of Figure 2.43). From the point where the viscosity line crosses the test isotherm, a vertical line was drawn which run downwards to the x-axes where the value of the constant “ $C_m$ ” was read off. This procedure was followed with for all base oils at each test temperature. Table 4.1 shows the values obtained for  $C_m$ .

Table 4.1: Values for  $C_m$  with temperature.

Temperature (°C)	Constant $C_m$ for Piezoviscous calc ( $\times 10^{-9}$ )						
	GI (4cSt)	GIII S1 (4cSt)	GIII S1 (6cSt)	GIII S2 (4cSt)	GIII S2 (6cSt)	PAO (4cSt)	GIII+ (4cSt)
40	1.70	1.69	1.65	1.68	1.63	1.70	1.70
60	1.45	1.45	1.40	1.45	1.40	1.47	1.40
80	1.20	1.20	1.19	1.20	1.19	1.20	1.20
100	1.00	0.98	0.95	1.00	0.95	0.98	0.98
120	0.83	0.80	0.79	0.80	0.79	0.82	0.80

From this point, the changes in dynamic viscosities of the base oils due to an increasing pressure were obtained. Figure 4.2 shows graphs which relate the increase in dynamic viscosity to the applied load at 40 °C. On this figure, dynamic viscosity is given in the y-axes in units of Pa.s, and applied pressure in GPa is given in the x-axes. The SRV machine produces a data point every second. Since the load gradient was 40 N/min, this translates to a load increase of 0.67 N/s. This raw data was used to estimate the maximum Hertzian pressures ( $P_o$ ) and dynamic viscosities ( $\eta$ ) at each second during the load increase from which 5 seconds averages were calculated and presented in Figure 4.2. In Figure 4.2, it can be seen that the gradual increase in applied pressure resulted in a non-linear increase in dynamic viscosity which follows a power relationship. It is clear that an increase in applied pressure causes an increase in

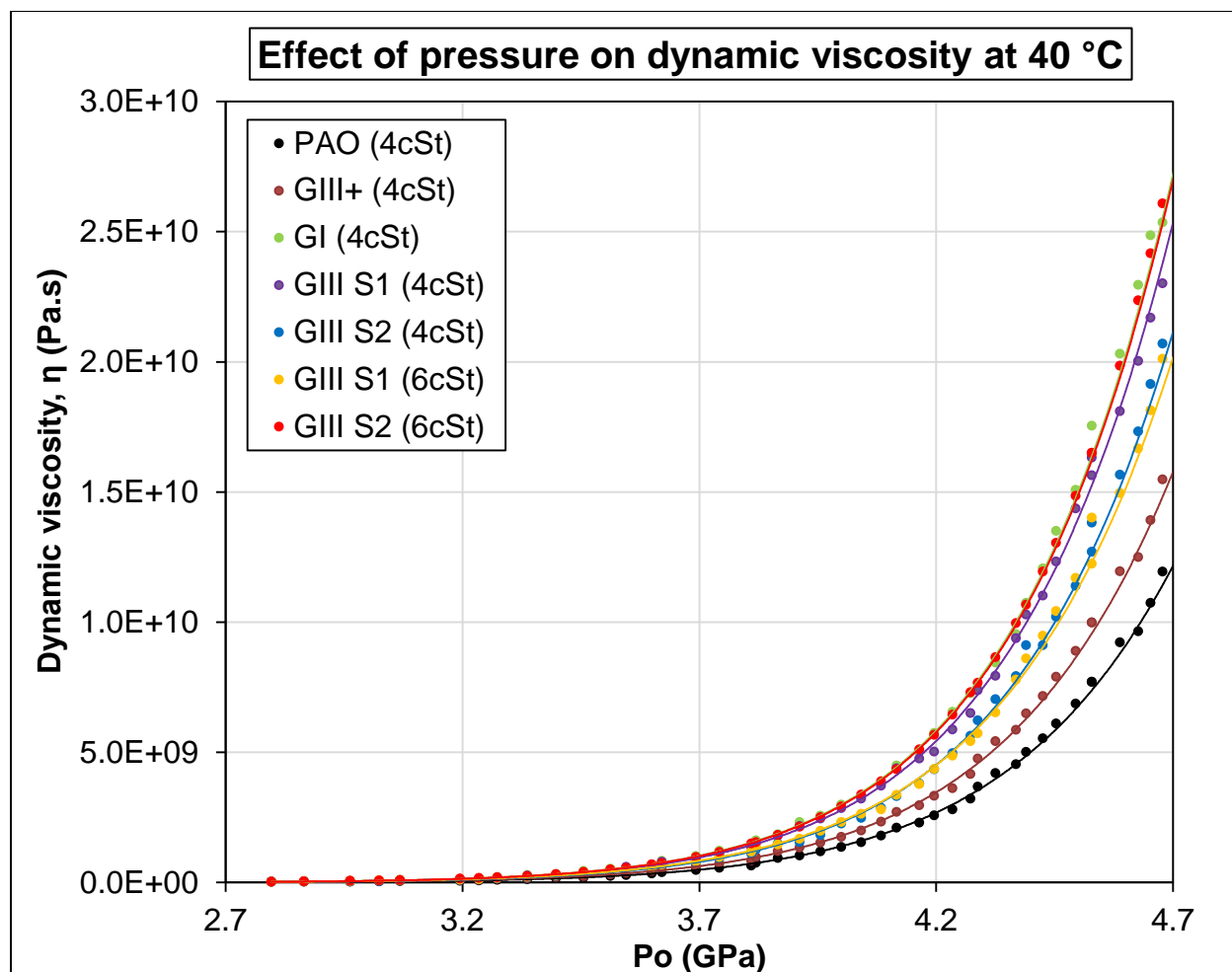


Figure 4.2: Effect of applied pressure on dynamic viscosity (Viscosity Pressure isotherms) at 40 °C.

viscosity, however, the extent to which the viscosity increase is little between 2.7 and 3.7 GPa (50 and 150 N) and becomes very large between 3.7 and 4.7 GPa. All seven base oils under study show a significant increment in the dynamic viscosity values. The piezoviscous behaviour observed from highest to lowest between 3.2 and 4.7 GPa is in the order GI (4cSt) and GIII base oils which are followed by the GIII+ (4cSt) and PAO (4cSt) base oils. It is clear from Figure 4.2 that the base oils assumed very large values of dynamic viscosities as the pressure was increased. The dynamic viscosities obtained at 60, 80, 100 and 120 °C are presented in Figures 4.3 to 4.6.

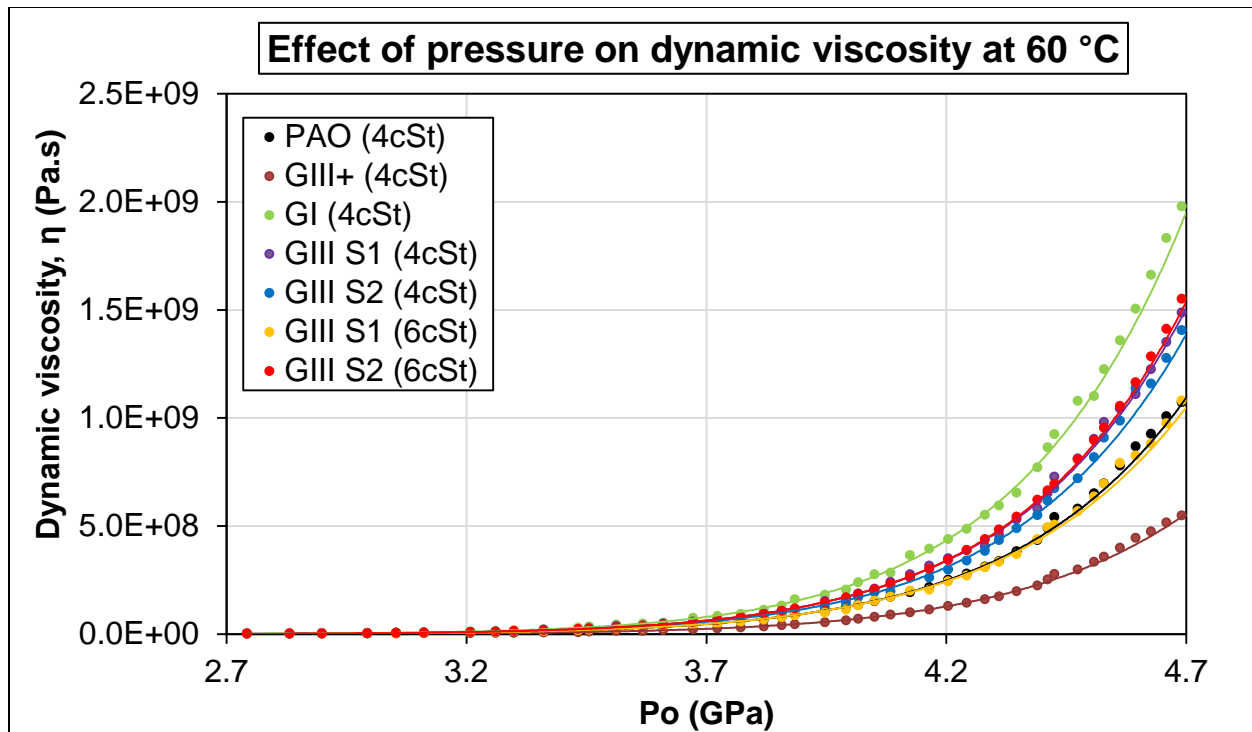


Figure 4.3: Viscosity-pressure relationships at 60 °C.

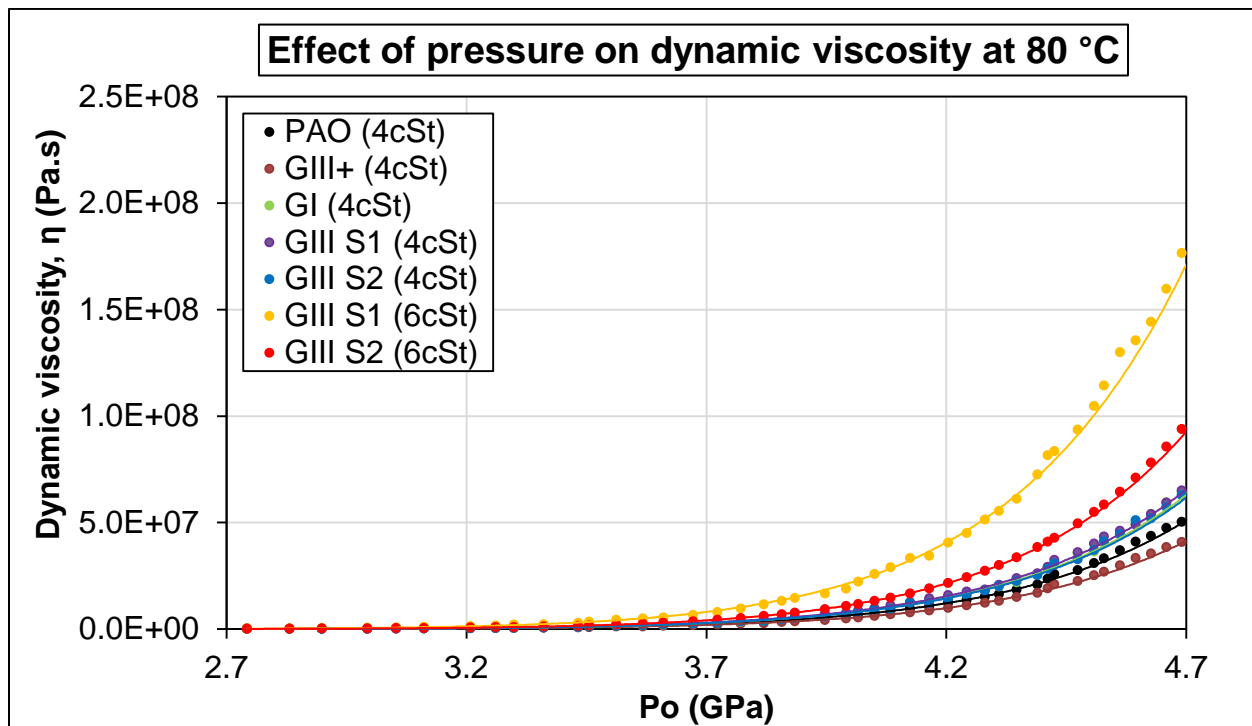


Figure 4.4: Viscosity-pressure relationships at 80 °C.

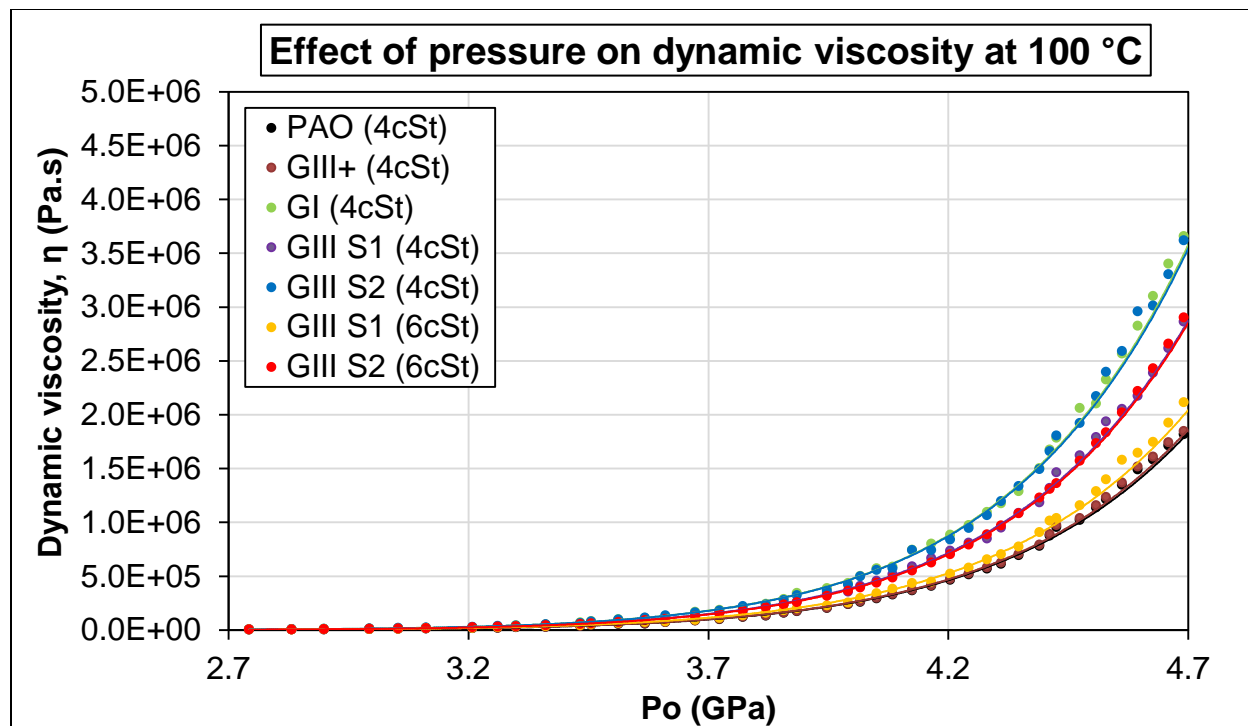


Figure 4.5: Viscosity-pressure relationships at 100 °C.

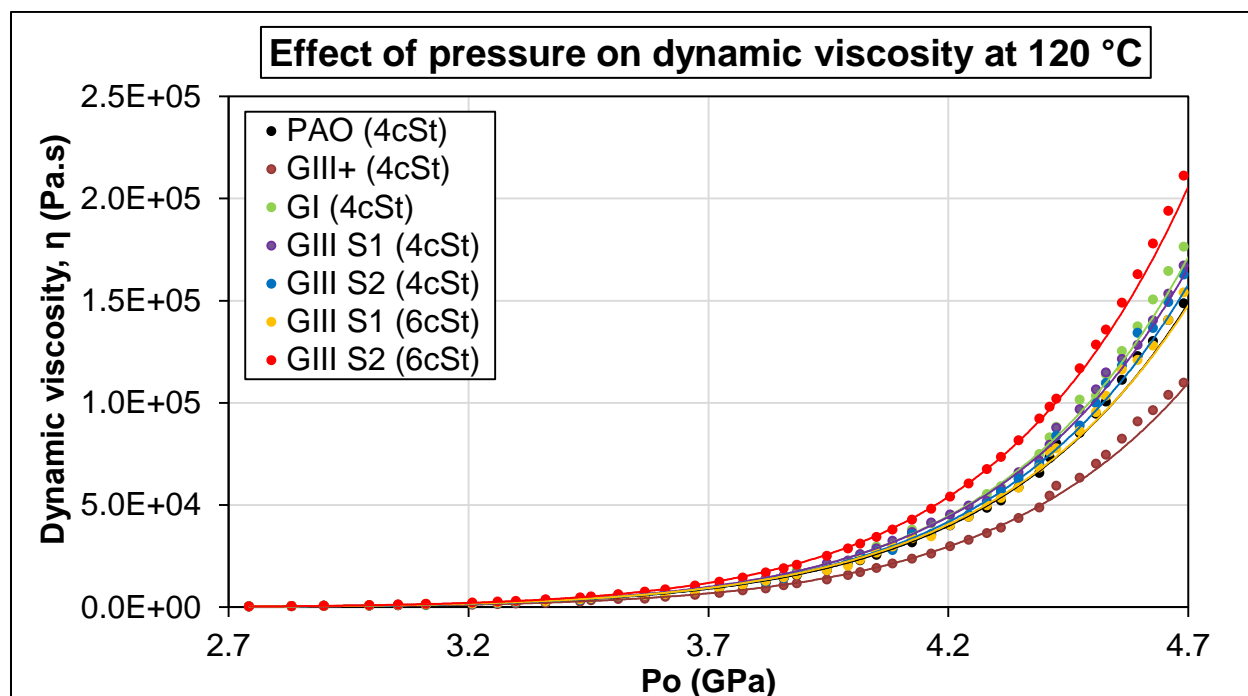


Figure 4.6: Viscosity-pressure relationships at 120 °C.

From Figure 4.2 to 4.6, it is not very clear what the dynamic viscosity differences are between 2.7 and 3.2 GPa. As a better representation and to observe the effect of temperature on the piezoviscous effect, the percentage increments in the dynamic viscosity of each base oil, between the Hertzian pressure range 2.7 to 4.7 GPa, were calculated from the raw data at 40, 60, 80, 100 and 120 °C, and presented in Figure 4.7.

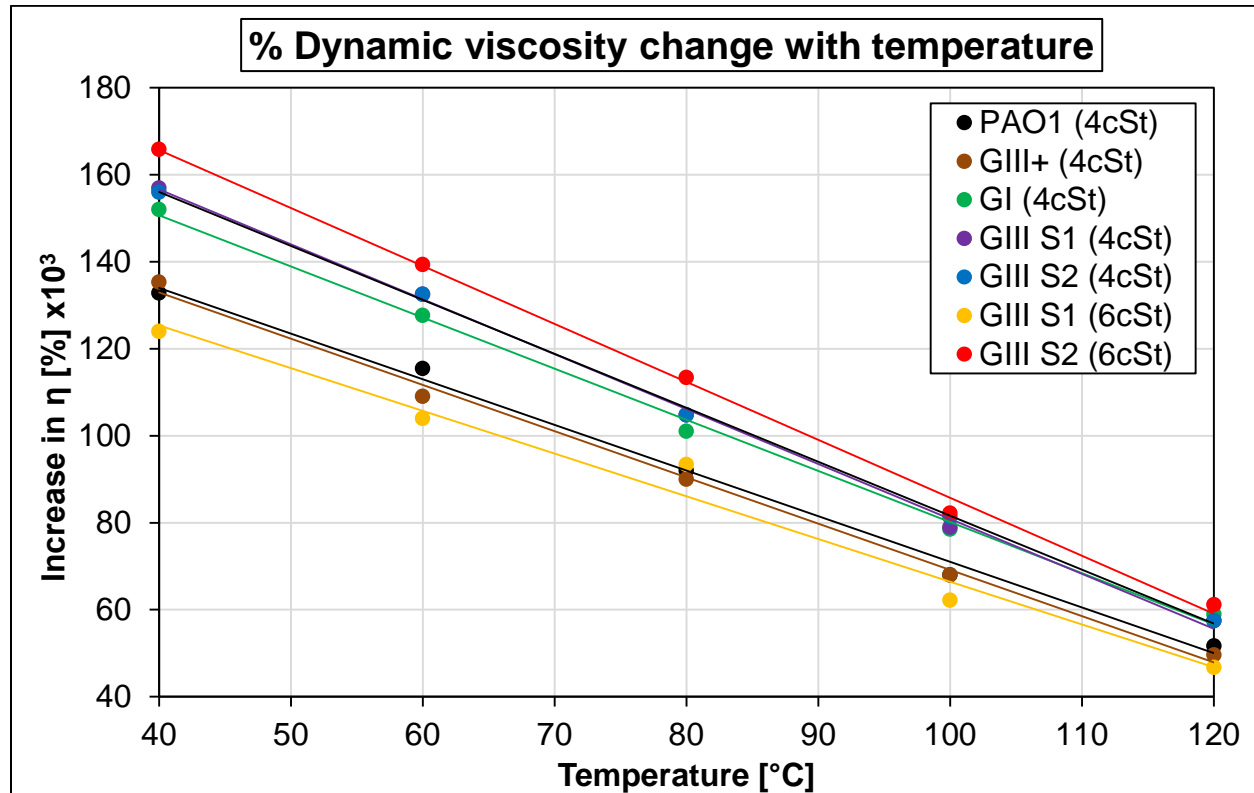


Figure 4.7: Percentage increment in absolute viscosity with temperature.

It should be noted that Figures 4.2 to 4.6 show the actual calculated values of dynamic viscosities assumed by the base oils at each pressure stage, while Figure 4.7 shows the extent to which the dynamic viscosity of each base oil increased as the pressure increased from 2.7 to 4.7 GPa at each test temperature. In Figure 4.7, the percentage increment in dynamic viscosity (y-axis) of the base oils are given at the five test temperatures (x-axis). The legend shows the colors of the curves representing each of the base oils under study. It can be observed in Figure 4.7 that the effect of pressure

on dynamic viscosity is dependent on temperature. As the temperature was increased from 40 °C to 120 °C, the extent to which the dynamic viscosity increased decreased, as the pressure was increased from 2.7 to 4.7 GPa.

Fernandez *et al* (2014) concluded that the piezoviscous effect increases with branching degree and decreases with the level of saturation. A high degree of molecular branching results in an increase in the shear stress within the molecules under the application of pressure which lowers molecular mobility and causes thickening, whilst a high level of saturation gives a decreased shear stress within molecules under the application of pressure and therefore leads to less thickening (Fernandez *et al*, 2014 and Ichiro, 2017). The PAO (4cSt) is the most saturated; hence it consistently assumed lower values of dynamic viscosity with an increasing pressure up to 80 °C where values are very close to the GIII+ (4cSt) values. The curve lies above the GIII+ (4cSt) graph at 120 °C. The GIII+ (4cSt) base oil also has a high level of saturation and therefore assumes the second smallest values of viscosity between 40 and 100 °C and the smallest values at 120 °C. The GIII group of base oils has more or less similar level of saturation and branching and therefore the viscosity values will lie along a similar band of values as is clearly visible at all the experimental temperatures. The GI (4cSt) base oil is the least branched and saturated and therefore consistently gave high values of dynamic viscosities throughout the pressure range.

The results above show a clear relationship between the piezoviscous effect and the level of saturation of the base oils. A high level of saturation seems to result in a high VI and lower effects of temperature and pressure on dynamic viscosity. The relationship between the branching level as stipulated by Fernandez *et al* (2014) is not entirely clear as it appears to be highly temperature dependent but does not show a consistent trend with an increasing temperature. The PAO (4cSt) and GIII+ (4cSt) have high branching levels but showed a smaller piezoviscous effect (Stachowiak & Batchelor, 2014: 57). This may be due to the fact that the paraffinic mineral base oils have very complex structures and the branches are not formed from the same molecules. This therefore results in different molecular bonds which respond differently to temperature. The



stipulation made by Fernandez *et al* (2014) is based on that the branching level is known to increase with viscosity since it increases the volume of the molecule and therefore higher viscosity base oils are expected to have a higher piezoviscous effect. It seems that increased molecular branching with high saturation levels gives lower shear strength (low piezoviscous effect) while increased molecular branching with less saturation give a larger shear strength (high piezoviscous effect) (Ichiro, 2017).

## 4.2 Friction

The operating frequency (50 Hz) and stroke length (2 mm) resulted in a mid-stroke ball velocity ( $u_b$ ) of 0.2 m/s on the SRV4<sup>®</sup> tribometer. The mid-stroke velocity was used for all calculations in this investigation. Each test was repeated three times and each reported trend represents average data from three experiments. The SRV machine had a sampling rate of 32 measurements per second for the coefficient of friction. Therefore, each value reported per second is an average of 32 measurements. In this investigation, 5 seconds averages are reported (meaning every data point presented is an average of 5 values). The average standard deviation of the coefficient of friction calculated between three experiments ranged from  $\pm 0.002$  to  $\pm 0.01$ , and the graphs showing the standard deviations for each lubricant at the five test temperatures are presented in Appendix D.

### 4.2.1 Effects of water on friction

The relative humidity (RH) in the test chamber during all the frictions test was maintained at 20%. Though this low RH value was chosen to maintain a low atmospheric water vapor content, the possible effect of water on friction cannot be ignored since water is present in three different forms in oils. The change in the block temperatures from 40 to 120 °C affected the chamber temperature, which may have affected the rate of absorption of water vapor from the atmosphere by the base oils under study. Table 4.2 shows the recorded average chamber temperatures at each test temperature, and the corresponding changes in vapor and partial pressures of water.

Table 4.2: Effects of temperature on water absorption (Cooper & Fevre, 1969).

Block/Interface	Temperature (°C)		$P_w^*$ (kPa), at interface temperature	RH (%)	$P_w$ (kPa), at interface
	Chamber	Average			
40	25	32.5	7.36	20	1.47
60	25.5	42.75	19.87	20	3.97
80	26.5	53.25	47.27	20	9.45
100	28	64	101.00	20	20.20

The oil interface temperatures were taken to be equal to the block temperatures. Therefore, the test/interface temperatures were used to obtain the vapor pressures of water (from the steam tables) and the corresponding partial pressures at 20% RH. It can be seen from Table 4.2 that the partial pressure of water vapor at the interface increased by over factors of two with increasing temperature. This means, according to the Henry's law, the solubility of water vapor in the oils also increased proportionally (Yaws, 2010). The increase in temperature also resulted in a decrease in the oils viscosities as was seen in the previous discussions. This therefore resulted in an increasing diffusion coefficient, which indicated increased water diffusion rates (molecular fluxes) as was indicated by Fogler (2006:770). Therefore, it can be concluded that the dissolved water content of each base oil increased as the temperature was increased.

The exact solubilities and diffusion rates were not calculated as this was not part of the aim of this investigation, however, observations on the possible effects of these increased absorption rates on the coefficient of friction (COF) were made. It should also be noted that since water boils at 100 °C, the effect of the activity of the water molecules on the COF might be more severe due to the boiling of dissolved water. No absorption at 120 °C. Yaws & Yadav (2010) highlighted the effect of the hydrocarbon chain lengths and boiling points on solubility. The solubility values were found to be decreasing with increasing hydrocarbon chain lengths at 25 °C. It is expected for the base oils under study to show different friction behaviours at each test temperature as a result of water absorption (if any) coupled by the oscillatory motion under an increasing load. The oscillatory motion may be serving as a catalyst for the diffusion process. It is known that the synthetic base oils have high water absorption abilities, due to their higher polarity (Ichiro, 2017). Therefore, the PAO base oil is expected to be the most affected by water vapor especially between 60 and 100 °C. The least affected should be the GI (4cSt) base oil due to its non-polar property. The GIII base oils are expected to show intermediate effects.

#### 4.2.2 Effects of load and temperature on the coefficient of friction

Figure 4.8 contains graphs showing the effects of the normal load ( $F_N$ ) on the coefficient of friction (COF) at the temperatures 40, 60, 80, 100 and 120 °C. The normal load was gradually increased 50 N to 250 N. The curves in Figure 4.8 to Figure 4.14 show the COF on the y axes plotted against the applied normal load on the x axes. The legend shows the colors of the curves corresponding to a specific test temperature in °C. The title each figure shows the relevant lubricant whose data is presented on the graph. It should be noted that on the graphs, the normal load (x-axes) increases from the right to the left. Therefore, the graphs will be interpreted following this direction of the increasing load. This was to ensure that the trends on these graphs correspond well with those discussed in later sections of this report.

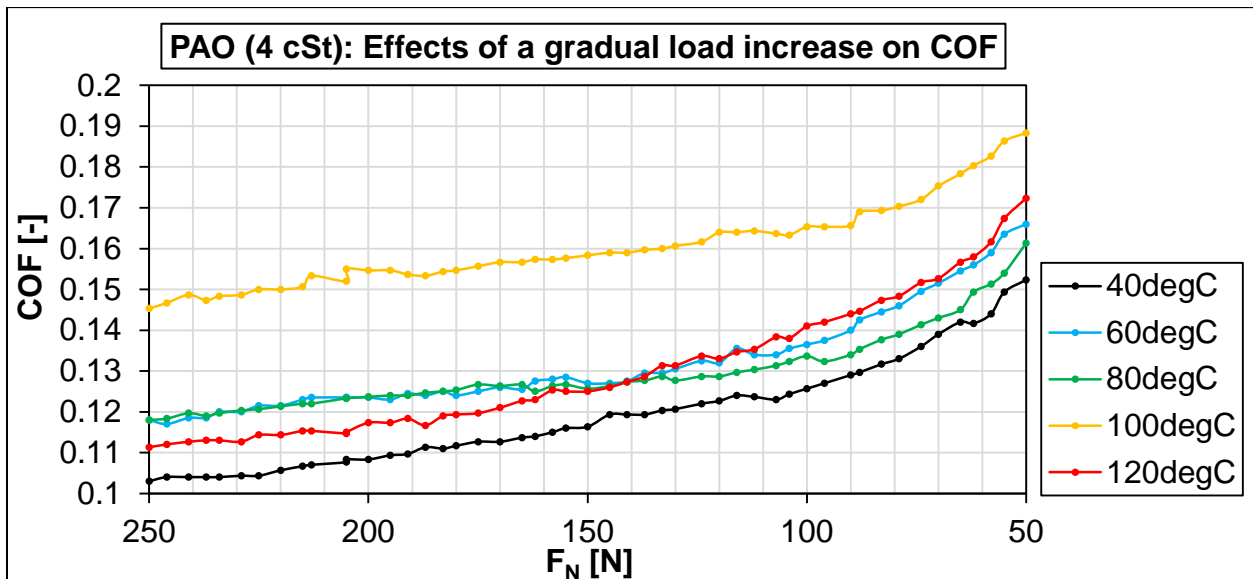


Figure 4.8: Gradual load increase at different temperatures.

Figure 4.8 shows the graphs obtained with the PAO (4cSt) base oil. It can be seen that as the load was gradually increased from 50 N to 250 N, the COF decreased progressively. At 40 °C, as the load was increased, the COF decreased from an average value of 0.152 at 50 N to 0.103 at 250 N. A similar trend is observed at 60 °C, however, the COF values are higher. As the load was gradually increased, the COF

decreased from 0.166 at 50 N to 0.118 at 250 N. At 80 °C, an interesting curve was observed which lies between the curve at 40 °C and that obtained at 60 °C. At 80 °C, the COF values decreased from 0.161 at 50 N to 0.118 at 250 N. Another observation made with the 80 °C curve was the decrease in the COF of 0.043, which is smaller than that obtained at 40 °C (0.049) and 60 °C (0.048), this implies that the increasing load between 50 N and 200 N has a smaller effect on COF at 80 °C. At 100 °C, higher COF values were obtained as the load was gradually increased. The COF decreases from an average value of 0.188 to 0.145, giving a change of 0.043 in COF. At 120 °C, a more significant effect of the increasing load on the COF is observed, the COF decreases from an average value of 0.172 to 0.111. The COF values obtained as the load increased between 50 N and 200 N are higher than those obtained at 40, 60, and 80 °C, however, as the load increased from 200 N to 250 N, the COF values became smaller than those at 60 and 80 °C, with the final value 0.111 and 250 N. Lower COF values were obtained from the PAO base oil at 120 °C between 160 N and 250 N, compared to those obtained at 60, 80 and 100 °C.

A temperature from 40 °C to 60 and 80 °C showed a smaller effect on the COF since the curves sit closer together, whereas the significant differences in the curves are in their gradients, signifying the larger effect from the increasing load on the COF at these temperatures. Another important observation on this graph is that the curve obtained at 100 °C stands far apart from the curves obtained at 40, 60, 80 and 120 °C. This implies that temperature has a more significant effect on the COF when the temperature is varied between 80, 100 and 120 °C. The COF values increased when the temperature was increased from 80 to 100 °C, and decreased between 100 and 120 °C. This observation appears to be related to the presence of dissolved water.

### **Contributing effects of water**

It is known that synthetic oils normally contain much more dissolved water than conventional mineral oils (Zheng-bing et al, 2015). The increase in temperature from 40 to 100 °C increases the adsorption rates of the dissolved water molecules on the steel surfaces, which reduces the surface free energy of the metal surfaces, lowering the

adsorption rate of the PAO molecules during sliding. Water has no lubricating properties (e.g. high viscosity), therefore more direct asperity collisions are probable due to the decreased film viscosity (thickness). Therefore this contributes to the increased COF values. It also appears as though the evaporation of dissolved water at 100 °C disturbs the adsorption process of oil molecules and contributes to the large COF values obtained. Water has a strong affinity for steel surfaces and its random adsorption on the available sites of the metal surfaces results in formation of an unstable and less ordered adsorbed oil film, which leads to increased molecular collisions and shear stresses in the inner sections of the oil film due to the poor alignment of the oil molecules to the sliding motion. An increase in temperature catalyzes this effect, hence the increased COF values at each load stage at higher temperatures.

Cai *et al* (2015) also found that the presence of dissolved moisture in a PAO (4cSt) base oil seemed to increase molecular shear stresses at the contact interface. Also, the number of water molecules absorbed from the atmosphere increased with increasing temperature, largely in the range 75 to 100 °C. This increased water absorption resulted in an increase in dissolved water. It was noticed that an increase in dissolved water by an additional 1 % (wt) beyond saturation promoted increased wear (friction). The co-existence of dissolved and emulsified water caused increased friction. These observations show that a temperature increase from 40 to 100 °C was accompanied by a decreased viscosity, increased water absorption rate and possibly, increased wear which could be contributing to the resulting increase in the COF values. An increase in temperature beyond 100 °C resulted in the evaporation of water molecules out of the lubrication interface, leaving the lubrication process to be solely reliant on temperature and oil molecular behaviour. It seems that the PAO molecules have low shear stresses, as is observed at 120 °C, which gives easier shearing of the oil film and therefore, low friction. This observed friction behaviour (decreasing COF with increasing load) is summarized in the discussion section which will follow later for all base oils, because it appears to be common to all base oils under investigation.

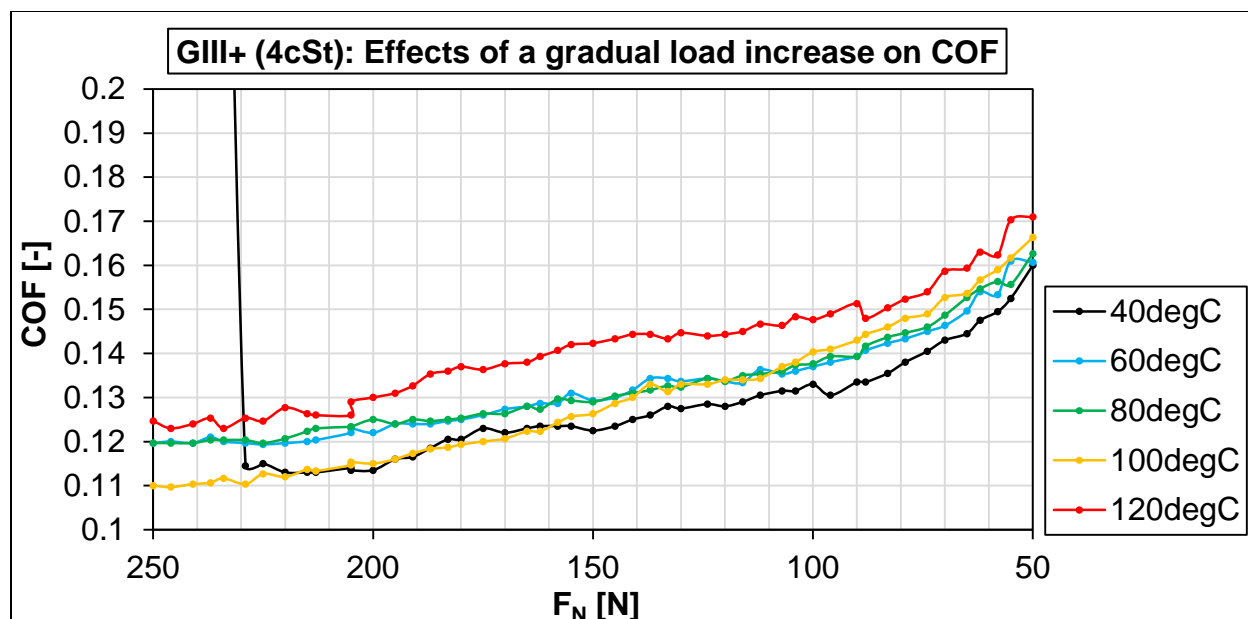


Figure 4.9: GIII+ (4cSt): Gradual load increase at different temperatures.

The GIII+ (4cSt) graphs are shown in Figure 4.9 above. It can be seen that the curves obtained at 40, 60, 80, 100 and 120 °C lie closer together, with the 120 °C curve with the highest COF values. This indicates of good thermal stability. The 40 °C curve lying below the others, gave low average COF values decreasing from 0.16 at 50 N to a lowest value of 0.112 at 220 N after which a sudden rise in the COF was observed at 230 N. This observation indicates loss of lubricity by the base oil and direct contact of the steel ball and disc surfaces. Clearly, this is a function of the load which indicates that the film formed by the oil molecules was squeezed out of the contact area due to the sliding motion at this high load. This also indicates that the GIII+ (4cSt) base oil has poor adsorption capability at 40 °C and higher sliding loads, which means that their oil molecules may have not formed an ordered layer on the sliding surfaces. This compromises the stability of the film formed and may be causing increased molecular shear stresses which may be promoting film removal during sliding and thereby exposing the ball surface to the disc surface. The very low sulfur content could be contributing to this lowered lubricity since sulphur is known to reduce wear (friction) at moderate temperatures (Stachowiak & Batchelor, 2014: 57).

Also, the GIII+ base oil has high polarity, which means it has high affinity for the steel surfaces, however, it forms weak bonds (van der Waals) with the surface since it bonds via the H-atom in the C-H-molecules. This indicates physisorption (Nilsson *et al*, 2008: 137). It appears at 40 °C there is no available heat energy to promote a stronger form of adsorption (i.e., covalent or chemisorption) hence the removal of the oil film on the surface by the sliding motion at 230 N. Due to the complexity of the molecular structures of paraffinic base oils it is difficult to tell their exact molecular arrangement. However, it is well known that they are highly saturated due to the severity of hydrocracking during manufacture. Therefore this makes them highly polar since C-H bonds give larger electron negativity (0.3) than the C-C (0.0) and C-S (0.1) bonds (Ichiro, 2017). Another contributing factor to the poor adsorption strength of the oil molecules is the lower surface energy on the steel surfaces due to occupation of adsorption sites by water molecules which form stronger bonds during adsorption (via lone pair through the O-atom) (Nilsson *et al*, 2008: 137).

Due to the high polarity, the GIII+ base oil just like the PAO base oil has a high dissolved water content, therefore the competition for adsorption sites remains high (Meirong *et al*, 2017 and Ichiro, 2017). This situation improves with the increasing temperature as no breakthrough is observed at the higher temperatures. This indicates the availability of enough energy to make the molecules more flexible, increasing the probability of increased surface coverage by the electron negative atoms. Apart from high surface coverage, high heat energies may have lead to a stronger “covalent like” bonding between the C-H atoms of the oil molecules and the steel surface between 60 and 120 °C. In order for the bond to be created, the internal C-H bond is weakened (lengthened) to reduce the bond-order and simultaneously the C-C bond is strengthened (shortened) and the H atom pointing towards the surface bonds with the surface due to its higher affinity (Nilsson *et al*, 2008: 119). This means that the oil molecule has taken a small step towards dehydrogenation. This created an interaction of the molecular orbitals involving the C-H groups that point to the surface with the s-p and d-bands in the metal which leads to a weak electron-pairing (covalent) between the C-H and metal atoms (Nilsson *et al*, 2008: 119).



The 100 °C curve has the lowest COF value at 250 N which is 0.11. A clear trend of the COF with the increase in temperature (Increase from 40 to 100 °C, and decrease between 100 and 120 °C) is observed. Also a more stable response to an increasing temperature was also observed, accompanied by smaller gaps between the graphs on the y-axis, denoting a stable response of the COF due to an increasing temperature. Clearly, this is a benefit of the highly saturated molecular structures with decreased amounts of double bonds and contaminants. These form stable films which are less prone to surface reactions. The effect due to load is prevalent at 100 and 120 °C between 200 N and 250 N where the slopes of the graphs increasing, showing a bigger effect of the increasing load on the COF. Figure 4.10 shows the GI (4cSt) graphs.

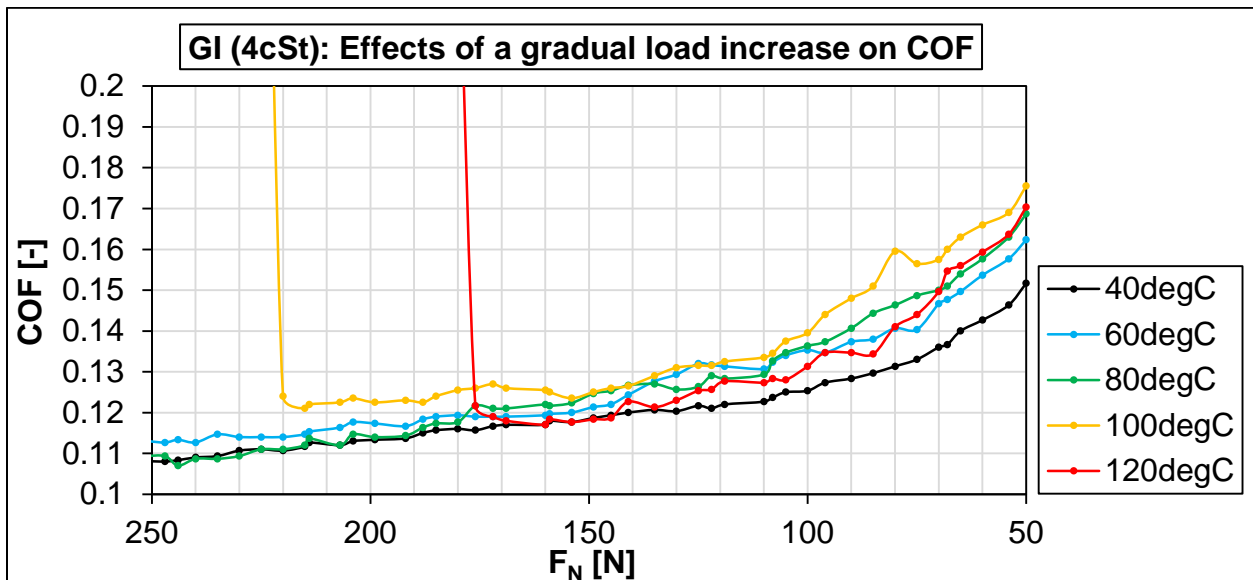


Figure 4.10: GI (4cSt): Gradual load increase at different temperatures.

It can be seen that the gradual load increase resulted in a gradual decrease in the COF. The curves obtained at 40, 60 and 80 °C start at different values of the COF at a load of 50 N, with the 40 °C curve having an average COF of 0.152, followed by 0.162 at 60 °C and 0.169 at 80 °C. An increase in temperature from 40 to 80 °C results in an increase COF at the low loads. Between the loads 190 N and 250 N, the 40 and 80 °C curves lie on top of each other, assuming similar values of COF. This denotes the smaller effect of the increasing temperature on the COF between these loads. This is a combined

effect of the lowered molecular shear stresses and increased contact area due to asperity deformations caused by the sliding motion. The 40, 60 and 80 °C curves converged towards a COF value of 0.11 as the load approached 250 N. This implies that the GI (4cSt) base oil had similar friction behaviour at 40, 60 and 80 °C between 200 to 250 N. This indicates good thermal stability. On the contrary, an increase in temperature from 40 °C to 80 °C resulted in higher COF values at low to moderately high test loads (50 N to 170 N). The effect of an increasing load as the temperature increases from 40 °C to 120 °C becomes more significant between 50 and 150 N, shown by the constant increases in the gradients of the graphs as the temperature increases. At 100 °C, the COF decreases as the load is increased up to 220 N where breakthrough was observed. Similar behaviour was observed at 120 °C where a breakthrough occurred at 176 N. These breakthroughs are associated with oil film breakdown since they appear to be influenced by temperature and load.

The GI (4cSt) base oil contains large fractions of unsaturated double bonds in its molecular structures. It is well known that double bonds are prone to dissociation and formation of radicals at high temperatures and high stresses. Clearly, at 100 °C and 220 N some molecular bonds were dissociated, resulting in a breakdown of a bigger molecule to a small one. This caused a decrease in the molar mass of the molecules formed at the sliding contact. The dissociated molecules cannot handle any sliding stresses higher than those formed at 220 N, hence the film breakdown, exposing the ball surface to the disc surface and resulting in very high friction due to the loss of lubricating film (Ichiro, 2017). The above observation indicates a limit in the load-carrying capacity. At 120 °C, the molecular bonds are even weaker (flexible) than at 100 °C due to the increased heat energy absorbed by the molecules. This resulted in the bonds being dissociated at a lower normal load of 176 N. The mechanism of dissociation is similar to that discussed above. There may have been radical reactions taking place at the surfaces which may have contributed to these breakthroughs (Ichiro, 2017). However, this cannot be confirmed since surface analysis was not done in this investigation. The presence of dissolved water proves to have an influence on the COF as is observed from the 120 °C curve that lies below the 100 °C curve. As was

discussed with the PAO (4cSt) base oil previously, the absence of dissolved water at 120 °C leaves the lubrication solely to the oil molecules, which prove to give better lubricity subject to the lower COF values. The presence of dissolved water in the GI (4cSt) base oil increases the COF.

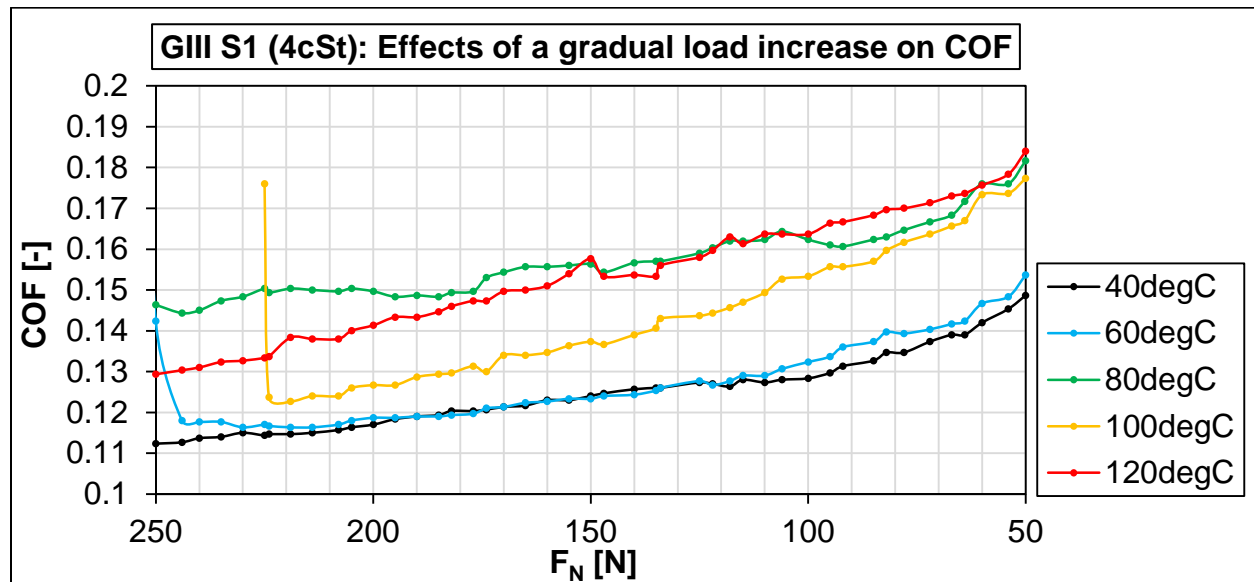


Figure 4.11: GIII S1 (4cSt): Gradual load increase at different temperatures.

The GIII S1 (4cSt) graphs in Figure 4.11 show a different type of response to a gradually increasing load and increasing temperature. The temperature increase from 40 °C to 60 °C did not result in a large change in the COF as the load was gradually increased. The 40 °C and 60 °C curves lie very close to one another especially in the load range 120 N to 220 N. At 60 °C, as the load was increased from 200 N to 250 N the COF went through minimum value (0.116 at 230 N) and a significant increase in the COF occurred at 244 N. From the shape of this curve, it can be seen that the onset of loss of lubrication occurs at 244 N. It can also be observed that a further increase in temperature from 60 °C to 80 resulted in a large gap between the lower temperature curves (40 °C and 60 °C) and the 80 °C curve. The temperature is observed to have a large effect on the COF between 60 and 80 °C, and little effect outside these temperatures. The load has a largest effect on the COF at 100 °C and 120 °C, shown

by the larger gradient in the COF trend between (150 N and 250 °C). The above indicates low thermal stability between 60 and 120 °C.

Since this is a hydro-processed base oil with a significant level of saturation, it has high polarity. Also, there are low levels of naphthenic and aromatics with double bonds on the chemical structure which may indicate a potential for reactivity at elevated temperatures. Therefore, the adsorption strength of the oil film may be quite high subject to adsorption via two mechanisms i.e.:

1. Electron pair sharing - through the breakage of the C-C double bonds, creation of a parallel bond via the C atoms where radicals are formed;
2. van der Waal forces - via the H atom for molecules with no C-C double bonds.

However, even with the high adsorption strength, the overall film strength may be compromised by the presence of double bonds on the molecules which may be in the inner layer of the shearing film. This is the case with all hydro-processed base oils. At high temperatures and high loads, these bonds may be dissociated and as was discussed with the GI (4cSt) base oil, this dissociation results in lowering of molar mass and film strength. Ultimately, there is always a probability for film breakdown. The observed increase in COF 100 °C is due to the above. Also, oil film removal from the contact surface due to poor adsorption strength is also possible, and this may be the case at 60 °C. Lastly, the least effect of water observed with these less saturated base oils (GI and GIII) are due to their molecules forming stronger covalent bonds through electron-pair sharing with the steel surfaces via the C-C atoms with double bonds. The C atoms with the dissociated double bond lie parallel to the steel surface and two C atoms bond at a time. This type of bonding increases adsorption area coverage and limits the area for adsorption by water (Ichiro, 2017 and Nilsson *et al*, 2008: 119).

The GIII S2 (4cSt) graphs are shown in Figure 4.12 above. From Figure 4.12, it can be observed that the 60 °C curve lies below the 40 °C curve. This is indicative of a better friction reduction ability of the GIII S2 (4cSt) base oil at 60 °C. At 40 °C, the oil molecules are more compact, and have a lower level of flexibility compared to at 60 °C.

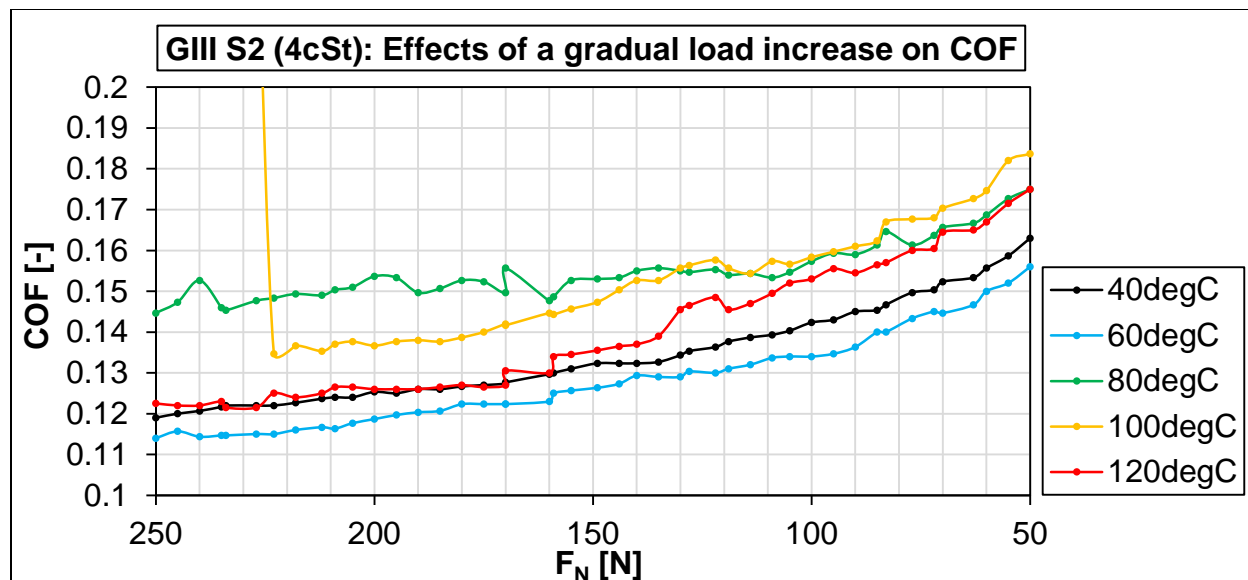


Figure 4.12: GIII S2 (4cSt): Gradual load increase at different temperatures.

These more compacted structures at 40 °C form stiffer lubricating films and have a higher molecular shear stresses under sliding. The stiffer layer allows for more direct contact between asperities and more aggressive surface changes hence the higher COF values (Stachowiak & Batchelor, 2014: 577). An increase in temperature to 80 °C and then 100 °C is observed to increase the COF throughout the gradual load increase. At 120 °C, the curve is observed to have values of the COF (0.175 to 0.122) which are lower than those at 80 °C (0.175 to 0.145) and 100 °C (0.184 to 0.135), per given load stage, as the load is increased from 50 N to 250 N. The increasing load was observed to have a larger effect on the COF at 100 °C and 120 °C, shown by a large decrement in the COF at these temperatures. A breakthrough at 100 °C and 234 N was observed.

Overall, this friction behaviour is very similar to that observed with the GIII S1 (4cSt) base oil in the previous discussion. These two base oils are in the same API group and share behavioural and physical properties. However, they were manufactured from different crude oil sources, hence the slight differences especially at 120 °C. No consistent trend can be determined from the resulting COF with an increasing temperature under an increasing load for both the GIII S1 (4cSt) and GIII S2 (4cSt) base oils. It appears the base oil has high molecular instabilities caused by the

changes in temperature, subject to no observable trend in observed COF with the increasing temperature. This is mainly due to the complexity molecular structures, which respond inconsistently to a consistently increasing temperature. Therefore, with the forever changing temperature conditions in real life operations, one cannot predict precisely how this base oil will behave.

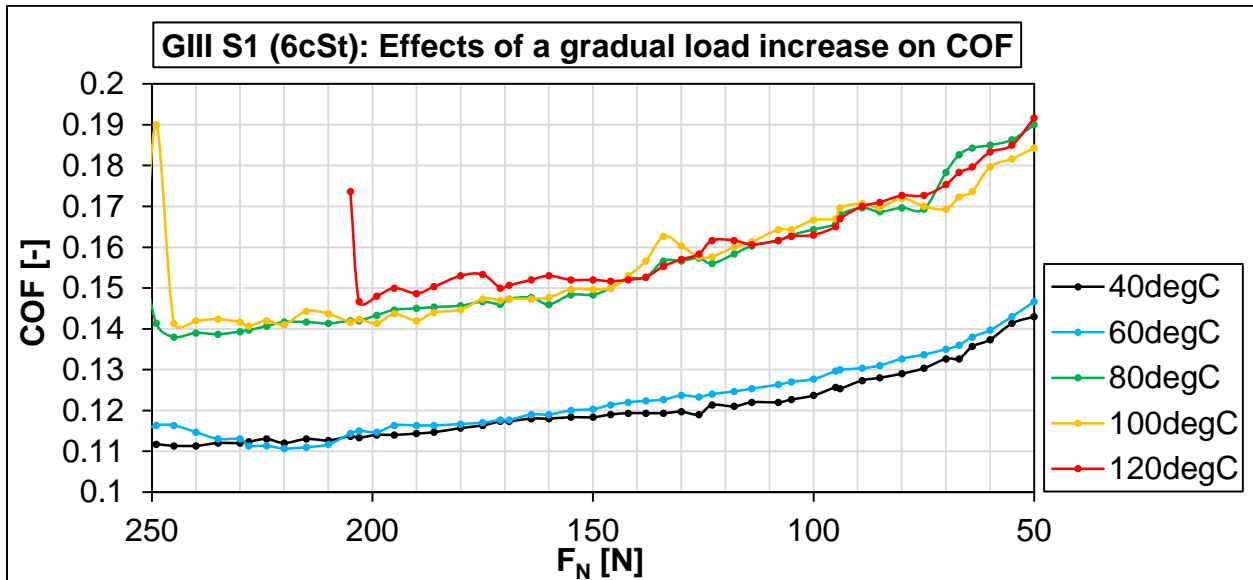


Figure 4.13: GIII S1 (6cSt): Gradual load increase at different temperatures.

The GIII S1 (6cSt) graphs in are shown in Figure 4.13. A large gap in the COF values is observed between the 40 and 60 °C curves and the 80, 100 and 120 °C curves. It is clear that an increase in temperature from 60 °C to 80 °C significantly affects friction behaviour of the GIII S1 (6cSt) base oil. This behaviour is viscosity related and strongly highlights the temperature region of significant viscosity loss. On the other hand, a very consistent COF response to increasing temperature is observed. At 40 and 60 °C the oil film is thick enough to separate the oscillating ball and disc surfaces. The observed COF may be solely due to the internal friction due to molecular collisions and shearing during sliding, hence the similar values of COF at each load stage.

The friction behaviour of the oil film is not significantly affected by the increase in temperature from 40 to 60 °C. However, the increasing load does have an effect on the COF both at 40 °C and 60 °C, subject to the gradual decrease in the COF from 0.143 to 0.112 and 0.146 to 0.116 respectively. An increase in temperature from 40 to 80 °C causes a drastic drop in dynamic viscosity, resulting in a thinner lubricating film being formed by the oil molecules. High viscosity is a result of high molecular branching giving larger molecular sizes. Due to the larger molecular sizes, an increase in temperature increases molecular flexibility which results in a thinner lubricating film with increased molecular collisions (shear stress) and a more clogged up film structure under the application of pressure (Fernandez *et al*, 2014 and Ichiro, 2017). This also allows more direct asperity contacts, and increases the amount of sliding force required to deform the contacting asperities and shear the oil molecules at a given load stage (Mia *et al*, 2010). The lower viscosity GIII S1 (4cSt) base oil also showed this behaviour between 50 and 150 N. This behaviour is more apparent at higher a viscosity. A further increase in temperature from 80 °C to 100 °C and then to 120 °C shows no significant effect in the COF with the increasing load between 50 to 150 N. Only beyond 150 N do we observe the 120 °C curve lying above the 80 °C and the 100 °C. This shows that a change in temperature between these values does not have a significant effect on friction behaviour between 50 and 150 N. A gradual rise in the COF at a load of 247 N at 80 °C is observed, which becomes more apparent at 100 °C and 245 N and at 120 °C and 205 N. The rigidity of molecular bonds is further lowered at 100 and 120 °C, making them more flexible and prone to bond dissociation which resulted in the observed film breakdowns. The molecular behaviour allows for consistent shear strengths and surface modifications due to sliding at all three temperatures. This can be the benefit of using the GIII S1 (6cSt) base oil for practical applications in this range of temperatures.

The effect of the increasing load is observable at the higher temperatures, subject to the decrease in the COF and the breakthroughs at 80, 100 and 120 °C. The increase in temperature from 80 °C to 120 °C decreases the load carrying capacity of the GIII S1 (6cSt) base oil. The onset of loss of lubricity begins at higher loads at 80 °C

compared to at 100 and 120 °C. This is subject to the dissociation of the molecular bond(s) by the sliding motion giving lowered film strength. Film breakdown results, due to the lowered film strength (Ichiro, 2017). Clearly, this is a process catalyzed by high temperature and high normal stresses during sliding. Since this is also a hydro-processed base oil, it is less prone to surface reactions as compared to a solvent refined base oil (GI (4cSt)) due to the low sulphur content and increased saturation levels. However, there is a possibility that a change in film/surface properties arises because of contributing surface radical reactions (Stachowiak & Batchelor, 2014: 57). The GIII S2 (6cSt) base oil results are shown in Figure 4.14.

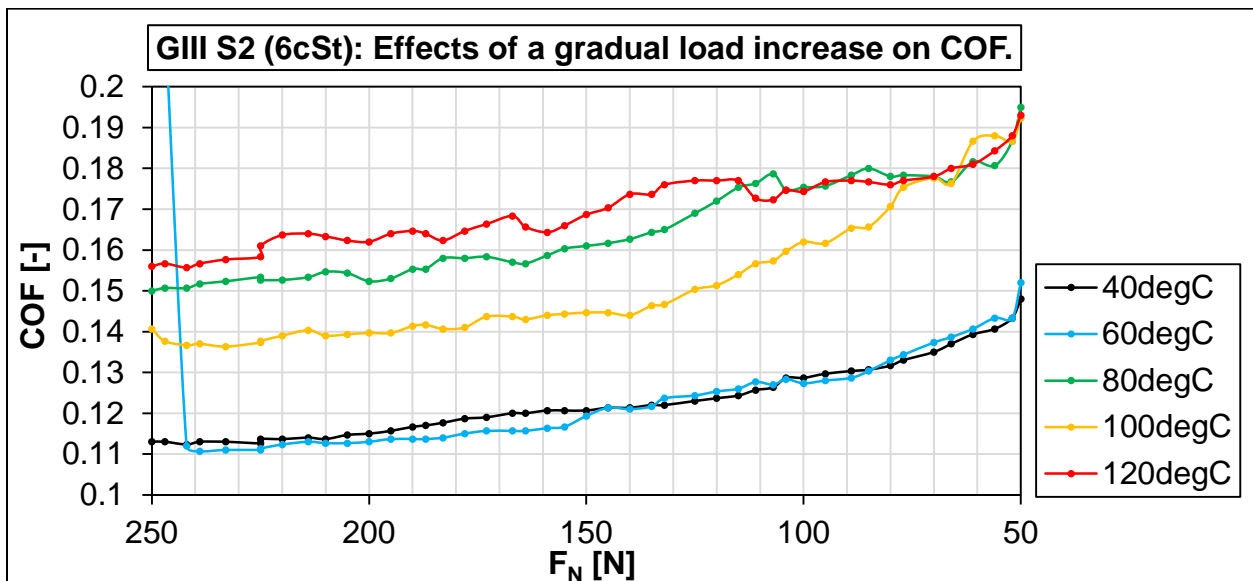


Figure 4.14: GIII S1 (6cSt): Gradual load increase at different temperatures.

A significant influence of temperature on the COF between 60 and 80 °C is observed. This behaviour is similar to that observed with the GIII S1 (4cSt) and GIII S1 (6cSt) base oils. The influence of temperature on the COF between 80, 100 and 120 °C was more significant subject to the large changes in the COF values as the load was increased, largely between 150 N and 250 N. This behaviour was observed with the 4cSt sister of this base oil (GIII S2 4cSt). At 60 °C, a breakthrough is observed when the load reached 242 N, just after the curve reaches its lowest COF value of 0.110 at 240 N.



This shows a load carrying capacity of the GIII S2 (6cSt) at 60 °C. The friction behaviour of this base oil shows to be the least affected by an increase in temperature from 40 to 60 °C, this appears to be a result of a higher viscosity resulting in formation of a thick lubricating film which separates the oscillating ball and disc surfaces. No consistent trend in the friction behaviour can be determined between 80 and 120 °C where the viscosity of the oil is lower. This inconsistency was also observed with the GIII S2 (4cSt) base oil. This appears to be a low viscosity problem of the base oils from supplier 2 (S2).

### **Discussion of friction results**

The initial part of this discussion focuses on the thermal effects, followed by the observed gradual decrements in the COF as the applied load was increased from 50 N to 250 N. The second part focuses on the effect of water on the friction behaviour of the base oils. It should be noted that the load increments begin after the running-in period, meaning that this process begins on a slightly decreased surface roughness.

### **Stress augmented thermal effects**

The oscillatory motion of the steel ball on the disc is produced by the applied shear force, and is opposed by friction. Despite more than a hundred years of research there is still surprisingly little deep understanding of how the applied forces, the friction, and the relative motion are connected at an atomic and molecular scale (Spikes, 2018). However, it is known that the inevitable result of friction due to asperity collisions is the release of heat especially at high speeds as in the current investigation. Therefore, a considerable amount of energy is dissipated in this manner (Stachowiak & Batchelor, 2014: 513). Since the true contact area between opposing asperities is always considerably smaller than the apparent contact area, the frictional energy and resulting heat at these contacts becomes highly concentrated with a correspondingly large temperature rise as illustrated schematically in Figure 4.14A (Spikes, 2018 and Stachowiak & Batchelor, 2014: 513).

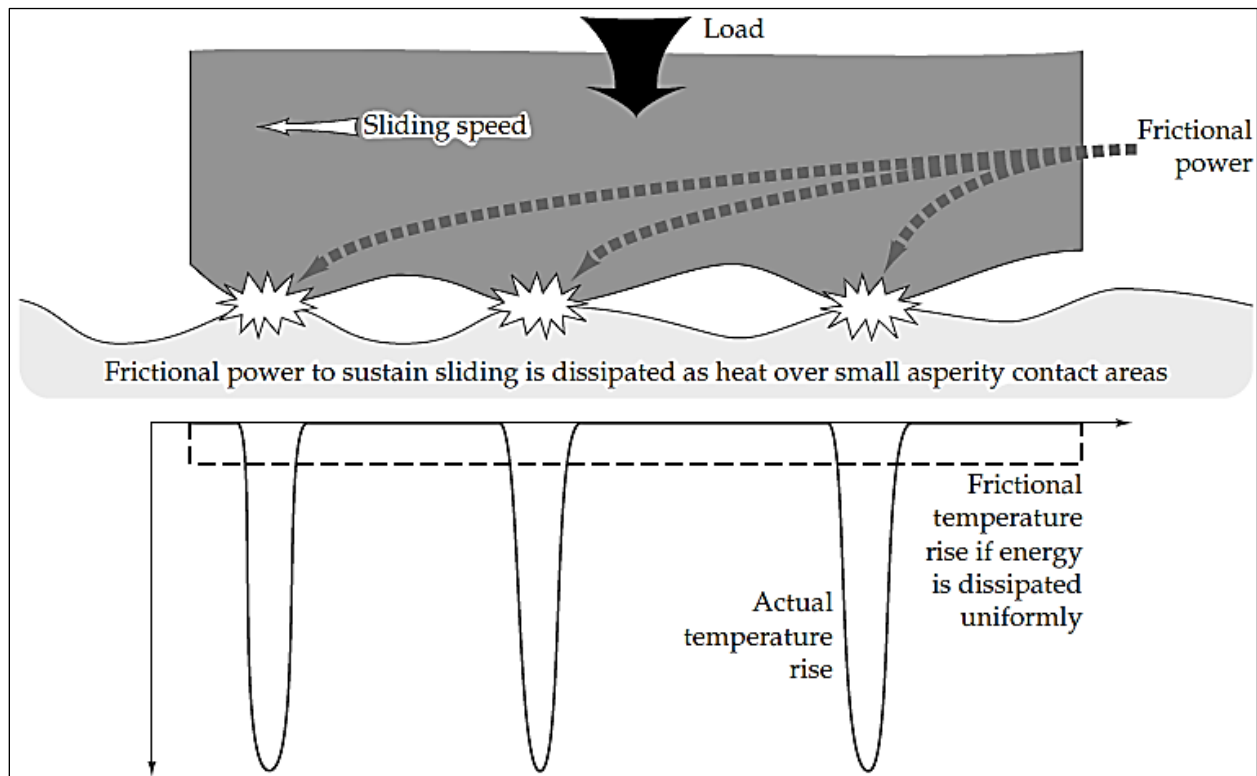


Figure 4.14A: Concentration of frictional energy (power) at the asperity contacts.

In some cases, the temperatures can rise to two times the operating temperature (Bushan, 2013: 286 – 289 and Stachowiak & Batchelor, 2014: 347 - 353). Therefore, due to this effect, the temperature at the contact points is always significantly higher than the actual test temperature. Meaning, each base oil was always subjected to a higher temperature than that set for each test. The comments made with regard to the evaporation of water molecules at the contact interfaces at a test temperature of 100 °C were made with the above in consideration. Likewise with the bond dissociations observes with the unsaturated base oils due to thermal activation at the contact interfaces.

### Decrease in COF with increasing load

It should be noted that the COF ( $\mu$ ) for lubricated contacts is given by:

$$\mu = f_a \mu_a + f_p \mu_p + f_d \mu_d \quad (2.18a)$$

Therefore, the COF's reported from each experiment represent the friction force (at a given load stage) required to:

1. Shear the viscous base oils and adhesive junctions on the sliding steel surfaces
2. Deform the prominent asperities.
3. Plough through deformed asperities and wear particles.

The main contributing factor to the lowered COF is absorption (adhering) of the oil molecules on the oscillating surfaces with the increasing load and with increasing temperature. Polar molecules display an affinity to steel surfaces, and the higher the polarity the higher the affinity (Ichiro, 2017). All base oils in this investigation showed some level of polarity. It is also known that polarity is induced by high temperatures, therefore, more affinity and absorption of oil molecules is expected at high temperatures due to increased molecular mobility which increases the probability for molecules to move to the metal surface. Sliding also provides the energy to oil molecules for adsorption and therefore protecting the film against sliding (Ichiro, 2017). The smoothness in the friction curves indicate the stability of the molecular films formed by each base oil and the ease of intermolecular molecular shearing.

For each test, as the increase in the normal load was initiated from 50 N, the viscosity of the lubricating oil between the sliding steel ball and disc surfaces also increased due to the piezoviscous effect, and as a result, a more significant load transfer to the more prominent asperities occurred (Mia *et al*, 2010). With this higher load, plastic yielding of the asperities resulted, allowing them to deform under the friction stress applied (Stachowiak & Batchelor, 2014: 577). This resulted in the flattening of the prominent asperities due to the sliding motion (tangential stress introduced), which increased the area of contact between the asperities. These surface changes result in indentations made on the contact surfaces, increasing the overall contact area (Bhushan, 2013: 94). Because for all materials, whatever their modulus of elasticity, the surfaces in a Hertzian contact deform elastically (Stachowiak & Batchelor, 2014: 318). Therefore, the high normal pressures especially at high temperatures (80, 100 and 120 °C) cause the ball specimen to deform, changing the shape from round to oval (another contributing factor

to the increased contact area). The increased contact area between interacting asperities allowed for the oil molecules to adsorb over a larger area and the applied load to be distributed over larger contact area. Ultimately each point of the deformed asperity now carried a lesser amount of the normal load since the increase in the contact area results in a reduction in the normal pressure (Stachowiak & Batchelor, 2014: 577). The decreased normal pressure at each asperity point now allowed lower molecular shear stress which enables lower friction force for sliding to occur. The lower friction force is indicated by the decreased COF.

This is in-line with Amonton's law of friction which states that the friction force is proportional to the applied load, providing that this force is also proportional to the real contact area. Therefore, an increase in contact area will decrease the friction force proportionally (Stachowiak & Batchelor, 2014: 503 & Bhushan, 2013: 236). Also, this is actually the mechanism of running-in as explained by van Drogen (2009: 1), and the shape of the friction curves correspond to the one he found. Each new load stage can be viewed as a new "running-in" period. Therefore, the continuous increase in load can be viewed as an instantaneous continuous series of short running-in stages, which result in continuous decrease in surface roughness due to the continuous asperity deformation, and ultimately, a continuous reduction in friction force as indicated by the gradual decrease in COF. Wear also plays a role in the increased contact area and therefore cannot be ignored. Wear results in indentations on the contacting surfaces. The wear debris (if any) trapped between the sliding surfaces can also lead to direct contact between the oscillating ball and the disk, especially on the edges. This results in a direct increase in contact area. Therefore the real area of contact between the ball and the disc is clearly larger than that which can be estimated by Equation 2.2 by Hertz. Equation 2.2 only factors in the effects of elastic deformation under the increasing load and excludes the contributions of wear. This means that the real contact area is under-approximated.

The differences observed from the starting points of the COF curves observed from Figure 4.8 to Figure 4.14 at the different temperatures are an indication of the level of

surface changes which occurred during the running-in period and the loss in viscosity of the base oils. The viscosity loss of the base oils as a result of the increases in temperature results in thinner lubricating films which promote more severe contact of the prominent asperities during sliding, this results in increased friction at the 50 N starting load (Stachowiak & Batchelor, 2014: 586). Hence the larger the starting COF values at 50 N as the temperature increases. This is observable with all the base oils under study from 40 and 120 °C with the exception of the PAO (4cSt), GI (4cSt) and GIII S2 (4cSt) where the observed COF at 120 °C and 50 N are lower than those at 100 °C and 50 N. This is an effect related to the evaporation of the dissolved water in the base oils 100 °C. At 120 °C these three base oils show signs of pure low molecular shear stresses which allow easier sliding and more smoother surface changes (asperity deformation). There is a clear benefit of a low frictional energy with using these base oils for operations at 120 °C. The presence of water leads to an increased COF. The irregularities observed on some of the curves (especially at 100 and 120 °C) may be caused by the breaking off of one or more asperities from the metal surface during deformation and formation of transfer particles since at these temperatures, asperity collisions are more direct due to the lowered oil viscosities. The movement, reshaping and removal of the transfer particles from the contact area due to the sliding movement and increasing load increase results in an increased uneven friction. Surface analysis is required to confirm the above.

### **Seizure (Breakthrough)**

The observed sudden increases in the COF are an indication of sudden loss in lubricity at the contact zone. Seizure is characteristic of both the steel surfaces and the base oil behaviour. From a metal surface perspective, during oscillation and with the increasing load, the interacting surfaces are polished to some level of smoothness, and the load-carrying capacity can be lowered as the surfaces get smoother (Stachowiak & Batchelor, 2014: 586). It has often been observed that if the surface is too smooth then there is a risk of sudden seizure with high contact loads, whereby the small asperities play a useful role as a reservoir for the lubricant by entrapment between asperities. In a

situation where the contact stresses are very high, the trapped lubricant can be expelled by asperity deformation to provide a final reserve of lubricating oil. The main effect of severe contact loads is to remove the oil film from asperity peaks during contact with opposing interacting surfaces and cause any lubricating effect to rapidly disappear, even though it has been well developed at the specific temperature and low loads (Stachowiak & Batchelor, 2014: 586). From the lubricant perspective, the main property of oils resulting in removal is poor adsorption due to low polarity or unavailability of adsorption site due to the presence of dissolved water which occupies some sites under the given conditions (Meirong et al, 2017). The breakdown of the lubricant/molecular film is caused by the high pressure asperity points during sliding. High pressures and sliding motion cause more collision of molecules and increased molecular shear stresses. Shearing can dissociate chemical bonds in a molecule directly and therefore, result in film breakage (Ichiro, 2017). After seizure has occurred, adhesion between the asperities occurs due to the true contact between the metal surfaces at the area when lubrication has been lost (Stachowiak & Batchelor, 2014: 586). When the steel ball and disc make true contact in the absence of a base oil in the contacting area, instantaneous electron exchange takes place between the metal surfaces creating an electrostatic bond. The bond (adhesion) between the steel surfaces requires a high friction/sliding force to break. Hence the increased COF values soon after seizure (Stachowiak & Batchelor, 2014: 586). A further increase in the COF might be observed with the continuous application of pressure after seizure, due to the increase in contact area due to the normal stress, and junction growth (elongation of the area of contact due to the sliding force applied). Both these effects contribute to the amount of friction force required to initiate further sliding under the changes surface characteristics (Stachowiak & Batchelor, 2014: 577).

### **Effects of water on the COF**

The presence of dissolved water in base oils cannot be avoided. The 20% RH chosen for this investigation only ensured that the not too much moisture is available in the atmosphere, which can be absorbed by the oils. This prevented dissolving of water in

oils beyond saturation. The effects of water on the COF was clearly observable with PAO (4cSt), GI (4cSt) and GIII S2 (4cSt) base oils where the observed COF curves at 120 °C lie below those at 80 and 100 °C. This clearly shows that the presence of water increases friction. Water has no lubricating properties, but has high polarity and forms a strong bond when it adsorbs on metal surfaces through lone pair electron exchange via the O atom. This makes water a strong competitor for adsorption sites on steel surfaces, which have a high surface energy. Occupation of adsorption sites by water decreases the surface energy of the metal and this leads to poor adsorption by the oil molecules (even with high polarity) and also minimizes the available area for adsorption. This leads to poor film formation by the oil molecules and increased shear stresses under high normal pressures during sliding, which ultimately increases the friction force required to shear the oil film over the prominent asperities on the metal surface. The poor adsorption by oil molecules may lead to easy desorption by the sliding motion (Ichiro, 2017 and Nilsson *et al*, 2008: 137).

## **Summary**

The GIII+ (4cSt) and PAO (4cSt) base oils showed the most stable friction response at each of the five test temperatures indicative of the high thermal stability. The GIII S1 (4cSt), GIII S2 (4cSt), GIII S1 (6cSt) and GIII S2 (4cSt) base oils showed frequent irregularities in their COF curves, accompanied by breakthroughs between 80 and 120 °C. The base oils from supplier 1 (GIII S1 (4cSt) and GIII S1 (6cSt)) showed similar behaviour. The increase in temperature from 60 to 80 °C had the largest effect in the COF, whereas, the effect is minimal between 40 and 60 °C, and 80 and 120 °C. Base oils from supplier two showed a different response. The GIII S2 (4cSt) showed a consistent effect of temperature, resulting in an increase in the COF between 40 and 100 °C, and a slight decrease from 100 to 120 °C. A slightly similar behaviour was observed with the GIII S2 (6cSt), except the large effect of temperature between 80 and 100 °C which resulted in a significant increase in the COF.

## 4.2.2 Stribeck curves

The experimental Stribeck curves obtained with the seven base oils under investigation are shown in Figure 4.11 to Figure 4.17. Each figure shows the coefficient of friction (COF) plotted against the dimensionless Stribeck parameter ( $Sp$ ), also referred to as the Hersey number. Each figure pertains to a specific base oil, which the name is the title of the figure. Also, each curve on the figures pertains to a specific test temperature, represented by a unique color which is specified on the legend. The figures will be analysed from the right to the left, following the direction of the increasing load, since the load is the denominator of the abscissa. To analyse the curves, it should be noted that the hydrodynamic regime is fixed in the range  $4 \times 10^{-5} < Sp < 1 \times 10^{-3}$ , the mixed lubrication regime is in the range  $2 \times 10^{-6} < Sp < 4 \times 10^{-5}$  and the boundary lubrication regime range is  $1 \times 10^{-7} < Sp < 2 \times 10^{-6}$ , as was shown in Figure 2.39 of section 2.4.6.

Figure 4.11 shows the Stribeck curves obtained with the PAO base oil. The 40 °C Stribeck curve shows that the PAO base oil operated in the elastohydrodynamic regime in the range  $4 \times 10^{-5} < Sp < 5.9 \times 10^{-5}$ , which corresponds to a load increase from 50 N to about 140 N. This is accompanied by a gradual decrease in the COF from 0.152 to 0.128.

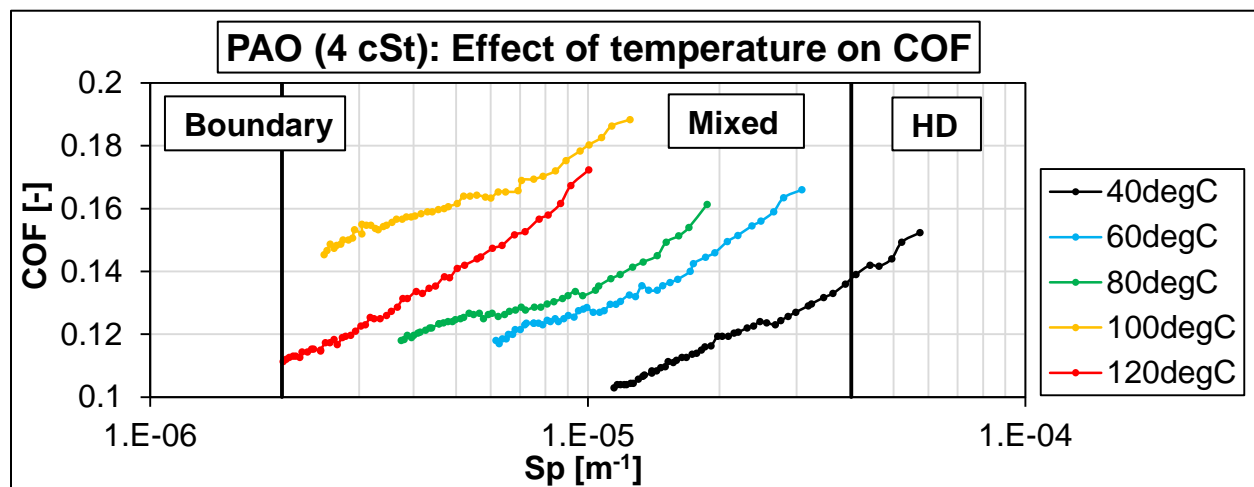


Figure 4.11: Effect of temperature on Stribeck curves.



As the load was increased from 150 N to 250 N, the conditions crossed over to the mixed lubrication regime, in the range  $1.2 \times 10^{-5} < Sp < 4 \times 10^{-5}$ . At 60 °C, it can be observed that the curve lied in the mixed regime, the same is observed at 80 °C, 100 °C and 120 °C, as the load gradually increases from 50 N to 250 N. It was expected that for high pressure non-conforming contacts, the mixed/elastohydrodynamic (EHD) lubrication would predominate as is stipulated in literature (Vengudusamy *et al*, 2014).

However, the Stribeck curves as shows in Figure 4.11 are erroneous. The observed behaviour cannot be a true reflection of the oils real friction behaviour taking into account that in the mixed/elastohydrodynamic lubrication regime, the elastic deformation and the pressure-viscosity effects are significant. The Stribeck parameter, as it stands, does not incorporate the pressure-viscosity effects, which play a significant role in non-conformal Hertzian contacts, as was stipulated by Brandao *et al*, (2012), Hamrock *et al* (2004: 7), Stachowiak & Batchelor (2014: 17) and Vengudusamy *et al* (2014). It is clear that the Stribeck parameter is not dimensionless and it cannot be properly defined for a ball and disc contact as the length of the contact cannot be properly specified. Also it does not take into account the differences, or rather, the changes in viscosity at the differing operating conditions, and this applied for all the curves obtained with the remainder of the base oils as shown in figures 4.12 to 4.17.

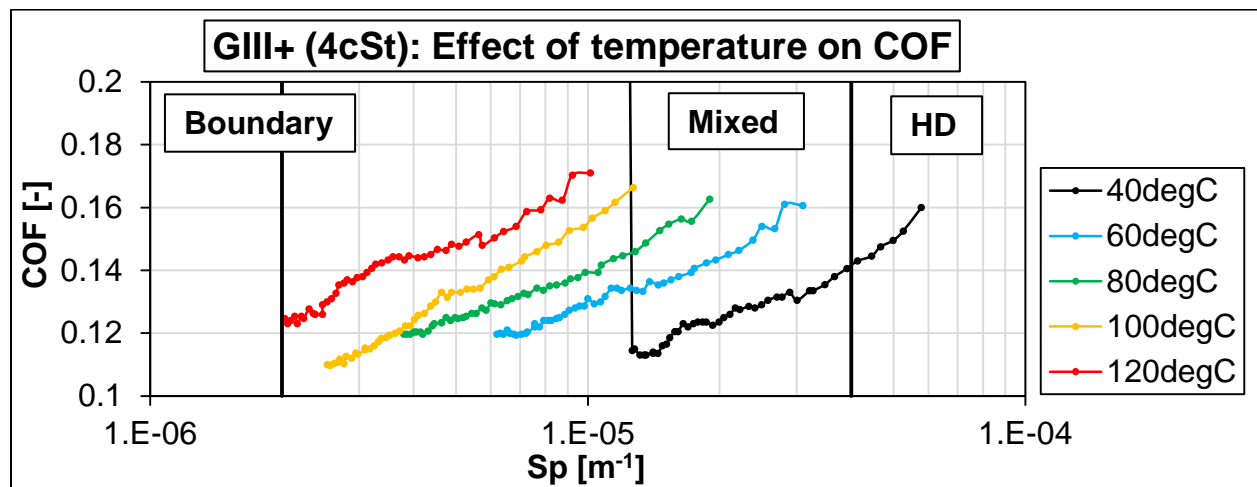


Figure 4.12: Effect of temperature on Stribeck curves.

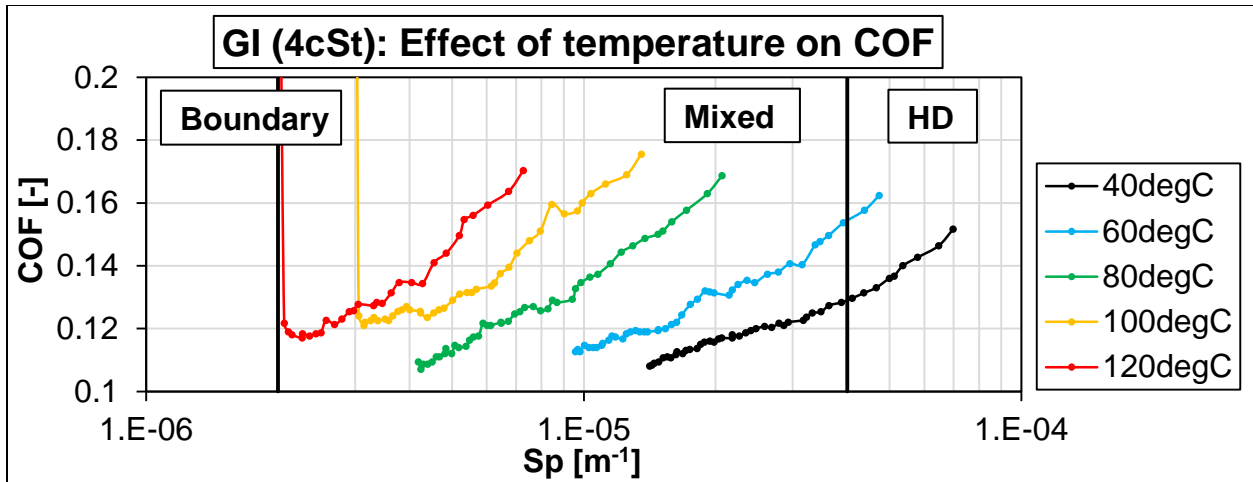


Figure 4.13: Effect of temperature on Stribeck curves.

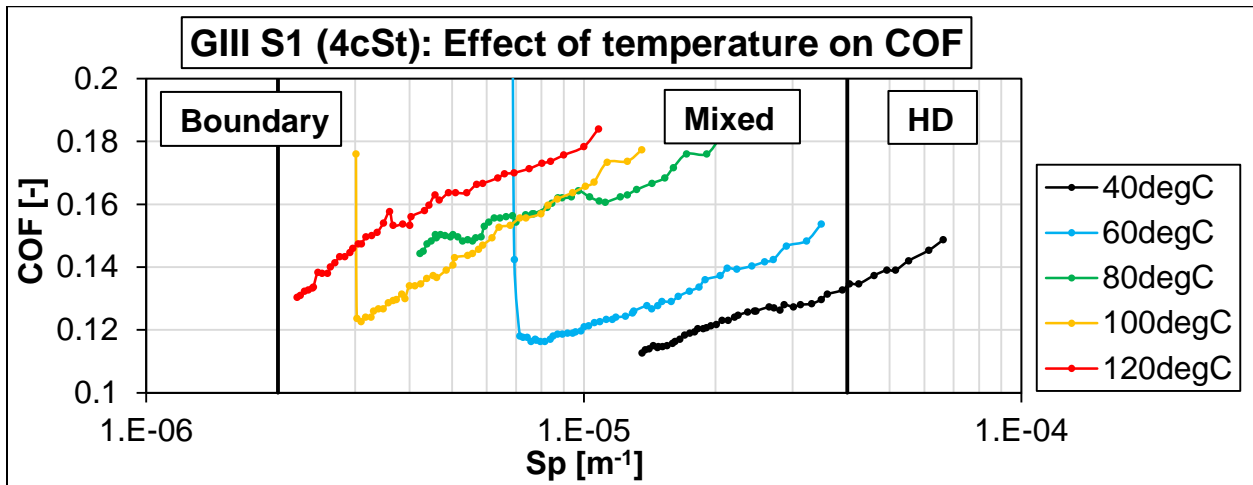


Figure 4.14: Effect of temperature on Stribeck curves.

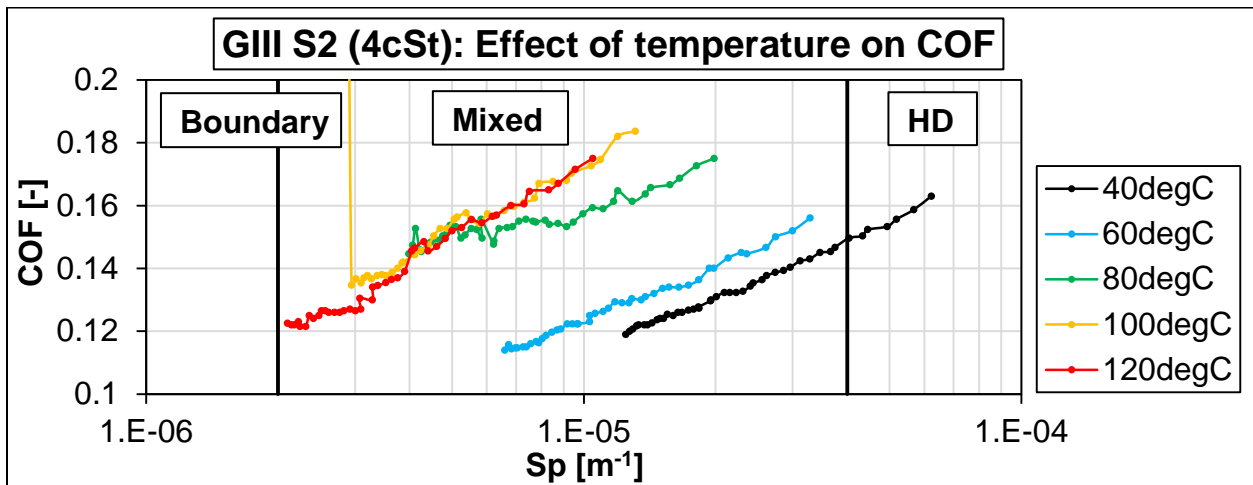


Figure 4.15: Effect of temperature on Stribeck curves.

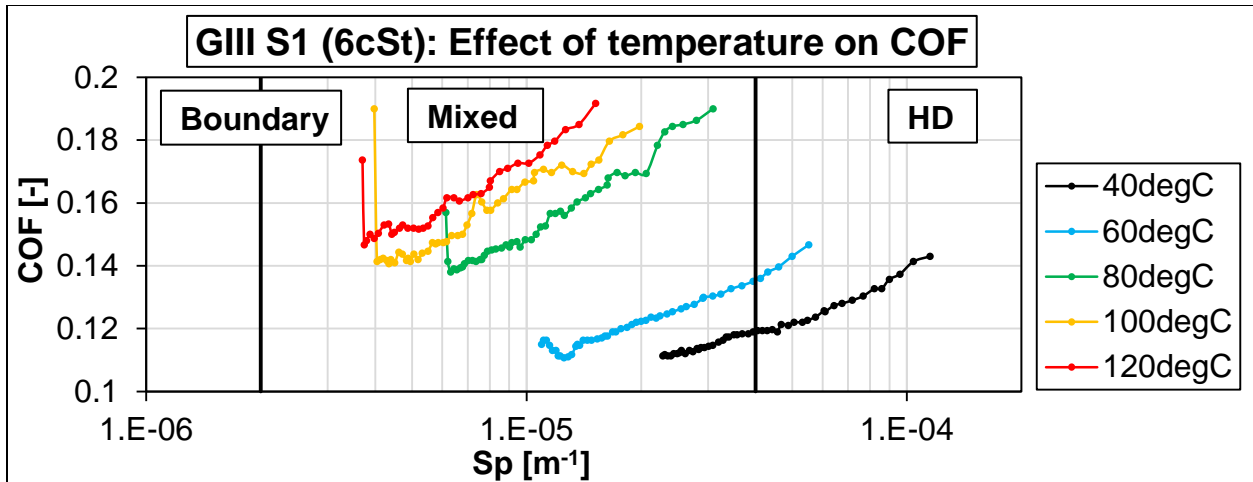


Figure 4.16: Effect of temperature on Stribeck curves.

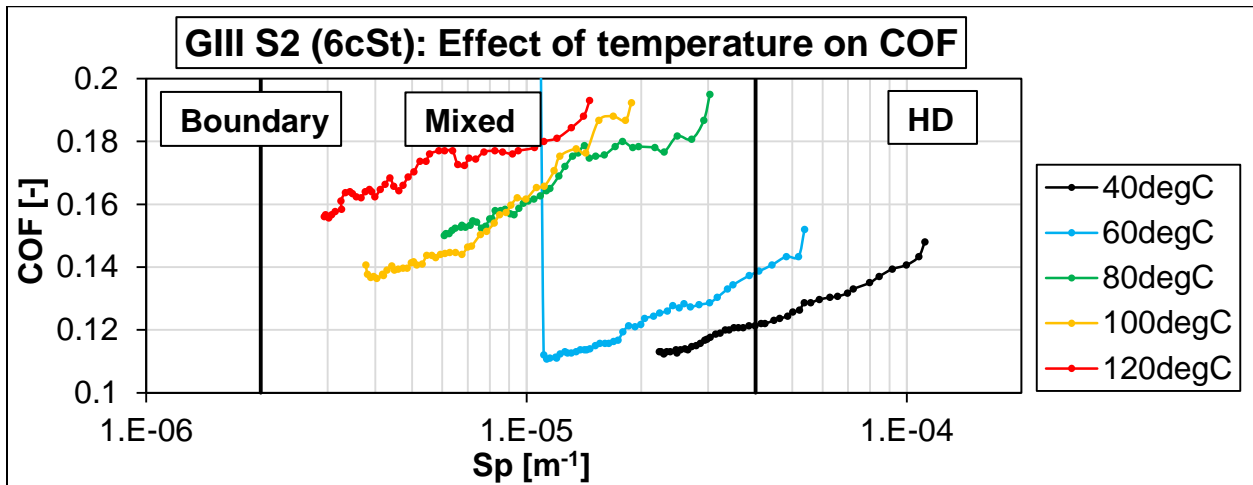


Figure 4.17: Effect of temperature on Stribeck curves.

To correct this discrepancy the below is considered:

1. The Stribeck curve was developed for journal bearings of known length. It was originally used to show the transition from the **hydrodynamic**, mixed and then to boundary film lubrication conditions. This is evident in the fact that the abscissa parameter in the Stribeck curve is  $(\mu\Gamma)/F_N$  and can only be dimensionless when the length of the journal bearing is specified. Ball bearings on the other hand, due to the hertzian nature of the contact, normally operate under the **elastohydrodynamic**, mixed or boundary lubrication regimes, where the pressure-viscosity effects of the lubricant play an important part in terms both of

film thickness and of coefficient of friction (Brandao *et al*, 2012 and Hamrock *et al*, 2004: 7). Due to this, to use the Stribeck curve to show transitions in lubricating regimes for ball bearings, the pressure-viscosity coefficient must be included in the calculation of the Stribeck parameter (Hamrock *et al*, 2004: 7).

2. Since the base oils investigated in this study have different viscosities under the chosen operating conditions, the effect of viscosity on the coefficient of friction cannot be excluded in the Stribeck curves obtained, especially at low loads (Vengudusamy *et al*, 2014).

Therefore, the viscosity-pressure coefficient ( $\alpha$ ) must be incorporated in the Stribeck parameter. This modification takes care of the pressure-viscosity effects of the lubricant on the friction coefficient. This way, the friction contribution is only due to surface condition and/or the molecular behaviour (Vengudusamy *et al*, 2014). It is desirable for the parameter to be dimension-less (Brandao *et al*, 2012). Thus, the modified, and now dimensionless, Stribeck parameter ( $S_p$ ) is given as:

$$S_p = u_b \eta_o \alpha^{0.5} F_N^{-0.5} \quad (4.1)$$

Where  $\eta_o$  is the dynamic viscosity at oil inlet temperature and atmospheric pressure and  $\alpha$  the pressure-viscosity coefficient at oil inlet temperature (Vengudusamy *et al*, 2014, Brandao *et al*, 2012). Two important remarks about the modified Stribeck parameter made by different authors are:

1. As remarked by Gold *et al* (2001), oils of different base stock (mineral or PAO), as in the present work, have significantly different  $\alpha$  even if they have the same kinematic viscosity. The inclusion of  $\alpha$  in this modified Stribeck parameter is a way of accounting for the different nature of the base oils of each lubricating oil considered.
2. In the context of the present work where the geometry, the surface roughness and the specimen materials were the same in all tests, the introduction of  $\alpha$  into the Stribeck parameter formula ensures that the parameter remains

dimensionless and ensures that equal values of the parameter correspond to the same lubrication regime. Such would not be the case when using the usual parameter  $(u\eta)/F_N$  for the abscissa (Vengudusamy *et al*, 2014 & Brandao *et al*, 2012).

This allows for relative comparison of surface conditions such as tribofilm formation obtained from different base oils investigated in this study. As was remarked in the previous section, the transition from EHD to boundary film lubrication always occurs for similar values of the modified Stribeck parameter ( $S_p$ ). For the modified Stribeck parameter, the lubrication regimes are located as follows (Brandao *et al*, 2012 & Sander *et al*, 2015):

- $S_p \geq 1 \times 10^{-7}$ : EHD lubrication.
- $1 \times 10^{-9} \leq S_p \leq 1 \times 10^{-7}$ : Mixed film lubrication.
- $S_p \leq 1 \times 10^{-9}$ : Boundary film lubrication.

This means that each regime of lubrication has a definite position in the abscissa, and this remains true across a wide range of operating conditions (Brandao *et al*, 2012).

#### 4.2.3 Pressure-viscosity coefficient: Effects of temperature

The pressure-viscosity coefficient ( $\alpha$ ) is a function of the molecular structure of the lubricant and its physical characteristics such as molecular interlocking, molecular packing and rigidity and viscosity-temperature characteristics (Stachowiak and Bachelor, 2014: 17). The viscosity-pressure dependence can be generalised by assuming a relation between  $\alpha$  and kinematic viscosity ( $\eta_k$ ), at atmospheric pressure, as can easily be measured without a high-pressure rig. The suitable empirical equation that was used as presented by Brandao *et al* (2012), Gold *et al* (2001) and Vengudusamy *et al* (2014), for mineral and polyalphaolefin base oils is:

$$\alpha = s\eta_k^t \quad (4.2)$$

Where  $s$  and  $t$  are parameters given in the Table 4.3 for paraffinic mineral oils and polyalphaolefin, chosen as recommended by Gold et al (2001) and Vengudusamy *et al* (2014) for high pressures.  $\eta_k$  is the oils kinematic viscosity at atmospheric pressure. The values given by Gold's equation are clearly dependent on the lubricant formulation and on the temperature.

Table 4.3: Parameters for Equation 3.2; obtained at 0.2 GPa contact pressure.

<b>Base oil type</b>	<b>s</b>	<b>t</b>
Paraffinic mineral	0.99	0.14
Polyalphaolefin	0.73	0.13

For mineral and synthetic lubricant oils the viscosity-pressure coefficient decreases with temperature, and increases with viscosity at atmospheric pressure, this model implies that a change to another higher-viscosity lubricant has an impact similar to that of a temperature change without changing the oil (Brandao *et al*, 2012; Gold *et al*, 2001; Stachowiak and Bachelor, 2014: 17 & Vengudusamy *et al*, 2014). Figure 4.18 shows the correlation of the calculated  $\alpha$  values and temperature, for the temperatures 40, 60, 80, 100 and 120 °C.

It can be seen that all curves show a decreasing trend as temperature is increased from 40 °C to 120 °C. The two 6 cSt base oils had the highest  $\alpha$  values, ranging from 16.2 GPa<sup>-1</sup> and 16.1 GPa<sup>-1</sup> at 40 °C, to 12 GPa<sup>-1</sup> and 1.2 GPa<sup>-1</sup> at 120 °C for GIII S1 (6cSt) and GIII S2 (6cSt) base oils respectively. On the 4 cSt group of base oils, the GI (4cSt) had a trend dissimilar to the trend from the other base oils in this group. This base oil has an  $\alpha$  value of 14.3 GPa<sup>-1</sup> at 60 °C, which is the highest in this group, and an  $\alpha$  value of 11 GPa<sup>-1</sup>, which is the lower than that of GIII S1 (4cSt), GIII S2 (4cSt) and GIII+ (4cSt), at 120 °C.

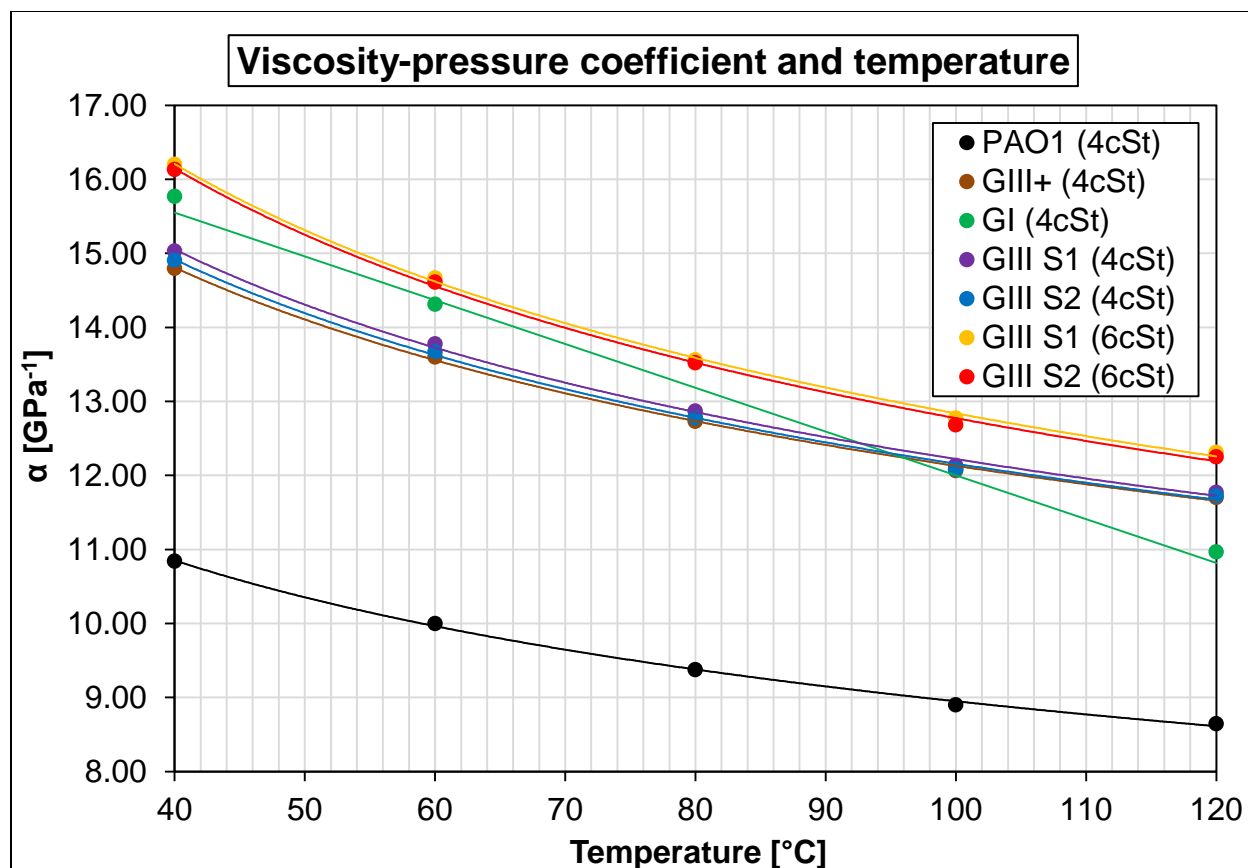


Figure 4.18: Correlation of viscosity-pressure coefficient and temperature.

This trend is similar to that observed when dynamic viscosity is correlated with temperature. An increasing temperature had a big effect on the  $\alpha$  of the GI (4cSt) base oil. The PAO (4cSt) base oil had the lowest  $\alpha$  values at temperatures 40, 60, 80, 100 and 120 °C. The values ranged from 10.8 GPa<sup>-1</sup> at 40 °C to 8.6 GPa<sup>-1</sup> at 120 °C as can be observed on Figure 4.18.

The trends from the two 6 cSt base oils seem very similar as the temperature increases from 40 °C to 120 °C, so as those of the 4 cSt base oils, except for the GI (4cSt) base oils, which shows a more linear trend, beginning at an  $\alpha$  of 15.77 GPa<sup>-1</sup> at 40 °C and going to 10.97 GPa<sup>-1</sup> at 120 °C. The GI (4cSt) base oils had the largest decrement of  $\alpha$  (4.8 GPa<sup>-1</sup>) as the temperature was moved from 40 °C to 120 °C. This indicates the bigger influence of increasing temperature on  $\alpha$  value of the GI (4cSt) base oils.

The above confirm the finding by Brandao *et al* (2012) and Sander *et al* (2015), which is that: for mineral and synthetic lubricant oils the viscosity-pressure coefficient decreases with temperature, and increases with viscosity at atmospheric pressure. Gold *et al* (2001) also remarks that oils of different base stock (mineral or PAO), as in the present work, have significantly different  $\alpha$  even if they have the same kinematic viscosity. Gold *et al* (2001) and Sander *et al* (2015) further stipulated that the pressure-viscosity is a strong function of temperature which is also evident from the results obtained in this study.

#### 4.2.4 Modified Stribeck curves

Figure 4.19 shows the Stribeck curves obtained with the PAO (4cSt) base oil. It can be seen in Figure 4.19 that as the load was gradually increased from 50 N to 250 N, under all test temperatures (40 °C, 60 °C, 80 °C, 100 °C and 120 °C), the PAO base oil operated in the mixed film regime with  $1 \times 10^{-9} \leq S_p \leq 1 \times 10^{-7}$ . For the purpose of analyses, the mixed lubrication regime was sectioned into two i.e., Lower mixed regime (near boundary lubrication) and upper mixed regime (near EHD lubrication).

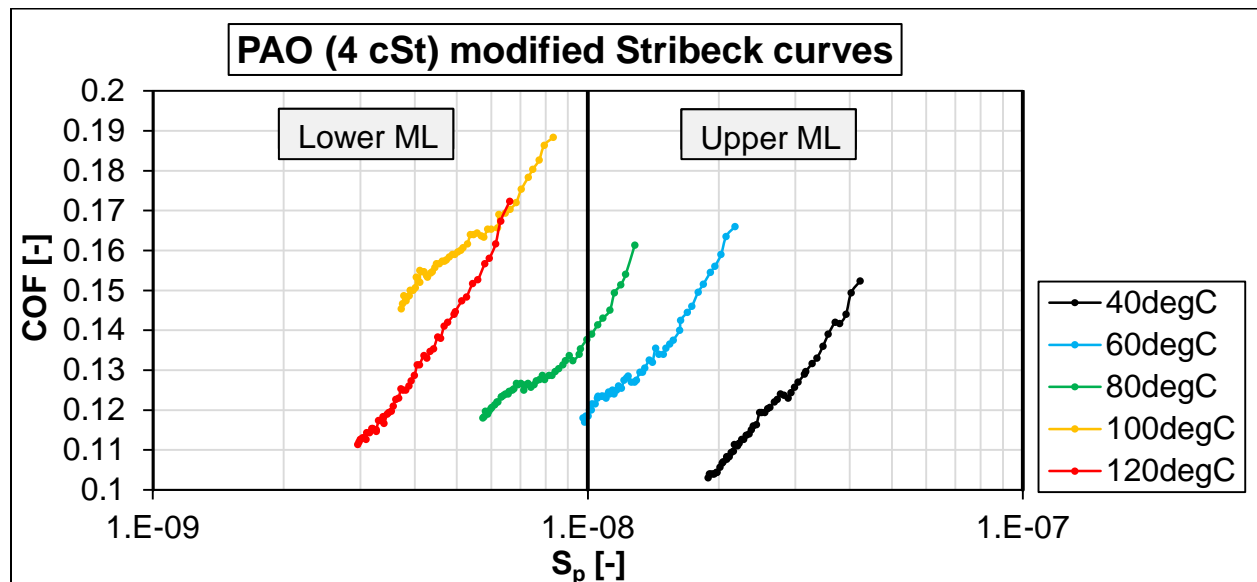


Figure 4.19: PAO (4cSt) modified Stribeck curves.



Therefore:

- $1 \times 10^{-9} \leq S_p \leq 1 \times 10^{-8}$ : Lower mixed film lubrication.
- $1 \times 10^{-8} \leq S_p \leq 1 \times 10^{-7}$ : Upper mixed film lubrication.

The above was done in observation that the mixed film regime was the dominating operating regime in this study. In Figure 4.19, it can be seen that as the temperature was increased from 40 °C to 60 °C, and from 80 °C to 100 °C, the stribeck curves shifted upwards (resulting in higher COF values especially between 80 and 100 °C). The curves also shifted to the left (resulting in lower  $S_p$  values). This shows the direct effect of an increase in temperature on the COF, with a smaller effect between 60 °C to 80 °C. The effect of temperature on  $S_p$  is consistent between 40 °C and 100 °C, resulting in a constant decrease in  $S_p$  values from the upper mixed film regime ( $S_p \geq 1 \times 10^{-8}$ ), to the lower mixed film regime ( $S_p \leq 1 \times 10^{-8}$ ). The curve for 120 °C lies below and to the left of the 100 °C curve, with lower  $S_p$  and COF values as the load was increased. This is again, a clear contribution of dissolved water.

It appears the presence of water at the contact interfaces also has an effect on the operating regime ( $S_p$ ), as the 120 °C curve would lie above and further to the left of the 100 °C curve, following the trend of the other curves with the increase in temperature (decrease in viscosity). The observation reported by Ichiro (2007) that water causes a viscosity drop at the contact points is true. This results in a thin lubricating film at the contact area which gives more direct asperity contact. This pushes the operation to the boundary regime, hence the low  $S_p$  values. It could be that in the absence of dissolved water, the 100 °C curve would lie to the right of the 120 °C curve, like wise with the 40, 60 and 80 °C curves. The pressure-viscosity coefficient of the PAO showed a consistent response to temperature, so did the dynamic viscosity. Therefore, it is clear that the observed inconsistency in Figure 4.19 is due to an external contaminant.

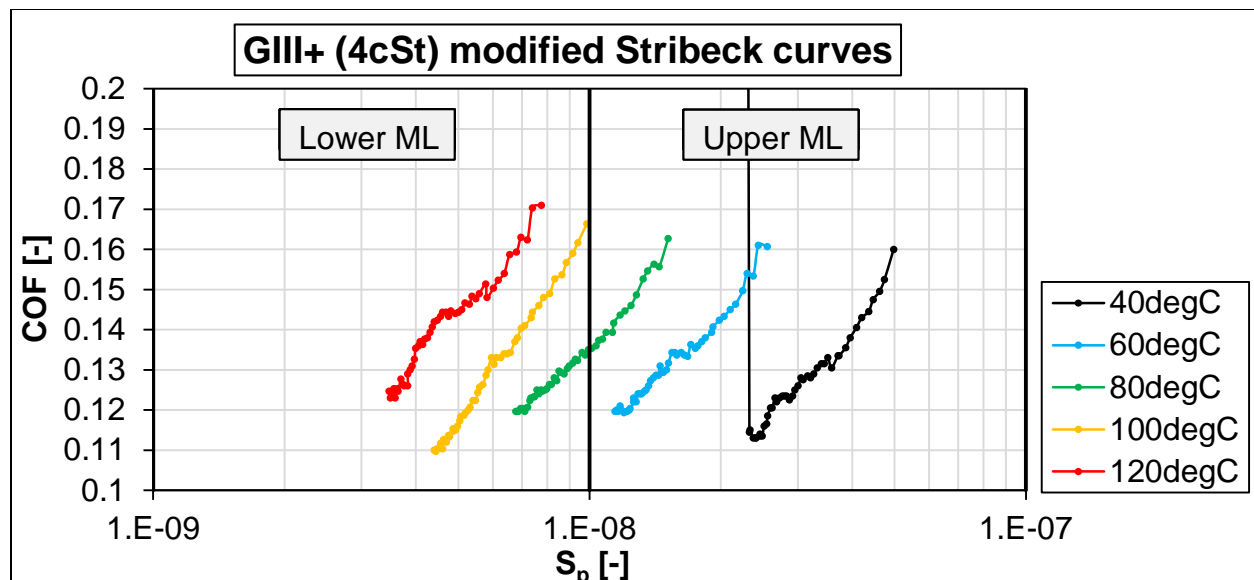


Figure 4.20: GIII+ (4cSt) modified Stribeck curves.

Figure 4.20 shows the Stribeck curves obtained with the GIII+ (4cSt) base oil. On this figure, it can be seen that the curves obtained at the different test temperatures (40 °C, 60 °C, 80 °C, 100 °C and 120 °C) do not show a significant difference in the COF range covered with the load increase from 50 N to 250 N. The curves lie next to one another and only slight increase in the COF is observed as the temperatures were increased from 40 °C to 120 °C at each load stage. However, the  $S_p$  shows to be affected significantly by temperature.

Although the full operation was in the mixed lubrication regime for all test temperatures, at 40 and 60 °C the GIII+ (4cSt) base oil allowed full operation in the upper mixed regime ( $1 \times 10^{-8} \leq S_p \leq 1 \times 10^{-7}$ ), as the load was increased from 50 N to 250 N. Only at 80 °C did the stribeck curve cross to the lower mixed regime where  $6.9 \times 10^{-9} \leq S_p \leq 1 \times 10^{-8}$  between 150 N to 250 N, while the upper mixed regime was dominant between  $1 \times 10^{-8} \leq S_p \leq 1.7 \times 10^{-8}$  (50 N and 150 N). At 100 and 120 °C, the Stribeck curves lie in the lower mixed film lubrication. The increasing temperature shifted the strives from the lower to upper mixed film regime and also improved the load carrying capacity of the GIII+ (4cSt), characteristic of the breakthrough at 40 °C and none at the higher temperatures. No observable sign of the influence of water on the operating regimes.

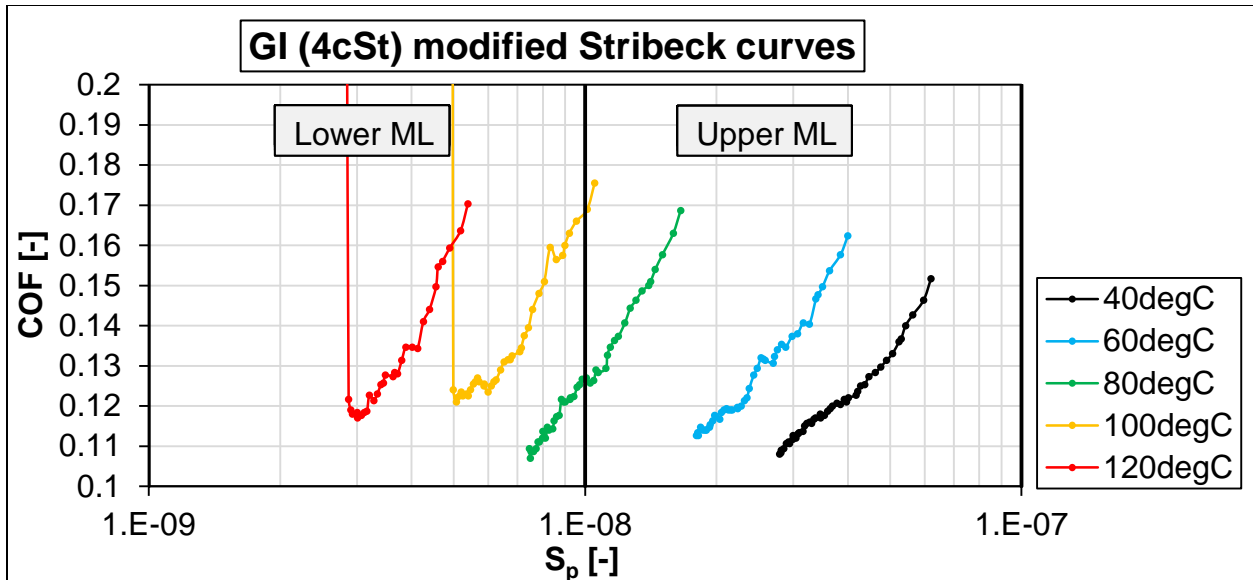


Figure 4.21: GI (4cSt) modified Stribeck curves.

The GI (4cSt) base oil Stribeck curves are shown on Figure 4.21. On this figure, it can be seen that this base oil operated in the mixed film regime, with the Stribeck curves shifting from the upper mixed regime to the lower mixed regime as the test temperature was increased from 40 °C to 120 °C, and also, each curve shows a gradual decrease in the COF as the applied load was increased gradually from 50 to 250 N. At 40 and 60 °C, the operation was fully in the upper mixed film regime, and at 80 °C, the curves crossed into the lower mixed regime between  $7.7 \times 10^{-9} \leq S_p \leq 1 \times 10^{-8}$ , which corresponds to the load range 150 N to 250 N. At 100 °C, the GI (4cSt) base oil operated in the upper mixed film regime where  $1 \times 10^{-8} \leq S_p \leq 1.1 \times 10^{-8}$  between 50 N and 80 N, and thereafter crossed into the lower mixed film between  $5 \times 10^{-9} \leq S_p \leq 1 \times 10^{-8}$  which is in the load range 80 N and 230 N where a breakthrough was observed. At 120 °C, the curve lies in the lower mixed film regime  $2.9 \times 10^{-9} \leq S_p \leq 5.5 \times 10^{-8}$  as the load was increased from 50 N to 200 N where a breakthrough occurred. It is clear that the increase in temperature from 40 °C to 120 °C causes the base oil to shift operation from upper mixed film regime to lower mixed film regime, and also lowers the load carrying capacity of the film formed by the oil. The same effect on  $S_p$  is observed with the increasing load, however, the effect is not as significant as that caused by temperature.

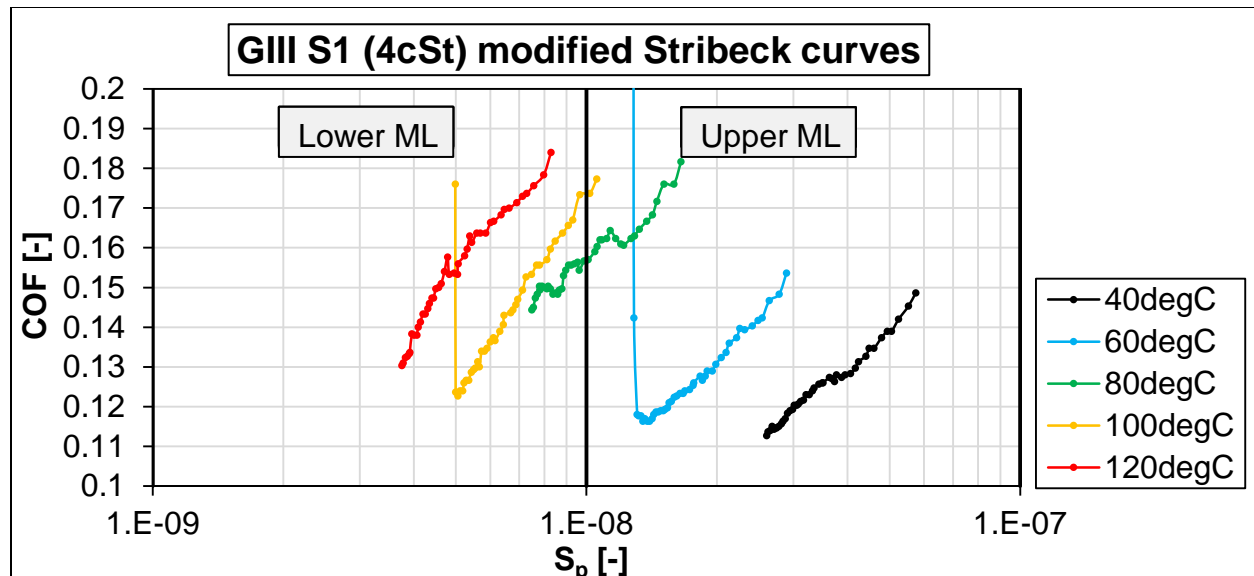


Figure 4.22: GIII S1 (4cSt) modified Stribeck curves.

Figure 4.22 shows the Stribeck curves as obtained with the GIII S1 (4cSt) base oil. This base oil operated in the mixed film lubricating regime under all test conditions. The effect of an increasing temperature from 40 °C to 80 °C as the operating load was gradually increased can clearly be seen, characteristic of the shifting of the curves upwards and to the left of the graph, resulting in an increase in the COF and a decrease in the  $S_p$  respectively. At 40 and 60 °C, the base oil operated in the upper mixed film regime with  $S_p$  range  $2.7 \times 10^{-8} \leq S_p \leq 5.9 \times 10^{-8}$  and  $1.4 \times 10^{-8} \leq S_p \leq 2.9 \times 10^{-8}$  respectively.

At 80 °C, the base oil operated in the upper mixed film regime in the range  $1 \times 10^{-8} \leq S_p \leq 1.7 \times 10^{-8}$  between 50 N and 160 N and crossed into the lower mixed film regime covering the range  $7.5 \times 10^{-9} \leq S_p \leq 1 \times 10^{-8}$  between 160 N and 250 N. The bigger gap between the 60 °C curve and the 80 °C curve shows the significant impact of temperature on the COF and on the  $S_p$ . At 120 °C, the curve crosses from the upper mixed film regime at around 65 N where  $S_p = 1 \times 10^{-8}$  and proceeds deep in the lower mixed film regime as the load was increased from 65 N to 250 N covering the range  $5 \times 10^{-9} \leq S_p \leq 1 \times 10^{-8}$ . The 120 °C curve lies fully in the upper mixed film regime between 50 and 250 N and in the range  $3.8 \times 10^{-9} \leq S_p \leq 8.2 \times 10^{-9}$ .

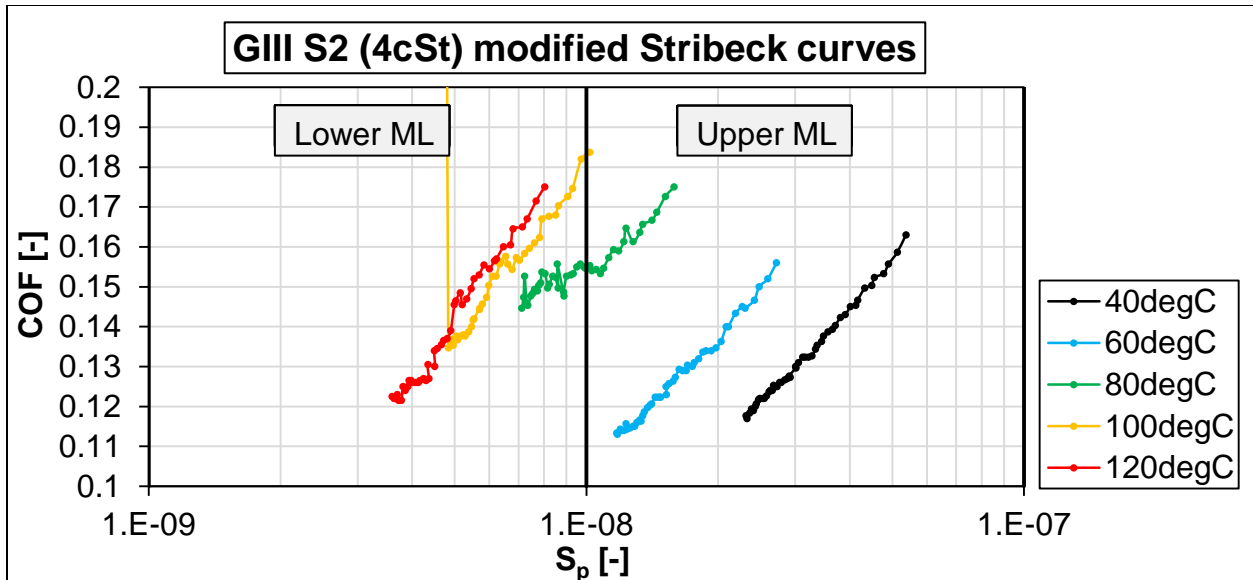


Figure 4.23: GIII S2 (4cSt) modified Stribeck curves.

In Figure 4.23, it can be seen that the GIII S2 (4cSt) base oil also operated in the mixed film lubrication regime under all the experimental conditions. Upper mixed film lubrication dominated at 40 °C and 60 °C. The cross over to the upper mixed film regime took place at 80 °C and 180 N, and at 100 °C at 55 N. The increase in temperature from 60 °C to 80 °C shows the largest increment in COF. The 120 °C curve lies in the lower mixed film lubrication regime.

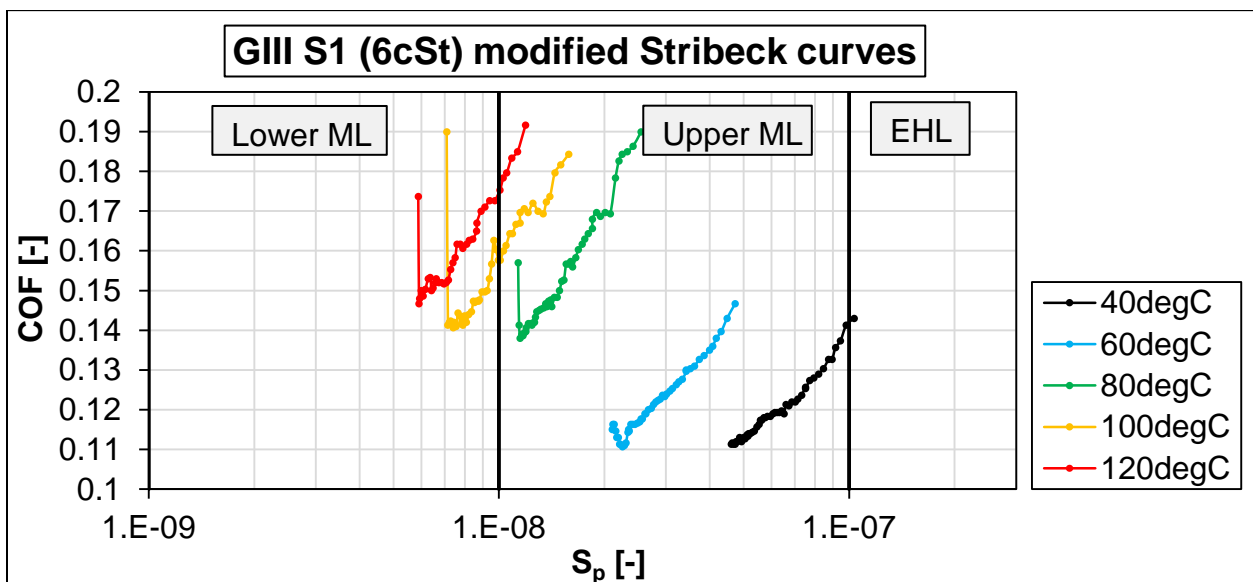


Figure 4.24: GIII S1 (6cSt) modified Stribeck curves.

The GIII S1 (6cSt) base oil operated in the elastohydrodynamic lubrication regime and mixed film lubrication regime. This is shown in In Figure 4.24. At 40 °C, as the load was increased from 50 N to 55 N, the GIII S1 (6cSt) base oil operated in the EHD lubrication regime with the  $S_p$  lying between  $1.1 \times 10^{-7}$  and  $1 \times 10^{-7}$ , and the COF decreased from 0.143 to 0.141. As the load was increased further from 55 N to 250 N, the operation crossed into the upper mixed film lubrication regime with  $S_p$  values of  $4.6 \times 10^{-8} \leq S_p \leq 1 \times 10^{-7}$ , where the COF decreased from 0.141 to 0.111. The curves obtained at 60 and 80 °C lie fully in the upper mixed film regime. At 100 and 120 °C, the curves cross from the upper mixed film regime to the lower mixed film regime at 150 N and 110 N respectively, with COF being 0.16 and 0.174 at the boundary. The effect of temperature on  $S_p$  is larger between 40 and 80 °C and smaller between 80 and 120 °C. This is due to the decreased further drop is viscosity and film thickness at higher temperatures due to the limited room for flexibility caused by the bigger, branched and more compact molecular structure of this base oil (Fernandez *et al*, 2014)..

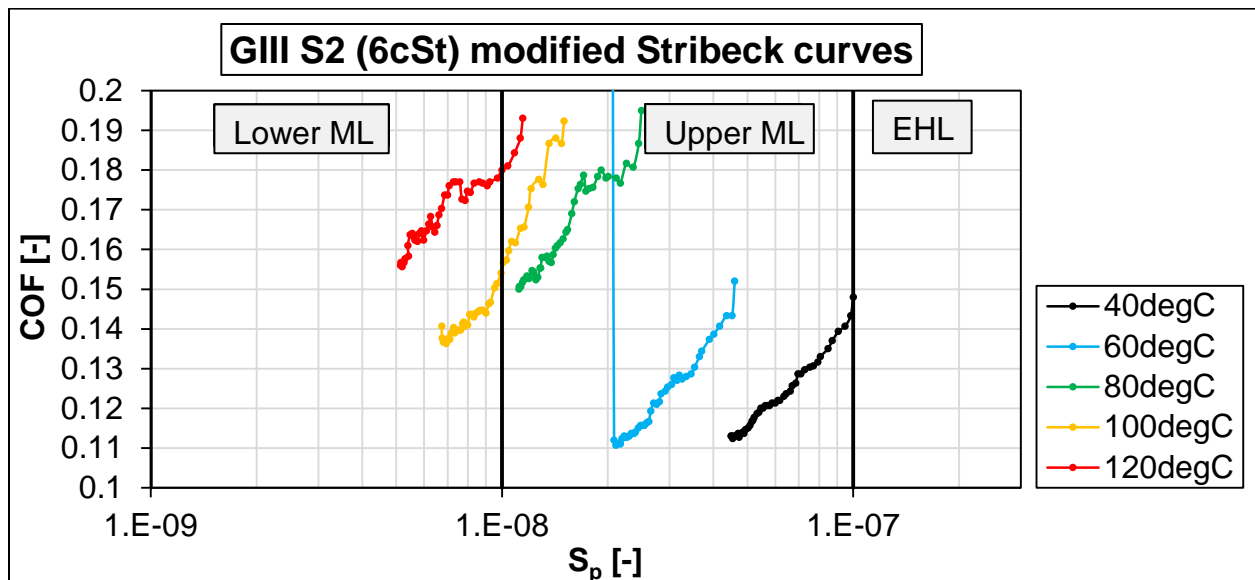


Figure 4.25: GIII S2 (6cSt) modified Stribeck curves.

Figure 4.25 shows the Stribeck curve obtained from the test done with the GIII S2 (6cSt) base oil. At 40 °C, the curve begins at the boundary between elastohydrodynamic

regime and mixed film regime at 50 N, and then proceeds down to the upper mixed film lubrication regime as the load was gradually increased up to 250 N. The 60 °C curve lies fully in the upper mixed film regime, showing a slightly wider change in COF compared to the 40 °C curve. However, the increase of temperature from 40 °C to 60 °C does not show a significant impact on the COF, the effect is more significant on the  $S_p$ . The 80 °C curves lies far above and slightly to the left the 40 °C and 60 °C curves, showing the large effect the change in temperature from 60 °C to 80 °C has on the COF and  $S_p$ . The 80 °C curve also lies in the upper mixed film regime. The 100 °C and 120 °C curves cross the boundary between the upper and lower mixed film regime, both beginning on the upper mixed regime as the load was increased from 50 N, with  $S_p$ 's of  $1.6 \times 10^{-8}$  and  $1.3 \times 10^{-8}$  respectively. The 100 °C curve crosses into the lower mixed regime at a load of 115 N with a COF of 0.154. The 120 °C curve crosses into the lower mixed regime at a load of 65 N with a COF of 0.18.

## Discussion

All the Stribeck curves show that the increase in temperature resulted in lower  $S_p$  values, which signified a change in lubricating regime from EHD to mixed mixed lubrication regime (upper and lower), as the load was gradually increased from 50 N to 250 N. It is clear that the regime transition is dependent on the film thickness formed by the base oil or how well the oil manages to keep the interacting surfaces apart from each other at each temperature. The film thickness formed by each base oil is a function of:

1. Dynamic viscosity: larger viscosity provides good separation by forming a thick lubricating film. Large  $S_p$  values result, as was seen with the GIII S1 (6cSt) and GIII S1 (6cSt) base oils.
2. Normal pressure (load): Normal pressures compress the film molecules at the contact points, and thus decreasing the film thickness which leads to lower  $S_p$  values. This was observed with all base oils under study. It is now clear that the piezoviscous effect does not prevent a decrease in molecular film thickness.

3. Temperature: high temperatures result in increases molecular flexibility and decreased rigidity (firmness).
4. Water: It was clear with the PAO, GI and GIII S2 base oils that the presence of dissolved water increased the COF friction. It may be true that water leads to low  $S_p$  values between 40 and 100 °C due to its lack of lubricating characteristics. However, The Stribeck curves do not indicate this effect because the oil film viscosities used for the  $S_p$  are not those measured in real time at the contact points. The absence of water (120 °C) allowed formation of a firm and stable lubricating films with an unaffected film thickness.

The impact of dissolved water on the  $S_p$  is not clearly visible with the rest of the base oils as only minute amounts of dissolved water are present (Zheng-bing *et al*, 2015). The mixed film lubrication regime dominated during the experiments, and a shift from mainly upper mixed film to lower mixed film at the temperature was increased from 40 °C to 120 °C and, where 80 °C appears to be the border temperature, as the load was increased. The gradual increase of the operating load from 50 N to 250 N has more influence on the gradients of the Stribeck curves, subject to the large decrease in the COF given by all the test oils, as the load was increased. The increasing load appears to have a smaller effect on the  $S_p$  with all seven test oils.

From these results, the effect of viscosity on the operating regime ( $S_p$ ) is clearly visible. Both the 6 cSt base oils (GIII S1 (6cSt) and GIII S2 (6cSt)) began their operation in the EHD regime (Where  $S_p \geq 1 \times 10^{-7}$ ) at 40 °C and proceeded into the mixed regime as the as applied load was gradually increased. Whereas the 4 cSt base oils only cover the mixed film lubrication regime. The GIII+ (4cSt) showed the most consistent and stable response to an increase in temperature and the gradual load increase. The Stribeck curves, as shown on Figure 4.20, have a similar shape and separated more evenly due to the increase in test temperatures. This is an indication of a good and consistent film forming ability subject to the consistent changes in  $S_p$  under all experimental conditions (Vengudusamy *et al*, 2014). Temperature had a significant impact on the COF and film forming ability of the PAO (4cSt) base oil.



#### 4.2.5 Modified Stribeck curves: Comparison of the base oils

Figure 4.26 to Figure 4.30 compare the Stribeck curves obtained from the friction tests at the five experimental temperatures. This is to observe the effect of the chemical make of the base oils on the COF and on  $S_p$ . Figure 4.26 compares the curves obtained at 40 °C, and figures 4.27, 4.28, 4.29 and 4.30 compare the curves obtained at 60, 80, 100 and 120 °C respectively. On each figure the COF (y-axis) is plotted against the modified Stribeck parameter (x-axis) which is on the log scale. As was done in the previous sections, the curves will be read from the right to the left, following the direction of an increasing load on the abscissa. On the title of each figure is the temperature at which the Stribeck curves were obtained the legend shows the colour of the Stribeck curve corresponding a specific base oils.

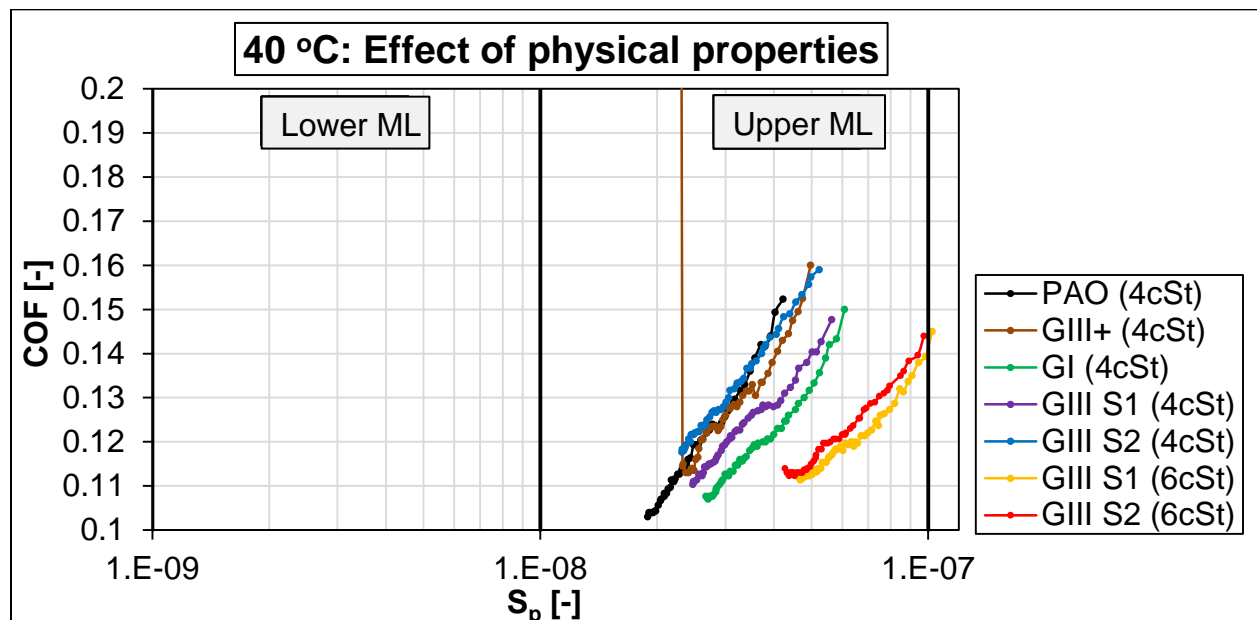


Figure 4.26: Comparison of base oil friction at 40 °C.

On Figure 4.26, it can be seen that the GIII S1 (6cSt) base oil lies on the further most right, followed by the GIII S2 (6cSt). As the load was gradually increased from 50 N to 250 N, the GIII S1 (6cSt) base oil operated in the elastohydrodynamic regime between 50 N and 55 N, COF values decreased from 0.143 to 0.141, and  $S_p$  between  $1.1 \times 10^{-7}$  and  $1 \times 10^{-7}$ , and then crossed into the upper mixed film regime between 55 N and 250 N

and  $S_p$  of  $1 \times 10^{-7}$  and  $4.6 \times 10^{-7}$ , and showed a COF decrement from 0.141 to 0.111. To the left of this curve is the GIII S2 (6cSt) curve which begins at the boundary between the hydrodynamic regime and the mixed film regime and end in the mixed film regime as the load was increased from 50 N to 250 N, with  $S_p$  of  $1 \times 10^{-7}$  and  $4.49 \times 10^{-8}$ . It is clear that between  $S_p$  of  $4.6 \times 10^{-8}$  and  $1 \times 10^{-7}$  these two curves lie very close together, giving very close COF values. These two base oils appear to be the least affected by the increasing load, subject to the shorter curves covering a smaller COF range compared to the 4cSt base oils. This could be because a large contribution to friction is the intermolecular shear stresses as compared to direct asperity contact.

To the left of these two curves is the solvent refined GI (4cSt) base oil curve, followed by the hydro-processed GIII S1 (4cSt) base oil curve. In the 4 cSt group of base oils, the GI (4cSt) Stribeck curve lied the further most to the right as the load was increased from 50 N to 250 N, giving values of  $S_p$  of  $6 \times 10^{-8}$  and  $2.6 \times 10^{-8}$  and COF of 0.150 and 0.107 respectively. This curve followed by the GIII S1 (4cSt) base oil curve with  $S_p$  of  $5.8 \times 10^{-8}$  and  $2.5 \times 10^{-8}$  and COF of 0.148 and 0.110 respectively.

Looking further to the left on Figure 4.26, there are three curves from the 4 cSt group of base oils; GIII+ (4cSt), GIII S2 (4cSt) and the PAO (4cSt) base oils curves which lie close to one another in the upper mixed film lubrication regime. As the load was increased from 50 N to 250 N, the GIII S2 (4cSt) curve starts at a  $S_p$  of  $5.2 \times 10^{-8}$  to  $2.4 \times 10^{-8}$  and COF of 0.148 to 0.110. At a  $S_p$  value of  $4.8 \times 10^{-8}$ , this curve crosses with the GIII+ (4cSt) curve which starts at  $S_p$  of  $5 \times 10^{-8}$  and 50 N to  $2.4 \times 10^{-8}$  and 235 N where a breakthrough occurs. Between  $S_p$  of  $4.8 \times 10^{-8}$  and  $2.4 \times 10^{-8}$  the GIII+ (4cSt) curve lies below the GIII S2 (4cSt) curve. The PAO (4cSt) curve starts at a  $S_p$  of  $4.2 \times 10^{-8}$  and  $1.9 \times 10^{-8}$ , at 50 N and 250 N. The PAO (4cSt) curve covers the lower most values of COF, 0.106 to 0.102, between  $S_p$  of  $2.1 \times 10^{-8}$  and  $1.9 \times 10^{-8}$ , and 220 N and 250 N.

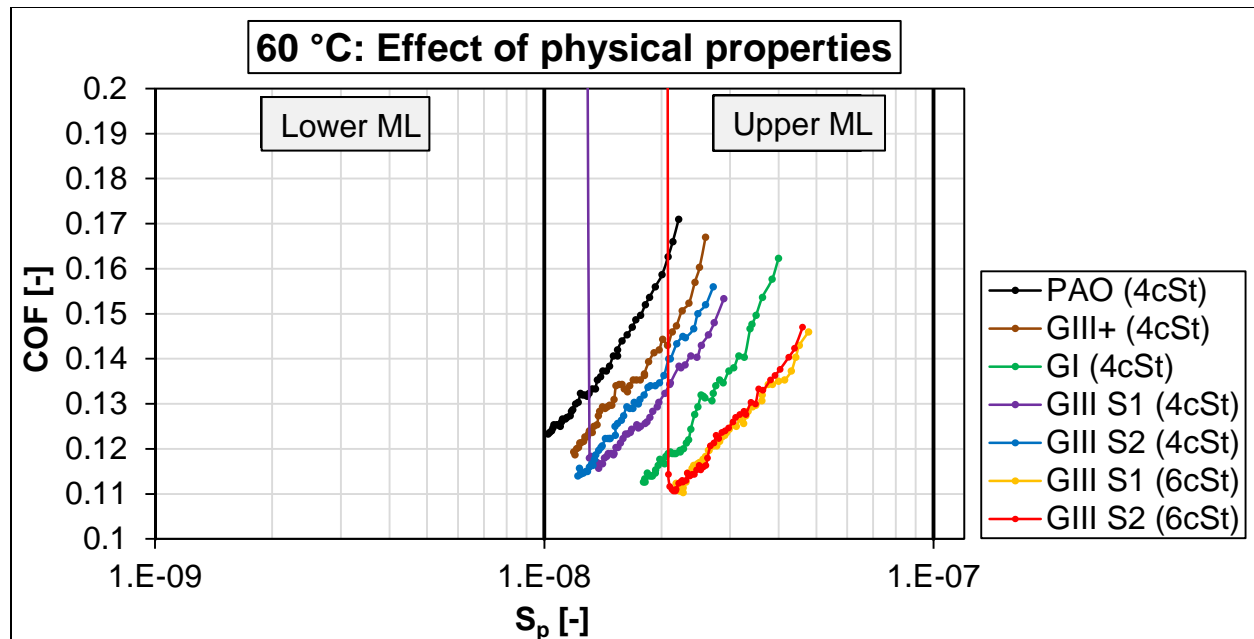


Figure 4.27: Comparison of base oil friction at 60 °C.

Figure 4.27 shows the Stribeck curves as obtained at 60 °C. It can be seen that all the curves on this figure lie in the upper mixed film lubrication regime, and the curves lie distinctly apart. From the further most right of the graph, two Stribeck curves (GIII S1 (6cSt) and GIII S2 (6cSt)) are observed which lie on top of one another, with close  $S_p$  values between  $4.8 \times 10^{-8}$  to  $2.1 \times 10^{-8}$ , and COF values between 0.148 to 0.110, as the load was gradually increased from 50 N to 250 N. The GIII S2 (6cSt) curve starts at a COF of 0.148 at 50 N, which decreases to the lowest COF value of 0.111 at 247 N where a sudden rise in the COF was observed. The GI (4cSt) Stribeck curve lies above the two 6cSt curves, followed by the GIII S1 (4cSt) curve which begins at a  $S_p$  value of  $3 \times 10^{-8}$  and COF of 0.153 at 50 N, and curves down to a final  $S_p$  value of  $1.5 \times 10^{-8}$  at 250 N where a sudden rise in COF was observed. Slightly above these curves lies the GIII S2 (4cSt) curve, followed by the GIII+ (4cSt) curve and lastly, the PAO (4cSt) curve starting a  $S_p$  of  $2.2 \times 10^{-8}$ , with an average COF of 0.171 at 50 N, and crossing to the lower mixed film regime as the load is increased, ending at  $S_p$  of  $1.05 \times 10^{-8}$  and a COF of 0.123 at 250 N respectively.

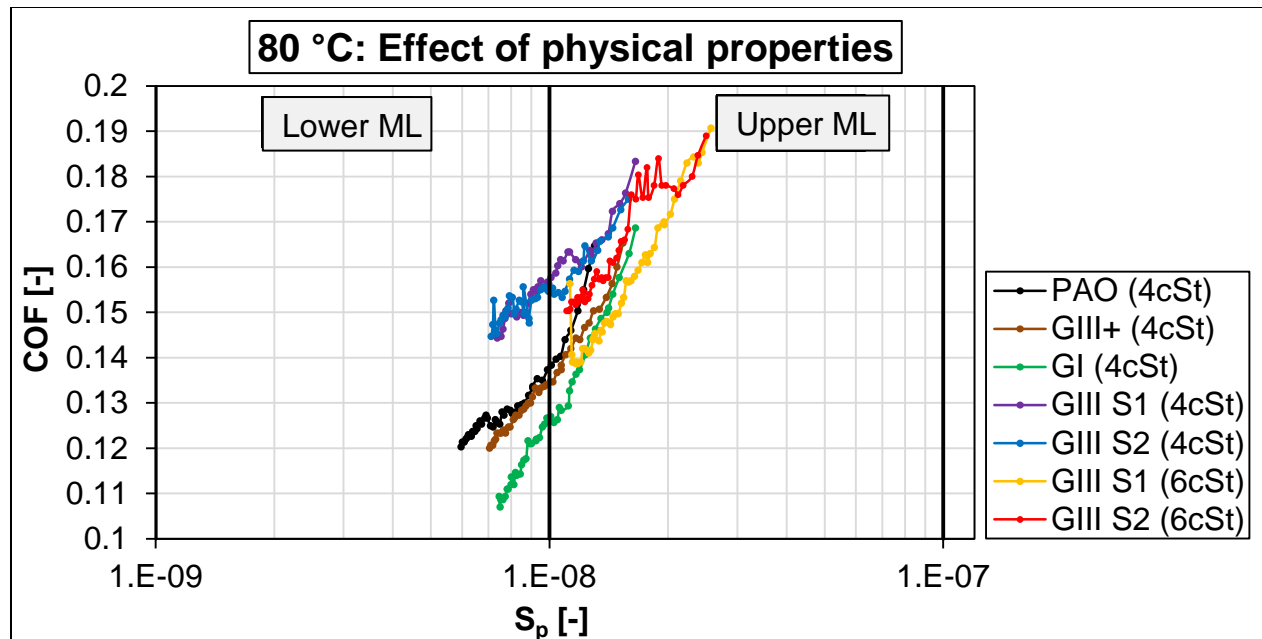


Figure 4.28: Comparison of base oil friction at 80 °C.

Figure 4.28 shows the Stribeck curves as obtained at 80 °C. Firstly, it can be seen that all the curves on this Figure 4.28 lie in the mixed film lubrication regime. It can be observed that in the range  $1 \times 10^{-8} \leq S_p \leq 2 \times 10^{-8}$ , the Stribeck curves lie close together, and outside this range, the curves lie further apart and a clear distinction between them can be made. At  $S_p \geq 2 \times 10^{-8}$ , lies the GIII S1 (6cSt) and GIII S2 (6cSt) Stribeck curves, which lie close to each other starting from a COF of 0.191 and 0.189 respectively. As the load was gradually increased the descended towards lower COF and  $S_p$  values, until at a  $S_p$  of  $2.2 \times 10^{-8}$  and COF of 0.175, where the curves separate and the GIII S1 (6cSt) curve continues below the GIII S2 (6cSt) with lower COF values up to a load of 248 N corresponding to a  $S_p$  of  $1.2 \times 10^{-8}$ . The GIII S2 (6cSt) curve proceeds above the GIII S1 (6cSt) curve with irregularities in the COF, showing an unstable film, between  $S_p$  range  $1.9 \times 10^{-8}$  to  $1.7 \times 10^{-8}$  (Vengudusamy *et al*, 2014). The GIII S2 (6cSt) curve proceeds rather downwards with decreasing COF values up to a  $S_p$  of  $1.2 \times 10^{-8}$ .

In the lower mixed film regime ( $1 \times 10^{-9} S_p \leq 1 \times 10^{-8}$ ), it can be observed that the GI (4cSt) curve lies below all the other curves from an  $S_p$  of  $1 \times 10^{-8}$  and COF of 0.126 to an  $S_p$  of  $7.5 \times 10^{-9}$  and COF of 0.105. Above this curve is the GIII+ (4cSt) and PAO (4cSt) curves

which lie close to one another, between  $7 \times 10^{-9} < S_p < 1 \times 10^{-8}$ , from where they separate, and the PAO (4cSt) proceeds to an  $S_p$  of  $6 \times 10^{-9}$  with a COF of 0.12. Above these curves are the GIII S1 (4cSt) and GIII S2 (4cSt) Stribeck curves which lie on top of each other from an  $S_p$  of  $1 \times 10^{-8}$  to an  $S_p$  of  $7.1 \times 10^{-9}$  and a COF of about 0.155 to a COF of 0.144 for both GIII S1 (4cSt) and GIII S2 (4cSt) respectively. Within this range of  $S_p$ 's, the GIII S2 (4cSt) curve shows a lot of irregularities in the COF, which mean that the base oil forms an unstable film between the oscillating ball and disc specimen (Vengudusamy *et al*, 2014).

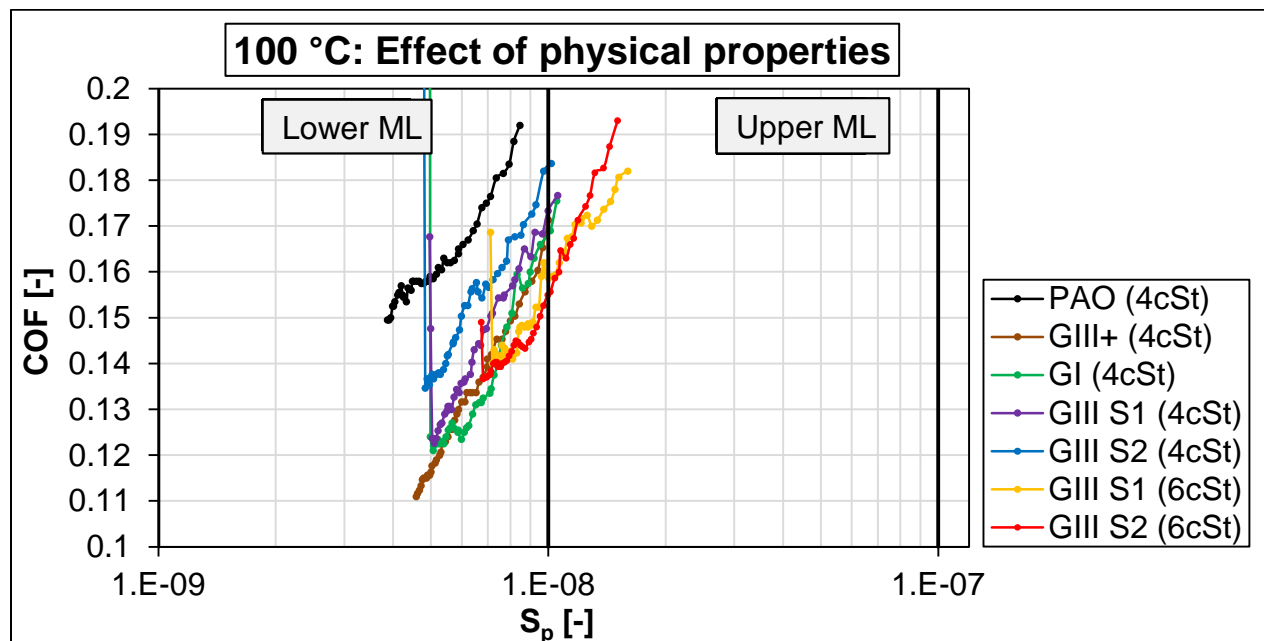


Figure 4.29: Comparison of base oil friction at 100 °C.

Figure 4.29 shows the Stribeck curves obtained at 100 °C. All the curves in Figure 4.29 lie in the mixed film lubrication regime covering both the upper and lower mixed film regimes. From the further most right of the figure, two Stribeck curves, GIII S1 (6cSt) and GIII S2 (6cSt), are observed which show a decreasing trend as the load was gradually increased from 50 N to 250 N, beginning at COF's of 0.193 and 0.182 and  $S_p$ 's of  $1.6 \times 10^{-8}$  and  $1.7 \times 10^{-8}$  at 50 N respectively. As the load was increased the GIII S2 (6cSt) curve lies above the GIII S1 (6cSt) curve, and crosses it at an  $S_p$  of

$1.3 \times 10^{-8}$  and COF of 0.17, and continues below it into the lower mixed film regime, and up to  $S_p$  of  $6.8 \times 10^{-9}$  where a sudden rise in COF from 0.136 to 0.149 is observed.

The GIII S1 (6cSt) curve also shows a sudden rise in the COF from 0.14 to 0.169 at an  $S_p$  of  $7.1 \times 10^{-9}$ . These two curves lie the further most to the right on the graph giving larger values of  $S_p$  per given load stage, as the load was increased from 50 N to 250 N. Above these two curves in the lower mixed regime lies four Stribeck curves namely GI (4cSt), GIII+ (4cSt), GIII S1 (4cSt) and the GIII S2 (4cSt). The GIII+ (4cSt) curves covers the lowest COF values of 0.120 to 0.111 in the range  $4.6 \times 10^{-9} < S_p < 5.3 \times 10^{-9}$ . The PAO (4cSt) lies above all the curves in Figure 4.29 and to the further most left, covering the highest COF values (0.192 to 0.15) in the range  $2.9 \times 10^{-9} < S_p < 8.4 \times 10^{-9}$ .

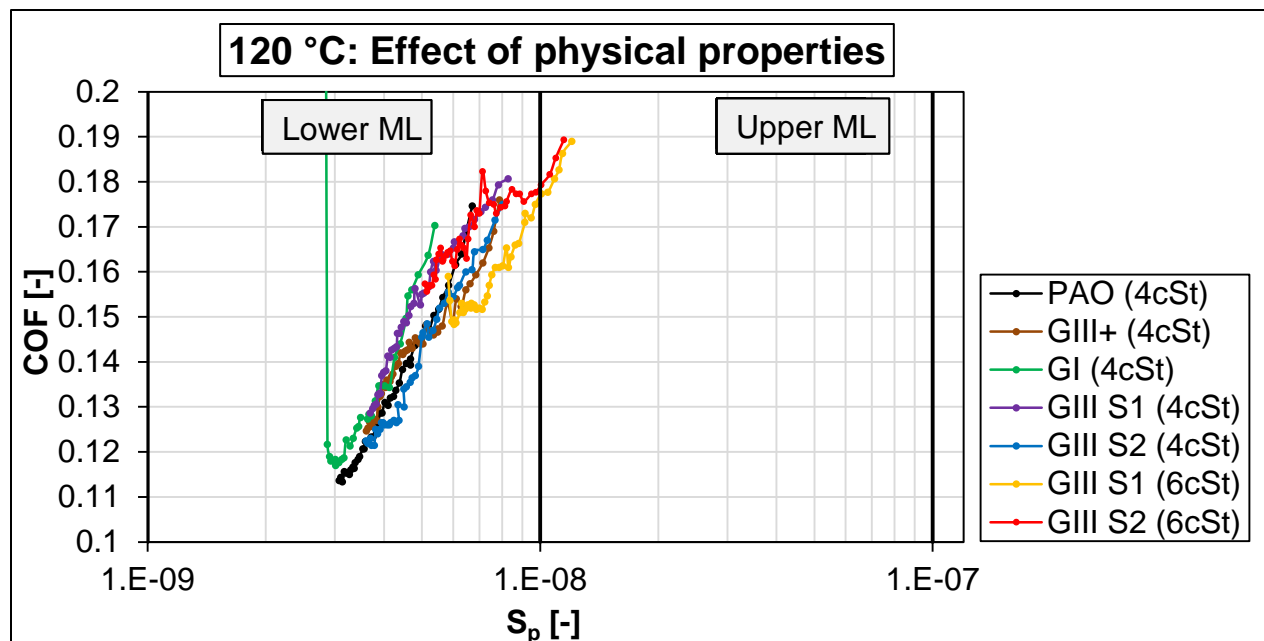


Figure 4.30: Comparison of base oil friction at 120 °C.

Figure 4.30 shows the Stribeck curves obtained at 120 °C. It can be seen that the Stribeck curves lie in the mixed film lubrication regime, and largely in the lower mixed film regime. In the upper mixed regime lies the GIII S1 (6cSt) and GIII S2 (6cSt) Stribeck curves, starting at  $S_p$  of  $1.20 \times 10^{-8}$  and  $1.15 \times 10^{-8}$  with both COF values of 0.189

respectively. The GIII S1 (6cSt) and GIII S2 (6cSt) curves cross into the lower mixed regime at a COF of 0.177 and 0.179. Beyond this point, the GIII S1 (6cSt) curve proceeds below the GIII S2 (6cSt) curve up to an  $S_p$  of  $5.8 \times 10^{-9}$ .

Nearing this point, the curve makes a dip with low COF of 0.148 and then rises to 0.159. The GIII S2 (6cSt) curves shows a decreasing trend in the lower mixed regime with a lot of irregularities in the COF. This curves stops at a  $S_p$  of  $5.3 \times 10^{-9}$  and a COF of 0.157. Looking deeper into the lower mixed regime, the GIII+ (4cSt) curve lies closely to the GIII S2 (4cSt) curve between  $8 \times 10^{-9}$  and  $5 \times 10^{-9}$  where they separate and the GIII S2 (4cSt) curve proceeds below the GIII+ (4cSt) curve up to an  $S_p$  of  $3.7 \times 10^{-9}$ . The PAO (4cSt) curve lies above the GIII+ (4cSt) and GIII S2 (4cSt) curves between the  $S_p$  range of  $6.7 \times 10^{-9}$  to  $5 \times 10^{-9}$  and lies in between these curves above the GIII S2 (4cSt) curve between  $S_p$ 's of  $5 \times 10^{-9}$  and  $3.1 \times 10^{-9}$ . Slightly to the left of this PAO (4cSt) curve is the GIII S1 (4cSt) Stribeck curve followed by the GI (4cSt) Stribeck curve lying in the  $S_p$  range of  $8.3 \times 10^{-9}$  to  $3.8 \times 10^{-9}$ , and  $S_p$  of  $5.4 \times 10^{-9}$  and  $2.8 \times 10^{-9}$  respectively.

### **Discussion:**

From the above results, the effect of viscosity on the operating regime ( $S_p$ ) and COF is clearly visible. Both the 6 cSt base oils (GIII S1 (6cSt) and GIII S2 (6cSt)) have consistently lied further to the left of the 4 (4cSt) base oils. At 40 and 60 °C, these two curves had the largest  $S_p$  values and the lowest values of COF at each load stage within the load range 50 N to 250 N. This indicated the good film forming ability of the two 6 cSt base oils (Vengudusamy *et al*, 2014). The vertical gap between the curves shows the differences in friction reduction of the base oils at a given test load, with the curve lying further below having better friction reduction capability with smaller COF (Fernandez *et al*, 2014).

At 40 and 60 °C, the base oil properties (i.e.,  $\alpha$  and viscosity) played a significant role in the observed friction behaviours, especially with the higher viscosity base oils (GIII S1 (6cSt) and GIII S2 (6cSt)). This is observed from the high  $S_p$  values and the

operation in the EHD film regime as indicated above. The application of normal forces increases the internal shear stresses in these base oils, and therefore increases the internal friction due to the molecular restrictions caused (Mia *et al*, 2010, Batchelor & Stachowiak, 2006:115 – 117 and Szeri, 2005: 120). However, the decreasing trends of the COF with the increasing load do not show any indication of this. This shows that even at 40 and 60 °C the external friction mechanisms dominate the friction process. Meaning, the surface changes on the ball and disc interfaces (asperity deformation and increase in contact area) have the larger contribution to the COF observed as they result in a decreased shear force at each load stage.

In mixed lubrication, the friction coefficient for a given average sliding speed is lower for the lubricant with higher viscosity because it is more difficult to squeeze higher viscosity lubricants out of the contact zone. Longer squeezing times lead to shorter times for asperities to come in contact and to smaller friction coefficients. Therefore, the higher viscosity base oils (i.e., GIII S1 (6cSt) and GIII S2 (6cSt)) are better able to support hydrodynamic sliding at relatively high loads (Tu and Fort, 2004).

Thicker films were generated by the GIII S1 (6cSt) and GIII S2 (6cSt) between the oscillating ball and the disc, keeping the two surfaces separated. These base oils were found to have the largest  $\alpha$  and viscosity values at 40 and 60 °C. Since the thickness of the generated oil film is “normally” proportional to the viscosity under a constant load, it can be seen that the more viscous oils give better lubricity, since the generated films would be thicker and a better separation of the two surfaces in contact would be achieved in practical situations (Stachowiak & Batchelor, 2014: 317). These observations are confirm the finding reported by Hamrock *et al* (2004: 7), that under constant operating conditions, the common features of hard EHL are that the local elastic deformation of the solids enable the generation of liquid films which are consistent and the asperity interaction can be prevented significantly. Therefore, the frictional resistance to motion is due to lubricant shearing (Hamrock *et al*, 2004: 7).



Proceeding to at 80, 100 and 120 °C, the GIII S1 (6cSt) and GIII S2 (6cSt) curves proceeded to cover the largest  $S_p$  values, however, with increased COF values. This is a result of now regular asperity contacts in the mixed film regime and internal friction within the oils with the increasing load (Dresel & Mang, 2017: 17). As the temperature increases, a drop in viscosity is observed which makes close asperity contact possible (Stachowiak & Batchelor, 2014: 317). The increase in temperature weakens the intermolecular forces and allows more mobility of the molecules. However, since these base oils were found to have higher VI's, the loss in viscosity is not very large. Therefore, due to the larger viscosities (larger molecular sizes) of the oils, frictional resistance within the molecules under the application of stress is higher, and therefore gives increased friction (Dresel & Mang, 2017: 20).

Looking at the base oils from the two suppliers (S1 and S2), at 40 °C the base oils from supplier 1 (GIII S1 (4cSt) and GIII S1 (6cSt)) gave lower values of COF and higher  $S_p$  values between 50 N and 250 N, compared to those from supplier 2 (GIII S2 (4cSt) and GIII S2 (6cSt)) respectively. At 60, 80 and 100 °C, the GIII S1 (4cSt) base oil continues to give lower COF and higher  $S_p$  values than its counterpart GIII S2 (4cSt) base oil, while the GIII S1 (6cSt) and GIII S2 (6cSt) base oils showed very similar behaviour. At 120 °C, the GIII S2 (4cSt) base oil continues to give lower COF and higher  $S_p$  values than its counterpart GIII S1 (4cSt) base oil, while the GIII S1 (6cSt) outperformed the GIII S2 (6cSt) base oil. The base oils are in the same API base oil group, hence the slightly similar behavioural and physical characteristics, but at certain operating conditions performance can be optimized by choosing one supplier over another.

Looking at the GI (4cSt) base oil at 40, 60 and 80 °C, where the curves lied to the left most of the 4 cSt group of oils and slightly below, giving higher  $S_p$  values and slightly lower COF values. Since the tests are conducted with an increasing load, the GI (4cSt) base oil owes its better friction and film forming behaviour to the higher  $\alpha$  and viscosity values it has at these temperatures, compared to the remainder of the 4 cSt base oils. The higher  $\alpha$  symbolizes better film formation and better molecular thickening under the continuous application of stress (pressure) (Brandao *et al*, 2012 & Fernandez *et al*,

2014). At 100 and 120 °C, the GI (4cSt) base oil gave lower  $S_p$  values and the highest COF values compared to the other 4 cSt base oils. Due to its lower VI, its rheological properties (viscosity and  $\alpha$ ) lowered as the temperature was increased. Due to the lower viscosity and  $\alpha$  at this temperature, poor film thickness formation resulted under the increasing applied load, and frequent close asperity contact resulted contributing to the increased friction observed (Brandao *et al*, 2012).

Looking at the PAO (4cSt) and GIII+ (4cSt) base oils, it can be observed that 40, 60, 80 and 100 °C the PAO (4cSt) lacks behind in terms of film forming capabilities. The GIII+ (4cSt) base oil curves lied to the right of the PAO (4cSt) curves giving higher  $S_p$  values at these temperatures, and also gave lower COF values at 60 and 100 °C. Clearly the GIII+ (4cSt) base oil had better friction reduction and film formation at these conditions. At 80 and 120 °C, the Stribeck curves of the two base oils lied closer together, with the PAO (4cSt) base oils assuming lower COF values at moderate to high loads (150 – 250 N). These two base oils continuously assumes lower COF values and higher  $S_p$  values compared to the GIII S1 (4cSt) and GIII S2 (4cSt) base oils, except at 40 and 60 °C. At 40 °C the GIII S1 (4cSt) base oil showed better film formation and both GIII S1 (4cSt) and GIII S2 (4cSt) showed better friction reduction and film formation at 60 °C.

The results obtained from this part of the work confirm a finding which is focused on the response of the COF with respect to the Stribeck parameter ( $S_p$ ). Many researchers have constructed Stribeck curves to study the friction behaviour of base oils by varying the operating speed, which is one way to vary the  $S_p$ . Many of the conducted studies have confirmed that the ability of a lubricating oil to be the most effective and leading to the most stable coefficient of friction, with respect to velocity, is attributed to the higher content of contaminants and the presence of sulphur. The performance of lubricating oil was also found to improve with the chain length and the presence of double bonds under low to moderate temperature conditions (Maru *et al*, 2013).

The results obtained confirm that this is true even when the Stribeck parameter is varied with respect in terms of the applied normal load. The GI (4cSt) base oil is the least saturated, and has the highest sulphur and contaminant content in the group of base oils selected for this study. It has proved to have better friction reduction and film formation compared to its API group 3 4 cSt counterparts at 40, 60 and 80 °C. Only at 100 and 120 °C does the GIII+ (4cSt) and PAO (4cSt) outperform the GI (4cSt) base oil. Again, this confirms the poor high temperature performance of group 1 base oils as was stipulated by Dresel & Mang (2017: 55). The increases in average COF values of the base oil with the increasing temperature in the mixed film regime are due to the fact that the film thickness is small and more direct asperity contact is frequent, and becomes more significant with the increase in temperature and load. The increasing load is carried by both the base oil molecules and the surface asperities (Dresel & Mang, 2017: 13).

### 4.3 Film thickness

At this point, it became important to look at the film thicknesses generated by the base oils under study, to confirm the conclusions made on film forming abilities of the lubricants from the Stribeck curves as obtained in the previous section. In the theory section, it was discussed in section 2.4.4 that the film thickness frequently used to predict EHL film thickness is the minimum film thickness equation (Equation 2.41). It was observed that for the all of the friction tests conducted in this investigation, the resulting friction was in the mixed/partial lubrication regime. In this regime, regular direct asperity contact between the deformed asperities is inevitable, especially with the increasing load at high operating temperatures where the oil viscosities are low (Stachowiak & Batchelor, 2014: 338).

The friction tests in this study were conducted with an increasing load, and with the increasing load, the contact area increases and consequently the number of asperity contacts increases (Stachowiak & Batchelor, 2014: 335). Due to this, the minimum film thickness ( $h_0$ ) has no meaning in the mixed to near boundary film lubrication, since the minimum film thickness will assume a value of zero where direct asperity contact becomes prevalent between the interacting surfaces.

According to Hamrock *et al* (2004: 498), the interacting surfaces in are separated by a film of almost constant thickness that is well represented by a central value over much of the Hertzian contact zone. Secondly, Stachowiak & Batchelor (2014: 338) reports that in mixed EHL the asperity pressure is nearly uniform in the central part of the lubricant film in mixed or partial lubrication. Therefore, based on the above, the film thicknesses in this investigation were thus approximated using the central film thickness equation given below by (Hamrock *et al*, 2004: 498 and Stachowiak & Batchelor, 2014: 324).

$$h_c = 2.69U^{0.67}G^{0.53}W^{-0.067}(1 - e^{-0.68k}) \quad (4.1)$$

With:

$$W = \frac{F_N}{E^*R_x^2} \quad (2.42)$$

$$U = \frac{u_{avg}\eta_o}{E^*R_x} \quad (2.43)$$

$$G = \alpha E^* \quad (2.44)$$

$$u_{avg} = u_b = 0.2 \text{ m.s}^{-1}$$

Where  $h_c$  is the central film thickness in nm,  $U$  is the speed parameter,  $G$  is the materials parameter,  $W$  is the load parameter and  $k$  is the ellipticity parameter with a value of 1 for a ball-on-disc configuration (Hamrock *et al*, 2004: 7).

Figure 4.8 contains five subfigures which show the film thickness generated by each of the base oils under investigation as the test load was gradually increased from 50 N to 250 N, at the five experimental temperatures i.e., 40, 60, 80, 100 and 120 °C. Each subfigure shows the film thickness as predicted at a specific temperature which is given on the top left corner of each subfigure. On each subfigure, the applied normal load ( $F_N$ ) is given on the x-axis and central film thickness ( $h_c$ ) on the y-axis which is given in nanometers (nm). The legend for all the subfigures is shown at the bottom of Figure 4.31. From Figure 4.31, it can be seen that the central film thickness decreased progressively with the gradual load increase for all base oils, at all the test temperatures.

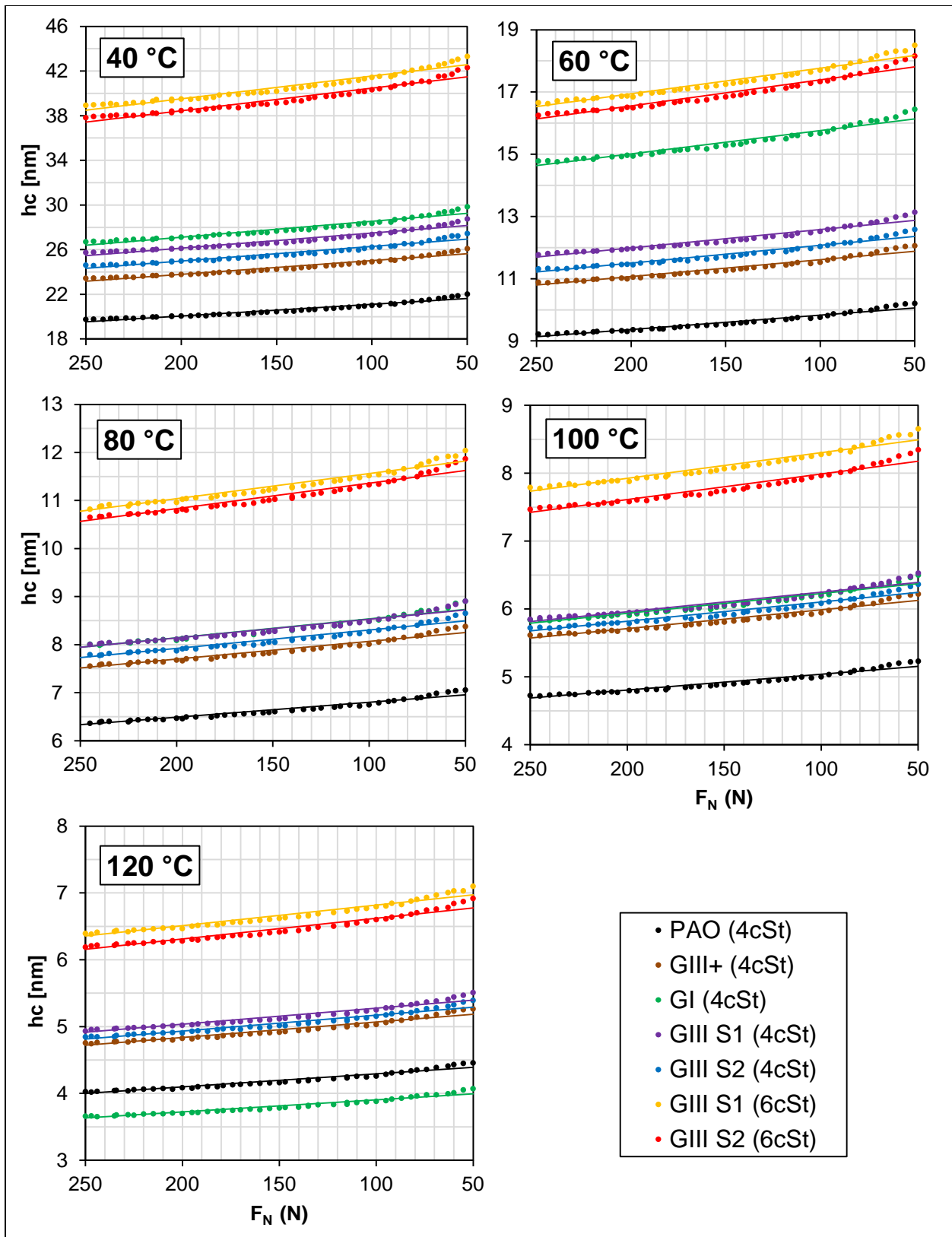


Figure 4.31: Central film thickness against applied load.

Looking at the 40 °C subfigure, the curve lying the further most above with the largest values of  $h_c$  is the GIII S1 (6cSt) curve, starting at  $h_c$  of 43 nm and ranging down to 39 nm as the load increased from 50 N to 250 N respectively. Immediately below this curve lies the GIII S2 (6cSt) curve with  $h_c$  starting at 42 nm to 37 nm.

Below the two 6 cSt curves, lies the GI (4cSt) curve, followed by the GIII S1 (4cSt) and GIII S2 (4cSt) curves respectively. These three curves lie close to each other with  $h_c$  values ranging from 29 nm to 27 nm, 28 nm to 25 nm and 27 nm to 24 nm for GI (4cSt), GIII S1 (4cSt) and GIII S2 (4cSt) curves respectively. Below these three curves lies the GIII+ (4cSt) curve with  $h_c$  range 26 nm to 24 nm, followed by the PAO (4cSt) curve with  $h_c$  range 22 nm to 19 nm.

At 60 °C, the curves lie in a similar order to those at 40 °C, with the GIII S1 (6cSt) curve lying above all other curves, followed by the GIII S2 (6cSt) and the GI (4cSt) curve respectively. The calculated  $h_c$  values are ranging between 18.5 nm to 16.5 nm, 18 nm to 16.1 nm, and 16.4 nm to 14.7 nm for the GIII S1 (6cSt), GIII S2 (6cSt) and the GI (4cSt) base oils respectively. Looking further below the GIII S1 (4cSt), GIII S2 (4cSt) and GIII+ (4cSt) curves lie closely below each other, followed by the PAO (4cSt) curve which has a  $h_c$  range 10.2 nm to 9.2 nm as the normal applied load was increased from 50 N to 250 N. At 80 °C, the two curves, GIII S1 (6cSt) and GIII S2 (6cSt), lie further above the 4 cSt curves with  $h_c$  ranging from 12.1 nm to 10.7 nm and 11.8 nm to 10.5 nm respectively in the applied load range 50 N to 250 N. Below these two curves lies the GI (4cSt) and GIII S1 (4cSt) curves which are sitting on top of each other with  $h_c$  range 8.9 nm to 8 nm. Further below lie the GIII S2 (4cSt) and GIII+ (4cSt) curves followed by the PAO (4cSt) curve with  $h_c$  range of 7 nm to 6.3 nm in the applied load range 50 N to 250 N.

At 100 °C, the two curves, GIII S1 (6cSt) and GIII S2 (6cSt), lie above with  $h_c$  ranging from 8.6 nm to 7.8 nm and 8.3 nm to 7.5 nm respectively, in the applied load range 50 N to 250 N. The gap on the y-axes between these two curves is noticeably larger than that at 40, 60 and 80 °C between 50 N to 250 N. Below these two curves lies the

GIII S1 (4cSt) curve which starts at  $h_c$  of 6.5 nm to 5.8 nm, followed closely by the GI (4cSt) and GIII S2 (4cSt) curves with  $h_c$  range 6.4 nm to 5.8 nm and 6.3 nm to 5.7 nm. Closely below these two curves lie the GIII+ (4cSt) curves followed by the PAO (4cSt) curve which lie further below with  $h_c$  range of 6.2 nm to 5.6 nm and 5.2 nm to 4.7 nm respectively, in the applied load range 50 N to 250 N. Once again, the visible effect of the absence of water.

At 120 °C, once again the two curves, GIII S1 (6cSt) and GIII S2 (6cSt), lie further above the 4 cSt curves with  $h_c$  ranging from 7.1 nm to 6.4 nm and 6.9 nm to 6.2 nm respectively in the load range 50 N to 250 N. The gap on the y-axes between these two curves is again noticeably larger than that at 40, 60 and 80 °C. Below these two curves lies the GIII S1 (4cSt) curve which starts at  $h_c$  of 5.5 nm to 4.9 nm, followed by the GIII S2 (4cSt) curve with  $h_c$  range 5.4 nm to 4.8 nm. Closely below these two curves lie the GIII+ (4cSt) curves followed by the PAO (4cSt) curve which lie further below with  $h_c$  range of 5.3 nm to 4.7 nm and 4.5 nm to 4 nm, respectively in the load range 50 N to 250 N. The GI (4cSt) curve lies further below, with the smallest film thickness values in the 50 N to 250 N load range. The curve starts at 4.1 nm and decreases to 3.6 nm.

## **Discussion**

From Figure 4.31, it is clear that the operating load has a direct effect on the film thickness, as formed by each of the base oils under investigation. As the load was gradually increased from 50 N to 250 N, a decrease in the film thicknesses was observed for all base oils under investigation and at the five different test temperatures. Also observable in Figure 4.31, the two higher viscosity base oils GIII S1 (6cSt) and GIII S2 (6cSt), seem to be consistently forming larger films between the oscillating steel ball and disc, with the GIII S1 (6cSt) giving larger films than the GIII S2 (6cSt), which decrease progressively as the test load increased from 50 N to 250 N. This is observed at all the test temperature i.e 40, 60, 80, 100 and 120 °C. This observed behaviour is characteristic to the high pressure-viscosity coefficient ( $\alpha$ ) values of the GIII S1 (6cSt) base oil at the test temperatures as discussed in the previous sections. According to



Vengudusamy *et al*, (2014), a higher  $\alpha$  depicts higher film formation capability under hydrodynamic loads, and therefore, a lubricating oil with a higher  $\alpha$  will generate a thicker film under hydrodynamic pressure. This explains the consistently larger values of  $h_c$  obtained for the GIII S1 (6cSt) and GIII S1 (6cSt) base oils.

The gaps between the curves as observed in the subfigures in Figure 4.31 are observed to correspond with the differences in the  $\alpha$  values of the base oils at each test temperatures as given in Figure 4.18. This means that the differences in the calculated  $\alpha$  for the seven different base oils at a specific temperature are a direct indication of the differences in their film thicknesses. At 40 °C, the calculated  $\alpha$  values in decreasing order are GIII S1 (6cSt) > GIII S2 (6cSt) > GI (4cSt) > GIII S1 (4cSt) > GIII S2 (6cSt) > GIII+ (4cSt) > PAO (4cSt). This behaviour corresponds to that of the film thickness curves as shown in Figure 4.31 for 40 °C. This order remains at 60 °C, however, the  $\alpha$  values are lower at this temperature and as a result the obtained film thickness values are lower. Also noted, the decrement in  $\alpha$  of the GI (4cSt) from 40 °C to 60 °C is the smallest, and resulting in film thickness values slightly closer to those obtained for the GIII S1 (6cSt) and the GIII S2 (6cSt) base oils at 60 °C in the applied load range 50 N to 250 N. At 80 °C the above mentioned order changes, where the  $\alpha$  value (12.8 GPa<sup>-1</sup>) of the GI (4cSt) base oil is the same as that of the GIII S1 (4cSt) and hence the film thickness curves of the two base oils lie closely on top of each other in Figure 4.18 at 80 °C.

It is importance to highlight the observations made from the film thickness calculated from the GIII+ (4cSt) and PAO (4cSt) base oil curves. From Figure 4.18, the  $\alpha$  values of the GIII+ (4cSt) base oil are consistently larger than those of the PAO (4cSt) base oil at the five experimental temperatures, and therefore, it is expected of the GIII+ (4cSt) base oil to generate thicker films at the given test conditions. The GIII+ (4cSt) base oil has consistently resulted in larger  $h_c$  values, which decreased gradually with the gradual load increase, compared to those of the PAO (4cSt) base oil at all the test temperatures. This is shown in Figure 4.31 by the film thickness curves of the GIII+ (4cSt) base oil which lie above those of the PAO (4cSt) base oil at 40, 60, 80, 100 and 120 °C.

## 5. Conclusions

Seven base oils were used to lubricate a steel–steel reciprocating sliding contact at a temperature range of 40 – 120 °C, under a gradually increasing normal load (range: 50-250N). The results show that the interface interaction between lubricating oil and frictional materials plays an important role in friction reduction. Therefore, the optimization of the lubrication condition highly depends on the physical and chemical properties of the solid–liquid interface. This study has shown that a severely hydrocracked GIII+ base oil has better film forming capability compared to the to the PAO base oil between, owing to its high saturation level giving higher polarity. At high temperatures (100 and 120 °C) the overall film forming capabilities of the GIII+ and PAO base oils under study proved to be similar, shown by the  $S_p$  ranges covered at each test temperature between the 50 and 250 N loads. Therefore, the GIII+ can is a potential alternative for the PAO base oil.

The effect of load should always be considered when selecting base oil properties. High polarity (high affinity) alone is not enough to conclude good lubricity. The type of adsorption mechanism followed influences the strength of the bonding the metal surface and the presence of water disturbs/minimizes the adsorption. The highly saturated (PAO and GIII+) base oils tend to follow the C-H bonding via the H atom which creates a weak bond (van der Waals), while the less saturated base oils (GI and GIII), due to the higher presence of double bonds in their molecules form stronger covalent bonds through electron-pair sharing with the steel surfaces via the C-C atoms where a double bond is broken. The highly saturated (PAO and GIII+) base oils have showed good thermal stability and less reactivity compared to the less saturated base oils (GI and GIII). This property gives the highly saturated (PAO and GIII+) base oils the ability to operate at high temperatures (100 and 120 °C) and handle high normal loads (250 N). Whereas the less saturated base oils (GI and GIII) experience bond dissociations which result in film breakage mostly observed between 80 and 120 °C.

Further notable general observations are summarized as follows:

## **5.1 Physical Properties**

### **5.1.1 Effects of temperature on viscosity**

It was found that:

1. A temperature increase from 40 °C to 120 °C resulted in a decrease in the dynamic viscosities of all seven base oils under study.
2. The base oil which showed the largest viscosity decrement was the GI (4cSt).
3. The base oil which showed the lowest viscosity decrement was the GIII+ (4cSt).

### **5.1.2 Viscosity Index**

It was found that:

1. The GIII+ (4cSt) base oil had the highest VI with a value of 131.
2. The base oil with the lowest VI was the GI (4cSt) base oil.
3. The VI behaviour arranged in decreasing order and represented by the base oils is: GIII+ (4cSt) > GIII S2 (4cSt) > PAO (4cSt) and GIII S1 (4cSt) > GIII S1 (6cSt) > GIII S2 (6cSt) > GI (4cSt).

### **5.1.2 Effects of pressure on viscosity**

It was found that:

1. For all base oils under study, the piezoviscous effect decreased as the temperature was increased from 40 °C to 120 °C.
2. The piezoviscous effect is higher for base oils with low saturation levels.
3. The piezoviscous effect is lower for highly saturated base oils (PAO (4cSt) and GIII+ (4cSt)).
4. The GIII+ (4cSt) and PAO (4cSt) base oils showed very similar piezoviscous behaviour with an increasing pressure.

### **5.1.3 Pressure viscosity coefficient**

It was found that:

1. The pressure-viscosity coefficient decreased with increasing temperature.
2. The base oils with the highest pressure-viscosity coefficient at all experimental conditions were the GIII S1 (6cSt) and GIII S2 (6cSt) base oils.
3. The base oil with the lowest pressure-viscosity coefficient at all experimental conditions was the PAO (4cSt) base oil.

### **5.2 Effects of load on COF**

It was found that:

1. A gradual load increase resulted in a decrease of the coefficients of friction.
2. At particular temperatures, the gradual load increase resulted in a sudden rise in the COF. This was observed with the GIII+ (4cSt) base oil at 40 °C and 230 N. This was also observed with the GI (4cSt) at 100 °C and 240N and at 120 N and 176 N.

### **5.3 Effects of temperature on COF**

It was found that:

1. With increasing temperature the COF increased.
2. The base oils base supplier 1 (GIII S1 (4cSt) and GIII S1 (6cSt)) showed similar friction behaviour with increasing temperature and a gradual load increase. The increase in temperature from 60 to 80 °C had the largest effect in their COF values, whereas, the effect is minimal between the range: 40 to 60 °C, and 80 to 120 °C.
3. Base oils from supplier 2 showed differing friction behaviour. The GIII S2 (4cSt) showed a consistent increase in the COF with an increase in temperature

between 40 and 100 °C, and a slight decrease from 100 to 120 °C. A slightly similar behaviour was observed with the GIII S2 (6cSt), except for the large effect of temperature on the COF between 80 and 100 °C which resulted in a significant increase in the COF values per given load stage.

4. With the PAO (4cSt), temperature had a more significant effect on the COF when the temperature was increased from 80 to 100 and then 120 °C. The COF values increased when the temperature was increased from 80 to 100 °C, and decreased between 100 and 120 °C. A temperature from 40 °C to 60 and then 80 °C showed a lesser effect on the COF showed by the COF curves which sat closely together. The significant differences in the COF curves are in their gradients, signifying the larger effect from the increasing load on the COF at these temperatures. Similar behaviour was observed with the GI (4cSt) base oil.
5. With the GIII+ (4cSt) base oil, the increase in temperature resulted in a consistent increase in the COF per given load stage.

#### **5.4 Stribeck curves**

It was found that:

1. The friction behaviour of the base oils was controlled largely by the surface roughness, rheological properties of lubricant (i.e., viscosity) and the pressure–viscosity coefficient ( $\alpha$ ) and the contact conditions (i.e., temperature and the gradually increasing contact pressure).
2. The friction coefficient had a strong dependency on operating temperature, sliding load and base oil type.
3. The friction of the seven base oils was predominantly in the mixed film regime at all the experimental conditions. Only 40 °C, did the GIII S1 (6cSt) and GIII S2 (6cSt) cross into the EHD film regime at low loads (50 – 55 N).
4. The external friction mechanisms dominated the friction behaviour observed with all the base oils, even in the EHD regime where the physical properties of the

base oils play a huge role, and internal friction is significant with the increasing normal load.

5. Stribeck curves which make use of the modified Stribeck parameter are a convenient way to assess and compare lubrication behaviour of different base oils under the same operating conditions.
6. For two given base oils, the pressure-viscosity ( $\alpha$ ) coefficient can be used to predict the  $S_p$ 's (film forming behaviour) of base oils. For a specific base oil, the response of alpha to temperature gives a direct indication of the oils ability to operate under given  $S_p$  range.
7. For nonconformal steel surfaces of similar roughness, viscosity has a predominant effect on the film forming ( $S_p$ ) characteristics of the seven base oils at 40 and 60 °C.
8. The GIII+ (4cSt) base oil gave larger  $S_p$  values per load stage, in the mixed film regime, than the PAO (4cSt) base oil at the five test temperatures, under a gradually increasing load.
9. The PAO (4cSt) base oil gave lower COF values than the GIII+ (4cSt) base oil in the mixed film regime at 80 and 120 °C, between 200 and 250 N.
10. Base oils with lower  $\alpha$  values gave lower coefficient of friction values in mixed film lubrication at 80, 100 and 120 °C, per given load stage. The PAO (4cSt) base oil had the lowest  $\alpha$  values and gave the lowest COF values at 100 °C, between 200 to 250 N, in mixed film lubrication.

## 5.5 Film thickness

It was found that:

1. The pressure-viscosity ( $\alpha$ ) coefficient can be used to predict the film forming behaviour of base oils. For a specific base oil, the response of alpha to temperature gives a direct indication of the oils ability for form a lubricating film at a particular temperature.
2. The base oils with higher values of  $\alpha$  gave larger film thickness values.

3. The GIII+ (4cSt) base oil continuously gave higher central film thickness values in the mixed film regime, than the PAO (4cSt) base oil at the five test temperatures, under the gradually increasing load.
4. The GIII S1 (6cSt) and GIII S2 (6cSt) base oils had higher central film thickness values than the 4 (cSt) base oils at all experimental conditions.
5. The film thickness models do not predict film failure (breakthrough) or sudden rise in COF, as was observed on the Stribeck curves of the base oils. These models only give an indication of film formation behaviour of a lubricant under specific operating conditions.

## 6. Recommendations

1. It is recommended that friction experiments be conducted under a constant operating load, for a longer period and at the chosen temperatures, to further study the friction mechanisms categorized by the irregularities observed on the COF curves, especially with the 6 cSt base oils at high temperatures, and the exact mechanisms of the sudden film breakdowns observed in this investigation. This form of work will also allow surface analyses on the test specimen.
2. It is recommended that a GIII+ (6cSt) and PAO (6cSt) base oils be added on the sample matrix for further investigations. This is to investigate the effect of a higher viscosity of a highly saturated base oil on the coefficient of friction for these three base oils, compared to the already investigated GIII S1 (6cSt) and GIII S1 (6cSt) base oils, and to establish if there is a common benefit to tribological performance with an increased viscosity amongst the base oil.



## 7. References

1. ASTM D2270 (1993) "Standard Practice for Calculating Viscosity Index from Kinematic Viscosity at 40 and 100°C"
2. ASTM D7042 (2011) "Standard Test Method for Dynamic Viscosity and Density of Liquids by Stabinger Viscometer (and the Calculation of Kinematic Viscosity).
3. ASTM D7421 (2011) "Standard Test Method for Determining Extreme Pressure Properties of Lubricating Oils Using High-Frequency, Linear-Oscillation (SRV) Test Machine".
4. Anton Paar (2011) *Instruction manual: SVM 3000/G2*, Stabinger viscometer, Anton Paar GmbH, Austria.
5. Barus, C (1893) "Isothermals, Isopiestic, and Isometrics Relative to Viscosity" *American Journal of Science*, 45(83), 87-96.
6. Benadé, H (2014) *Evaluating the repeatability of friction and wear testing on a lubricant with dispersed hexagonal boron nitride nanoparticles*, MEng Dissertation, Dept Chem Eng, University of Pretoria.
7. Blau, PJ (2009) *Friction Science and Technology: from Concepts to Applications*, 2<sup>nd</sup> edition, CRC Press LLC, New York.
8. Brown, ST (2015) "Base Oil Groups: Manufacture, Properties and Performance", *Tribology & Lubrication Technology*, 4(15), 33 – 35.
9. Baker, L, Carey, JT, Gleeson, JW and Wu, MM (2007a) "Lubricant oil compositions containing GTL base stock(s) and/or base oil(s) and having improved resistance to the loss of viscosity and weight and a method for improving the resistance to loss of viscosity and weight of GTL base stock(s) and/or base oil(s) lubricant oil formulations", US Patent 11,637,342, assigned to ExxonMobil Research and Engineering Company, United States of America.
10. Bhushan, B (2013) *Introduction to Tribology*, 2<sup>nd</sup> edition, John Wiley & Sons Ltd, New York.
11. Bhushan, B (2001) *Modern Tribology Handbook*, Volume 1, CRC Press LLC, New York.

12. Brandao, JA, Meheux, M, Ville, F, Seabra, JHO and Castro, J (2012) “Comparative overview of five gear oils in mixed and boundary film lubrication” *Tribology International*, 47(12), 50 – 61.
13. Cai, Z, Zhou, Y, and Qu, J (2015) “Effect of oil temperature on tribological behaviour of a lubricated steel – steel contact” *Wear*, 332 – 333(15), 1158 – 1163.
14. Couseau, T, Bjorling, M, Graca, B, Campos, A, Seabra, J and Larsson, R (2012) “Film thickness in a ball-on-disc contact lubricated with greases, bleed oils and base oils” *Tribology International*, 53(12), 53 – 60.
15. Cooper, JR and Le Fevre, EJ (1969) *Thermophysical properties of water substances (Students tables in SI units)*, 1<sup>st</sup> edition, Elsevier, Butterworth-Heinemann.
16. Crittenden, B and Thomas, WJ (1998) *Adsorption Technology and Design*, 1<sup>st</sup> edition, Elsevier, Butterworth-Heinemann.
17. Dresel, W and Mang T (2017) *Lubricants and Lubrication*, 3<sup>rd</sup> edition, WILEY-VCH GmbH, Weinheim.
18. Donaghy, C, Calvert, RB and Oldfield, AS (2013a) “Automotive lubricant composition”, US Patent 13,472,021, assigned to Croda International PLC, GB and Uniqema Americas LLC, United States of America.
19. Dowson, D and Higginson, GR (1966) *Elastohydrodynamic lubrication: The fundamentals of roller and gear lubrication*, Pergamon, Oxford.
20. Evonik (2017) “Viscosity index” <http://oil-additives.evonik.com/product/oil-additives/resources/viscosity-index-en.html> [2017, December 13].
21. Fernandez, CMCG, Marques, PMT, Martins, RC and Seabra, JHO (2015) “Film thickness and traction curves of wind turbine gear oils” *Tribology International*, 86(15), 1 – 9.
22. Fernandez, J, Paredes, V, Gacino, FM, Comunas, MJP and Pensado, AS (2014) “Pressure-viscosity behaviour and film thickness in elastohydrodynamic regime of lubrication of ionic liquids and other base oils” *Lubrication Science*, 26(14), 449 – 462.
23. Fogler, HS (2006) *Elements of chemical reaction engineering*, 4<sup>th</sup> edition, Prentice Hall, United States of America.

24. Guo, J, Yang, Y, Zhang, D, Wu, W, Yang, Z and He, L (2018) "A general model for predicting apparent viscosity of crude oil or emulsion in laminar pipeline at high pressures" *Journal of Petroleum Science and Engineering*, 160(18), 12 – 23.
25. Gold, PW, Schmidt, A, Dicke, H, Loos, J and Assmann, C (2001) "Viscosity-Pressure-Temperature Behaviour of Mineral and Synthetic Oils" *Journal of Synthetic Lubrication*, 18(1), 51 – 79.
26. Hamrock, BJ, Schmid, SR and Jacobson, BO (2004) *Fundamental of Liquid Film Lubrication*, 2<sup>nd</sup> edition, Marcel Dekker, Inc., New York.
27. HSU, S, Ying, C and Zhao, F (2014) "The nature of friction: A critical assessment" *Friction*, 2(1), 1 – 26.
28. Ichiro, M (2017) "Molecular Science of Lubricant Additives" *Applied sciences*, 7(17), 445 – 478.
29. Johnson, M (2009) "Industrial liquid contaminants and their effect" *Tribology and lubrication technology*, 65(9), 26 – 31.
30. Kipp, DO (2010) Metal material data sheets, MatWeb – Division of Automatic Creation, Inc., Online, Knovel.
31. Langenhoven, J (2014) *The effects of humidity and soluble water content on the lubricity testing of a N-Hexadecane and palmitic acid test liquids*, MEng Dissertation, Dept Chem Eng, University of Pretoria.
32. Ma, L and Luo, J (2016) "Thin film lubrication in the past 20 years" *Friction*, 4(4), 280 – 302.
33. Maru, MM, Trommer, RM, Almeida, FA, Silva, RF and Achete, CA (2013) "Assessment of the lubricant behaviour of biodiesel fuels using Stribeck curves" *Fuel Processing Technology*, 116(13), 130 – 134.
34. Marusic-Paloka, E and Pazanin, I (2013) "A note on the pipe flow with a pressure-dependent viscosity" *Journal of Non-Newtonian Liquid Mechanics*, 197(13), 5 – 10.
35. Meirong, C, Qiangliang, Y, Feng, Z and Weimin, L (2017) "Physicochemistry aspects on frictional surfaces" *Friction*, 5(4), 361 – 382.
36. Mia, S, Mizukami, S, Fukuda, R, Morita, S and Ohno, N (2010) "High-pressure behaviour and tribological properties of wind turbine gear oil" *Journal of Mechanical Science and Technology*, 24 (10). 111 – 114.

37. Nilsson, A, Pettersson, L.G.M and Norskov, J.K (2008) *Chemical bonding at surfaces and interfaces*, 1<sup>st</sup> edition, Elsevier B.V., Netherlands.
38. Pawlak, Z (2003) *Tribochemistry of lubricating oils*, 1<sup>st</sup> edition, Elsevier B.V., Netherlands.
39. Ultrasonic cleaners made in China (2017) “Jeken ultrasonic cleaner limited”, <http://www.ultrasoniccleaners.en.made-in-china.com> [2017, November 28].
40. Roelands, CJA (1966) *Correlational Aspects of the Viscosity-Temperature-Pressure Relationship of Lubricating Oils*. Druk, VR.B, Groingen, Netherlands.
41. The Rotronic Humidity Handbook (2005) “Rotronic Instrument Corporation” [www.rotronic-usa.com](http://www.rotronic-usa.com), [12/2005].
42. Sander, DE, Allmaier, H, Pribsch, HH, Reich, FM, Witt, M, Fullenbach, T, Skiadas, A, Brouwer, L and Schwarze, H (2015) “Impact of high pressure and shear thinning on journal bearing friction” *Tribology International*, 81(15), 29 – 37.
43. Suh, NP, Mohsen M, Howard PS (1993) “Control of Friction” *Wear*, 173(93), 151 – 158.
44. Spikes, H (2018) “Stress-augmented thermal activation: Tribology feels the force” *Friction*, 6(1),1 – 31.
45. Stachowiak, GW and Batchelor, AW (2014) *Engineering Tribology*, 4th edition, Butterworth Heinemann, United States of America.
46. Szeri, AZ (2005) *Liquid film lubrication theory and design*, 1<sup>st</sup> edition, Cambridge University press, United Kingdom.
47. Tu, CF and Fort, T (2004) “A study of fiber–capstan friction. 1. Stribeck curves” *Tribology International*, 37(4), 701–710.
48. Van Drogen, M (2009) *The Transition To Adhesive Wear of Lubricated Concentrated Contacts*, PhD Thesis, University of Twente.
49. Vengudusamy, B, Grafl, A, Novotny-Farkaz, F and Schofmann, W (2014) “Influence of temperature on the friction performance of gear oils in rolling–sliding and pure sliding contacts” *Lubrication Science*, 26(14), 229 – 249.
50. Wheeler, G (2016) “Shortage Seen for High-VI Base Oils”, [http://pubs.lubesngreases.com/lubereport-asia/3\\_25/trends/-10608-1.html](http://pubs.lubesngreases.com/lubereport-asia/3_25/trends/-10608-1.html) [2016, June 21].

51. Yaws, C and Yadav, U (2012) "How temperature affects H<sub>2</sub>O solubility in cycloalkanes" *Oil and gas journal*, 110(12), 96 – 100
52. Yaws, CL (2010) "Calculating H<sub>2</sub>O solubility, Henry's law constant for cycloalkanes in crude" *Oil and gas journal*, 108(10), 54 – 57.
53. Zhang, XA, Zhao, Y, Ma, K and Wang, Q (2016) "Friction behaviour and wear protection ability of selected base lubricants" *Friction*, 4(1), 72 – 83.

## Appendices

### Appendix A

#### Viscosity determination at 120 °C.

Viscosities were determined using the Stabinger Viscometer SVM 3000 at five temperatures: 25, 40, 60, 80 and 100 °C. Using the data points obtained, a function was fitted which best correlates the measured viscosities ( $R^2 \approx 1$ ) with corresponding temperatures. For GIII+ (4cSt) below:

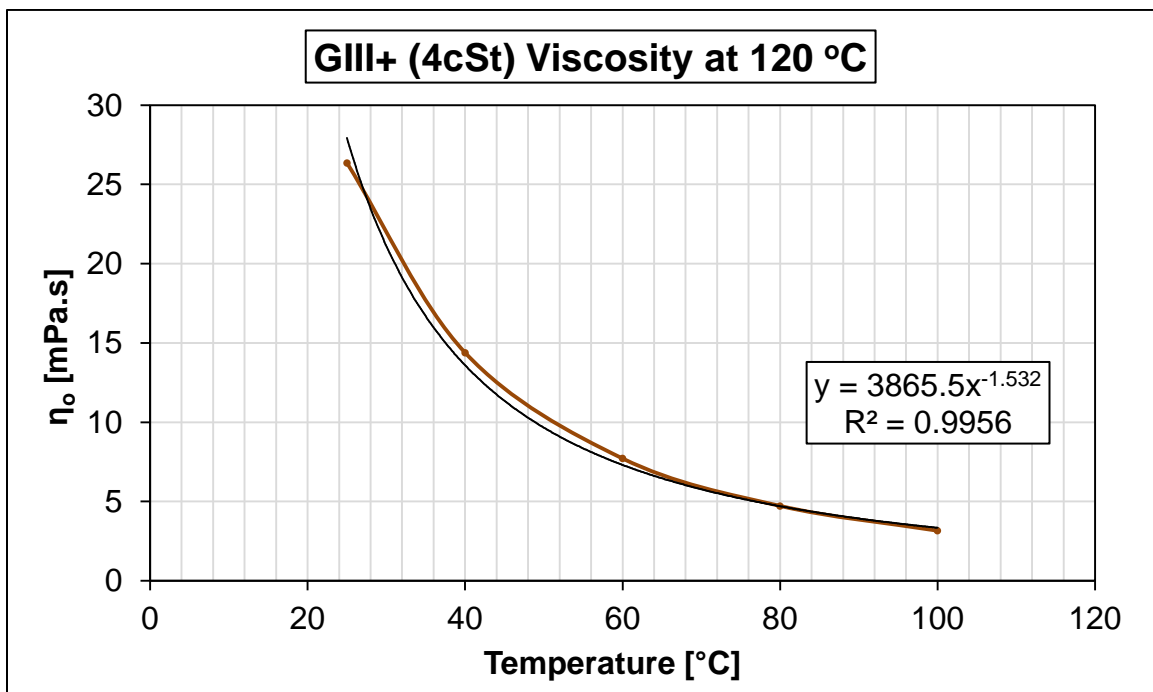


Figure 5.1: Viscosity determination at 120 °C.

The power function above gave a good correlation ( $R^2 = 0.9961$ ). This function was then used to estimate the dynamic viscosity at 120 °C which was found to be 2.52 mPa.s.

## Appendix B

### Hertzian Pressure calculation

The procedure followed to estimate the hertzian pressure in this study is as follows.

The normal applied loads (50 to 250 N) were substituted in equation Equation 2.7, shown below, which resulted in the maximum hertzian pressure  $P_0$  values at for each load stage.

$$P_0 = \frac{3F_N}{2\pi a^2} \quad (2.7)$$

The contact area radius ( $a$ ) was obtained from equation 2.2. For a steel ball of radius ( $R_b$ ) 10 mm:

$$a = \left[ \frac{3F_N R_x}{4E^*} \right]^{\frac{1}{3}} \quad (2.2)$$

$E^*$  is the contact modulus defined by:

$$\frac{1}{E^*} = \frac{1-\nu_b^2}{E_b} + \frac{1-\nu_d^2}{E_d} \quad (2.3)$$

And  $R_x$ , the reduced radius of curvature, is related to those of the individual components by the relation:

$$\frac{1}{R_x} = \frac{1}{R_b} + \frac{1}{R_d} \quad (2.4)$$

$\nu_b$  and  $\nu_d$  are poisson ratio for the steel ball and disc, whose values were 0.3, adopted from Table 2.1.  $E_b$  and  $E_d$  are the elastic moduli for the steel ball and disc respectively. Their values were 210 Gpa.  $R_b$  and  $R_d$  are the radii of the steel ball and disc, and their values were 0.01 m and 0.024 m respectively.

## Appendix C

### Piezoviscous effect results

Table 5.1 below shows the percentage viscosity increments for the seven base oils, which were as a result of the gradually increasing applied load at a given experimental temperature.

Table 5.1: % Increase in viscosity with pressure

Temperature (°C)	Viscosity increase (%) x10 <sup>3</sup>						
	GI (4cSt)	GIII S1 (4cSt)	GIII S1 (6cSt)	GIII S2 (4cSt)	GIII S2 (6cSt)	PAO (4cSt)	GIII+ (4cSt)
40	152.04	156.97	124.03	156.00	165.87	132.86	135.35
60	127.66	132.52	104.03	132.52	139.38	115.49	109.11
80	101.07	104.81	93.37	104.81	113.39	92.01	90.05
100	78.52	78.96	62.24	81.35	82.18	67.99	67.99
120	59.00	57.49	46.75	57.49	61.21	51.67	49.64

## Appendix D

### Standard deviation from COF raw data

In this appendix, the graphs showing the standard deviation from COF raw data are presented. At each test temperature, three friction tests were done and the standard deviation from the average COF values at each temperature was calculated using the corresponding three sets of data obtained.



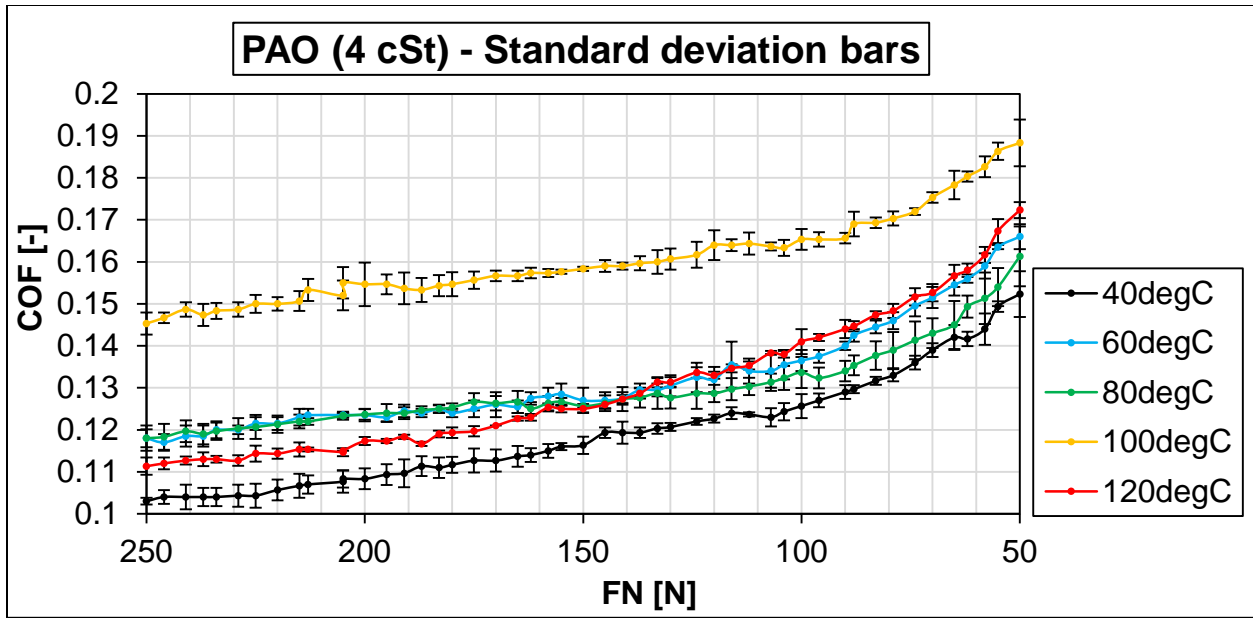


Figure 5.2: PAO (4cSt): Standard deviation from COF average values.

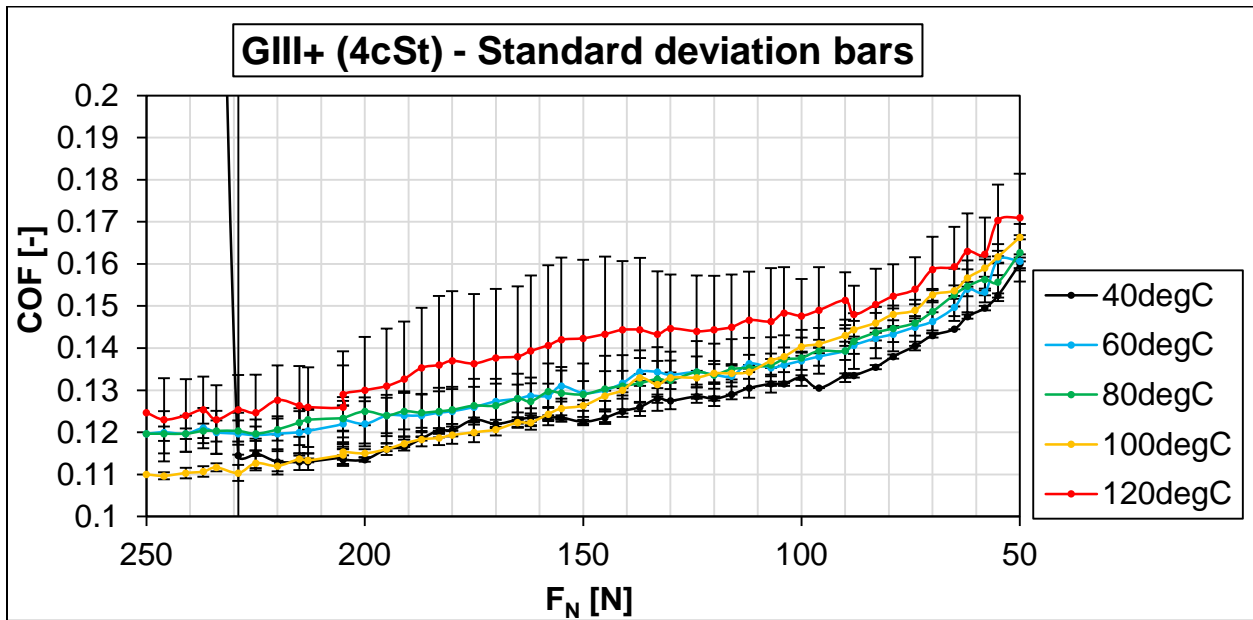


Figure 5.3: GIII+ (4cSt): Standard deviation from COF average values.

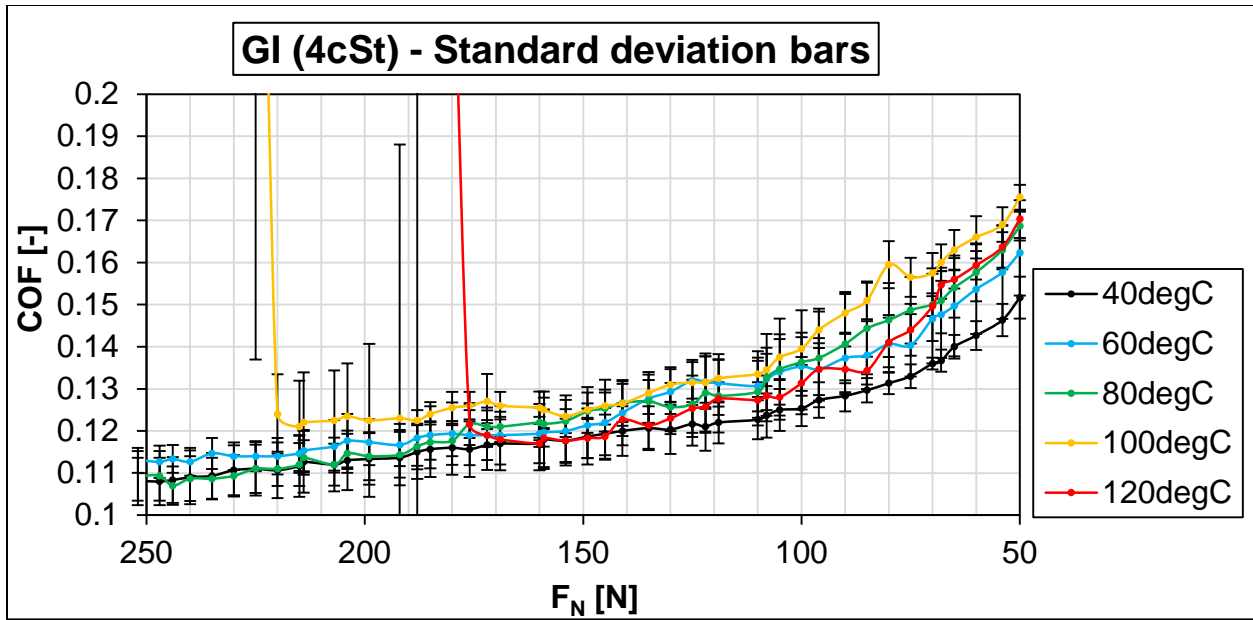


Figure 5.4: GI (4cSt): Standard deviation from COF average values.

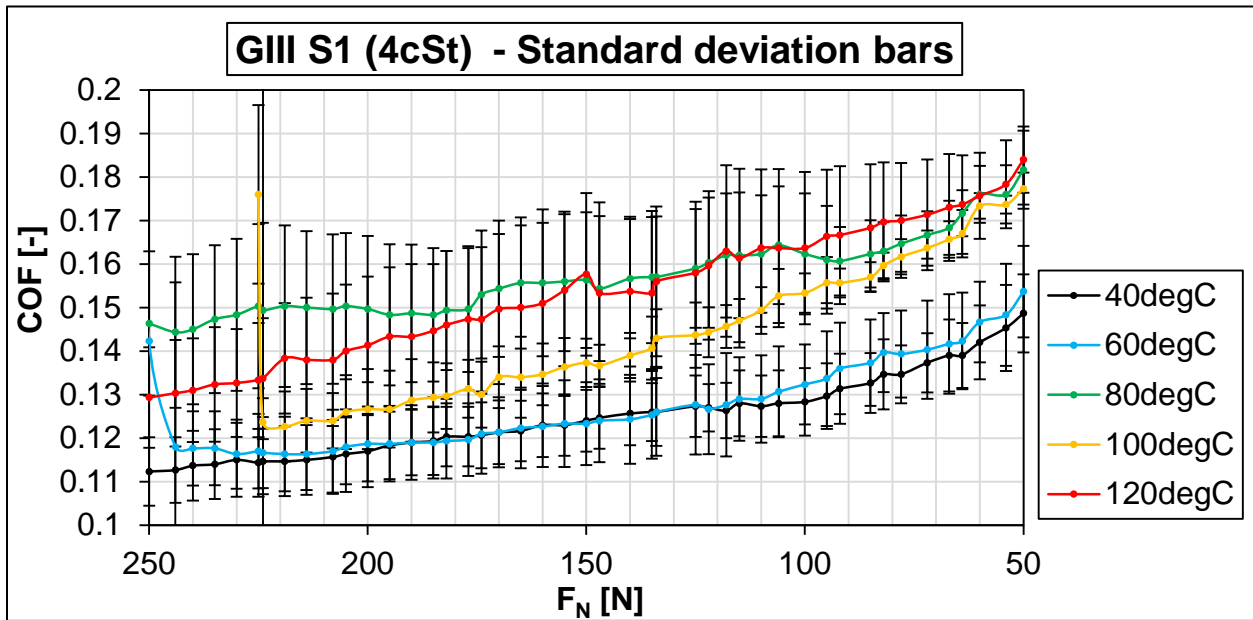


Figure 5.5: GIII S1 (4cSt): Standard deviation from COF average values.

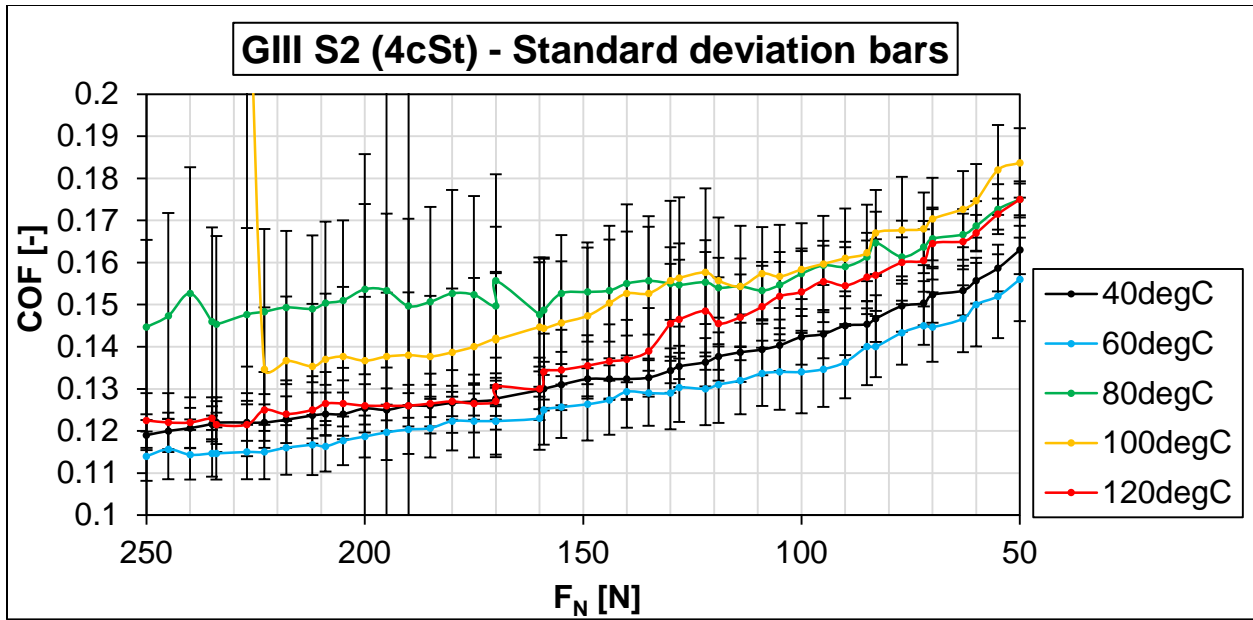


Figure 5.6: GIII S2 (4cSt): Standard deviation from COF average values.

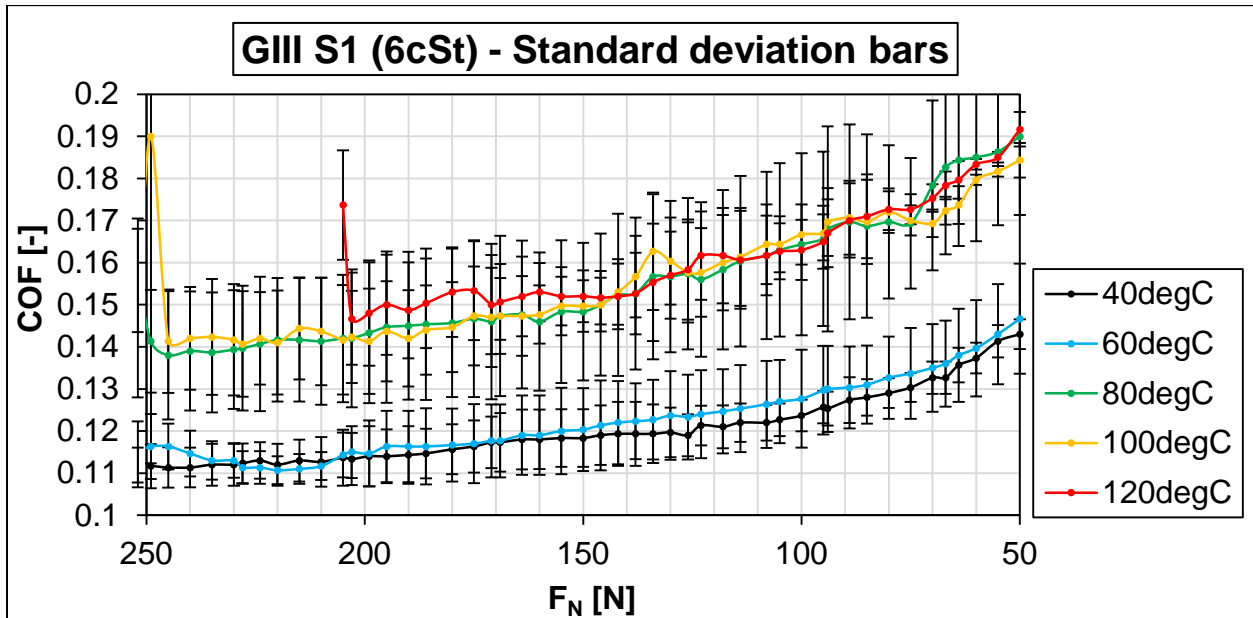


Figure 5.7: GIII S1 (6cSt): Standard deviation from COF average values.

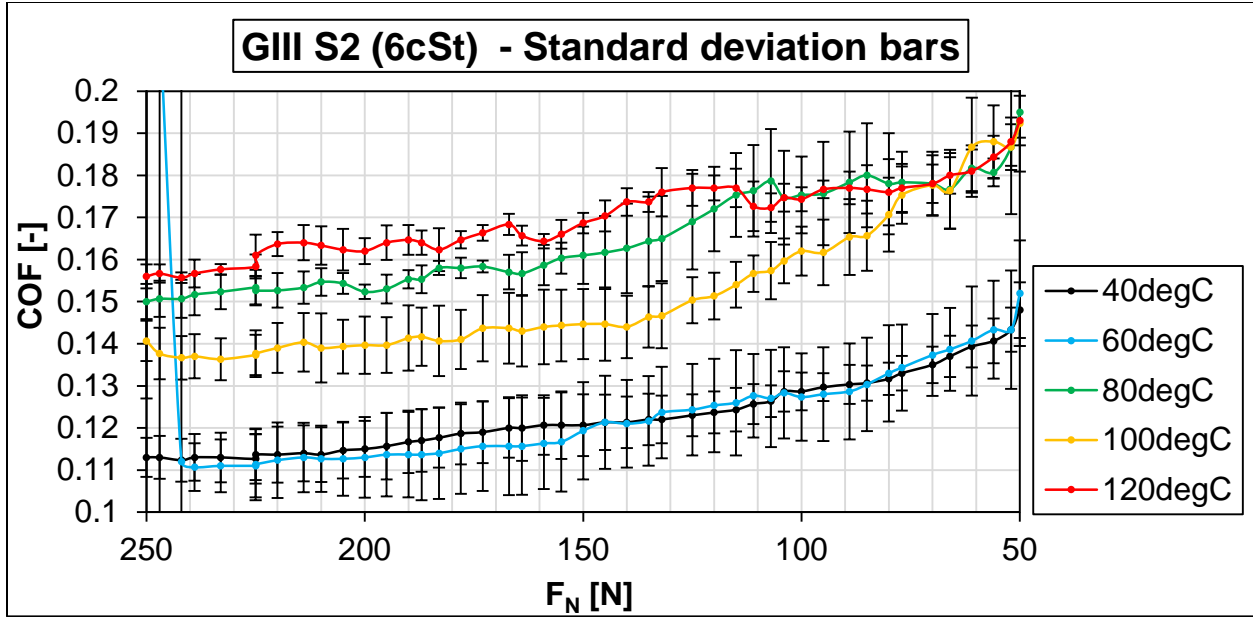


Figure 5.8: GIII S2 (6cSt): Standard deviation from COF average values.

## Appendix E

### Central film thickness calculation

The central thickness formula is given below. This formula was used to estimate the film thicknesses in the section 3 according to the following procedure:

$$h_c = 2.69U^{0.67}G^{0.53}W^{-0.067}(1 - e^{-0.68k}) \quad (4.1)$$

With: 
$$W = \frac{F_N}{E^*R_x^2} \quad (1.42)$$

$$U = \frac{u_{avg}\eta_o}{E^*R_x} \quad (1.43)$$

$$G = \alpha E^* \quad (1.44)$$

$$u_{avg} = u_b = 0.2 \text{ m} \cdot \text{s}^{-1}$$

Where  $h_c$  is the central film thickness in nm,  $U$  is the speed parameter,  $G$  is the materials parameter,  $W$  is the load parameter and  $k$  is the ellipticity parameter with a value of 1 for a ball-on-disc configuration (Hamrock *et al*, 2004: 7).  $E^*$  is the contact modulus defined by:

$$\frac{1}{E^*} = \frac{1-\nu_b^2}{E_b} + \frac{1-\nu_d^2}{E_d} \quad (2.3)$$

And  $R_x$ , the reduced radius of curvature, is related to those of the individual components by the relation:

$$\frac{1}{R_x} = \frac{1}{R_b} + \frac{1}{R_d} \quad (2.4)$$

The applied load ( $F_N$ ) range was: 50 N to 250 N at each of the five experimental temperatures. This was substituted in the load parameter ( $W$ ) equation.  $\nu_b$  and  $\nu_d$  are poisson ratio for the steel ball and disc, whose values were 0.3, adopted from Table 2.1.  $E_b$  and  $E_d$  are the elastic moduli for the steel ball and disc respectively. Their values were 210 Gpa.  $R_b$  and  $R_d$  are the radii of the steel ball and disc, and their values were 0.01 m and 0.024 m respectively. The pressure-viscosity was given by:

$$\alpha = s\eta_k^t \quad (3.2)$$

Where  $\eta_k$  is the kinematic viscosity at a constant temperature.  $s$  and  $t$  are parameters given in the Table 4.3 for paraffinic mineral oils and polyalphaolefin, chosen as recommended by Gold *et al* (2001).

Table 4.3: Parameters for pressure-viscosity calculation

Base oil type	s	t
Paraffinic mineral	0.99	0.14
Polyalphaolefin	0.73	0.13

## Appendix F

### Humidity control

In Figure 5.9, a schematic of the humidity control setup for the SRV test chamber is shown. The humidity control setup was to maintain a constant water content in the base oil samples by manually controlling the humidity of the atmosphere in the SRV test chamber.

The operation of this setup is as follows:

Compressed air is passed through a moisture trap and a particulate filter, to ensure that the supplied air is clean. The stream of air then goes into two columns (i.e., distilled water column and drying column containing inert silica [ $\text{SiO}_2$ ] granules) at 120 – 160 kPa. Air was bubbled through a column of distilled water when it was desired to increase the water content, or passed through a column of  $\text{SiO}_2$  drying particles when a low water content is desired. By controlling the ratio of air flow between the columns the required water content can be achieved and maintained. The conditioned air stream was then passed through the SRV test chamber, and exited through an outlet of similar size to the inlet. The SRV chamber contains a humidity sensor and indicator, which was used to continuously monitor the relative humidity in the test chamber during the friction tests.

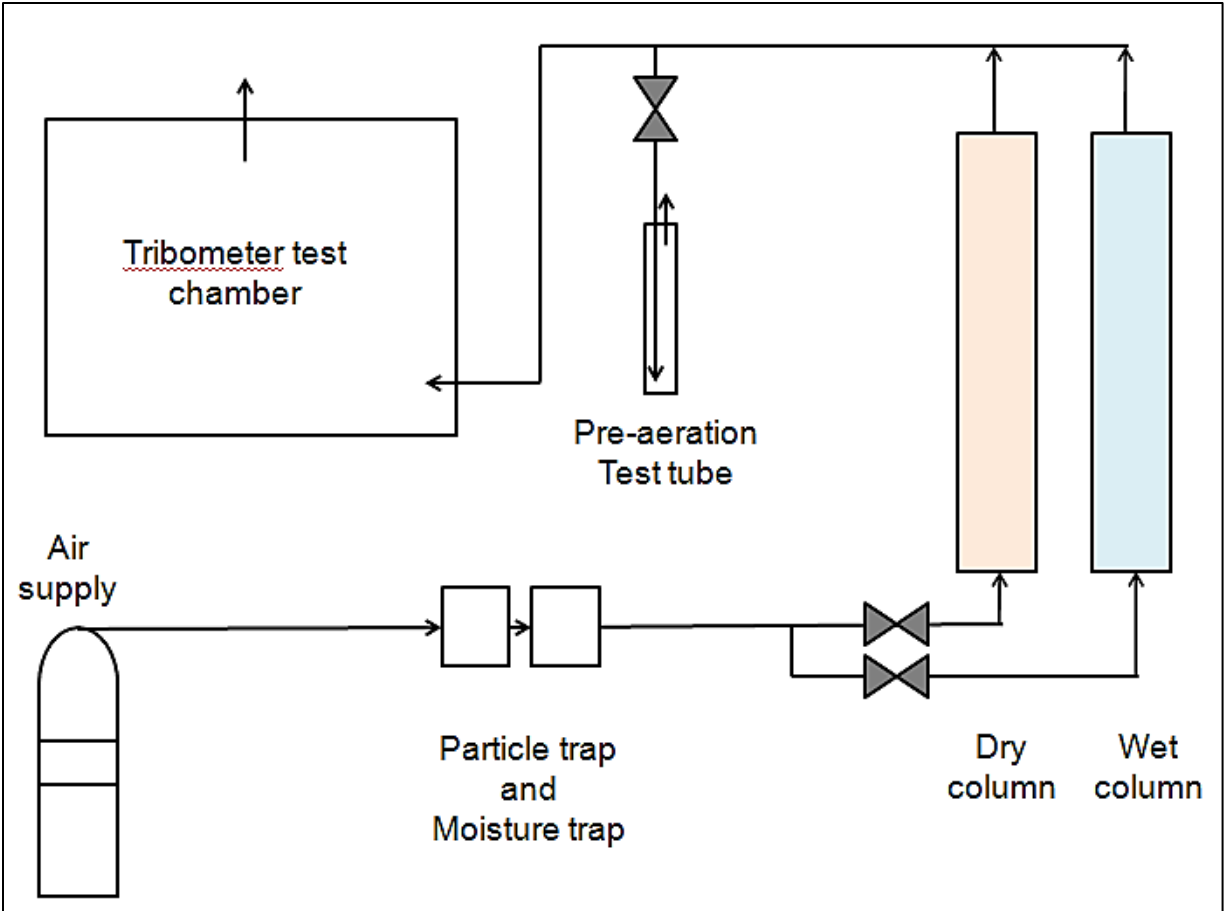


Figure 5.9: Humidity control setup, adopted from Langenhoven (2014).